

KING'S COLLEGE LONDON

DOCTORAL THESIS

A Multimodal Spatiotemporal Atlas for Cardiac Functional Assessment

Author:

Esther PUYOL ANTON

King's College supervisors:

Andrew KING

Julia SCHNABEL

Philips supervisors:

Paolo PIRO

Mathieu DE CRAENE

Hélène LANGET

*A thesis submitted in fulfillment of the requirements
for the degree of Doctor of Philosophy in the*

School of Biomedical Engineering & Imaging Sciences
King's College London

November, 2018



KING'S
College
LONDON

EPSRC
Engineering and Physical Sciences
Research Council

Abstract

The estimation of cardiac motion is an important aid in the quantification of the contractility and function of the left ventricular myocardium, as well in detecting cardiovascular disease. A statistical cardiac motion atlas provides a space in which the motions of a cohort of subjects can be directly compared. Statistical atlases have been proposed for characterising abnormal cardiac motion, as well as for detecting suspected disease as early as possible. Typically, such atlases are formed and applied using data from the same modality, e.g. cardiac magnetic resonance (MR) or 3D ultrasound (US). This thesis proposes a new pipeline to build a multi-modal cardiac atlas from both MR and US data. The hypothesis is that such an atlas will benefit from the synergies between the motion features derived from the two modalities.

The processing pipeline of the multimodal motion atlas formation initially involves normalisation of subjects' cardiac geometry and motion both spatially and over time, and extraction of motion descriptors, i.e. displacements. This step was accomplished following a similar pipeline proposed by other authors for single modality atlas formation. The main novelty of this project lies in the use of a dimensionality reduction algorithm to simultaneously reduce the dimensionality of both the MR and US derived motion data. Three different dimensionality reduction algorithms were investigated: Principal component analysis (PCA), Canonical correlation analysis (CCA), and Partial least squares regression (PLS). A leave-one-out cross validation was employed to quantify the accuracy of the three algorithms. Results show that Partial least squares regression resulted in lower errors, with a reconstruction error less than 2.5 mm for MR-derived motion data, and less than 3 mm for US-derived motion data.

The second part of the project aims to describe a diagnostic pipeline which uses as input only US data, but is at the same time informed by a training database of multimodal MR and US data. To this end, the previous multimodal cardiac motion atlas is used together with multi-view machine learning algorithms to combine and extract the most meaningful cardiac descriptors for classification using only US data. More specifically, two algorithms are proposed: multi-view linear discriminant analysis (MLDA) and multi-view Laplacian support vector machines (MvLapSVM). Furthermore, a novel regional multi-view approach is proposed to exploit the regional relationships between the two modalities. The proposed pipeline is evaluated on the classification task of discriminating between normals and patients with dilated cardiomyopathy. Results show that the use of multi-view classifiers together with a cardiac motion atlas results in a statistically significant improvement in accuracy compared to classification without the multimodal atlas. The highest accuracy for the global approach was achieved with the MvLapSVM algorithm and was 93.78%. In the regional case the highest accuracy was 95.78% using MvLapSVM.

Finally, the framework is extended to integrate automatically estimated strain values, and the strain values are used to validate the proposed pipeline for atlas formation and identification of DCM patients. Results show similar patterns using displacement and strain values. However, strain values consistently have slightly higher errors than displacement values.

Overall, I expect that the work presented in this thesis will have a significant impact on the assessment of cardiac function by enabling the exploitation of complementary information from multiple imaging modalities.

Acknowledgements

This thesis is the result of four years of hard work, persistence and devotion, yet its completion would not have been possible without the continuous support of many academics, colleagues, friends and family.

I would like to express my deep gratitude to my first supervisor, Dr. Andrew King, for his support, continuous guidance, stoic patience, immense knowledge and useful remarks through my learning process in this PhD. It is hard to imagine how I could succeed in this journey without his guidance. I am also very thankful to my second supervisors, Professor Julia Schnabel and Dr. Paul Aljabar for our frequent meetings in which they gave me the benefit of their vast experience and meticulous suggestions, which helped me to widen my research from various perspectives.

I would like to record my gratitude to my industrial supervisors, Dr. Paolo Piro, Dr. Mathieu de Craene and Dr. Hélène Langet for their encouragement, insightful comments and questions during our regular meetings. In addition I am thankful to them for all the good moments spent in Paris during my visits.

Thanks must be extended to all my colleagues in the School of Biomedical Engineering & Imaging Sciences for their support, daily companionship, multiple lunch times and pub evenings which made me feel at home. I want to specifically thank all other CDT students, I have been lucky to be a part of this group that has provided me with inspiration, energy and friendships. I would like to thank Emily, Giovanna and Adela, my close colleagues and friends, who were always there for me, both professionally and personally. Special thanks to Bram not only for all your hard work and help, your incredible insights and countless discussion, but more importantly, for all the coffee breaks, great conferences trips and good moments.

Outside of work, I'd like to thank my friends Anna, Cris, Monica, Jandro, Alberto, Jesus and Maria, who have been there during the difficult moments and have helped me keep sane and let go of work with dinners, drinks and trips. I am also very grateful for keeping our friendship strong, regardless of the distance.

Most of all, I would like to thank my parents for their constant encouragements, and for instilling in me the necessary strength, commitment and fortitude to undertake this task. Nothing would have been possible without their infinite love, support and trust.

Lastly, I would like to thank Marc, who decided to move to London with me four years ago, leaving a promising job in Paris to pursue my dream. He supported me during this time as a friend and partner by sharing the good and the bad of this journey. This thesis wouldn't be possible without you.

Esther Puyol Antón, November 2018

Publications

- E. Puyol-Antón, D. Peressutti, P. Aljabar, M. De Craene, P. Piro, and A.P. King. Towards a multimodal cardiac motion atlas. In *Biomedical Imaging (ISBI), 2016 IEEE 13th International Symposium on*, pages 32–35. IEEE, 2016
- E. Puyol-Antón, M. Sinclair, B. Gerber, M.S. Amzulescu, H. Langet, M. De Craene, P. Aljabar, P. Piro, and A.P. King. A multimodal spatiotemporal cardiac motion atlas from MR and ultrasound data. *Medical image analysis*, 40:96–110, 2017b
- E. Puyol-Antón, , M. Sinclair, B. Gerber, M.S. Amzulescu, H. Langet, M. De Craene, P. Aljabar, J. Schnabel, P. Piro, and A.P. King. Multiview machine learning using an atlas of cardiac cycle motion. In *International Workshop on Statistical Atlases and Computational Models of the Heart*, pages 3–11. Springer, 2017a
- E. Puyol-Antón, B. Ruijsink, W. Bai, H. Langet, M. De Craene, J.A. Schnabel, P. Piro, A.P. King, and M. Sinclair. Fully automated myocardial strain estimation from cine MRI using convolutional neural networks. In *Biomedical Imaging (ISBI 2018), 2018 IEEE 15th International Symposium on*, pages 1139–1143. IEEE, 2018a
- E. Puyol-Antón, B. Ruijsink, B. Gerber, M.S. Amzulescu, H. Langet, M. De Craene, J. Schnabel, P. Piro, and A.P. King. Regional multi-view learning for cardiac motion analysis: Application to identification of dilated cardiomyopathy patient. *IEEE Transactions on Biomedical Engineering*, 2018b

- E. Puyol-Antón, B. Ruijsink, H. Langet, M. De Craene, J.A. Schnabel, P. Piro, and A.P. King. Learning associations between clinical information and motion-based descriptors using a large scale MR-derived cardiac motion atlas. In *International Workshop on Statistical Atlases and Computational Models of the Heart*. Springer, 2018c
- B. Ruijsink, E. Puyol-Antón, M. Usman, J. van Amerom, P. Duong, M.N. Velasco Forte, K. Pushparajah, A. Frigiola, D.A. Nordsletten, A.P. King, et al. Semi-automatic cardiac and respiratory gated MRI for cardiac assessment during exercise. In *Molecular Imaging, Reconstruction and Analysis of Moving Body Organs, and Stroke Imaging and Treatment*, pages 86–95. Springer, 2017
- M. Sinclair, D. Peressutti, E. Puyol-Antón, W. Bai, M. Nordsletten, D. Hadjicharalambous, E. Kerfoot, T. Jackson, S. Claridge, C.A. Rinaldi, D. Rueckert, and A.P. King. Learning optimal spatial scales for cardiac strain analysis using a motion atlas. In *International Workshop on Statistical Atlases and Computational Models of the Heart*, pages 57–65. Springer, 2016
- M. Sinclair, W. Bai, E. Puyol-Antón, O. Oktay, D. Rueckert, and A.P. King. Fully automated segmentation-based respiratory motion correction of multiplanar cardiac magnetic resonance images for large-scale datasets. In *International Conference on Medical Image Computing and Computer-Assisted Intervention*, pages 332–340. Springer, 2017
- M. Sinclair, D. Peressutti, E. Puyol-Antón, W. Bai, S. Rivolo, J. Webb, S. Claridge, T. Jackson, D. Nordsletten, M. Hadjicharalambous, et al. Myocardial strain computed at multiple spatial scales from tagged magnetic resonance imaging: Estimating cardiac biomarkers for CRT patients. *Medical image analysis*, 43:169–185, 2018

- I. Oksuz, B. Ruijsink, E. Puyol-Antón, B. Aurelien, G. Cruz, C. Prieto, D. Rueckert, J.A. Schnabel, and A.P. King. Motion artefact detection for automatic quality assessment of large imbalanced cardiac MRI datasets. In *Medical Image Computing and Computer-Assisted Intervention–MICCAI 2018*. Springer, in press 2018
- I. Oksuz, B. Ruijsink, E. Puyol-Antón, M. Sinclair, D. Rueckert, J.A. Schnabel, and A.P. King. Automatic left ventricular outflow tract classification for accurate cardiac MR planning. In *Biomedical Imaging (ISBI), 2012 9th IEEE International Symposium on*, pages 462–465. IEEE, 2018

Contents

Abstract	i
Acknowledgements	iii
Publications	v
List of Figures	xi
List of Tables	xiv
Symbols and Abbreviations	xvi
1 Introduction	1
1.1 Motivation	1
1.2 Contributions	2
1.3 Outline	3
2 Clinical Background	5
2.1 Cardiac anatomy and function	5
2.2 Non invasive cardiac imaging	8
2.2.1 Cardiovascular magnetic resonance	8
2.2.2 Ultrasound	10
2.2.3 Other imaging techniques	12
2.3 Clinical descriptors of cardiac function	13
2.3.1 Global functional analysis	14
2.3.2 Motion and Deformation Analysis	17
2.4 Cardiovascular disease	20
2.4.1 Dilated cardiomyopathy	20
2.4.2 Ischaemic heart disease	23
2.5 Discussion	24
3 Machine learning and cardiac atlases	25
3.1 Machine learning	25
3.1.1 Single-view machine learning	26
3.1.2 Multi-view machine learning	30
3.2 Cardiac atlases	34
3.2.1 Anatomical atlases	34
3.2.2 Motion atlases	35
3.3 Statistical cardiac motion atlases	39

4 Materials	43
4.1 Multimodal data set	43
4.2 UK Biobank data set	47
5 Multimodal cardiac motion atlas formation	48
5.1 Introduction	48
5.2 Methods	49
5.2.1 LV geometry definition	50
5.2.2 MR/US alignment	50
5.2.3 LV motion estimation	52
5.2.4 Temporal normalisation	53
5.2.5 Spatial normalisation	55
5.2.6 Medial surface generation	56
5.2.7 Motion reorientation	57
5.2.8 Transform to local coordinate system	57
5.2.9 Remove vertices outside the FoV	58
5.2.10 Dimensionality reduction	58
5.2.11 Atlas application	61
5.3 Experiments and results	61
5.3.1 Error measures	62
5.3.2 UK Biobank data set experiments	64
5.3.3 Multimodal data set experiments	69
5.4 Discussion and conclusion	81
6 Multi-view classification	84
6.1 Introduction	84
6.2 Methods	85
6.2.1 Motion atlas formation	86
6.2.2 Multi-view classification: A global approach	86
6.2.3 Multi-view classification: A regional approach	89
6.3 Experiments and results	90
6.3.1 Cross validation and evaluation metrics	91
6.3.2 Evaluation of global multi-view learning methods	92
6.3.3 Evaluation of regional multi-view learning methods	96
6.3.4 Clinical validation	99
6.4 Discussion and conclusion	100
7 Strain analysis	103
7.1 Methods	105
7.1.1 Automatic 2D strain computation from cine MR data	105
7.1.2 3D strain for TAG and US data	111
7.1.3 Integration of 3D strain with atlas	115
7.2 Experiments and results	116
7.2.1 2D strain	116
7.2.2 3D strain values	122
7.2.3 Experiments	122

7.2.4	Integration of 3D strain values with motion atlas	128
7.3	Discussion and Conclusion	132
8	MR reference ranges for cardiac function from a large population	134
8.1	Methods	135
8.2	Materials	140
8.3	Experiments	141
8.3.1	Results: Reference ranges for ventricular global function .	142
8.3.2	Results: Reference ranges for strain values	150
8.4	Discussion and Conclusion	156
9	Conclusion	158
9.1	Summary	158
9.2	Clinical impact	159
9.3	Current Limitations and Future Directions	161
9.4	Conclusions	163
A	Exclusion criteria for UK Biobank	164
	Bibliography	168

List of Figures

2.1	Schematic diagram of the heart and main vessels attached to it.	6
2.2	Wiggers diagram showing different physiological parameters in a cardiac cycle.	7
2.3	Examples of cine MR sequence.	9
2.4	Examples of 3D TAG MR sequence.	10
2.5	Illustration of a 3D ultrasound acquisition.	11
2.6	2-D measurements for volume calculations using the biplane method of discs.	15
2.7	LVV curve for a cardiac cycle.	16
2.8	The effect of DCM on the geometry of the heart.	21
4.1	Examples of MR and 3D US acquisitions for a healthy volunteer and a patient suffering from DCM.	46
5.1	Overview of the proposed framework for spatiotemporal cardiac motion atlas formation.	49
5.2	Examples of estimated LV geometry at end-diastole overlaid onto 3 orthogonal slices from a cine MR SA, and US. Example of MR/US registration.	51
5.3	MR displacement field from the B-spline FFD registration in three orthogonal views.	52
5.4	US displacement field from the B-spline FFD registration in three orthogonal views.	53
5.5	Example of an MR and US LVV curve before and after temporal normalisation.	55
5.6	Illustration of the spatial normalisation step.	56
5.7	Illustration of the medial surface generation step.	57
5.8	Example of medial mesh with points outside FoV in black and divided into AHA regions.	58
5.9	Illustration of the metrics used for validation.	62
5.10	Pipeline for generating synthetic US derived displacement from the UK Biobank data set.	65
5.11	Reconstruction error for the UK Biobank data set for CCA, PLS and PCA.	67
5.12	Prediction errors for the UK Biobank data set for CCA, PLS and PCA and Pearson's correlation coefficient between the MR and US displacement data for the different Gaussian noise levels used.	68
5.13	Mean errors for the multimodal data set.	70

5.14	US LV volume before and after applying dimensionality reduction algorithms.	71
5.15	Rescaled LV volume for each subject over the cardiac cycle before applying the proposed temporal normalisation, after applying temporal normalisation and after rescaling with respect to the length of the cardiac cycle.	75
5.16	Mean errors for the multimodal data set using the proposed temporal normalisation, and using global rescaling by cardiac cycle length.	76
5.17	Euclidean distance between mean MR and US motion for PLS.	77
5.18	AHA segments on the base for the ED frame on MR and US, and the 17 standardised AHA segments.	77
5.19	Mean Euclidean distance between mean MR motion and the motion of each subject in the multimodal data set.	78
5.20	Mean Euclidean distance between mean US motion and the motion of each subject in the multimodal data set.	79
5.21	First 2 modes of variation for PLS with colour bars representing the Euclidean distance between the mean MR reconstructed medial mesh and the σ reconstructed medial mesh.	80
6.1	Overview of the proposed framework for forming and applying a motion atlas-based multi-view learning approach.	85
6.2	Overview of the proposed framework for the regional approach for multi-view classification.	90
6.3	Different approaches for classification: proposed method, single modality methods and multiple modality two-step method.	93
6.4	Weights for the majority voting scheme in the regional approach for classification.	98
6.5	Relationship between LVEF and misclassification rate for the preferred method for the global approach and the regional approach.	99
7.1	Overview of the proposed framework for automatic quantification of myocardial strain from cine MR sequence.	105
7.2	The VGG-like FCN architecture with 17 convolutional layers used for segmentation.	106
7.3	Example of motion correction algorithm, myocardial label in the SA and LA views is shown before and after alignment.	107
7.4	Example of motion tracking between ED and ES frame, showing the magnitude of the displacement field, and displacement field for components x,y and z.	107
7.5	Schema of the SA and LA segments with radial distance and circumferential distance.	108
7.6	Framework to generate the layers and segments of the myocardium.	110
7.7	Overview of the proposed framework for computing strains from 3D MR and 3D US images.	111
7.8	LV geometry definition and fitting volumetric dense mesh.	113
7.9	Strain computation from the hexahedral dense mesh.	114

7.10 Examples of estimated strains for a healthy volunteer and an is- chemic patient. Figure shows global strain curves, peak strain and TPK.	118
7.11 Bland Altman plots between CVI ₄₂ and the proposed pipeline for peak longitudinal and radial LA global strain.	120
7.12 Bland Altman plots between CVI ₄₂ and the proposed pipeline for peak radial and circumferential SA global strain.	121
7.13 Examples of estimated strains for a healthy volunteer and a DCM patient.	122
7.14 Examples of estimated strains for a healthy volunteer and a DCM patient from 3D US data.	123
7.15 Mean errors for embedding distance, reconstruction error and pre- diction error for the multimodal data set using estimated strain values.	128
7.16 Weights for the majority voting scheme in the strain regional ap- proach for classification.	131
8.1 Example of images with insufficient quality.	136
8.2 Examples of LV unrealistic curves excluded for the analysis.	137
8.3 Examples of automatic segmentation.	138
8.4 Example of realistic and unrealistic strain cruves.	139
8.5 Case selection flowchart for ventricular and strain analysis.	141

List of Tables

4.1	Study demographics: end-diastolic volume, end-systolic volume, ejection fraction and LV mass.	45
5.1	Mean and standard deviation of the errors with respect to the ground truth for LVESV, LVM and LVEF for the different dimensionality reduction algorithms.	72
5.2	Mean Euclidean distance for the longitudinal, radial and circumferential axes for the first 2 modes of variation for PLS.	81
6.1	US-based classification balanced accuracy, sensitivity and specificity of the proposed and comparative methods and Student's t-test results.	94
6.2	MR and US classification balanced accuracy, sensitivity and specificity of the proposed and comparative methods.	95
6.3	US-based classification balanced accuracy, sensitivity and specificity of global and regional approaches and Student's t-test results.	97
6.4	MR and US classification balanced accuracy, sensitivity and specificity of global and regional approaches and Student's t-test results.	98
6.5	Comparison between LVEF classifier and regional non-linear multi-view classifier: balanced accuracy, sensitivity and specificity and Student's t-test results.	100
7.1	Study demographics: end-diastolic volume, end-systolic volume, ejection fraction and age.	117
7.2	Comparison of strain results derived from CVI ₄₂ and the proposed pipeline for the healthy cohort.	119
7.3	Comparison of strain results derived from CVI ₄₂ and the proposed pipeline for the ischemic patients.	119
7.4	Estimated strain values from TAG and 3D US data on the multimodal database	124
7.5	Estimated longitudinal regional strain values from TAG and 3D US data on the multimodal database.	125
7.6	Estimated radial regional strain values from TAG and 3D US data on the multimodal database.	126
7.7	Estimated circumferential regional strain values from TAG and 3D US data on the multimodal database.	127

7.8	US derived strain classification accuracy, sensitivity and specificity of global and regional approaches using the estimated strain values and <i>t</i> —test results.	130
7.9	MR and US derived strain classification accuracy, sensitivity and specificity of global and regional approaches and <i>t</i> —test results.	131
8.1	Baseline characteristics for the healthy cohort from the UK Biobank data set.	140
8.2	LV global function reference ranges and LV filling and ejection rate for the healthy population regardless of their age groups, and then by gender.	145
8.3	LV global function reference ranges in a traffic light format for Caucasian man.	146
8.4	LV global function reference ranges in a traffic light format for Caucasian woman.	147
8.5	LV global reference function ranges for Caucasian man detailing mean, lower reference limit and upper reference limit by age group.	148
8.6	LV global reference function ranges for Caucasian woman detailing mean, lower reference limit and upper reference limit by age group.	149
8.7	LV strain reference ranges for the healthy population regardless of their age groups, and then by gender.	151
8.8	LV strain reference ranges for Caucasian man in a traffic light format.	152
8.9	LV strain reference ranges for Caucasian woman in a traffic light format.	153
8.10	LV strain reference ranges for Caucasian man detailing mean, lower reference limit and upper reference limit by age group.	154
8.11	LV strain reference ranges for Caucasian woman detailing mean, lower reference limit and upper reference limit by age group.	155

Symbols and Abbreviations

Chapter 1: Abbreviations

CT	Computed Tomography
DCM	Dilated cardiomyopathy
LV	Left Ventricle
MR	Magnetic resonance
MWMA	Myocardial wall motion analysis
TAG	Tagged MR
US	Ultrasound

Chapter 2: Abbreviations

2Ch	2-chamber
4Ch	4-chamber
AC	Atrial contribution
CO	Cardiac output
CVD	Cardiovascular disease
ED	End diastolic
ES	End systolic
FoV	Field-of-view
HF	Heart failure
HR	Heart rate
IHD	Ischaemic heart disease
LA	Long-axis cine MR
LVEDV	LV end diastolic volume
LVESV	LV end systolic volume
LVEF	LV ejection fraction
LVM	Left Ventricular Mass

LVSV	LV stroke volume
LVV	Left ventricular volume
PAFR	Peak atrial filling rate
PER	Peak ejection rate
PET	Positron emission tomography
PFR	Peak filling rate
RF	Radio frequency
RV	Right ventricle
SA	Short-axis cine MR
SPECT	Single-photon emission computed tomography
SSFP	Steady State Free Precession
SR	Strain rate

Chapter 3: Abbreviations

AHA	American Heart Association
CCA	Canonical correlation analysis
CAP	Cardiac Atlas Project
ICA	Independent component analysis
FFD	Free-form deformation
LDA	Linear discriminant analysis
ML	Machine learning
MED	Maximum entropy discrimination
MKL	Multiple kernel learning
MvML	Multi-view machine learning
PCA	Principal component analysis
SDE	Shannon's Differential Entropy
SPM	Statistical parametric mapping
SVM	Support vector machine

Chapter 4: Abbreviations

ICD	International Classification of Diseases
-----	--

Chapter 5: Abbreviations

IRTK	Image Registration Toolkit
GT	Ground truth
NIPALS	Nonlinear iterative partial least squares
PLS	Partial least squares regression
SSM	Statistical shape model

Chapter 5: Symbols

n, N	Cardiac phase, total number of cardiac phases
k, K	Subject, total number of subjects
m	vertex of the mesh
D	Size of the MR and US-derived matrix displacements
L	Number of components retained by the dimensionality reduction algorithm
σ_l	Standard deviation of the combined MR/US cloud formed by the embedding
$\mu_R, \sigma_R, \mu_M, \sigma_M$	Mean and standard deviation of a Gaussian distribution
$\mathbf{v}_{m,n,k}$	Spatial coordinates of vertex m of the mesh
$\psi^{3D+n}(\mathbf{v}, n)$	3D+ n transformation
ϕ_{aff}^k	Affine transformation
$\tilde{\phi}_{aff}$	Average affine transformation
$\hat{\phi}_{aff}^k$	Average similarity transformation
ϕ_{TPS}^k	Thin Plate Spline transformation
ϕ^k	Transformation from the subject-specific coordinate system to the unbiased LV mesh
$\mathbf{u}_{m,n,k}$	LV displacement
$\mathbf{u}_{m,n,k}^{atlas}$	LV displacements in the atlas coordinate system.
$\mathbf{J}_{\phi^k(\mathbf{v}_{m,ED,k})}$	Jacobian of the anatomical transformation
$\mathbf{x}_{m,n,k}$	MR-derived displacements on the local coordinate system
$\mathbf{z}_{m,n,k}$	US-derived displacements on the local coordinate system
$\dot{\mathbf{x}}_k$	MR-derived displacements row vector on the local coordinate system

$\dot{\mathbf{z}}_k$	US-derived displacements row vector on the local coordinate system
X	MR-derived displacements matrix
Z	US-derived displacements matrix
C_{xx}	Covariance matrices of MR
C_{xx}	Covariance matrices of US
C_{xz}	Cross-covariance matrices of MR/US
C_{zx}	Cross-covariance matrices of US/MR
λ_{PCA}	Eigenvalues of PCA algorithm
λ_{PLS}	Eigenvalues of PLS algorithm
λ_{CCA}	Eigenvalues of CCA algorithm
\mathbf{w}_x	Projection matrices computed from X using a dimensionality reduction algorithm
\mathbf{w}_z	Projection matrices computed from Z using a dimensionality reduction algorithm
$\hat{\mathbf{x}}_k$	Reconstructed \mathbf{x}_k vector
$\hat{\mathbf{z}}_k$	Reconstructed \mathbf{z}_k vector
α_k	Embedded X vector
γ_k	Embedded Z vector
$E_d^k(MR - US)$	Embedding distance
$E_D^k(MR - MR)$	Reconstruction error for MR
$E_D^k(US - US)$	Reconstruction error for US
$E_D^k(MR - US)$	Prediction error

Chapter 6: Abbreviations

BACC	Balanced accuracy
MLDA	Multi-view linear discriminant analysis
y MvLapSVM	Multi-view Laplacian support vector machines
y RBF	Radial basis function
y RSCV	Repeated stratified cross-validation
SEN	Sensitivity
SPE	Specificity
TP	True positives
TN	True negatives

FP	False positives
FN	False negatives

Chapter 6: Symbols

D_s	Size of the MR and US-derived matrix displacements by AHA segment
LL	Number of classes
σ_{RBF}	RBF kernel was used, and the
S_{bx}	Between-class matrices for MR
S_{bz}	Between-class matrices for US
γ	Regularisation parameter
α_x	Weight vectors for MR
α_z	Weight vectors for US
ξ_x	Slack variables for MR
ξ_z	Slack variables for US
G_x	Gram matrices for MR
G_z	Gram matrices for US
L_x	Graph Laplacian for MR
L_z	Graph Laplacian for US
K_x	Kernel matrices for MR
K_z	Kernel matrices for US
$y_i \in \{-1, 1\}^K$	Classification labels
$k(\cdot, \cdot)$	Kernel function
μ_i	mean of X in the class i
τ_k	Embedded vector for subject k
\hat{y}_k	Predicted label
\hat{y}_k^s	Predict a label for AHA region s
$\mathbf{g}_{x,k}$	Gram matrices from views X for subject k
$\mathbf{g}_{z,k}$	Gram matrices from views Z for subject k
$\dot{\mathbf{x}}_k^{AHA_s}$	MR displacements in atlas space by AHA segment
$\dot{\mathbf{z}}_k^{AHA_s}$	US displacements in atlas space by AHA segment
X_{AHA_s}	MR-derived displacements matrix for AHA segment s
Z_{AHA_s}	MR-derived displacements matrix for AHA segment s

Chapter 7: Abbreviations

BN	Batch-normalisation
ICC	Interclass correlation coefficient
MR-FT	MR feature tracking
FCN	Fully-convolutional network
ReLU	Rectified linear unit
SD	Standard deviation
TPK	Time to peak

Chapter 7: Symbols

v	View (SA or LA)
cc	Circumferential
ll	Longitudinal
rr	Radial
j	Strain component (cc , rr or ll)
s, S	Segment, total number of segments
q, Q	Layer, total number of layers
v	View (i.e. SA or LA)
d_r	Radial distance
d_c	Circumferential distance
z	Edge of the mesh
d_z^n	Length of edge z at cardiac phase n for subject k
$d_{j,v,k,s}^{ED}$	Length at ED for the segment
d_c	Circumferential segment arclength
d_r	Transmural distance
$E_{j,v}^n$	Strain component j
$E_{cc,SA}^n$	Circumferential strain from SA sequence
$E_{ll,LA}^n$	Longitudinal strain from LA sequence
$E_{rr,SA}^n$	Radial strain from SA sequence
$E_{rr,LA}^n$	Radial strain from LA sequence
$\epsilon_{m,n,k}$	Strain for hexahedral mesh on Euclidean coordinate system
$E_{m,n,k}$	Strain for hexahedral mesh on local coordinate system
$E_{m,n,k}^{atlas}$	Strain for hexahedral mesh on local coordinate system in the atlas space.

$\hat{e}_{rr}, \hat{e}_{cc}, \hat{e}_{ll}$	Unit column vectors in the radial, circumferential and longitudinal direction
$F_{m,n,k}$	Strain tensor
$F_{m,t,k}^{atlas}$	Strain tensor on the atlas space

Chapter 8: Abbreviations

BMI	Body mass index
BSA	Body surface area
QC	Quality control
RVEDV	RV end diastolic volume
RVESV	RV end systolic volume
RVEF	RV ejection fraction
RVSV	RV stroke volume
HFpEF	Heart failure with preserved ejection fraction

Chapter 8: Symbols

$E_{ll,LA\ 2CH}$	Longitudinal strain from 2Ch LA sequence
$E_{ll,LA\ 4CH}$	Longitudinal strain from 4Ch LA sequence
$E_{rr,SA}$	Radial strain from SA sequence
$E_{cc,SA}$	Circumferential strain from SA sequence

1 | Introduction

1.1 Motivation

Accurate assessment of cardiac function is crucial in aiding diagnosis for a wide range of cardiovascular pathologies as well as for optimisation of related clinical procedures. Left-ventricular (LV) function has been traditionally assessed using global indicators such as ejection fraction, stroke volume or ventricular mass. The main drawback of such indicators is that they do not provide localised information about ventricular function, and so their diagnostic power is limited. Myocardial wall motion analysis (MWMA) offers a potential solution to this problem. Using MWMA, myocardial wall motion is assessed from imaging data resulting in parameters such as displacements, velocities, strains and strain rates. This allows for a more spatially and temporally localised assessment of LV function.

3D tagged (TAG) magnetic resonance (MR) imaging is increasingly accepted as the gold standard for MWMA due to its excellent image contrast and coverage ([Jasaityte et al., 2013](#)). However, its clinical use is limited by lack of access to scanners, high acquisition cost and a lack of expertise in acquiring the data. Instead, ultrasound (US) is commonly used in the clinic due to its low acquisition cost and portability. However, coverage of the heart using US is restricted due to limited acoustic windows.

In recent years, cardiac atlases have been proposed as a way of analysing cardiac motion in the context of population variation, and MWMA parameters such as displacements and velocities have been exploited in such approaches. Typically, cardiac motion atlases have focused on the LV, as it is the chamber primarily investigated for diagnosing cardiac diseases.

To date, all such techniques have been based on motion information estimated from a single imaging modality (MR, US or Computed Tomography (CT)). Several factors suggest that information from multiple modalities may be complementary and offer advantages. For instance, the spatial and/or temporal resolutions of the modalities may differ, or motion tracking algorithms may exploit different imaging characteristics such as speckle in US. Therefore, using the combined information may provide a richer description of cardiac function.

The first part of this thesis seeks to develop and evaluate methods for building a multimodal cardiac motion atlas from MR and US data, which would be able to relate the MWMA parameters derived from the two modalities. This will open up the possibility of exploiting this relationship to enable a diagnostic pipeline based on US data that is at the same time informed by a training database of multimodal (MR and US) data, which is the focus of the second part of the thesis.

1.2 Contributions

The original contributions of this thesis to the field of cardiac motion atlases can be summarised as follows:

- **Multimodal atlas.** To date all previous works on cardiac motion atlases have been based on a single modality. The proposed multimodal cardiac motion atlas will combine imaging data from MR imaging, which is increasingly accepted as the gold standard for characterising cardiac function and anatomy, and US data, which is commonly used in the clinic for assessing cardiac function. A potential advantage of this multimodal cardiac motion atlas is that it could combine the strengths of both modalities.
- **Diagnostic pipeline.** A novel extension to the developed multimodal atlas is proposed to enable it to be applied to the task of identifying dilated cardiomyopathy (DCM) patients using only US data but at the same time taking advantage of the implicit relationship between MR and US learned from the atlas. This may provide a better understanding of the mechanisms responsible for the development and progression of this disease which could assist therapeutic planning and improve treatments.

- **Automatic strain assessment.** A fully automatic pipeline to quantify myocardial longitudinal, radial and circumferential strain from cine MR sequences is presented. This pipeline is then extended to work on TAG and US data and integrated into the motion atlas-based diagnostic pipeline. Strain is a MWMA parameter that is widely understood clinically and so its use may be beneficial for clinical translation.
- **Reference ranges of ventricular function.** The automatic strain assessment pipeline is applied to a large-scale database. To the best of the author’s knowledge this is the first time that strain values have been computed for such a large-scale database, and the ranges computed can provide a reference standard in clinical practice.

The next Section outlines how this thesis is organised and where each proposed method is described and evaluated.

1.3 Outline

The thesis is organised into 9 Chapters, which are outlined below.

Chapter 2 first provides an overview of currently available techniques for assessment of cardiac function, focusing on LV motion. In the second part of the Chapter, background is provided on the cardiovascular diseases on which this thesis will focus. The objective of this Chapter is to provide a clear description of the problem that this thesis seeks to address, namely the accurate assessment of cardiac function.

Chapter 3 first provides an overview of machine learning techniques, with a special focus on multi-view machine learning. In the second part of the Chapter, the most relevant works on atlas formation proposed in the literature are reviewed, emphasising the key contributions of each work.

Chapter 4 contains a summary of all the medical image datasets used in the experiments of Chapters [5-8](#).

Chapter 5 introduces a novel pipeline for cardiac motion atlas formation from TAG and 3D US data. In this Chapter three different multi-view subspace learning algorithms are evaluated using a large scale mono-modal data set and a smaller multimodal data set.

Chapter 6 presents a novel extension to the multimodal atlas developed in the previous Chapter and demonstrates its application of the task of identifying DCM patients using only US data but at the same time taking advantage of the implicit relationship between MR and US learned from the atlas. This is made possible by the proposal of two multi-view learning algorithms: a global and a regional approach. This is the first work that has combined multiple modalities' imaging data and a cardiac motion atlas for disease diagnosis using multi-view machine learning approaches.

Chapter 7 describes a fully automated pipeline to compute LV strain from cine long and short-axis MR imaging. In addition, an extension of the pipeline to TAG and 3D US data is presented. The last part of the Chapter integrates this strain estimation technique into the motion atlas-based diagnostic pipeline.

Chapter 8 applies the proposed automatic pipeline described in Chapter 7 to a the cohort of normal healthy Caucasian participants in the UK Biobank project, establishing reference values for LV function (i.e. volume and strain).

Chapter 9 summarises the main contributions presented in this thesis and describes some limitations of the proposed methods. Moreover, a discussion on the clinical impact of the methods is presented along with an overview of future directions. Finally, conclusions are drawn.

2 | Clinical Background

This Chapter provides the background information necessary to understand the clinical context within which the work of this thesis is situated. Section 2.1 presents an introduction to the basics of heart anatomy and function, focusing on the aspects that are relevant for cardiac atlas formation. A brief summary of the imaging modalities used in this work is presented in Section 2.2. Section 2.3 presents a survey of the most used clinical descriptors of cardiac function, followed by a brief overview of DCM and ischaemic heart disease (IHD) in Section 2.4. Finally, Section 2.5 summarises key concepts and issues that this work seeks to address.

2.1 Cardiac anatomy and function

The heart is a complex and efficient mechanical pump, designed to deliver blood to the entire body through the circulatory system. The human heart has the dual role of circulating both oxygenated and deoxygenated blood, by supplying blood to the two compartments of the cardiovascular system, the systemic and pulmonary networks. Because of this dual function, the human heart is divided into two functional halves (see Figure 2.1), the left and right heart, driving the systemic and pulmonary systems, respectively. Each side is comprised of two chambers, the atrium and the ventricle, whose significantly in structure and function. The atria are thin-walled reservoirs of which main function is to receive blood from the venous system, whereas the ventricles are thick-walled pumps, ejecting blood to the arterial system. The right ventricle (RV) is wrapped around the LV, and its wall connects on two sides of the LV. As a result, the RV utilises part of the LV as a wall and this shared wall is called the septum.

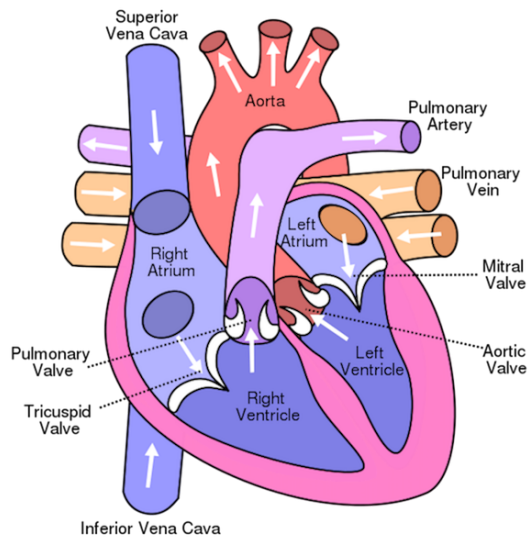


Figure 2.1: Schematic diagram of the heart and main vessels attached to it (figure adapted from Wikipedia – <https://en.wikipedia.org/wiki/Heart>).

The cardiac cycle is the periodic filling and ejection of blood from the ventricles, defined by the time interval between two successive RR peaks, where R is the point corresponding to the peak of the R wave in the QRS complex of the ECG. The repetition of the cardiac cycle is responsible for the rhythmical pumping function of the heart and for delivering blood to the entire body. A single cycle of cardiac activity can be divided into two basic phases (see Figure 2.2 for more details):

- *Diastole (ventricular filling):* The portion of the cycle when the ventricles are relaxed (not contracting). During this period blood from the left atrium fills the LV, leading to an increase in ventricular volume. Likewise, the same phenomenon runs simultaneously in the RV and right atrium. Diastole covers approximately two thirds of the cycle and it is commonly divided into four stages: isovolumetric relaxation, rapid inflow, diastasis and atrial systole. Diastole starts with the closure of the aortic and pulmonary valves (isovolumetric relaxation phase). Once ventricular pressure falls below atrial pressure, the atrioventricular valves open allowing blood to pass through the atria to the ventricles (rapid inflow phase). As diastole progresses, ventricular pressure rises and the rate of filling slows (diastasis phase). Subsequently, atrial systole occurs at end diastole (ED) causing a peak in atrial pressure providing an additional 20% of ventricular filling (atrial kick).

- *Systole:* The portion of the cycle during which blood is expelled rapidly out of the LV and into the aorta, and simultaneously oxygen-poor blood from the RV is pumped through the pulmonary valve and pulmonary artery to the lungs. Systole is divided into isovolumetric contraction and ejection. Ventricular systole initiates when the LV pressure increases sufficiently due to contraction, forcing the aortic valve to open. During this early contraction, ventricular pressure rises but there is no change in ventricular volume (isovolumetric contraction). Once the pressure in the LV and RV exceeds the pressure in the aorta and pulmonary artery, the aortic and pulmonary valves open and the ejection phase of systole begins. When the pressure in the ventricles falls below the pressure in the aorta and pulmonary artery, blood flow reverses briefly, causing the aortic and pulmonary valves to close, when the systole phase is complete.

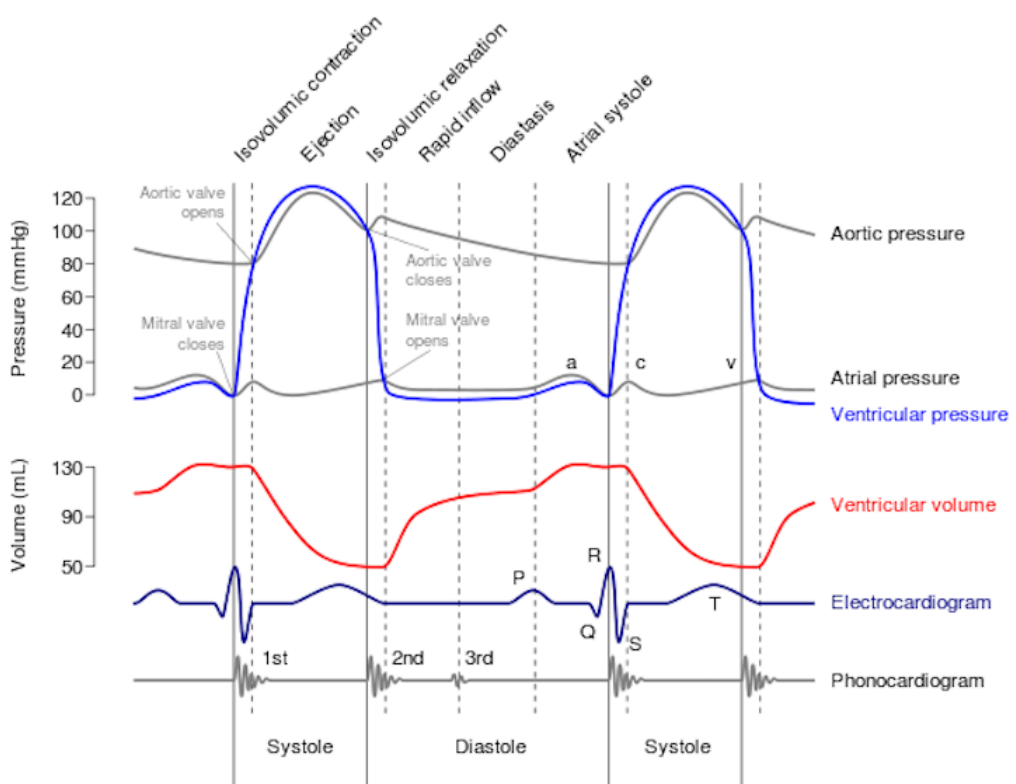


Figure 2.2: Wiggers diagram showing different physiological parameters in a cardiac cycle: pressure, volume and ECG (figure adapted from Wikipedia – https://commons.wikimedia.org/wiki/File:Wiggers_Diagram.png).

2.2 Non invasive cardiac imaging

Noninvasive cardiac imaging refers to several methods that can be used to obtain images related to the structure and function of the heart. As opposed to invasive techniques, which require catheters to be inserted into the heart, non-invasive tests are easier to perform, are generally safe, and can be used to detect various heart conditions, ranging from plaque in the arteries that supply the heart muscle to abnormalities that impair the ability of the heart to pump blood.

As mentioned in Section 1.1, the aim of this thesis is to build a multimodal cardiac motion atlas from MR and US data. This section aims to summarise the main characteristics of these two imaging modalities as well as their limitations for assessment of cardiac function. Section 2.2.1 describes in general terms MR imaging, followed by a description of US imaging in Section 2.2.2. Finally, Section 2.2.3 summarises other imaging techniques less used in a clinical setting to analyse cardiac function.

2.2.1 Cardiovascular magnetic resonance

MR is a non-invasive method of mapping the internal structure and certain aspects of function within the body. MR uses non-ionising electromagnetic radiation and radio frequency (RF) radiation in the presence of a high static magnetic field to produce high quality soft-tissue contrast images of the body in any plane. More specifically, MR imaging relies on positively charged hydrogen protons in the body, which when excited by a large magnetic field begin to spin at a frequency that is proportional to the strength of the magnetic field. The MR signal is generated by subjecting the atoms to RF pulsations, and the pulse sequences selected will determine the appearance of the image. By varying the parameters of the pulse sequence, different MR sequences have been proposed (Ridgway, 2010). In this thesis two different MR sequences are used:

- **Cine MR:** Steady State Free Precession (SSFP) is a family of sequences which are currently the backbone of cine MR imaging. SSFP produces high temporal resolution and excellent contrast MR images, and is a well-established tool to acquire anatomical and functional cardiac images. Different planes can be acquired (see Figure 2.3 for examples) but the most clinically used are short axis stack (SA), which shows a series of cross-sectional slices of the left and right ventricle, the 2-chamber (2Ch) long-axis (LA) view, which shows the LV, left atrium and mitral valve; the 3Ch LA view that shows the aortic valve, left ventricular outflow tract, mitral valve, LV and left atrium; and the 4Ch LA view that shows the four chambers of the heart and the mitral and tricuspid valves.

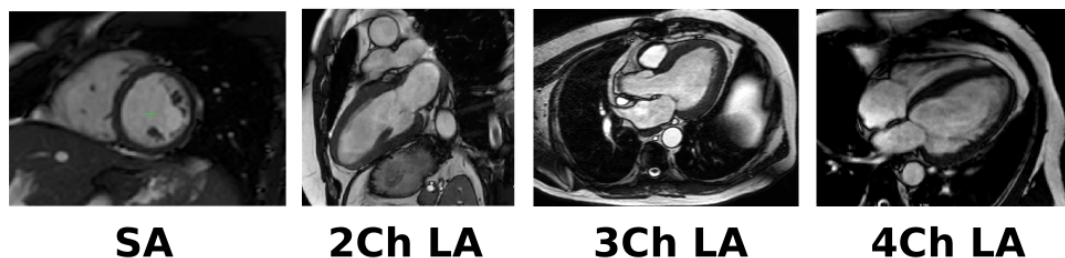


Figure 2.3: Examples of cine MR sequence, from left to right: multi-slice SA, 2Ch LA, 3Ch LA and 4CH LA sequence.

Using the SSFP sequence, it is possible to discriminate very well between blood and myocardium, and to easily track the radial motion of the myocardium. However, quantitative analysis of regional myocardial function in the longitudinal and circumferential axes is less accurate due to the lower number of LA images and a lack of contrast inside the myocardium ([Shi et al., 2012](#)).

- **TAG:** Myocardial tagging is a technique used to assess the regional function of the heart. Prior to the acquisition, TAG sequences modulate the magnetisation gradient to null the signal of the myocardium generating a grid pattern (myocardial tags). During the acquisition, the tags deform following the motion of the underlying tissue ([Young et al., 1993](#)). TAG images enable tracking of the motion of physiological points in the heart wall, which can be used to analyse the local wall motion. The main limitations of TAG images are the lower temporal resolution and the lack of anatomical information. Figure 2.4 shows an example of a TAG MR sequence in ED.

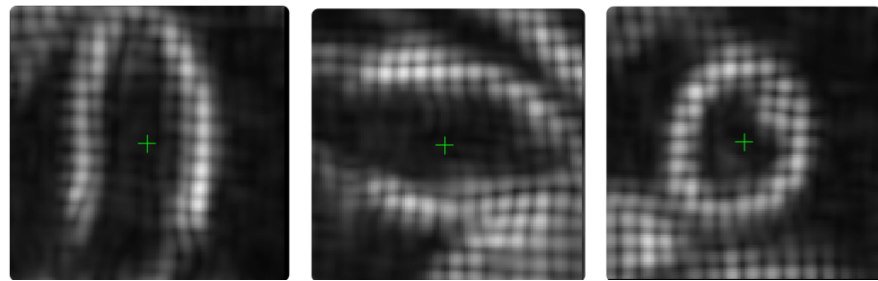


Figure 2.4: Examples of 3D TAG MR sequence.

The combination of these two MR modalities allows extraction of structural information from cine MR images and functional information from TAG images, that can be used to robustly estimate MR-based functional descriptors.

2.2.2 Ultrasound

Cardiac US, also known as echocardiography, uses US acoustic waves to map the interfaces between tissues. In particular, the acoustic waves are sent from the transducer, propagate through different tissues, and then return to the transducer as reflected echoes. The returned echoes are converted back into electrical impulses by the transducer crystals and are further processed to form the US image. Generally, US waves are affected by mechanical absorption, diffraction and scattering effects, that cause loss of energy and characteristic image artefacts, such as the speckle effect, tissue inhomogeneities, multiple and off-axis reflections and shadowing.

Several modes of US are used in medical imaging, but this thesis focuses on apical 3D US. 3D ultrasound usually acquires a large number of consecutive tomographic images using a 2D matrix array. Cardiac 3D US is normally gated to avoid distortion of the 3D data set due to movement. Tomographic images are rearranged according to the phase of the cardiac cycle and a 3D data set is reconstructed by combining only tomographic images at the same phase of the cardiac cycle. Figure 2.5 shows an example of a gating technique for 3D scanning of the heart, how the 3D volume is reconstructed from gated images, and a transthoracic apical 3D acquisition.

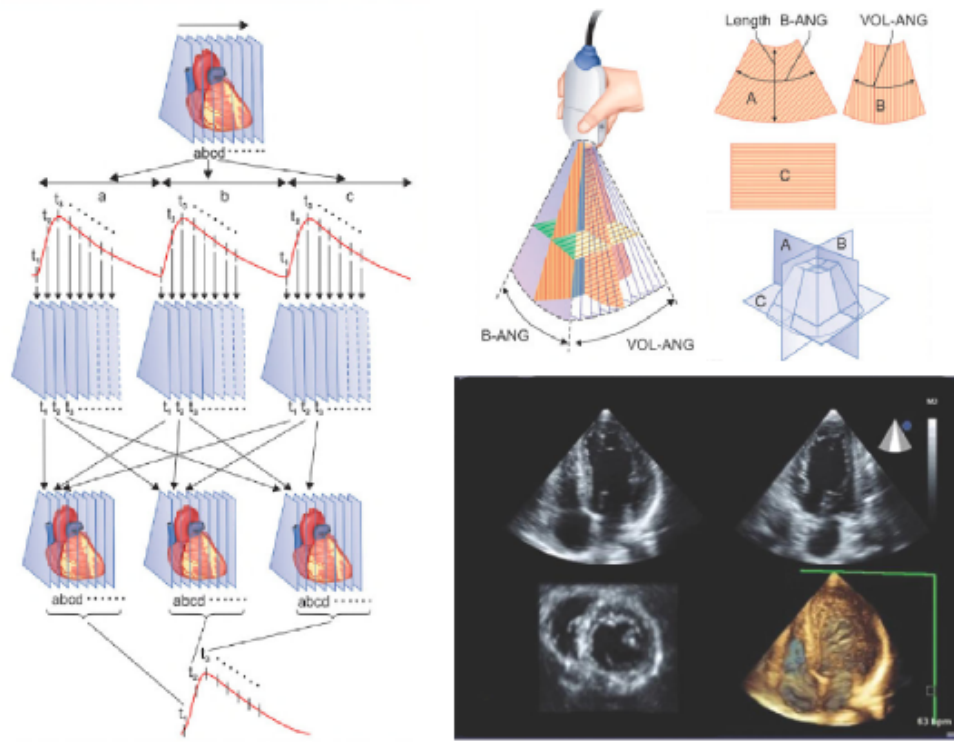


Figure 2.5: Illustration of a 3D ultrasound acquisition: **Left:** Example of a gating technique for 3D scanning of the heart, a set of consecutive tomographic images are acquired and rearranged according to the phase of the cardiac cycle; **Top right:** example of the principle of 3D real-time imaging and **Bottom right:** example of a transthoracic apical 3D acquisition (figure adapted from Pinto et al. (2004)).

Compared to the conventional 2D US, 3D US offers a number of advantages: (1) quantification of full cardiac chamber volumes (LV and RV) and their function; (2) visualisation of the 3D structure and dynamic motion of the heart, especially heart valves. The main limitations of 3D US compared to 2D are the lower temporal and spatial resolution, higher cost and therefore more limited availability in the clinic.

US imaging has a number of limitations that are related to the way that the images are formed. For instance, they can have missing regions in the cardiac wall, where the angle of incidence of the beam is too oblique. Other parts may be masked by speckle noise or hidden by shadowing artefacts. These areas can cause problems in the assessment of cardiac function since there is little information to base estimates on. Furthermore, US images typically consist of a cone-shaped region in the centre of the image, which contains the US signal, while the surrounding pixels do not contain any signal. Therefore, another challenge is that some parts of the heart (e.g. the apex) can be outside this field of view (FoV) of the US images.

2.2.3 Other imaging techniques

Although MR and US are the two main imaging modalities to assess cardiac function, other imaging modalities are also used and these are briefly described below:

X-ray is a form of ionising electromagnetic radiation that penetrates bone and soft tissues and can either be absorbed, scattered or remain unchanged depending on the density of the tissue. The variation in absorption of different tissues is what is detected and depicted in the resulting image. Chest x-ray is a commonly performed diagnostic in patients experiencing heart failure as it produces images of the heart, lungs, airways, blood vessels and the bones of the spine and chest and can help to visually identify enlarged heart, blood vessel problems and accumulation of fluid in the lungs. However, because of its projective nature, X-ray imaging generates 2D images only and has poor contrast and structural detail.

Computed tomography uses a combination of many X-ray measurements taken from different angles to produce cross-sectional images. Most of the common CT machines have rotating gantries that quickly rotate around the subject and use algorithms such as filtered back projection or iterative reconstruction to accurately reconstruct the corresponding transverse slices. Cardiac CT is sometimes performed to gain knowledge about cardiac or coronary anatomy, in particular of coronary arteries and pulmonary vasculature to detect or diagnose coronary artery disease as CT images have high spatial resolution and boundary contrast, particularly in bony areas. The main drawback of this modality is the high radiation dose delivered to the patient.

Molecular and nuclear imaging enables the visualisation and interrogation of specific biological targets and pathways that precede or underlie changes in morphology, physiology, and function of the heart. This test can be used to detect abnormal blood flow to the heart muscle and metabolism of the myocardium from blockages or narrowing in the coronary arteries and the presence of prior heart attacks. The most commonly used nuclear imaging technique is single-photon emission computed tomography (SPECT), which uses a gamma camera to scan the heart from multiple angles. SPECT imaging can give information about blood flow to tissues and chemical reactions (metabolism) in the body. Another nuclear imaging modality that has recently been studied is positron emission tomography (PET), which enables visual image analysis of multiple different metabolic chemical processes and is thus one of the most flexible imaging technologies. One particular advantage of this technique is that it gives the ability to measure absolute myocardial blood flow, and can be combined with CT or MR to provide both functional and anatomical assessment. Despite these benefits, PET remains predominantly a research tool in cardiology.

2.3 Clinical descriptors of cardiac function

Cardiac function is routinely assessed in clinical practice with the use of imaging techniques such as those described above. A number of descriptors are typically calculated from the imaging data that provide indirect information on the actual physiological processes. Of these techniques, cardiac MR is considered to be the gold standard due to its excellent image contrast and coverage ([Jasaityte et al., 2013](#)). However, US is the most commonly used diagnostic tool in the clinic due to its low acquisition cost and portability.

LV systolic function is the most important prognostic factor in a variety of cardiac disorders, and accurate, serially reproducible, noninvasive methods for assessing LV function are essential for the management of patients. This section provides a survey of the most widely used clinical descriptors of cardiac function, which can be divided into global functional analysis (section [2.3.1](#)), and motion and deformation analysis ([2.3.2](#)).

2.3.1 Global functional analysis

In practice, routine clinical assessment of cardiac function still relies on simple global volumetric measures such as volume, mass and ejection fraction (EF). These and other basic parameters will be outlined in the following paragraphs.

Left ventricular volume (LVV) is a basic parameter required to derive other LV indexes like EF. MR and US are the most used modalities to assess this quantity. The most commonly used 2D method for LVV measurement is the biplane method of discs (modified Simpson's rule) ([Lang et al., 2005](#)). The principle underlying this method is that the LV blood pool can be divided into a stack of individual ellipsoidal discs (see Figure 2.6 for more detail). The LVV is calculated as the sum of the volumes of each individual ellipsoid, which mathematically can be formulated as follows:

$$LVV = \frac{F\pi}{4} \sum_{i=1}^h a_i b_i \quad (2.1)$$

where h is the number of ellipsoidal discs used to divide the LV, a and b are the diameters of the individual ellipsoids, and F is the height of each ellipsoidal disc.

In the case of 2D US, the 2Ch and 4Ch apical views are used to compute the LVV, and a and b correspond to the diameters estimated from each view. The number of ellipsoidal discs is computed as a fraction of the maximum long axis length between the two views. In the case of a cine short-axis MR sequence, in each ventricular slice the LVV is calculated as the sum of the pixels that belong to the blood pool multiplied by the slice thickness. In the case of a 3D US sequence, LV endocardial contours can be traced in every slice, and then reconstructed to create an endocardial surface in the 3D space. These reconstructed surfaces can be used to calculate LVV.

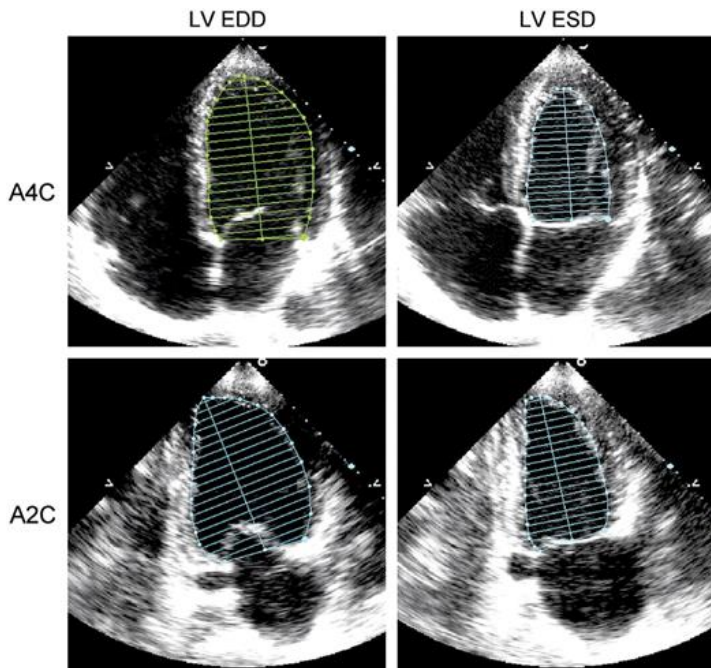


Figure 2.6: 2-D measurements for volume calculations using the biplane method of discs (modified Simpson's rule), in the apical four-chamber and apical two-chamber views (Figure adapted from ([Lang et al., 2005](#))).

The LVV can be calculated at any cardiac phase. Commonly used indicators are the LV ED volume (LVEDV) and the LV end systole volume (LVESV).

LV stroke volume (LVSV): is defined as the volume ejected between the end of diastole and the end of systole, i.e.

$$LVSV = LVEDV - LVESV \quad (2.2)$$

LV ejection fraction (LVEF): is a global index of LV fibre shortening and is generally considered as one of the most meaningful measures of the LV pump function. It is defined as the ratio of the LVSV to the LVEDV, i.e.

$$LVEF = \frac{LVSV}{LVEDV} \quad (2.3)$$

Left Ventricular Mass (LVM) is determined from the LV muscle volume and the specific gravity of muscle (1.05 g/ml). LV muscle volume is equal to the total ventricular volume contained within the myocardial boundaries of the ventricle (epicardial volume minus endocardial volume).

Cardiac output (CO): measures the amount of blood pumped by the heart per minute, and it is calculated as the LSVV multiplied by the average heart rate (HR), i.e.

$$CO = HR \cdot LSVV \quad (2.4)$$

The above mentioned parameters are the most commonly used in the clinic for cardiac functional assessment. However, they focus on the ED and end systolic (ES) phases, which limits their ability to describe the full complexity of cardiac cycle motion. To avoid this limitation, a number of other parameters have been proposed to assess other phases of the cardiac cycle (see Figure 2.7 for more details).

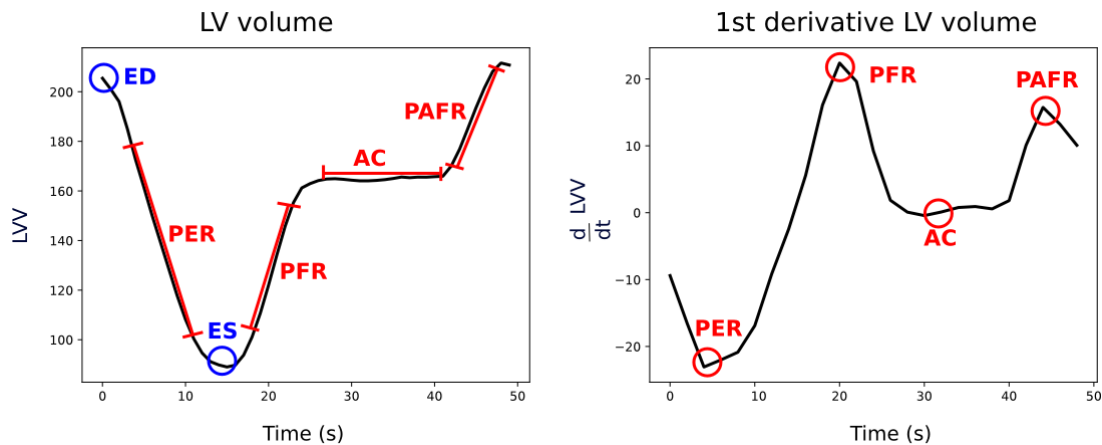


Figure 2.7: LVV curve for a cardiac cycle, in blue ED and ES frames, in red PER, PFR, AC and PFR parameters.

Peak ejection rate (PER): measures the slope of the ejection phase of the cardiac cycle. PER can be computed as the maximal negative first derivative of cardiac volume in systole.

Peak filling rate (PFR): measures the slope of the rapid inflow phase of the cardiac cycle. PFR can be computed as the maximal positive first derivative of cardiac volume in diastole.

Atrial contribution (AC): measures the slope of the diastasis phase of the cardiac cycle. AC can be computed as the maximal negative first derivative of cardiac volume in diastole.

Peak atrial filling rate (PAFR): measures the slope of the atrial systole phase of the cardiac cycle. PAFR can be computed as the second maximal positive first derivative of cardiac volume in diastole.

These measures are not routinely computed as they require LV segmentation of the full cardiac cycle. However, there have been multiple studies that have shown that these measures might help in the diagnosis of cardiac diseases (Bianco et al., 1985, Miller et al., 1986).

2.3.2 Motion and Deformation Analysis

Global measures are important indices for cardiac disease diagnosis. However, they do not provide regional information. A quantitative assessment of regional parameters can be beneficial for the diagnosis of disease and the evaluation of its severity. A number of techniques have been proposed to describe and quantify local motion of the heart. Most of them are based on determining the boundary wall of the ventricle, and subsequently tracking it using motion tracking algorithms (Rueckert et al., 1999, Beg and Khan, 2006, McLeod et al., 2011). The wall motion estimated in this way can be used to compute local motion parameters. Examples of such parameters are described below:

Ventricular wall motion can be characterised using either displacements or velocities. Displacements measure the change in position of a moving object over time, and the displacement fields reflect the movement of anatomical structures. Displacements can be expressed as follows:

$$u_i^t = x_i^t - x_i^0 \quad (2.5)$$

where x_i^t represents the coordinates of a point i on the ventricular wall at time t .

Similarly, velocity measures the direction and rate of motion, and can be computed as follows:

$$v_i^t = \frac{x_i^t - x_i^{t-1}}{\Delta t} \quad (2.6)$$

where $\Delta t = \frac{1}{T}$, and T is the duration of the cardiac cycle.

Myocardial deformation can be expressed as either strain or strain rate. In contrast to ventricular wall motion parameters, deformation refers to the change in shape resulting from contraction and it allows discrimination between active and passive myocardial tissue movement (shortening or thickening). Strain defines the total deformation of a region of tissue during the cardiac cycle relative to its initial configuration at the onset of the cardiac cycle, and it is normally expressed in percentages. Strain can be described using a Lagrangian, Eulerian or Natural description.

Lagrangian strain measures the distance between two material points in the myocardium, and can be mathematically represented for a one-dimensional object by the following equation:

$$\varepsilon(t) = \frac{L(t) - L_0}{L_0} \quad (2.7)$$

where $L(t)$ is the distance between the points at a given time t , and L_0 is the initial distance.

Eulerian strain is similar to the Lagrangian strain, but instead of normalising by the initial length, it is normalised with respect to the final length. However, Eulerian strain is not normally used in cardiology ([Pedrizzetti et al., 2016](#)). Mathematically it can be described as:

$$\varepsilon(t) = \frac{L(t) - L_0}{L_T} \quad (2.8)$$

where $L(t)$ is the distance between the points at a given time t , and L_T is the distance at the last time frame T .

Natural strain represents the instant length change and it is independent of initial length. Instead it employs a reference length that changes as the object deforms. Mathematically it can be expressed for a one-dimensional object by the following equation:

$$\varepsilon_N(t) = \int_{t_0}^t \frac{1}{L(t)} \frac{dL(t)}{dt} dt = \ln \left(\frac{L(t)}{L_0} \right) \quad (2.9)$$

Where $L(t)$ and $dL(t)$ are the length and the first derivative of the length at a time frame t .

Under a small deformation assumption, Lagrangian and Natural strain are approximately equal, however, for large deformations the differences between both strains are relevant. Large deformations can occur in the myocardium during ventricular contraction and relaxation. ([Voigt et al., 2014](#)).

In practice, strain can be computed by taking a tissue segment along any specified direction. In cardiology, strain is generally computed in three directions: longitudinal, circumferential and radial. Endocardial strains are computed when the segment of tissue is taken from the endocardial border, and these are more frequently used in clinical studies because they better represent the functional purpose of myocardial contraction, which reduces the endocardial surface of the cavity to eject the stroke volume. Therefore, endocardial strains correlate best with volumetric measurements like ejection fraction. Likewise, epicardial strains can be evaluated along the epicardial border.

Strain rate (SR) is the rate of strain change over the course of time. In both types of strain, i.e. Lagrangian and Natural, strain rate is simply the first derivative of strain:

$$\begin{aligned} SR(t) &= \frac{d\varepsilon(t)}{dt} = \frac{1}{L_0} \frac{dL(t)}{dt} \\ SR_N(t) &= \frac{d\varepsilon(t)}{dt} = \frac{1}{L(t)} \frac{dL(t)}{dt} \end{aligned} \quad (2.10)$$

In 3D imaging, the above-mentioned concepts apply in principle to all three one-dimensional (longitudinal, circumferential, and radial) displacement and strain components.

Rotational mechanics. The rotational deformation of the LV around its long axis is described by two parameters. Twist represents the difference in the systolic rotation of the myocardium in an apical and basal short-axis plane, and it is reported in degrees. Twist can be calculated as follows:

$$\text{Twist} = (\theta_{apex} - \theta_{base}) \cdot (P_{apex} - P_{base}) \quad (2.11)$$

where $\theta_{apex} - \theta_{base}$ is the angle difference between the apical counterclockwise and basal clockwise rotation and P_{apex} and P_{base} are the mean epicardial apical and basal radii respectively.

Torsion is the twist normalised to the distance between the respective image planes, and it is reported in degrees/cm. Torsion can be calculated as follows:

$$T = \frac{\text{Twist}}{2h} \quad (2.12)$$

where h is LV length in the longitudinal plane.

The parameters described above have been all used to better understand impaired LV function in multiple disease groups. Several studies have showed that regional wall motion parameters are more sensitive measures for myocardial function than global measures (e.g. EF) and allow earlier identification of disease. For example, for subjects with coronary artery disease, strain has been used to localise infarct areas (Götte et al., 1999, 2001) which exhibit a significant reduction of intramural strain after transmural myocardial infarction. Similarly, patients with nonischemic dilated cardiomyopathy have reduced strain and decreased contractility and an associated increased torsion (Nelson et al., 2000). Finally, there have been a few studies on hypertrophic cardiomyopathy patients showing that, although, global LV function is preserved, regional myocardial contraction and strain rate are both impaired in hypertrophied as well as in nonhypertrophied regions (Mishiro et al., 1999, Young et al., 1994).

2.4 Cardiovascular disease

The experiments presented in this thesis focus on two cardiovascular diseases (CVD): DCM and IHD. A brief summary of these pathologies is presented in the following sections. For a broader discussion of the different types of CVD the interested reader is referred to Mendis et al. (2011).

2.4.1 Dilated cardiomyopathy

Cardiomyopathies are a group of myocardial disorders in which structural and functional abnormalities of the heart muscle develop in the absence of clear cardiovascular causes, such as hypertension, valvular disease, coronary artery disease or congenital abnormalities. DCM is the most common type of non-ischaemic cardiomyopathy. The global myocardial dysfunction is progressive and often irreversible, resulting in heart failure (HF) in the majority of patients (Yancy et al., 2013, Bozkurt and Mann, 2007).

The main characteristic of DCM is the enlargement of the LV (Figure 2.8), with occasionally dilation also observed for the left atrium and RV (Rihal et al., 1994). Focusing on the LV, both LVEDV and LVESV increase significantly (Young et al., 2001), due to the impaired contractile function of the myocardium, often leading to a decrease in the LSVV (Mu et al., 2010). Cardiac dilation is typically accompanied by moderate wall thinning (Mu et al., 2010, Young et al., 2001), while the shape of the ventricle changes from elliptical to spherical (Laskey et al., 1984).

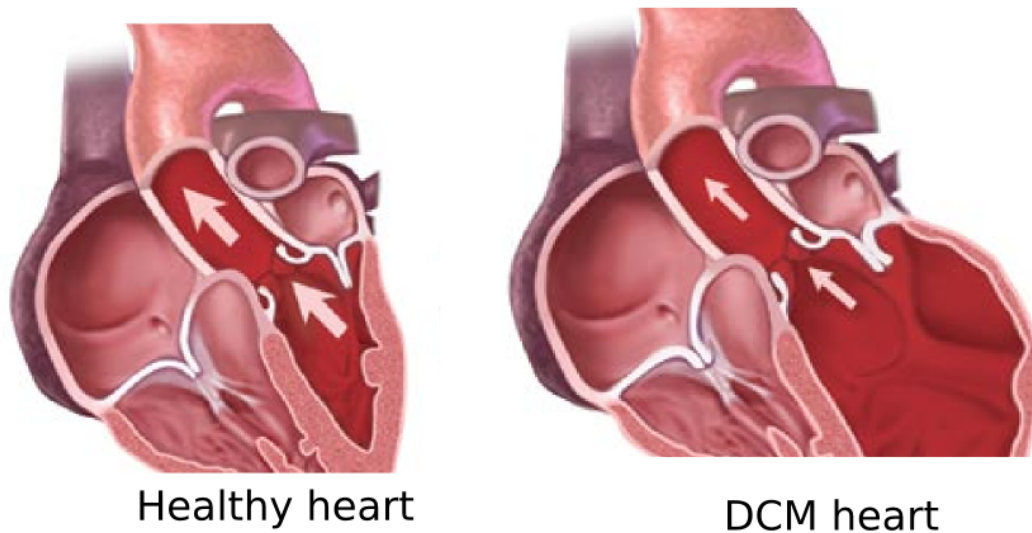


Figure 2.8: The effect of DCM on the geometry of the heart. The LV is significantly dilated and the myocardial wall becomes thinner and weaker. Enlargement is often observed in all cardiac chambers (figure adapted from American Stroke Association – www.strokeassociation.org).

The incidence of DCM is estimated to be between 5 and 8 per 100,000 people and it is the third most common cause of HF (of America et al., 2010). Low survival rates —25% mortality rate over one year and 50% mortality rate over five years —illustrate the need for a better understanding of the disease and the mechanisms underpinning its development and progression. No successful treatment options have so far been available and also due to the severity and irreversibility of the disease, DCM is one of the most common indications for heart transplantation.

Identification and prognostication of DCM relies primarily upon imaging data such as US or MR, as they allow accurate quantification of LV function, and identification and localisation of scar. The diagnostic criteria for DCM are (Yancy et al., 2013): LV or biventricular enlargement and depressed myocardial performance, reduced global LVEF, global contractile dysfunction of one or both ventricles, and signs of high LV filling pressure. Features of regional wall motion abnormalities, such as mechanical dyssynchrony and reduced regional myocardial strain, are known to have additional beneficial value for improved disease classification and treatment stratification. However, such regional parameters are still underused due to the labour intensity of currently available methods (Merlo et al., 2014).

Numerous treatments have been suggested for DCM, ranging from pharmaceutical therapies to invasive procedures. DCM patients are commonly administered beta blockers and ACE inhibitors to control afterload myocardial oxygen consumption and abnormal heart rhythm. For example, beta blockers, such as metoprolol, have been found to increase LVEF and LVSV and in some cases cause reverse remodelling for DCM patients (Eichhorn et al., 1994). Minimally invasive surgical procedures have also been used to treat DCM patients. The most commonly used is cardiac resynchronisation therapy, as it can help to correct disorganized contractions by circumventing the left bundle branch block with pacing leads and restoring synchrony to LV contraction, thus improving the pump function and causing reverse remodelling (Doltra et al., 2014).

The main limitation of current approaches for DCM diagnosis is related to the variation of etiologies of the disease. Actually, more than 75 known conditions can present the DCM phenotype (Bozkurt and Mann, 2007). Due to the multi-factorial development of the disease, determination of its origin and thus appropriate treatment for each patient is a challenging task. Furthermore, DCM patients have reported heterogeneous regional values for myocardial perfusion, systolic function, asynchrony and myocardial work. A long term aim of the work presented in this thesis is to find new local descriptors that can help to further stratify DCM patients.

2.4.2 Ischaemic heart disease

IHD, also known as coronary heart disease, refers to a group of diseases which includes stable angina, unstable angina, myocardial infarction, and sudden cardiac death, and its primary cause is obstruction of the epicardial coronary arteries, as a result of development of atherosclerotic plaques (Fihn et al., 2012). A common symptom is anginal-type chest pain or tightness, pressure, or discomfort.

IHD may develop into ischemic cardiomyopathy causing dilatation and enlargement of the left ventricle, leading to regional alterations in function. The identification of kinetic disorders and dyssynchrony can change the patient management.

IHD remains a major public health problem, as it is estimated that 1 in 3 adults in the United States (about 81 million) has some form of CVD, including >17 million with IHD and nearly 10 million with angina pectoris (Go et al., 2014). Among persons 60 to 79 years of age, approximately 25% of men and 16% of women have IHD, and these figures rise to 37% and 23% among men and women ≥ 80 years of age, respectively (Go et al., 2014).

Initial identification of IHD relies on historical and physical examination to be categorised as stable or unstable. Acute IHD typically can be identified by changes of the ST segment (interval between ventricular depolarization and repolarization) on the ECG. To determine the severity of stable IHD patients, coronary angiography is considered the gold standard (Fihn et al., 2012). However, stress testing (i.e. stress echocardiography, stress nuclear myocardial perfusion SPECT and myocardial perfusion PET) are also recommended for initial assessment. The care of patients with IHD includes pharmacological therapies, such as beta blockers, calcium channel blockers, and nitrates (Fihn et al., 2012). Often, a combination of these agents is used for control of symptoms.

2.5 Discussion

Cardiovascular diseases are the leading cause of mortality and morbidity in the world to-day, according to the World Health Organisation ([Organization, 2007](#)). Better understanding the motion of the heart through the cardiac cycle is crucial in aiding diagnosis in a wide range of CVDs as well as for the optimisation of related clinical procedures. A range of global parameters have been used to quantify cardiac function. There is significant interest in the use of more local motion/deformation parameters but techniques do not yet exist for robust automated estimation of such parameters. The aim of this thesis is to investigate the use of a motion atlas for multimodal cardiac functional assessment based on such local parameters.

Such atlases permit the extraction of highly localised motion and deformation parameters, and therefore have the potential to produce a much richer description of cardiac function. The use of motion atlases for the statistical analysis of normal and pathological cardiac motion has gained increasing interest over the past decade. The intuition behind such approaches is that pathological changes in the heart lead to altered electromechanical behaviour, and therefore observing the mechanics of cardiac motion may lead to the uncovering of clinically useful information about the pathology. In the context of this thesis, the next Chapter provides a literature review of machine learning and cardiac atlases. Chapters [5](#) and [6](#) propose a new motion atlas-based diagnostic pipeline to identify DCM patients. Finally, Chapter [7](#) aims to estimate the use of LV strain for DCM and IHD diagnosis.

3 | Machine learning and cardiac atlases

Whilst the previous Chapter provided the clinical background for the thesis, this Chapter presents a technical background on the key methods and concepts that underpin the novel techniques presented. First, Section 3.1 reviews the field of machine learning, with a special focus on multi-view machine learning in subsection 3.1.2. Subsequently, Section 3.2 reviews the most important works from the field of cardiac atlases. Finally, Section 3.3 describes how cardiac atlases have been extended to capture population variation using machine learning approaches, resulting in statistical cardiac atlases.

3.1 Machine learning

This section is organised as follows: the first part presents a review of the field of single-view machine learning, then the second part focuses on the multi-view machine learning algorithms that will be used during this thesis in combination with the multimodal cardiac motion atlas. Single-view machine learning refers to machine learning algorithms that uses only one type of data (i.e. view) for the learning strategy. In contrast to single view learning, multi-view machine learning aims to learn a joint representation of all the views by exploiting the complementary views of the same input data and at the same time improving the learning performance.

3.1.1 Single-view machine learning

Machine learning (ML) is the study of computer algorithms which can learn complex relationships or patterns from empirical data and make accurate decisions (Mitchell et al., 1997, Nasrabadi, 2007). ML algorithms can be organised into different categories based on different principles. For example, depending on the utilisation of labels of training samples, they can be categorised into:

- (1) **Supervised learning algorithms** try to model relationships and dependencies between the target prediction output and the input features or observations such that we can predict the output values for new data based on the learnt relationships (Alpaydin, 2014, Friedman et al., 2001). Supervised learning problems can be further grouped into regression and classification problems (see below for a definition of these terms).
- (2) **Unsupervised learning**, also known as cluster analysis, aims to discover relationships between the input features or reveal the latent variables behind the observations (Friedman et al., 2001). Typically, unsupervised learning algorithms assume that the observations are independently and identically distributed and come from a common distribution. Unsupervised learning comprises tasks such as clustering, dimensionality reduction, including manifold learning, outlier detection and blind source separation.
- (3) **Semi-supervised learning** falls between supervised and unsupervised learning (Chapelle et al., 2006), and these techniques were developed to overcome the limits of labelled data in large databases. During the training process semi-supervised algorithms use a mix of labelled and unlabelled data to learn the mapping between the observations and the targets. Examples of semi-supervised learning include semi-supervised classification, regression and information recommendation systems. Active learning is a special case of semi-supervised ML in which a learning algorithm is able to interactively query the individual examples to obtain the desired output at new data points.

(4) **Reinforcement learning aims** to learn a mapping from situations to actions so as to maximise a scalar reward or reinforcement signal (Kaelbling et al., 1996). Reinforcement learning is different from supervised learning where an input is mapped to a desired output by using a dataset of labelled training instances. One of the main differences is that the reinforcement learning agent is never told the optimal action, instead it receives an evaluation signal indicating the goodness of the selected action. Examples of reinforcement learning include automatic decision and structured prediction.

Another division of ML algorithms can be based on the task that the algorithm has to solve. The most common ML tasks are:

Regression and classification. Classification is the problem of identifying to which of a set categories a new observation belongs, while regression aims to predict continuous variables given a set of input variables. To solve these tasks, the learning algorithm is usually asked to estimate a function that assigns an input observation to a category identified by a numeric code, in the case of a classifier, or a continuous variable in the case of regression. Some of the most common supervised ML algorithms are described below, but for a broader discussion of the different types of ML algorithm the interested reader is referred to Nasrabadi (2007), Kotsiantis et al. (2007).

Linear discriminant analysis (LDA) (Fisher, 1936) is a classification algorithm that tries to find an optimal projection, which can maximise the distances between samples from different classes and minimise the distances between samples from the same class.

Support vector machines (SVM) (Cortes and Vapnik, 1995) is a classification algorithm that maps the data into a high dimensional space, and finds the hyperplane that maximises the margin between the two classes; SVM can also be used as a regression method, maintaining all the main features that characterise the maximal margin.

Decision trees build regression or classification models in the form of a tree structure (Rokach and Maimon, 2014), and predict the value of a target variable based on several input variables.

Based on the underlying method that can be used to achieve the previous tasks, ML algorithms can be divided into:

(1) Ensemble learning refers to the procedures employed to train multiple ML models and combine their outputs, treating them as a committee of decision makers (Dietterich, 2002). The principle is that the strong decision, with all weak classifiers combined appropriately, should have a better overall accuracy than any individual committee member. The most popular commonly used version of ensemble learning is AdaBoost (Freund and Schapire, 1997), where during the training process, the weights of incorrectly classified examples are increased so that the weak learner is forced to focus on the hard examples in the training set.

(2) Dimensionality reduction aims to obtain more compact representations of the data with limited loss of information. In general, dimensionality reduction algorithms can be divided into linear techniques, that embed the data into a low dimensional space using a linear projection matrix, and non-linear techniques, which assume that the data lie on a non-linear manifold. Non-linear techniques can be further divided into full spectral techniques that perform an eigendecomposition of a full matrix that captures the covariances between dimensions or the pairwise similarities between data points; and sparse techniques that solve a sparse generalised eigenproblem, and focus on retaining the local structure of the data. Among the most used linear dimensionality reduction algorithms are: principal component analysis (PCA) (Hotelling, 1933), which estimates an orthogonal linear transformation that transforms the data into a low dimensional space whilst preserving as much of the variance in the data as possible; and independent component analysis (ICA) (Hyvärinen and Oja, 2000), which aims to decompose a signal into independent non-Gaussian signals. Examples of non-linear dimensionality reduction algorithms are Isometric Feature Mapping (Tenenbaum et al., 2000), which attempts to preserve the pairwise geodesic distances between data points in the embedded space; and Locally Linear Embeddings (Roweis and Saul, 2000), which tries to build a neighbourhood-preserving embedding by assuming that there are linear mappings that transform the high-dimensional coordinates of each neighbourhood to global intrinsic coordinates on the manifold. For further description of different dimensionality reduction algorithms proposed in the literature, the interested reader is directed to the following review papers (Cayton, 2005, Thangavel and Pethalakshmi, 2009).

(3) Graph matching techniques learn how to match two data sets, which can be represented by graphs consisting of nodes and links that connect the nodes. The nodes represent local features of the data and edges correspond to the relational aspects between features. Graph matching problems can be divided into exact and approximate graph matching. In exact graph matching the mapping between the nodes of the two graphs must be edge preserving, while in approximate graph matching this requirement is relaxed such that graphs with slightly different topologies can still be matched. A widely used approach for graph matching is to first obtain a signature for each node in both graphs, which captures each node's relation to all other nodes in the graph. Then, the Hungarian algorithm (Gori et al., 2005) can be applied to find the optimal matching between the nodes. For more detail the interested reader is directed to the following review papers (Nickel et al., 2016, Caetano et al., 2009).

Application of single-view ML:

Applications of single-view ML include natural language processing, medical diagnosis, bioinformatics, video surveillance, and financial data analysis. This section reviews the some of the most common applications and the types of algorithms used in the different areas:

- **Image recognition:** One of the most common uses of ML is image recognition, which involves automatically detecting or classifying a several pre-learned objects or object classes from digital images. Some examples of image recognition are face detection and character recognition. In this category most of the algorithms used are supervised and semi-supervised as they have labelled data to identify objects from digital images or videos.
- **Speech Recognition:** aims to map an acoustic signal containing a spoken natural language utterance into the corresponding sequence of words intended by the speaker (Rabiner and Juang, 1993). Up to 2012 the state-of-the-art speech recognition methods were a combination of hidden Markov models and Gaussian mixture, which are unsupervised techniques. After 2012 with the increase in size of available training sets, most of the proposed algorithms are based on the deep learning method called long short-term memory. Speech recognition applications include voice user interfaces, such as voice dialing, call routing, domestic appliance control.

- **Natural language processing** is an area of ML concerned with the interactions between computers and human languages, in particular how to make computers understand and manipulate human language. Different classes of ML algorithms have been applied to natural language processing tasks, but most of them are unsupervised or semi-supervised methods. Some applications are machine translation, text categorisation, spam filtering and information extraction.
- **Statistical Arbitrage:** In finance, statistical arbitrage refers to automated trading strategies that involve the simultaneous buying and selling of security portfolios according to predefined or adaptive statistical models. Most of the trading algorithms proposed in the literature aim to find historical correlations and general economic variables, that will be used as input for a classification or regression problem. In the case of classification, the categories might be sell, buy or do nothing, and in the case of regression, the ML algorithms may try to predict the the expected return of one stock over a future time horizon.
- **Medical Diagnosis:** ML techniques have been proposed to automate the analysis and diagnosis from medical images. ML is also being used for data analysis, such as detection of irregularities in the data a automatic interpretation of clinical reports. In medical diagnosis, most of the algorithms proposed have been supervised as the main interest is to detect diseases as classification-based problems. Unsupervised learning techniques have been used for feature extraction, and automatic detection of biomarkers.

3.1.2 Multi-view machine learning

This thesis aims to incorporate multimodal (MR and US) data into a cardiac motion atlas, which raises the question of how best to exploit these data for diagnosis. Combining (or fusing) the information from the multiple views can help to exploit their natural strengths and reduce redundancies. Therefore, multimodal data fusion has gained considerable attention in the literature in recent years. When applied in a ML context, this concept is known as multi-view machine learning (MvML).

MvML aims to learn one function to model each view and jointly optimises all the functions to improve the generalisation performance. For example, the views can be multiple measurement modalities, such as simultaneously recorded audio and video, or different information extracted from the same source, for example, RGB-D cameras which capture high quality synchronised videos of both colour and depth. In the context of this thesis, MR and US will be considered as two ways of viewing the mechanics of the heart, and this perspective enables exploitation of the rich literature from the field of MvML.

A naive solution for multi-view learning is to concatenate the data of the multiple views and apply single-view learning algorithms directly. However, the main problem with this approach is over-fitting, as the number of features would increase dramatically. Another problem is that it would not take advantage of specific statistical properties of each view. Different views often contain complementary information, and multi-view learning can exploit this information to learn a joint representation that is more expressive than that of single-view learning methods. To overcome these problems, several MvML algorithms have been proposed to improve generalisation performance.

Based on the strategies that algorithms use to combine the data, multi-view learning methods can be divided into four main categories ([Zhao et al., 2017](#)):

(1) Co-training style algorithms: Co-training was introduced by [Blum and Mitchell \(1998\)](#). It is one of the first strategies proposed for multi-view learning, and aims to maximise mutual agreement between different views. Co-training algorithms are mostly used for solving semi-supervised problems, where labelled and unlabelled data are available. They first train classifiers from each single view based on the labelled data, and then iteratively let each classifier label the unlabelled instances that they predict with the highest confidence. The newly labelled examples from one classifier may provide useful information for the other classifiers under the independence assumption between classifiers. Therefore, each classifier is updated with the newly labelled data. Co-training relies on two assumptions: sufficiency (each view is sufficient for correct classification) and conditional independence (the two views of any example are conditionally independent given the class label). The main algorithms proposed for co-training are co-EM ([Brefeld and Scheffer, 2004](#)), co-testing ([Muslea et al., 2000](#)) and co-clustering ([Yang et al., 2012](#)).

Relevant literature from the medical field includes Yu et al. (2011) who combined clinical features and image-based features using Bayesian co-training for the task of survival prediction for lung cancer, Prasad et al. (2008) proposed to use robust co-training with active learning to automatically score the presence and severity of bronchial abnormalities in CT lung images using different types of features extracted from the images.

(2) Co-regularisation style algorithms: Co-regularisation algorithms minimise disagreement between learning functions of different views using a regularisation term. The regularisation term can be used to construct a linear or non-linear transformation from the different views to a new space, under a constraint that the multiple transformed feature sets should be as aligned as possible. These algorithms are mostly used for dimensionality reduction algorithms and are typically based on canonical correlation analysis (CCA) (Hotelling, 1936), and its non-linear extension, Kernel CCA (Bach and Jordan, 2002). In the literature these algorithms are also known as multi-view subspace learning approaches. The regularisation term can be applied to the label information, and add constraints for intra-class and inter-class characteristics. This approach enables co-regularisation style algorithms to be used for supervised multi-view classification, and such methods are often based on LDA. Some examples are multi-view linear discriminant analysis (Sun et al., 2016) and multi-view discriminant analysis (Kan et al., 2012).

Finally, the regularisation term can be used to combine the data and label information by use of classifiers or regressors, and ensure that the outcomes of the classifiers or regressors are as consistent as possible. Such approaches have been mostly based on the SVM algorithm and are for multi-view semi-supervised learning. Some examples are two-view SVM (Farquhar et al., 2006), or the multi-view Laplacian support vector machines algorithm introduced by Sun (2011). Note that there is a close link between multi-view co-regularisation algorithms and manifold alignment, and often the two terms can be considered as synonyms, although typically manifold alignment approaches have tended to be semi-supervised or unsupervised (e.g. Ham et al. (2005)). Relevant literature in the medical field includes Guerrero et al. (2014), who adapted the Laplacian eigenmaps method to learn a joint low-dimensional representation of brain MR images acquired either at 1.5 or 3 Tesla, and Lorenzi et al. (2016), who used partial least squares to analyse the joint variation between genotype and phenotype in Alzheimer's disease patients.

(3) Margin-consistency style algorithms: Margin-consistency algorithms have been recently proposed to make use of the latent consistency of classification results from multiple views, and they are based on the maximum entropy discrimination principle that aims to combine maximum entropy theory and maximum likelihood estimation. Instead of making restrictions directly on the discriminant or regression function, margin-consistency style algorithms enforce the margins (distance from the decision surface to the closest data point) from two views to be identical. These algorithms are mostly used for multi-view classification, and some examples are multi-view maximum entropy discrimination (MED) (Sun and Chao, 2013) and consensus and complementarity based MED (Chao and Sun, 2016). The only work that has used margin-consistency style algorithms in the medical field was proposed by Chao (2017) to identify specific genes that relate to alcohol dependent patients using multi-view bi-clustering analysis to relate genotype and phenotype features.

(4) Deep learning style algorithms: Deep learning algorithms attempt to model high-level abstractions of the data using architectures composed of multiple non-linear transformations. Deep multi-view learning is still in its infancy as a field, but two-main strategies have been adopted to date: the first is based on autoencoders, where the objective is to learn a compact representation that best reconstructs the inputs (Ngiam et al., 2011), and the second is an extension of the classical CCA to deep learning (Andrew et al., 2013).

(5) Multiple kernel Learning algorithms: Another type of MvML algorithm that has been proposed in the literature is multiple kernel learning (MKL) algorithms. MKL was originally developed to control the search space capacity of possible kernel matrices to achieve good generalisation but has been widely applied to problems involving multi-view data. MKL finds the optimal linear or non-linear combination of multiple kernels (Gönen and Alpaydin, 2011, Bach et al., 2004), addressing issues relating to differences in representation, variability and dimensionality. However, MKL is not designed to integrate the sources of information from each view, and it works by simply placing weights over the kernels (Bach et al., 2004). Furthermore, MKL can be used to combine feature mappings of the same or multiple views. MKL has been applied in medical imaging.

For example, in the context of cardiac imaging, Peressutti et al. (2017) used MKL to combine motion data extracted using a cardiac motion atlas with non-imaging data. Sanchez-Martinez et al. (2017) proposed to use MKL to jointly analyse the variability of multiple velocity patterns from a stress protocol to improve the characterisation of HF with preserved ejection fraction patients. Finally, Marciniak et al. (2017) proposed a MKL-based framework to classify between patients with ventricular fibrillation and patients presenting with other non-arrhythmic symptoms when they are hospitalised.

3.2 Cardiac atlases

The remainder of this Chapter is organised as follows: this section presents a review of the two main types of cardiac atlas, which are: anatomical atlases and motion atlases. The final section focuses on statistical atlas-based approaches proposed for determining new biomarkers that can characterise myocardial function and potentially aid in disease stratification.

The term ‘cardiac atlas’ refers to the ensemble of mathematical and statistical models of cardiac anatomy and function, which enable standardised analysis of statistical variations present within and among patient groups, as well as classification of individual phenotypes within known population distributions.

3.2.1 Anatomical atlases

Anatomical atlases aim to create an average shape model of the anatomy, which can be used as a standard reference for comparing subjects from a population in a common coordinate system. In addition, an anatomical atlas can be seen as a framework for deriving indicators that can characterise anatomical variation. A typical pipeline for the construction of anatomical atlases is composed of three stages:

1. **Geometry definition.** Segmentation of the anatomical structure(s) of interest and extraction of the characteristic landmarks for creating a 3D mesh.

2. **Spatial normalisation.** Spatial normalisation aims to register all individual subjects to a reference space to establish correspondences between different shapes and to compute an average shape. To remove bias towards differences in subject-specific geometries, this alignment is performed in two steps: 1) a global transformation that describes the differences in pose and size of the transformed shape with respect to the atlas; 2) a local registration that describes any local nonlinear transformation required to match the anatomies.
3. **Variability analysis.** Analysis of the variability of the subjects' feature positions with respect to the average shape.

Based on this pipeline, [Frangi et al. \(2002\)](#) proposed a framework for constructing an anatomical atlas of the LV and RV from MR data. Furthermore, they used the constructed atlas to propagate atlas-based landmarks to the individual shapes, and then analysed the variability of the shapes using PCA.

In 2010, the Cardiac Atlas Project (CAP) established a large-scale MR database for statistical analysis of cardiac anatomy. [Medrano-Gracia et al. \(2014a\)](#) used this database to build an anatomical atlas to characterise global shape variation using PCA for an adult asymptomatic population. In the same year, [Zhang et al. \(2014\)](#) used the CAP database to form another anatomical atlas to identify differences between myocardial infarct patients and asymptomatic patients. These works added an extra step to the pipeline described above to correct for acquisition bias as the CAP database was acquired using different imaging protocols.

3.2.2 Motion atlases

Cardiac motion atlases provide a space of reference in which population comparisons of motion (i.e. displacements and velocities) and deformation (i.e. strains and strain rates) can be carried out. Compared to the anatomical atlases described previously, motion atlases need to integrate the motion of each subject into the atlas coordinate system.

To this end, many authors have attempted to extend the 3D models described in the previous section to take into account both the inter-subject variation, related to the variation in size and geometry of cardiac structures among the population; and the intra-subject variation, related to the deformation of the heart’s anatomy though the cardiac cycle. In recent years a number of approaches have been developed for the construction of such atlases, but the general pipeline remains the same for all of them. These steps transform the subject-specific motion/deformation data so that they can be directly compared, removing biases due to heart orientation, size, shape and cardiac phase. In general, motion atlas construction entails the following steps:

1. **Geometry estimation:** Commonly, this first stage is achieved by segmenting the anatomy of interest and generating a 3D mesh that will represent it.
2. **Motion estimation:** Motion tracking algorithms can be divided into: generic methods that can be applied to any image modality; and modality specific methods that try to take advantage of the nature of the data to estimate the motion.

Generic image-based methods are typically based on diffeomorphic non-linear image registration techniques, which estimate one-to-one differentiable mappings between the images to register. Generic methods can be classified as: (1) B-spline-based methods that encode deformations using B-splines. A widely used algorithm is the B-spline free-form deformation (FFD) registration (Rueckert et al., 1999) that ensures a continuous, differentiable and invertible motion field (Duchateau et al., 2011, De Craene et al., 2012b); (2) Optical flow-based methods, where the deformation is modeled by considering its velocity over time according to the Lagrange transport equation (Arnol’d, 2013). When the velocity fields vary over time, large diffeomorphic deformations can be estimated using the Large Deformation Diffeomorphic Metric Mappings technique (Beg and Khan, 2006). The main limitation of this approach is the computational cost, as the complex partial differential equations have to be solved to integrate the velocity field over time along a geodesic path. A possibility to overcome this limitation is to use stationary velocity fields, which can be more efficiently integrated through exponential maps (Arsigny et al., 2006).

Among the methods based on stationary velocities, logDemons (Vercauteren et al., 2009) is an efficient nonlinear registration algorithm based on the demons optimisation. Incompressibility of the myocardium can be enforced by constraining the velocity fields to be divergence-free (Mansi et al., 2011, McLeod et al., 2011).

The alternative to a generic approach is to design an algorithm that is tailored to a specific modality and exploits some of its key characteristics. For example, TAG-specific algorithms (Zhou et al., 2015, Arts et al., 2010) use the fact that TAG images are acquired in several directions providing different channels for recovering the motion field. For US-based motion estimation, speckle tracking algorithms (Crosby et al., 2009, Kaluzynski et al., 2001) analyse the motion of tissues in the heart by using the naturally occurring speckle pattern in the myocardium.

Cardiac motion can be represented in a motion cardiac atlas in a number of different ways, including intensity-based (Lu et al., 2009), displacement-based (Chandrashekara et al., 2003, Perperidis et al., 2005a, Garcia-Barnes et al., 2010, Bai et al., 2015b), velocity-based (Duchateau et al., 2011, 2012), and momentum-based (Ardekani et al., 2009) approaches. Other proposed motion representations include the use local motion descriptors such as local motion patterns (Guha and Ward, 2012, Peressutti et al., 2015) or multi-scale representations of cardiac deformation (Sinclair et al., 2018).

3. **Spatio-temporal normalisation:** Spatial normalisation aims to remove bias towards patient-specific LV geometries from the motion and deformation analysis, and temporal normalisation ensures temporal correspondence between subjects by removing differences in the length of the cardiac cycle. The spatio-temporal normalisation (De Craene et al., 2012a, Peressutti et al., 2015, Perperidis et al., 2005b) is normally addressed as a combination of a global and local registration.
4. **Motion reorientation:** To compare cardiac motions between all subjects, the motion is reoriented from the subject-specific coordinate system to the atlas coordinate system. Under a small deformation assumption (Ashburner, 2007), different techniques have been proposed for the parallel transport of motion fields depending on the type of cardiac motion:

- **PFV:** Push-forward action on velocities (Duchateau et al., 2011, 2012, De Craene et al., 2012a, Peressutti et al., 2017)

$$\mathbf{v}_t^{atlas} = J_{\phi(\mathbf{x}_{ED})} J_{\mathbf{x}_t}^{-1} \mathbf{v}_t \quad (3.1)$$

$$\mathbf{u}_t^{atlas} = \mathbf{u}_{t-1}^{atlas} \mathbf{v}_t^{atlas} \quad (3.2)$$

- **PFD:** Push-forward action on displacements (Rao et al., 2004, Perperidis et al., 2005b, Peressutti et al., 2017)

$$\mathbf{u}_t^{atlas} = J_{\phi(\mathbf{x}_{ED})} \mathbf{u}_t \quad (3.3)$$

- **PFS:** Push-forward action on strain (Peressutti et al., 2017, Sinclair et al., 2018)

$$\mathbf{s}_t^{atlas} = J_{\phi(\mathbf{x}_{ED})} \mathbf{s}_t J_{\phi(\mathbf{x}_{ED})}^{-1} \quad (3.4)$$

where \mathbf{v}_t is the velocities, \mathbf{u}_t is the displacements and \mathbf{s}_t is the strains; $J_{\phi(\mathbf{x}_{ED})}$ is the Jacobian of the transformation ϕ mapping each subject's reference ED surface to the atlas ED surface at location x ; and $J_{\mathbf{x}_t}$ is the Jacobian of the motion transformation mapping the reference ED surface to each cardiac phase t .

Although many authors have broadly followed this pipeline, their works differ in the techniques used to estimate the LV geometry and motion, and to represent the motion. For example, Medrano-Gracia et al. (2014c, 2013b) fitted a finite-element model to cine-MR sequences to estimate the LV geometry, whilst Sinclair et al. (2016) and Peressutti et al. (2017) employed a statistical shape model of the LV to enforce point correspondence amongst all LV geometries. Temporal normalisation has been achieved by landmark-based piecewise linear warping of cardiac timings (Rougon et al., 2004, Perperidis et al., 2005b, De Craene et al., 2012a) or by normalising by the length of the cardiac cycle (Sinclair et al., 2016, Peressutti et al., 2017). Spatial normalisation has been previously achieved using a combination of global and local transformations (De Craene et al., 2012a, Peressutti et al., 2017). Some authors have combined temporal normalisation with spatial normalisation to directly compute spatiotemporal deformations.

For example, Perperidis et al. (2005b) used a spatiotemporal registration method that finds the temporal and spatial transformation components at the same time using image information only. Durrelman et al. (2013) extended the piecewise linear regression for shape time-series by using piecewise geodesic interpolation.

The motion/deformation estimates have been made from imaging data acquired using MR (Perperidis et al., 2005a, De Craene et al., 2012a, Medrano-Gracia et al., 2014b, Sinclair et al., 2018, Peressutti et al., 2017), US (Duchateau et al., 2010, 2011), both MR and US (Puyol-Antón et al., 2017b) or CT (Hoogendoorn et al., 2013, Ardekani et al., 2009).

To date, most atlases have been built from less than 100 subjects (Chandrashekara et al., 2003, Rougon et al., 2004, Perperidis et al., 2005a, Duchateau et al., 2010, 2011, De Craene et al., 2012a, Lu et al., 2009, Garcia-Barnes et al., 2010, Peressutti et al., 2017). In a few cases, larger databases have been used to construct motion atlases, such as the CAP that contains 3000 subjects, consisting of 2864 asymptomatic volunteers from the MESA cohort and 470 patients with myocardial infarction from the DETERMINE cohort (Fonseca et al., 2011, Medrano-Gracia et al., 2013b, 2014b), and the Hammersmith data set (Bai et al., 2015b) that contains 1093 healthy subjects.

3.3 Statistical cardiac motion atlases

Historically, atlases aimed at providing a standard reference anatomy for comparing subjects in a common space. Over the years, atlases have evolved to represent, on top of a template anatomy, the variability of the anatomy within a population; such atlases are typically known as statistical atlases. In the context of this thesis, statistical cardiac motion atlases seek to establish a statistical description of the structure and the function of the heart over the cardiac cycle, in order to provide a deeper understanding of human cardiac pathologies.

Most of the techniques described in the previous section seek to create an average model of a given population by registration techniques. This section focuses on the extraction of statistical information about shape and motion across the population, which can be achieved using the atlas previously constructed and some statistical metrics or ML techniques.

For motion atlas, in many cases the motion representation in the atlas space is very high dimensional, and in order to be able to obtain meaningful descriptors, many authors have proposed the use of dimensionality reduction algorithms as a pre-processing step. Techniques proposed include PCA (Rougon et al., 2004, Perperidis et al., 2005a, Medrano-Gracia et al., 2010, Hoogendoorn et al., 2013, McLeod et al., 2013), ICA (Suinesiaputra et al., 2009, Medrano-Gracia et al., 2010), manifold learning (Duchateau et al., 2012), and bilinear spatiotemporal models (Hoogendoorn et al., 2009, Akhter et al., 2012), in which the inter-subject variation and inter-phase variation are encoded separately in two dimensions. More recently, Rohé et al. (2018) proposed a new low-dimensional subspace analysis called the barycentric subspace to study cardiac motion over the cardiac cycle. The barycentric subspace is a multiple reference approach that locally defines a submanifold of dimension k which generalises geodesic subspaces, and overcomes the need to choose a reference frame or mean value. The extracted low-dimensional parameters were used in a group-wise analysis to separate populations of healthy subjects and patients with Tetralogy of Fallot.

Another possible approach to reducing the dimensionality of the data is to use the 17-segment model proposed by the American Heart Association (AHA). This is conventionally used to divide image data into regional segments using criteria based on anatomical structures (Cerqueira et al., 2002), but it can also be used then to perform an analysis of the motion within each segment (Rougon et al., 2004, Suinesiaputra et al., 2009, Punithakumar et al., 2013). More specifically, the recommendation given by the AHA is to divide the left ventricle of the heart into 17 regions with six regions for the basal area (1-6), six regions for the mid area (7-12) and five for the apical areas (13-17). An advantage of dividing the myocardium into segments in this way is that the AHA delineation is widely understood by clinicians. However, coronary perfusion territories do not follow the AHA segment delineations so they may not be the optimal representation for diagnostic purposes. Motivated by this, Bai et al. (2015a) proposed an alternative parcellation of the LV based on motion information. Based on the AHA delineation, McLeod et al. (2012, 2013, 2015) proposed a polyaffine model to represent the 4D LV motion using a low number of parameters. In this approach, the motion of the myocardium was represented as an affine transformation for each of the 17 AHA segments, and inter-subject comparisons of these transformations was facilitated by conversion to a prolate spheroidal coordinate system.

Based on the motion descriptors extracted, different statistical methods have been used to analyse differences between groups. For example, [Duchateau et al. \(2010, 2011\)](#) introduced a framework to assess septal flash, which denotes an early septal inward/outward motion. From the motion atlas, they calculated the Hoteling's T-square distance between the velocity distributions of the atlas population and each individual. A higher value of abnormality corresponded to a lower p-value. Later, [De Craene et al. \(2012a\)](#) used statistical parametric mapping (SPM) on the velocity field obtained from the motion atlas to quantify motion abnormality. More recently, [Bai et al. \(2015b\)](#) applied SPM analysis on a larger database (1000 subjects) to study the impact of gender and age on regional myocardial wall thickness.

Supervised learning algorithms have been proposed to learn the representation of pathological motion patterns from a given population and to compare individuals to statistical models of a reference population. An example of the use of supervised learning methods is [Perperidis et al. \(2005a\)](#), who proposed a framework for differentiating normal patients from hypertrophic cardiomyopathy patients based on a k-weighted NN-classifier, using the first four principal components of the anatomical atlas.

[Punithakumar et al. \(2013\)](#) proposed a framework based on a naïve Bayesian classifier, for detecting and localising myocardial segments that show abnormality. The work used Shannon's Differential Entropy (SDE) as features, which were calculated in different regions. Comparing SDE to statistical moments, SDE measures the whole distribution information, which is more discriminative. [Medrano-Gracia et al. \(2013b\)](#) used a SVM classifier, with Bezier cubic control points as features, to classify normal, hypokinetic, akinetic and dyskinetic patients. For each segment, they trained the classifier to predict the Regional Wall Motion Abnormalities or Late Gadolinium Enhancement scores from the atlas coordinates.

In summary, statistical cardiac motion atlases have been widely applied in cardiac function assessment. Applications using a single modality have included the analysis of normal and pathological LV motion (De Craene et al., 2012a, Medrano-Gracia et al., 2013b, 2014b, Duchateau et al., 2011, 2012, Bai et al., 2015b), the identification of disease (Perperidis et al., 2005a, Punithakumar et al., 2013, Ardekani et al., 2009) and prospectively predicting treatment outcome (Duchateau et al., 2009, 2010, 2011, Peressutti et al., 2017, Sinclair et al., 2018). In the multimodal domain, Medrano-Gracia et al. (2013a) proposed an atlas-based method to correct shape bias between different MR sequence acquisitions. They showed that after applying bias correction they could improve the detection of statistical differences in regional shape and motion between cohorts. There have been no examples of fully multimodal statistical cardiac motion atlas to date.

In the context of this thesis, Chapter 5 focuses on multi-view co-regularisation dimensionality reduction algorithms, which aim to find a latent subspace shared by 3D MR and 3D US data to facilitate a more robust characterisation of cardiac motion using low cost 3D US data. Subsequently, chapter 6 focuses on multi-view co-regularisation supervised learning, which aims to infer a classification function from the multi-view labelled training data. Before describing these novel methodological contributions, the next chapter introduces the datasets that are used to evaluate the novel methods later in the thesis.

4 | Materials

This Chapter presents details of the two data sets used for the experimental work of this thesis. The first data set is the multimodal data set used in Chapters 5, 6 and 7 to generate the multimodal cardiac motion atlas and for its application to detect DCM patients. The second data set is the UK Biobank data set*, which is a national health resource that aims to improve diagnosis and prevention of a wide range of serious and life-threatening illnesses. UK Biobank recruited 500,000 people aged between 40-69 years in 2006-2010 from across the country to take part in this project. A cohort of 1000 subjects of this data set was used in Chapter 5 to validate the atlas formation. Furthermore, a subset of 100 subjects of the same data set was used in Chapter 7 for evaluation of automatic quantification of myocardial longitudinal, radial and circumferential strain from cine MR sequences. Finally, a healthy cohort of the UK Biobank was used to compute the reference ranges in Chapter 8.

The following subsections provide details of these two data sets. Please refer to the later Chapters for specific details of their use in this thesis.

4.1 Multimodal data set

The overall multimodal data set is a combination of three clinical MR and 3D US data sets. The first is the database used for the cardiac motion analysis challenge that was held at the 2011 MICCAI workshop “Statistical Atlases and Computational Models of the Heart: Imaging and Modelling Challenges” (STACOM'11) (Tobon-Gomez et al., 2013). The STACOM'11 database includes MR and US data from 15 healthy volunteers acquired at the Division of Imaging Sciences and Biomedical Engineering, King's College London, United Kingdom, and the Department of Internal Medicine II - Cardiology, University of Ulm, Germany.

*<https://www.ukbiobank.ac.uk/about-biobank-uk>. The research presented in this thesis was conducted using the UK Biobank Resources under application number 17806.

The second data set was acquired at the Division of Cardiology, Cliniques Universitaires St-Luc, Avenue Hippocrate 10-2881, B-1200 Brussels, Belgium. Subjects were prospectively recruited after giving written informed consent to the institutional review board-approved protocol (Comité Ethique Hospitalo Facultaire Université Catholique de Louvain, Brussels, Belgium). This contains MR and US data acquired from 26 healthy volunteers and 19 patients with DCM.

The third data set was more recently acquired at the School of Biomedical Engineering & Imaging Sciences, King's College London, United Kingdom, and contains MR and US data acquired from a further 9 healthy volunteers.

The first and second MR data sets were acquired using a 3T Philips Achieva System (Philips Healthcare, Best, The Netherlands), while the third data set was acquired using a 1.5T Philips Ingenia System (Philips Healthcare, Best, The Netherlands). The US data sets were all acquired using an iE33 3D echocardiography system (Philips Medical Systems, Bothell, WA, United States) with a 1-5 MHz transthoracic matrix array transducer (xMATRIX X5.1). Full-volume acquisition mode was used in which several smaller imaging sectors acquired over multiple cardiac cycles are combined to form a large composite volume.

In particular, the three data sets contain for each subject:

- **cine SA and LA:** a multi-slice SA cine-MR sequence covering the full heart, and two orthogonal LA planes (2Ch and 4Ch views) (TR/ TE = 3.0/1.5 ms, flip angle = 60°). Typical slice thickness was between 8.0 - 10.0 mm for SA and LA sequences respectively, with an in-plane resolution between 1.0 - 1.4 mm × 1.0 - 1.4 mm. Typical temporal resolution was between 25 and 30 frames per cycle. In this thesis, only the ED frames of the cine SA and LA data were used for geometry estimation (see Section 5.2). The cine SA and LA sequences were not used for motion estimation.
- **TAG:** a 3D tagged MR sequence in three orthogonal directions (TR/ TE = 7.5/3.2 ms, flip angle = 19°, tag distance between 7.7 -8.8 mm). The images have reduced FoV enclosing the LV, with typical isotropic 3D spatial resolution between 2.5 mm and 1.1 mm, and typical temporal resolution between 22 and 30 frames per cycle. The TAG data were used for motion estimation (see Section 5.2).

- **US:** an apical 3D LV full-volume ultrasound sequence. Typical image resolution and size varied from 0.7 mm - 1.0 mm and $208 \times 240 \times 176$ to $272 \times 256 \times 224$ voxels, respectively. Typical temporal resolution was between 15 and 23 frames per cycle. The US data were used for both geometry and motion estimation (see Section 5.2).

The three data sets described above were combined to form a single data set for the experiments described in this paper. The total amount of included cases was 19 patients with DCM and 50 healthy volunteers. Chapters 6 and 7 use the full cohort, while Chapter 5 only uses the volunteer subset. Demographics of the entire cohort are shown in Table 4.1. LV volume was computed from manual endocardial segmentations using Simpson's rule.

	Healthy volunteers	DCM patients	
Study population, <i>n</i>	50	19	
Age (years)	37 (20-77)	54 (30-79)	
MR	LVEDV (mL)	169.2 (24.8)	262.9 (79.3)
	LVESV (mL)	72.54 (14.1)	193.26 (74.7)
	EF (%)	56.9 (7.2)	27.9 (12.3)
	LVM (g)	101.7 (14.7)	73.2 (30.5)
US	LVEDV (mL)	128.5 (14.7)	237.7 (74.8)
	LVESV (mL)	61.1 (16.8)	174.2(72.6)
	EF (%)	52.07 (8.9)	24.1 (11.8)
	LVM (g)	92.9 (19.2)	66.8 (26.6)

Table 4.1: Study demographics: end-diastolic volume (LVEDV), end-systolic volume (LVESV), ejection fraction (EF) and LV mass (LVM). All expressed as mean (standard deviation) and age expressed as mean (min-max).

Figure 4.1 shows an example of LV MR and US acquisitions for a healthy volunteer and a patient suffering from DCM.

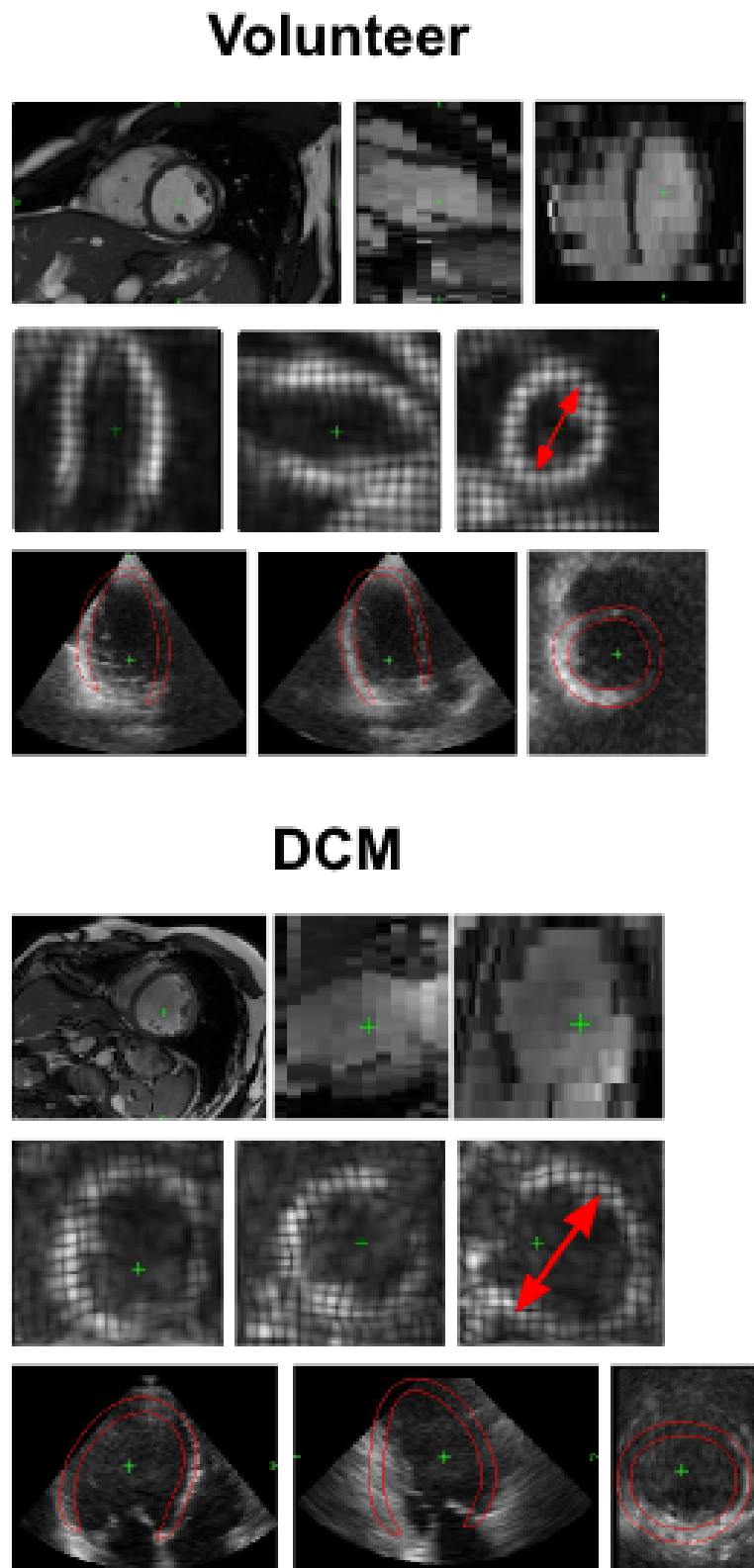


Figure 4.1: Examples of MR and 3D US acquisitions for a healthy volunteer (top: cine MR, middle: tagged MR, bottom: US), and a patient suffering from DCM. Red arrows indicate the dilation of the LV in the patient suffering from DCM compared to the healthy volunteer.

4.2 UK Biobank data set

The UK Biobank data set contains multiple imaging and non-imaging information from more than half a million 40-69 year-olds. From this data set, only subjects with MR imaging data were considered. MR imaging was performed in Cheadle, United Kingdom, on a clinical wide bore 1.5 Tesla scanner (MAGNETOM Aera, Syngo Platform VD13A, Siemens Healthcare, Erlangen, Germany). Although MR acquisitions include multiple sequences (Petersen et al., 2016), this thesis only utilises data from the following sequence:

- **cine SA:** a multi-slice SA cine-MR sequence covering the full heart (TR/ TE = 2.6/1.10 ms, flip angle = 80°). Slice thickness was 8.0 mm with 2.0 mm slice gap, an in-plane resolution of 1.8 mm × 1.8 mm. Temporal resolution was fixed to 50 frames per cycle.
- **cine LA:** two orthogonal LA planes (2Ch and 4Ch views) (TR/ TE = 2.7/1.16 ms, flip angle = 80°). Slice thickness was 6.0 mm with an in-plane resolution of 1.8 mm × 1.8 mm. Temporal resolution was fixed to 50 frames per cycle.

In Chapter 5 a cohort of 1000 subjects selected from this data set is used to generate synthetic multimodal data for analysing the performance of different atlas formation techniques (see Section 5.3.2). In Chapter 8 non-imaging data such as the International Classification of Diseases (ICD), medical conditions (i.e. hypertension, diabetes), body measures, blood pressure and medication are used to select two cohorts: (1) normal population, i.e. individuals without cardiovascular diseases or impairment, and (2) patients with ischaemia. A complete list of the exclusion criteria used to generate the normal population cohort is presented in Appendix A. These two cohorts are used in Chapter 7 to validate the proposed strain analysis technique.

5 | Multimodal cardiac motion atlases formation

5.1 Introduction

As mentioned in Section 3.2, all previous works on statistical cardiac motion atlases have used the same modality (usually MR) to build the atlas and to embed new subjects into it. This Chapter presents a novel method for building a spatiotemporal atlas from imaging data acquired from a cohort of subjects using two different modalities (MR and US), but to apply it to a new subject using only a single modality (US). The technique works by applying a multi-view subspace learning algorithm (Sun, 2013, Xu et al., 2013) (see Section 3.1.2 from literature review) to simultaneously reduce the dimensionality of the data from the two modalities into a common latent subspace. This is the first time that such a technique has been proposed in the area of atlas formation.

The proposed approach is evaluated using monomodal (MR) data from 1000 subjects from the UK Biobank database, and also using multimodal data (MR and US) acquired from a cohort of 50 volunteers (please refer to Chapter 4 for details of these two data sets). Furthermore, the atlas is used to analyse dominant cardiac motion patterns and the differences between motion data estimated using the two modalities.

The remainder of this Chapter is organised as follows. Section 5.2 describes the framework used to build the multimodal spatiotemporal cardiac motion atlas, including a description of the different multi-view learning algorithms employed. Section 5.3 is devoted to experiments on the UK Biobank data set and the multimodal data set. Finally, Section 5.4 discusses the findings of this Chapter in the context of the literature.

5.2 Methods

This section outlines the procedure used for multimodal spatiotemporal atlas formation, which is based on the work published in [Puyol-Antón et al. \(2016, 2017b\)](#). The proposed framework is illustrated in Figure 5.1 and the following subsections describe each of the stages in detail.

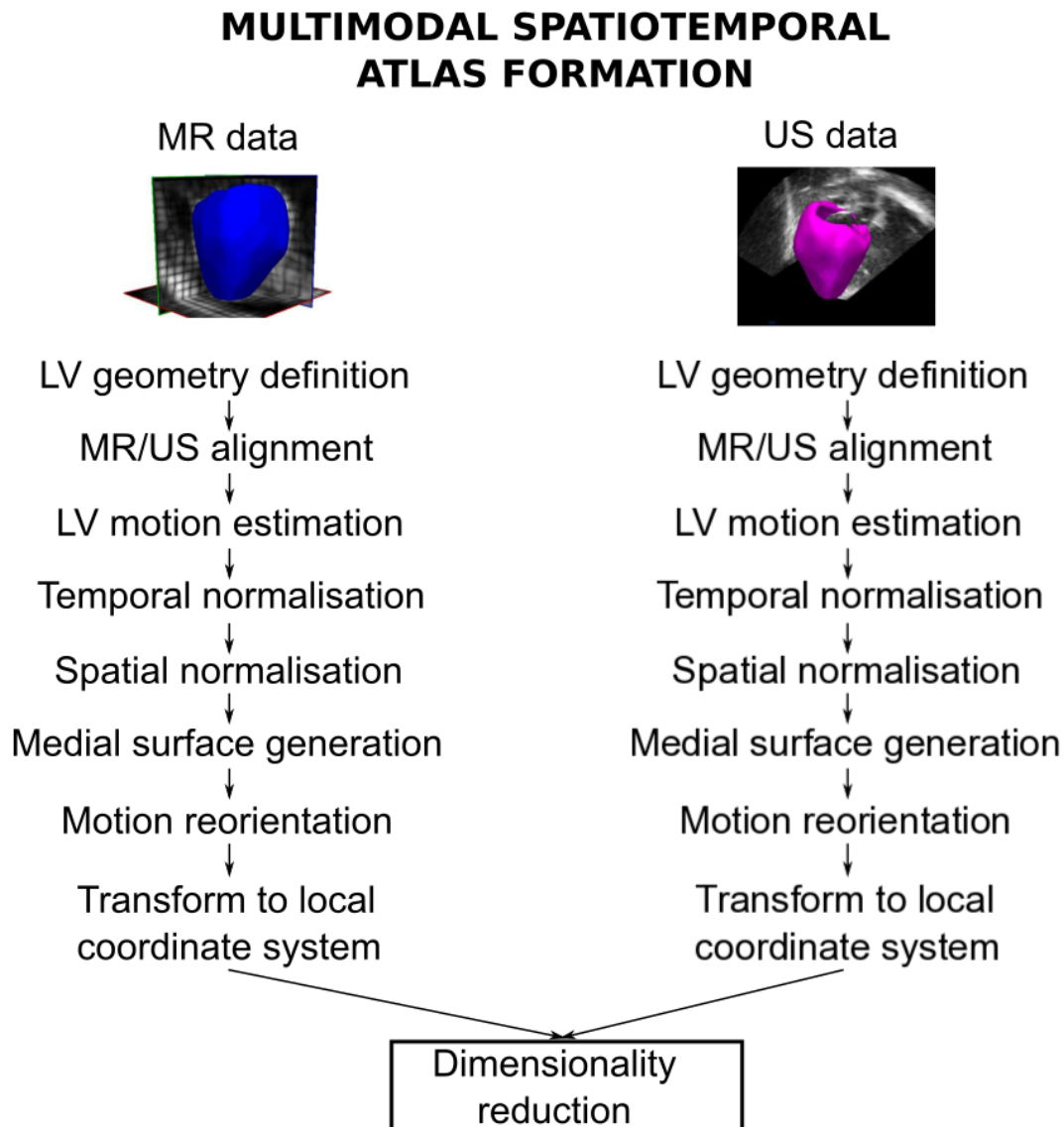


Figure 5.1: Overview of the proposed framework for spatiotemporal cardiac motion atlas formation.

5.2.1 LV geometry definition

For each subject, the LV myocardium was manually segmented in the ED cine MR SA/LA and 3D US images using ITK-SNAP (Yushkevich et al., 2006). The MR SA and LA segmentations were used to correct for breath-hold induced motion artefacts using the iterative registration algorithm proposed in Sinclair et al. (2017). The motion-corrected LA/SA segmentations were fused to form a 3D smooth myocardial mask. An open-source LV mesh-based statistical shape model (SSM) was optimised to fit to this LV binary mask following an initial rigid registration using anatomical landmarks (Bai et al., 2015b). The use of landmarks ensured that the LV mesh was aligned to the same anatomical features for each patient, and the endocardial and epicardial surfaces of the mesh were smoothly fitted to the myocardial mask, providing surface meshes with point correspondence for each of the subjects and a 17 AHA regions segmentation. An example of a mesh fitted to the cine MR SA and 3D US images is illustrated in Figure 5.2 (a-b), visualised using Eidolon* (Kerfoot et al., 2016).

5.2.2 MR/US alignment

In order to apply the mesh generated from cine SA to the TAG sequence, the cine SA and TAG sequences were rigidly aligned. To achieve this, first a detagged MR volume from the TAG sequence was generated using Eidolon (Kerfoot et al., 2016), and then an intensity-based rigid registration (Studholme et al., 1999) was used to align the detagged and cine SA sequences at ED. The rigid registration algorithm was implemented in the Image Registration Toolkit (IRTK) †

In order to compare US and MR-based motion estimation, the US and MR images should be represented in a common space. To achieve this, a Procrustes alignment (Gower and Dijksterhuis, 2004) was applied to align LV mesh points derived from each of the two modalities. The AHA segmentations generated in both meshes were used to ensure that the midseptum was in the same location in both modalities. An example of registered MR/US images is shown in Figure 5.2 (c-d).

*Eidolon URL: <https://github.com/ericspod/Eidolon>.

†IRTK URL: <https://github.com/BioMedIA/IRTK>.

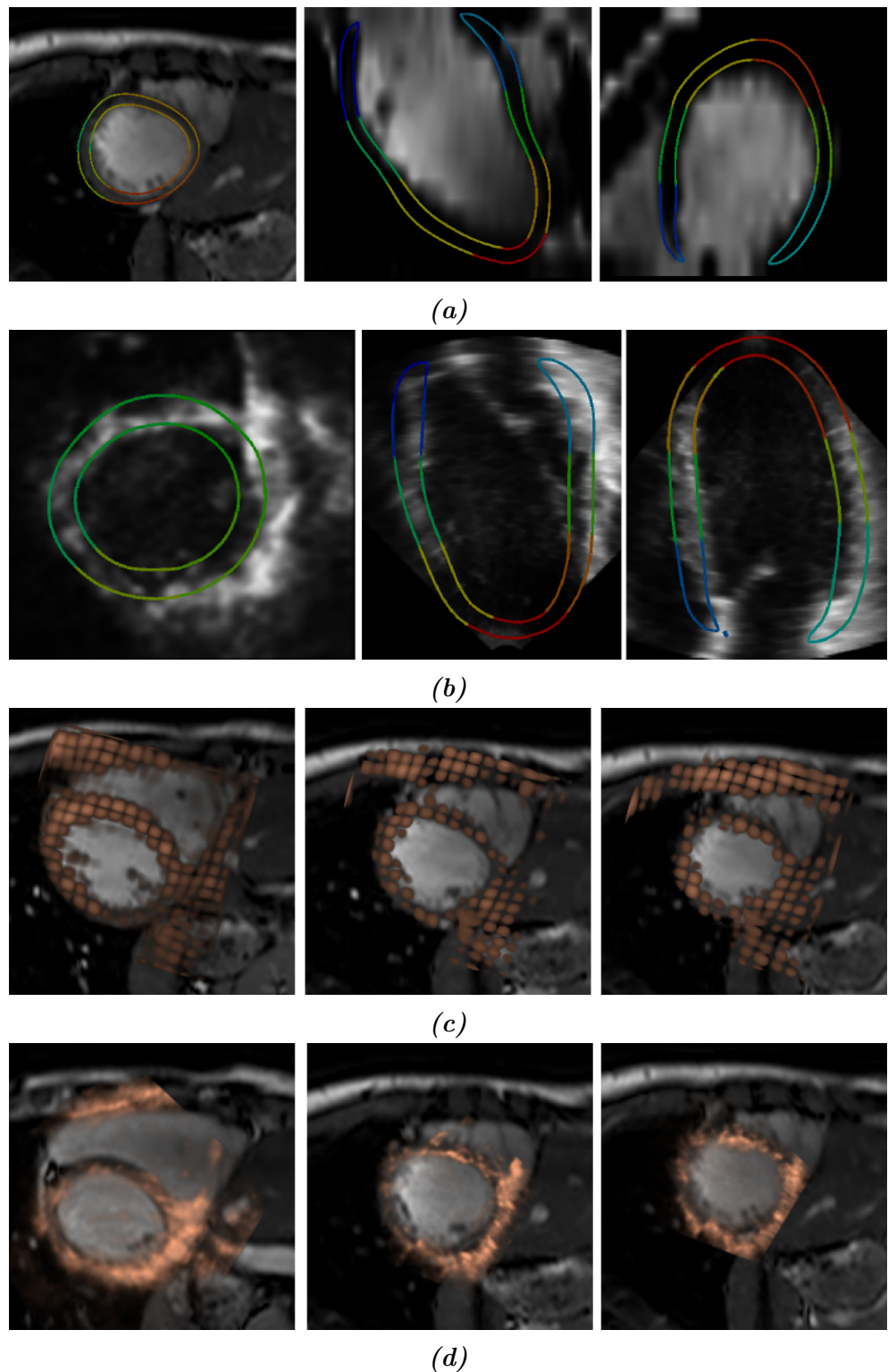


Figure 5.2: Examples of estimated LV geometry at end-diastole overlaid onto 3 orthogonal slices from: (a) cine MR SA, and (b) US. The colours represent the 17 AHA regions available from the SSM. Example of MR/US registration: (c) cine SA and TAG alignment using intensity-based rigid registration, and (d) MR/US registration using Procrustes alignment.

5.2.3 LV motion estimation

A 3D GPU-based B-spline FFD registration was used (Rueckert et al., 1999) to estimate LV motion between consecutive frames of the MR and US sequences. As described in Sinclair et al. (2016) and Peressutti et al. (2017), the sequentially estimated FFD displacement fields were composed to obtain the FFD transformation from each cardiac phase to the reference ED phase. Furthermore, a $3D+n$ cyclic B-spline was fitted to the composed 3D transformations in order to estimate a full cycle $3D+n$ transformation (Unser, 1999) using the IRTK software. The result of the motion estimation was, for each subject k , a smooth $3D+n$ transformation $\psi^{3D+n}(\mathbf{v}, n)$, where \mathbf{v} represents the spatial coordinates of the vertices and n is the cardiac phase. Figures 5.3 and 5.4 show an example of the estimated motion fields from the B-spline FFD registration for MR and US in the dx, dy, dz direction in three orthogonal views.

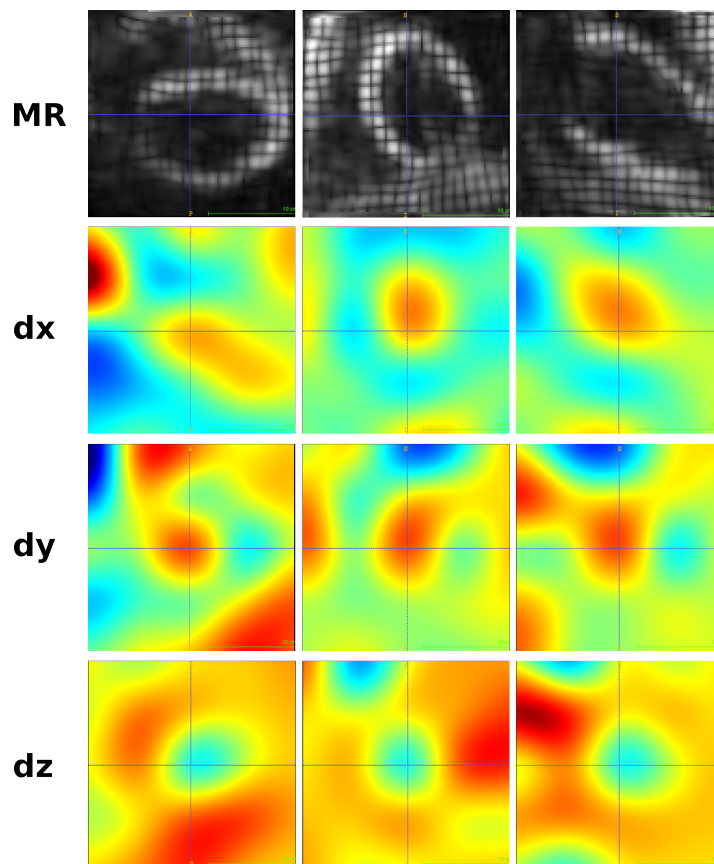


Figure 5.3: MR displacement field from the B-spline FFD registration for components x , y and z direction in three orthogonal views.

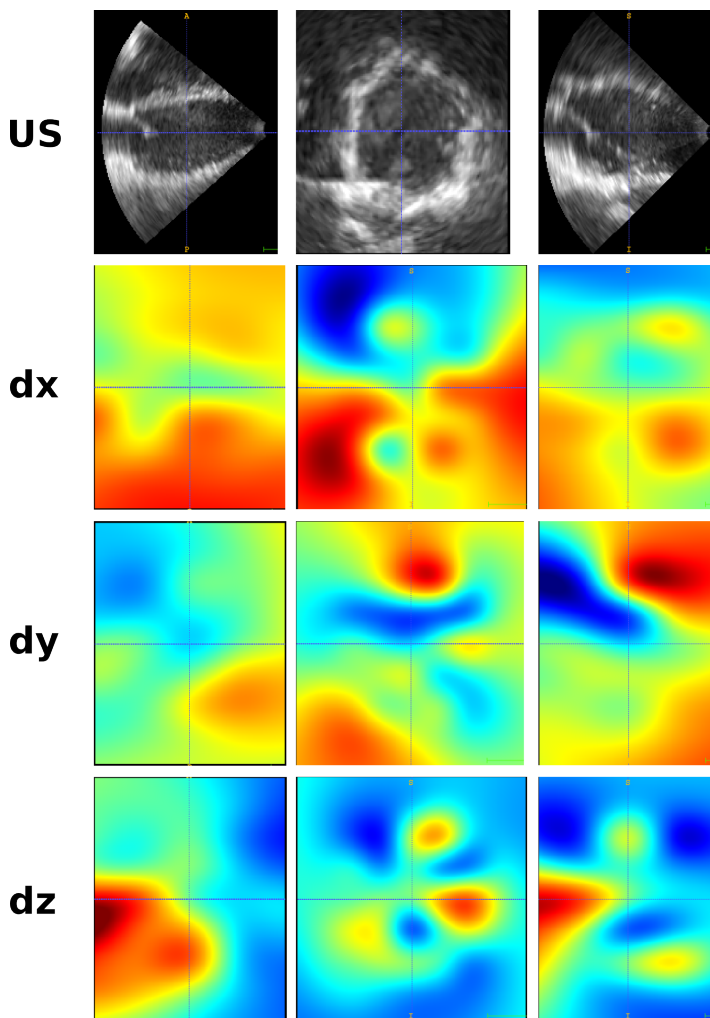


Figure 5.4: US displacement field from the B-spline FFD registration for components x , y and z direction in three orthogonal views.

5.2.4 Temporal normalisation

Temporal normalisation aims to ensure temporal correspondence between subjects. In cardiology, corresponding time-points can be defined as the timings of specific cardiac physiological states, e.g. the end of diastole/systole for a given ventricle (see Figure 2.2). In the cardiac atlas literature there have been two approaches for temporal normalisation: (1) a global normalisation only with respect to the length of the cardiac cycle (Peressutti et al., 2017); (2) alignment of specific cardiac timings (Duchateau et al., 2011). The second approach has the potential to establish a more precise temporal correspondence and so this is the approach adopted in this thesis (as described below). In Section 5.3.3 the impact of this approach on the multimodal atlas formation is evaluated and compared with a global scaling approach.

The following cardiac timings were automatically identified based on volume curves computed using the estimated geometries and motions for all subjects (note that the temporal normalisation step is applied separately to the MR and US data).

- **Beginning of the isovolumetric contraction phase (P1):** The point at ED at which the volume in the cavity is maximised - LVEDV. For both MR and US sequences, the ED frame corresponds to the first frame of the sequence.
- **Beginning of the isovolumetric relaxation phase (P2):** The point at ES at which the volume in the cavity is minimised - LVESV. This minimum volume is the point where the first derivative of the volume of the cavity is zero.
- **Beginning of the atrial systole phase (P3):** The point when the atrium contracts and increases the volume in the ventricle with only a small amount of blood. Atrial contraction is complete before the ventricle begins to contract. The point of maximum atrial contraction is the minimum of the second derivative of the volume of the LV cavity.

Temporal normalisation was achieved for each modality by aligning these three cardiac timings and using piecewise linear scaling to interpolate a fixed number of time points between them to ensure that the number of frames was equal for all of the subjects. Figure 5.5 shows an example of an MR and US LVV curve before and after temporal normalisation.

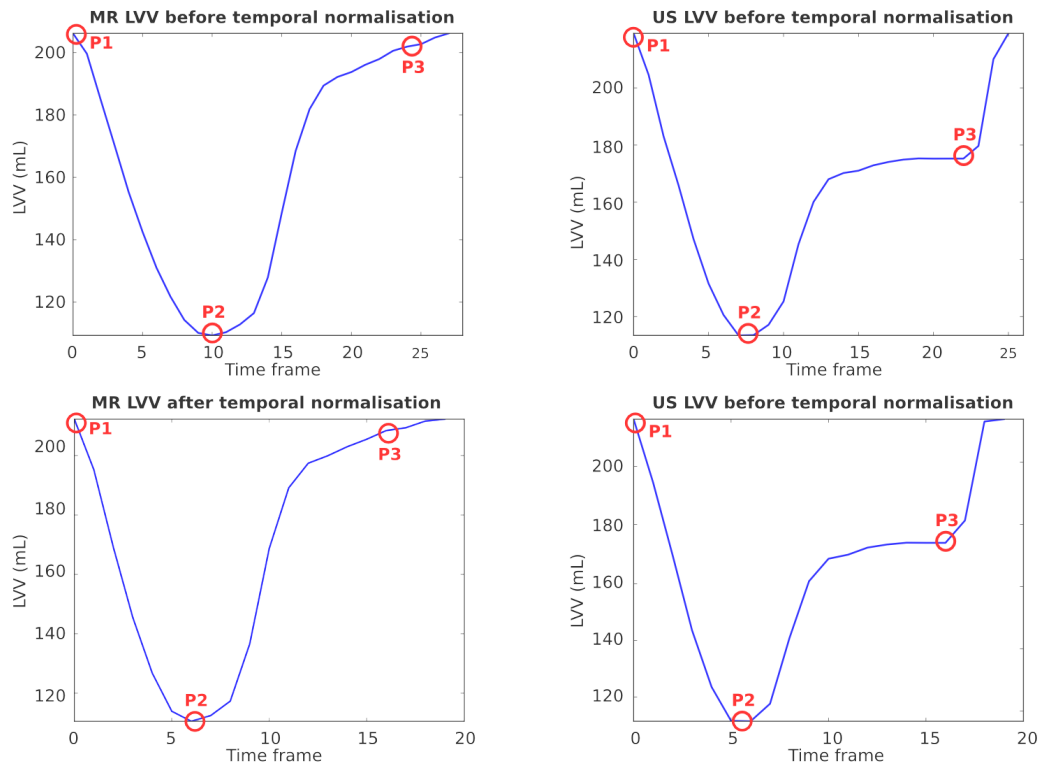


Figure 5.5: Example of an MR and US LVV curve before and after temporal normalisation.

5.2.5 Spatial normalisation

Spatial normalisation aims to remove bias towards differences in subject-specific LV geometries from the motion analysis. From the previous steps, LV meshes at ED were derived from K subjects from MR and US data. First, a Procrustes alignment was performed to register each mesh to a single mesh selected randomly from the subject cohort, producing a set of affine transformations $\{\phi_{aff}^k\}$, $k = 1, \dots, K$. An unbiased LV mesh was produced by first computing an average of the aligned meshes, and then transforming this average mesh by the inverse of the average affine transformation, which is denoted by $\tilde{\phi}_{aff} = \frac{1}{K} \sum_{k=1}^K \phi_{aff}^k$. The original transformation $\{\phi_{aff}^k\}$ was normalised to enforce an average similarity transformation equal to identity $\hat{\phi}_{aff}^k = \phi_{aff}^k \circ (\tilde{\phi}_{aff})^{-1}$.

A Thin Plate Spline transformation $\{\phi_{TPS}^k\}$ was used to align each mesh to the unbiased LV mesh. The resulting transformation from the subject-specific coordinate system to the unbiased LV mesh is given by $\phi^k = \phi_{TPS}^k \circ \hat{\phi}_{aff}^k$ (De Craene et al., 2012a).

Figure 5.6 shows an example of an LV mesh after the spatial normalisation step.

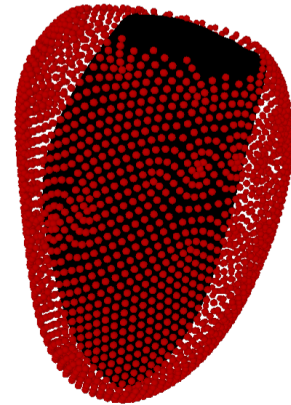


Figure 5.6: Illustration of the spatial normalisation step. Overlay of mesh before (black) and after (red) spatial normalisation.

5.2.6 Medial surface generation

In order to spatially reduce and regularise the number of vertices (≈ 22000) of the SSM mesh, a medial mesh with regularly sampled vertices (≈ 1000) was generated from the personalised SSM epicardial and endocardial meshes using ray-casting and homogeneous downsampling followed by cell subdivision. The same resampling strategy was employed for all personalised SSM meshes to maintain point correspondence, while reducing the dimensionality of the problem. Only points that were more than 3mm apart from each other were retained, thus reducing the number of vertices of the mesh. The use of a medial surface enables a more robust motion estimation compared to the endo- and epicardial surfaces of the SSM as it is likely to be less affected by motion tracking errors which can be caused by inaccuracies in the ED segmentation.

Figure 5.7 shows an example of the surface mesh and the medial mesh.

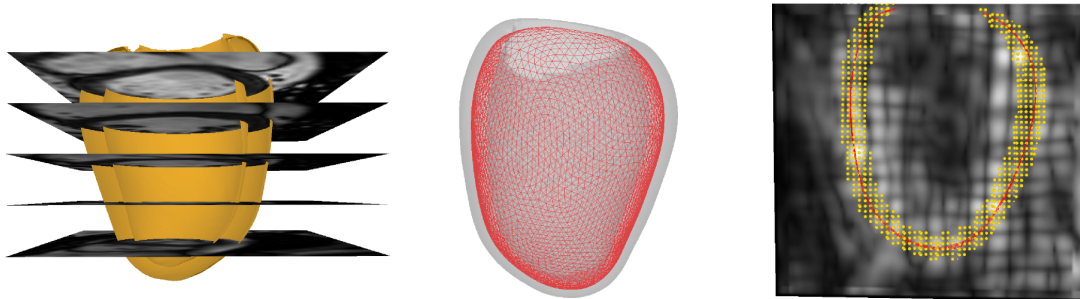


Figure 5.7: Illustration of the medial surface generation step. Left: 3D view of the SA image planes with a truncated LV mesh; Middle: The LV surface mesh (grey outline) with the medial surface (red). Right: LV SSM and medial surface cross-section at the ED phase of the TAG sequence.

5.2.7 Motion reorientation

For each subject k , for each modality, displacements $\mathbf{u}_{m,n,k} = \mathbf{v}_{m,n,k} - \mathbf{v}_{m,ED,k}$ were computed, where $\mathbf{v}_{m,n,k}$ corresponds to the spatial coordinates of vertex m at cardiac phase n for subject k . With the aim of comparing the LV motions from different subjects in the atlas coordinate system, displacement data for each subject were reoriented into the atlas coordinate system under a small deformation assumption (Ashburner, 2007) using a push-forward action (Rao et al., 2004, Duchateau et al., 2011):

$$\mathbf{u}_{m,n,k}^{atlas} = \mathbf{J}_{\phi^k(\mathbf{v}_{m,ED,k})} \mathbf{u}_{m,n,k} \quad (5.1)$$

where $\mathbf{J}_{\phi^k(\mathbf{v}_{m,ED,k})}$ is the Jacobian of the anatomical transformation ϕ^k mapping each subject's reference ED medial mesh to the atlas ED medial mesh, computed at location $\mathbf{v}_{m,ED,k}$.

5.2.8 Transform to local coordinate system

For a more intuitive understanding of the LV motion, displacements in the atlas coordinate system $\mathbf{u}_{m,n,k}^{atlas}$ were projected onto a local cylindrical coordinate system, providing radial, longitudinal, and circumferential information. The long axis of the LV ED atlas medial mesh was used as the longitudinal direction. We denote the resulting MR and US-derived displacements by $\mathbf{x}_{m,n,k}$ and $\mathbf{z}_{m,n,k}$ respectively, where k denotes the subject, n the cardiac phase and m the mesh vertex.

5.2.9 Remove vertices outside the FoV

For each subject, the vertices of the reference ED medial mesh that fell outside of the FoV of the MR or US images were removed from the analysis. The intersection of all subjects' FoVs was computed to only retain the points that fell inside the FoV for all subjects. Most of the vertices removed in this way belonged to the LV apex. After removing the vertices that are outside the FoV, the medial mesh had approximately 650 vertices.

Figure 5.8 shows an example of medial mesh divided into AHA regions and points outside FoV.

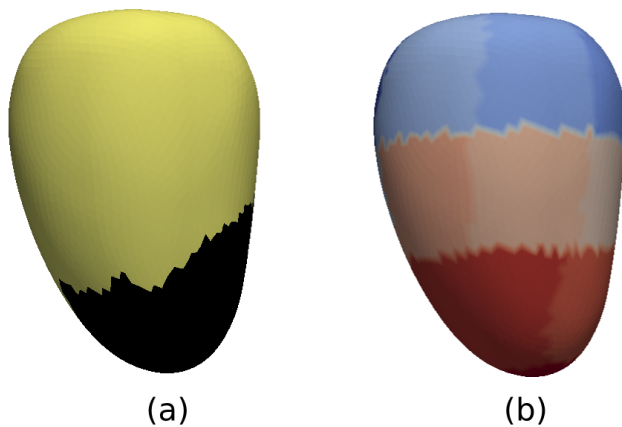


Figure 5.8: Example of medial mesh with points outside FoV in black (a) and divided into AHA regions (b).

5.2.10 Dimensionality reduction

As a result of the previous steps, the LV displacements of each subject are represented in a common atlas coordinate system. With the aim of combining the motion data from US and MR and reducing the dimensionality of the data, three different dimensionality reduction techniques were evaluated: PCA ([Hotelling, 1933](#)), CCA ([Hotelling, 1936](#)), and the 2 blocks partial least squares (PLS) regression algorithm ([Wegelin et al., 2000](#), [Wold, 1985](#)).

All of the evaluated dimensionality reduction techniques are linear. Therefore, they try to determine optimal linear mappings from the high dimensional spaces (i.e. displacement data derived from MR and US) to a low dimensional space whilst preserving as much information as possible. All algorithms represent the multi-view input data as vectors.

Consequently, the local MR displacements in atlas space $\mathbf{x}_{m,n,k}$ were concatenated into row vectors such that for subject k , $\dot{\mathbf{x}}_k \in \mathbb{R}^{1 \times D}$, where $D = (3 \times N \times M)$ with N the number of cardiac phases and M the number of points in the atlas medial surface mesh. The row vectors $\dot{\mathbf{x}}_k$ for each subject were stacked to produce a matrix $X = [\dot{\mathbf{x}}_1^T, \dots, \dot{\mathbf{x}}_K^T] \in \mathbb{R}^{K \times D}$, where K is the number of subjects. Likewise, the US displacements $\mathbf{z}_{m,n,k}$ were concatenated to form the matrix $Z = [\dot{\mathbf{z}}_1^T, \dots, \dot{\mathbf{z}}_K^T] \in \mathbb{R}^{K \times D}$. The high dimensional MR and US feature vectors formed in this way represent the inputs to the algorithms and their corresponding low dimensional embeddings represent the outputs.

Despite the differences between the proposed algorithms, all of them can be written as a generalised eigenproblem (Wilkinson, 1965). A key difference between them is that PLS and CCA are multi-view subspace learning algorithms and try to find basis vectors for two sets of variables (MR and US derived) such that the projections onto these basis vectors are mutually maximised based on certain criteria. PCA, on the other hand, estimates an orthogonal linear transformation that transforms the data from a single set of variables (i.e. a single modality) into a low dimensional space preserving as much of the variance in the data as possible. PLS and CCA were trained on multi-view MR and US derived data, whereas PCA was trained on MR derived data only and then applied to both MR and US derived data.

Below, the three proposed dimensionality reduction algorithms (PCA, PLS and CCA) are described using a common notation (Borga et al., 1997). In the following, C_{xx} and C_{zz} correspond to the covariance matrices of the first (i.e. MR) and second (i.e. US) data sets respectively, and C_{xz} and C_{zx} are the cross-covariance matrices of the two data sets (MR/US).

PCA

PCA was proposed in Hotelling (1933) to find an orthogonal linear transformation that transforms a set of variables into a new space where they are uncorrelated. This transformation is defined such that it finds the directions of maximum data variance.

$$\begin{aligned} \max_{\mathbf{w}} \quad & \mathbf{w}^T C_{xx} \mathbf{w} \\ \text{subject to} \quad & \mathbf{w}^T \mathbf{w} = 1 \end{aligned} \tag{5.2}$$

It can be reformulated as a generalised eigenvector problem as follows:

$$C_{xx} \mathbf{w}_x = \lambda_{PCA} \mathbf{w}_x \quad (5.3)$$

where λ_{PCA} and \mathbf{w}_x are the eigenvalues and eigenvectors respectively of the matrix C_{xx} .

PLS

PLS was proposed in [Wold et al. \(1984\)](#) to model the associations between blocks of observed variables. This work only focuses on the 2 blocks PLS regression algorithm that uses the nonlinear iterative partial least squares (NIPALS) algorithm ([Wegelin et al., 2000](#), [Wold, 1985](#)). PLS tries to find an orthogonal basis, such that the *covariance* between the set of projections onto these basis vectors is mutually maximised:

$$\begin{aligned} \max_{\mathbf{w}_x, \mathbf{w}_z} \quad & \mathbf{w}_x^T C_{xz} \mathbf{w}_z \\ \text{subject to} \quad & \mathbf{w}_x^T \mathbf{w}_x = 1, \mathbf{w}_z^T \mathbf{w}_z = 1 \end{aligned} \quad (5.4)$$

It can be reformulated as a generalised eigenvector problem as follows:

$$\begin{aligned} C_{xz} C_{zx} \mathbf{w}_x &= \lambda_{PLS}^2 \mathbf{w}_x \\ \mathbf{w}_z &= \frac{1}{\lambda_{PLS}} C_{zx} \mathbf{w}_x \end{aligned} \quad (5.5)$$

where λ_{PLS} and \mathbf{w}_x are respectively the eigenvalues and eigenvectors of the matrix $C_{xz} C_{zx}$.

CCA

CCA was proposed in [Hotelling \(1936\)](#) and aims to find basis vectors for two sets of variables such that the *correlation* between the projections of the variables onto these basis vectors is mutually maximised.

$$\begin{aligned} \max_{\mathbf{w}_x, \mathbf{w}_z} \quad & \mathbf{w}_x^T C_{xz} \mathbf{w}_z \\ \text{subject to} \quad & \mathbf{w}_x^T C_{xx} \mathbf{w}_x = 1, \mathbf{w}_z^T C_{zz} \mathbf{w}_z = 1 \end{aligned} \quad (5.6)$$

It can be reformulated as a generalised eigenvector problem as follows:

$$\begin{aligned} C_{xx}^{-1}C_{xz}C_{zz}^{-1}C_{zx}\mathbf{w}_x &= \lambda_{CCA}^2\mathbf{w}_x \\ \mathbf{w}_z &= \frac{1}{\lambda_{CCA}}C_{zz}^{-1}C_{zx}\mathbf{w}_x \end{aligned} \quad (5.7)$$

where λ_{CCA} and \mathbf{w}_x are respectively the eigenvalues and eigenvectors of the matrix $C_{xx}^{-1}C_{xz}C_{zz}^{-1}C_{zx}$.

5.2.11 Atlas application

As described in Section 5.2.7, the LV displacement vectors for MR and US were represented in a common coordinate system (see Eq. 5.1). To apply the dimensionality reduction algorithms (PCA, CCA, PLS) the set of all vectors at all time points for each subject was concatenated, forming the matrices $X = [\dot{\mathbf{x}}_1^T, \dots, \dot{\mathbf{x}}_K^T]$ and $Z = [\dot{\mathbf{z}}_1^T, \dots, \dot{\mathbf{z}}_K^T]$ respectively, where X is the MR-derived motion matrix, Z is the US-derived motion matrix and K is the number of subjects. The vectors $\dot{\mathbf{x}}_k$ and $\dot{\mathbf{z}}_k$ represent the concatenated displacement vectors from MR and US respectively, with size $(3MN)$ where M corresponds to the total number of vertices of the medial mesh (see Section 5.2.6) and N the total number of frames.

Hence, a subject can be embedded into the low dimensional space as:

$$\alpha_k = \mathbf{w}_x^T \dot{\mathbf{x}}_k \quad \text{and} \quad \gamma_k = \mathbf{w}_z^T \dot{\mathbf{z}}_k \quad (5.8)$$

where \mathbf{w}_x and \mathbf{w}_z are the projection matrices computed from X and Z using a dimensionality reduction algorithm (see Section 5.2.10, Eqs. 5.3, 5.5, and 5.7).

Furthermore, the low dimensional embeddings can be reconstructed in the original space as:

$$\hat{\mathbf{x}}_k = \mathbf{w}_x \alpha_k \quad \text{and} \quad \hat{\mathbf{z}}_k = \mathbf{w}_z \gamma_k \quad (5.9)$$

5.3 Experiments and results

This section describes the experiments performed on the UK Biobank and multimodal data sets. All experiments were carried out using the Python programming language, using standard Python libraries (Numpy, SciPy, etc.), VTK libraries, and the scikit-learn Python toolkit (Pedregosa et al., 2011).

The aim of the experiments was to evaluate the ability of the proposed multimodal statistical cardiac motion atlas to form meaningful low dimensional embeddings of multimodal data.

5.3.1 Error measures

For all experiments a common set of error measures was used. The three different evaluation metrics used are illustrated in Figure 5.9 and explained below.

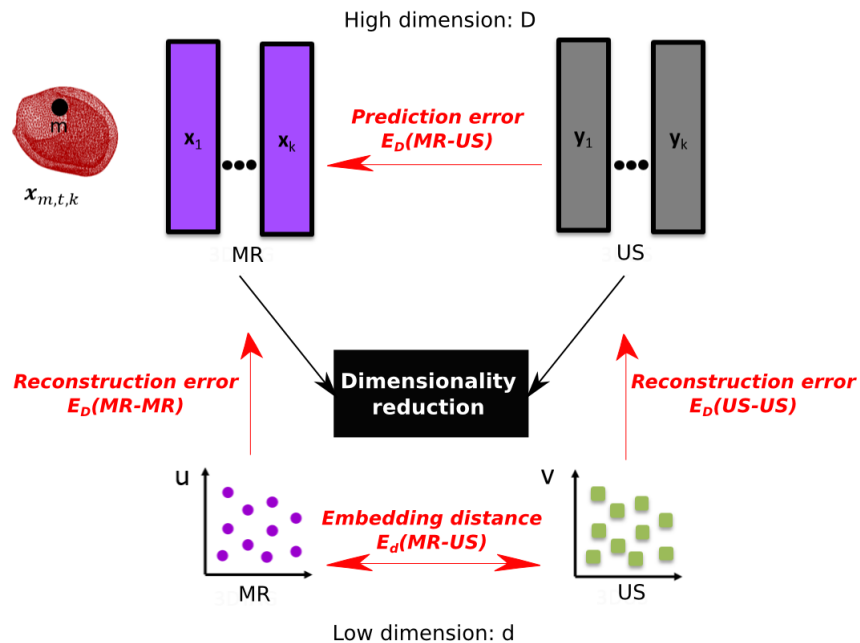


Figure 5.9: Illustration of the metrics used for validation.

Embedding distance:

The embedding distance corresponds to the normalised distance between the low dimensional coordinates obtained using the MR motion vector and those obtained using the US motion vector, and is defined as:

$$E_d^k(MR - US) = \sqrt{\sum_{l=1}^L \frac{(\alpha_{l,k} - \gamma_{l,k})^2}{\sigma_l}} \quad (5.10)$$

where L is the number of components retained by the dimensionality reduction algorithm, and σ_l is the standard deviation of the combined MR/US cloud of points formed by the embedding in dimension l for subject k .

Reconstruction error:

The reconstruction error is defined as the norm between the original motion vector and the reconstructed motion vector. It is computed separately for both $\dot{\mathbf{x}}_k$ (MR) and $\dot{\mathbf{z}}_k$ (US),

$$E_D^k(MR - MR) = \|\dot{\mathbf{x}}_k - \hat{\mathbf{x}}_k\| \quad (5.11)$$

$$E_D^k(US - US) = \|\dot{\mathbf{z}}_k - \hat{\mathbf{z}}_k\| \quad (5.12)$$

where $\hat{\mathbf{x}}_k$ and $\hat{\mathbf{z}}_k$ are the reconstructed vectors from the embedded coordinates $\boldsymbol{\alpha}_k$ and $\boldsymbol{\gamma}_k$ for subject k (see Eq. (5.9)).

Prediction error:

The prediction error is defined as the norm between the original MR motion vector and the predicted MR motion vector given the US motion vector.

$$E_D^k(MR - US) = \|\dot{\mathbf{x}}_k - \tilde{\mathbf{x}}_k(\mathbf{z}_k)\| \quad (5.13)$$

where $\tilde{\mathbf{x}}_k(\mathbf{y}_k) = \mathbf{w}_x \boldsymbol{\gamma}_k$ is the predicted vector for subject k .

The reconstruction errors are intended to measure how well the dimensionality reduction algorithm can find a common space in which correspondences between the two data sources are preserved whilst avoiding overfitting. The embedding and prediction errors are intended to measure how closely the MR and US data match. Therefore, these two measures quantify how well US-based motion data alone can be used to analyse a new subject using a multimodal atlas. In other words, how similar are the atlas embeddings based on MR and US data?

All metrics were computed for each subject using a leave-one-out cross validation. That is, the atlas was formed from K-1 subjects, then the left-out subject was used for embedding into the atlas. The mean of each metric was computed to form the final $E_d(MR-US)$, $E_D(MR-MR)$, $E_D(US-US)$ and $E_D(MR-US)$.

5.3.2 UK Biobank data set experiments

The UK Biobank data set was used to validate the robustness of the proposed dimensionality reduction algorithms for atlas formation. As described in Section 4.2, the data set was formed of a subset of 1000 subjects from the entire UK Biobank cohort.

First, the atlas formation pipeline (see Figure 5.10 for more detail), as described in Sections 5.2.1-5.2.8, was applied to the cine MR images from the UK Biobank cohort, resulting in a set of MR derived displacements for each subject in an atlas coordinate system. Next, to produce synthetic US derived displacements, Gaussian noise ($\mathcal{N}(\mu, \sigma)$) was added to the real MR derived displacements. These synthetic US derived displacements were stored and used later as a ground truth for the validation of the different algorithms. The mean and standard deviation of the Gaussian distribution determine the similarity between the motions of the two modalities.

Two experiments were carried out on this data set. In both cases, first the intrinsic dimensionality L of the MR data was estimated using PCA (which was typically between 15 and 35) and this was then used for the PCA, CCA and PLS algorithms.

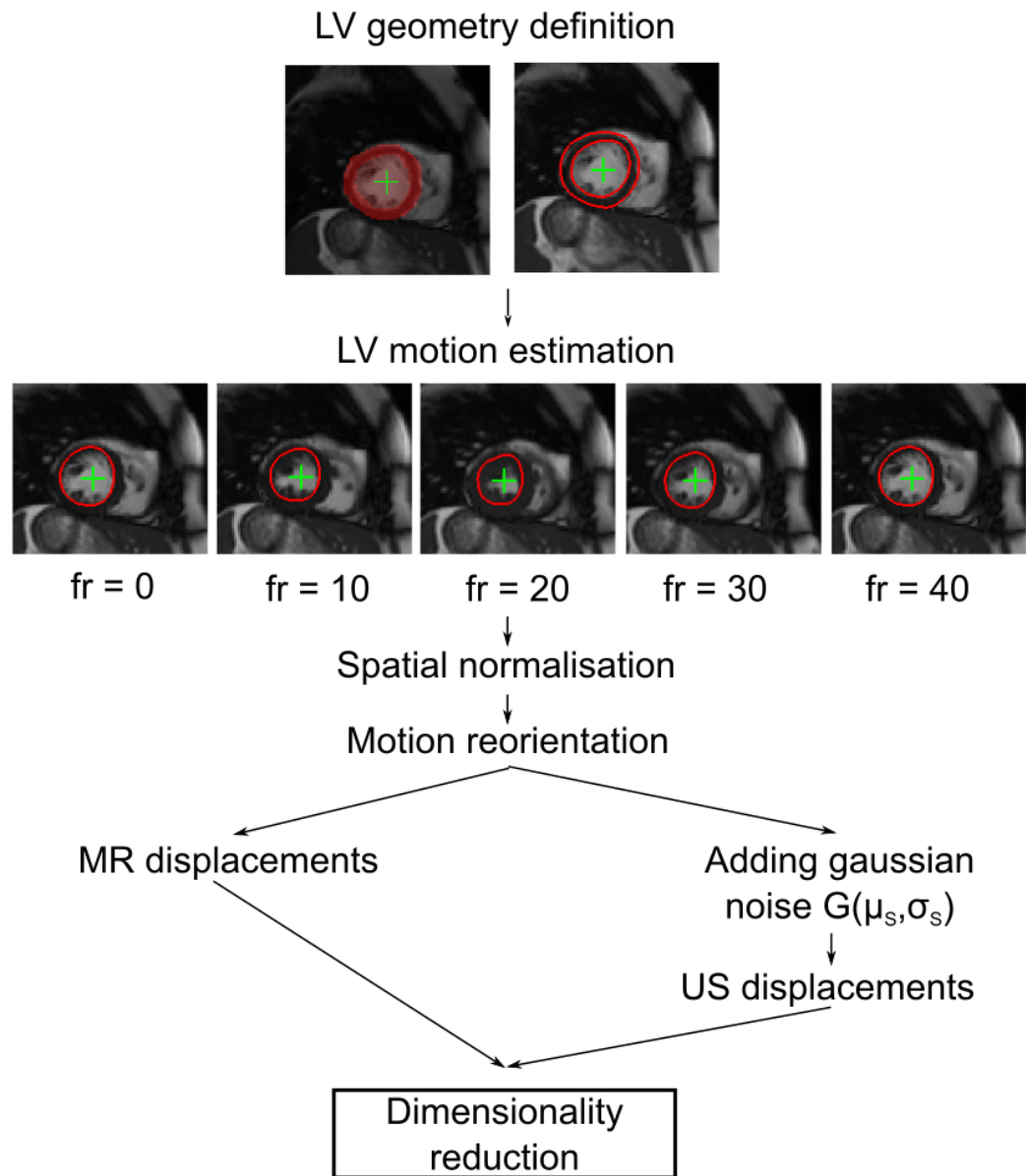


Figure 5.10: Pipeline for generating synthetic US derived displacement from the UK Biobank data set.

Assessment of reconstruction errors whilst varying the numbers of subjects and vertices

The first experiment aimed to assess the variability of the reconstruction error with regard to the numbers of vertices and subjects. For this experiment the amount of Gaussian noise added to produce the US displacements was fixed to realistic values estimated from the multimodal data set ($\mu_R = -0.25$ and $\sigma_R = 4$). Then, the number of vertices was varied between 150 to 950 by decimating the atlas mesh using the algorithm described in [Schroeder et al. \(1992\)](#), and the number of subjects was varied between 50 to 1000. For each combination, using a leave-one-out cross validation the $E_D(MR - MR)$ and $E_D(US - US)$ were computed. This experiment assesses the robustness of the three different dimensionality reduction algorithms with regard to number of features and samples.

Figure 5.11 shows intensity plots for the reconstruction errors for each dimensionality reduction algorithm used. The x-axis corresponds to the number of subjects varying from 50 to 1000, and the y-axis corresponds to the number of vertices varying from 150 to 950. Note that the intensity plots for $E_D(MR - MR)$ share the same colour bar, whilst those for $E_D(US - US)$ have different colour bars for CCA, PLS and PCA.

In general $E_D(MR - MR)$ errors were between 1.2 mm and 2.1 mm, whilst $E_D(US - US)$ for CCA and PLS were between 2.3 mm and 4.7 mm and for PCA between 4.5 mm and 7.2 mm. In all cases, errors increased as the number of subjects decreased and the number of vertices increased. As can be noticed from the intensity plots for $E_D(MR - MR)$, the CCA errors were higher for fewer subjects compared to PLS and PCA and the reconstruction error $E_D(US - US)$ was significantly lower for CCA and PLS compared to PCA.

Assessment of prediction errors

The second experiment computed the prediction error while varying amounts of Gaussian noise were added to the MR displacements to create the synthetic US displacements. For this experiment the number of vertices was fixed to 650 and the number of subjects to 50, which correspond to similar values to those used in the multimodal data set. The aim of this experiment was to assess how the variability between the MR and US data affected the evaluated algorithms.

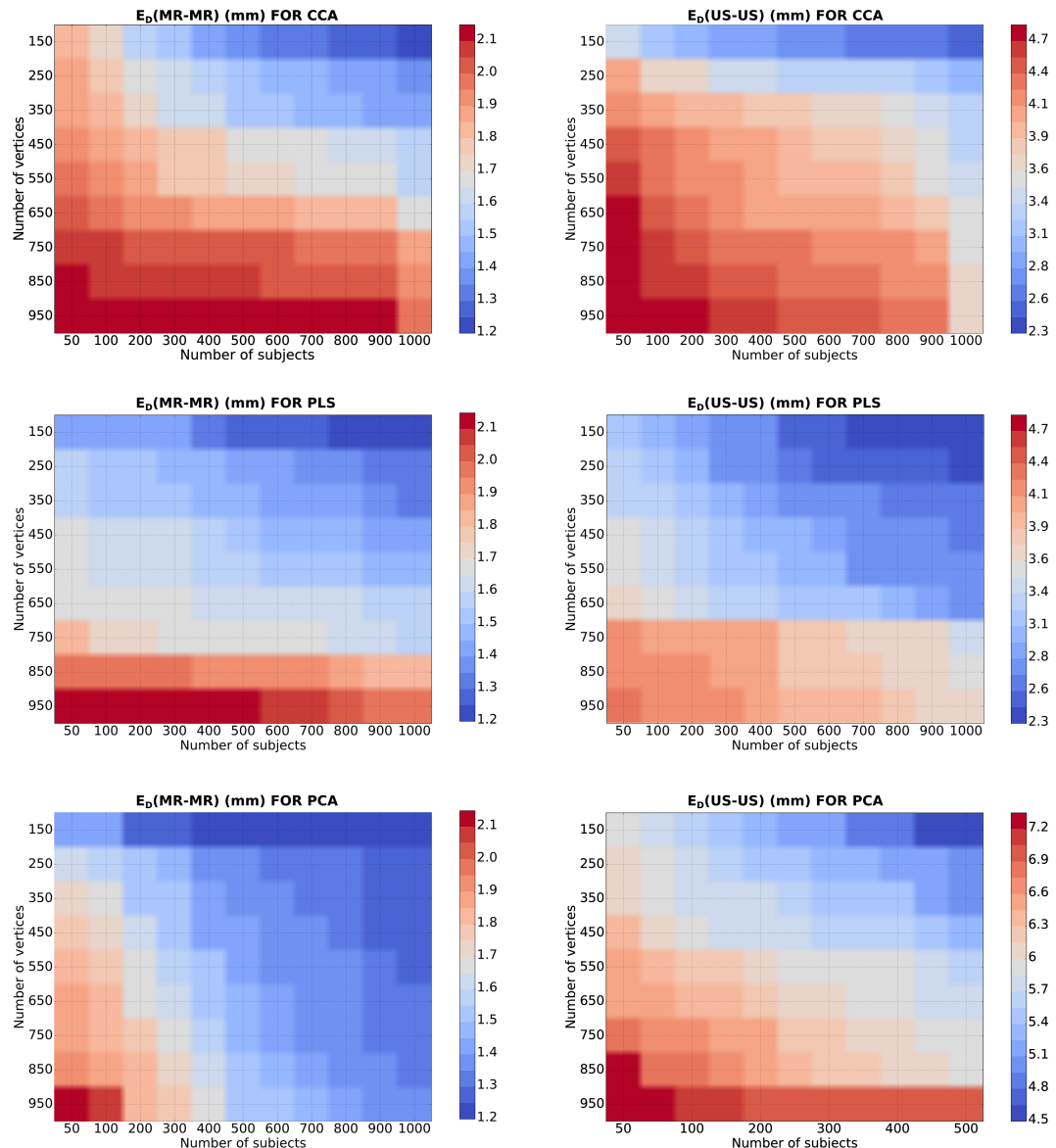


Figure 5.11: Reconstruction error in mm $E_D(MR - MR)$ and $E_D(US - US)$ for the UK Biobank data set for CCA, PLS and PCA.

Figure 5.12a shows the variation of the prediction error whilst varying the Gaussian noise level. The x axis corresponds to the amount of Gaussian noise used (σ_M from 5 mm to 50 mm). For a small σ_M (i.e. more correlated data) the $E_D(MR - US)$ is similar for the three methods, but as σ_M increases the PCA errors have a steep slope, whilst the errors for PLS and CCA increase less quickly.

With the aim of assessing the correlation between the two input variables, for each σ_M value the Pearson's correlation coefficient between the MR and US displacements was also computed (see Figure 5.12b). The values of these Pearson's correlation coefficients were used in the following section to relate the results of this experiment to the multimodal data set.

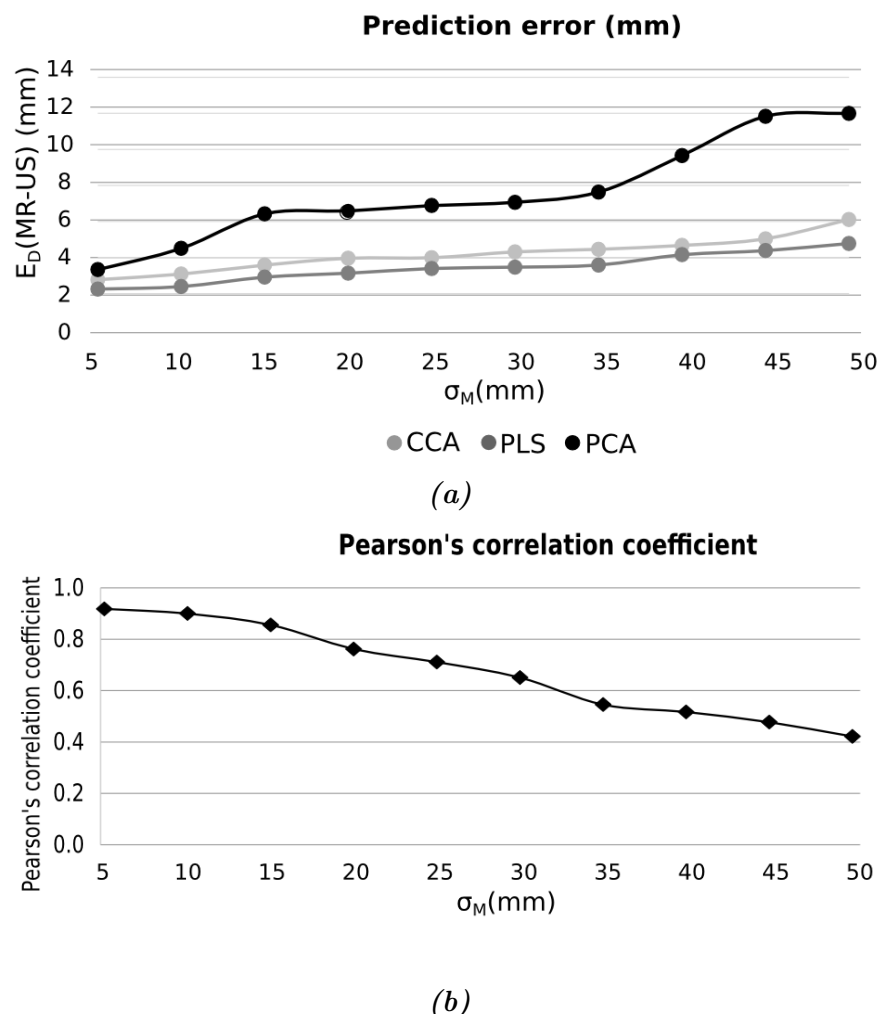


Figure 5.12: (a) Prediction errors in mm for the UK Biobank data set for CCA, PLS and PCA. (b) Pearson's correlation coefficient between the MR and US displacement data for the different Gaussian noise levels used.

5.3.3 Multimodal data set experiments

In the multimodal data set experiments, only the healthy volunteer data from the multimodal data set is used (see Section 4.1 for more information). The first experiment aims to validate the three proposed dimensionality reduction algorithms, showing how the LVV, LVM and the LVEF are affected by the use of the different algorithms. Then, a comparison between the proposed temporal normalisation step, which aligns specific cardiac timings across subjects and the other existing technique (Puyol-Antón et al., 2016, Peressutti et al., 2017), which only normalises with respect to the length of the cardiac cycle is presented by computing the LV volume and the dimensionality reduction errors using the two approaches. The next experiment is devoted to analysing the similarity between motions derived from MR and US using the proposed framework. The final experiment aims to analyse the main modes of variation of the displacements vectors extracted using the proposed dimensionality reduction algorithms.

Dimensionality reduction algorithms

In the following experiments, similar to the results presented on the UK Biobank data set, the intrinsic dimensionality of the real data was computed using PCA (retaining 95% of the variance, $d = 25$), and then used for the PCA, CCA and PLS experiments.

In order to validate the three proposed dimensionality reduction algorithms (PCA, CCA and PLS) the mean embedding distance $E_d(MR - US)$, the mean reconstruction errors $E_D(MR - MR)$ and $E_D(US - US)$, and the mean prediction error $E_D(MR - US)$ were computed using a leave-one-out cross validation (see Figure 5.13). The results show that CCA and PLS have much lower errors than PCA for all measures apart from $E_D(MR - MR)$. This is to be expected since PCA is trained on MR data only. However, an advantage of CCA and PLS is that they offer separate mappings for the two modalities, allowing the prediction of one given the other. Consequently, CCA and PLS have lower $E_D(US - US)$, $E_d(MR - US)$ and $E_D(MR - US)$ than PCA.

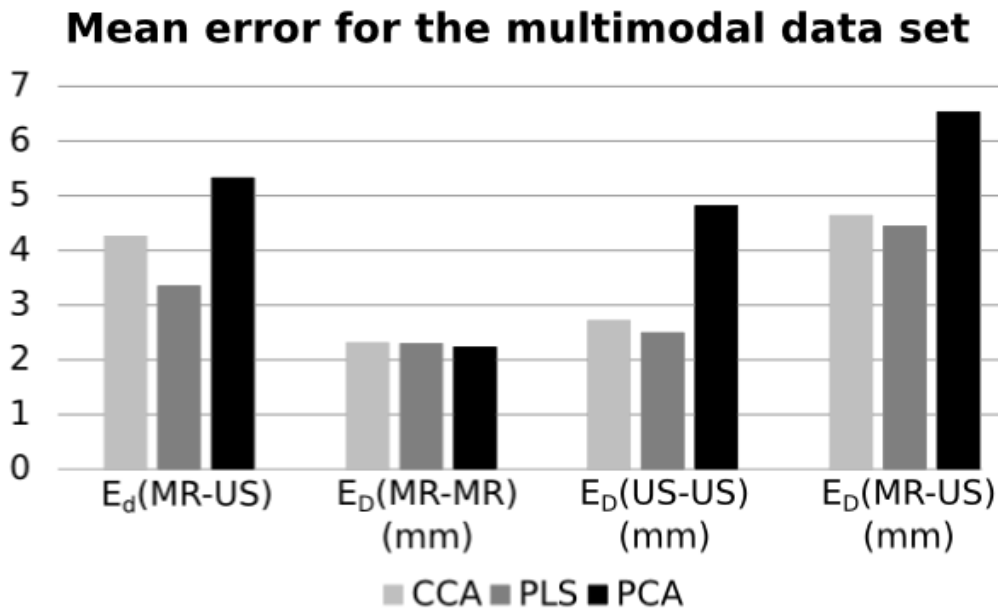


Figure 5.13: Mean errors for the multimodal data set.

For the multimodal data set, the Pearson's correlation coefficient between the MR and US displacement data is 0.71, which corresponds to a σ_M in the UK Biobank experiments of just under 25 mm (see Figure 5.12b). Figures 5.11, 5.12a and 5.13 show that for this σ_M the reconstruction error and prediction error on the UK Biobank data set and those found using the multimodal data set are similar. Finally, by comparing results obtained on the multimodal data set with the closest results of the UK Biobank data set (number of vertices = 650 and number of subjects = 50), it can be observed that the patterns are similar, i.e. for the MR data the three algorithms have similar errors, while for the US data PLS has the best results and PCA the worst.

LVV, LVM and LVEF

For a further analysis of the results obtained, the input medial mesh and the reconstructed medial mesh over the cardiac cycle were compared. To quantify the similarity between both medial meshes, LV volumes before and after applying the dimensionality reduction algorithms were computed. Ideally, the algorithms should preserve the main physiological characteristics. Figure 5.14 shows an example of LV volume comparison for a sample subject from the multimodal data set for the different algorithms proposed in this work.

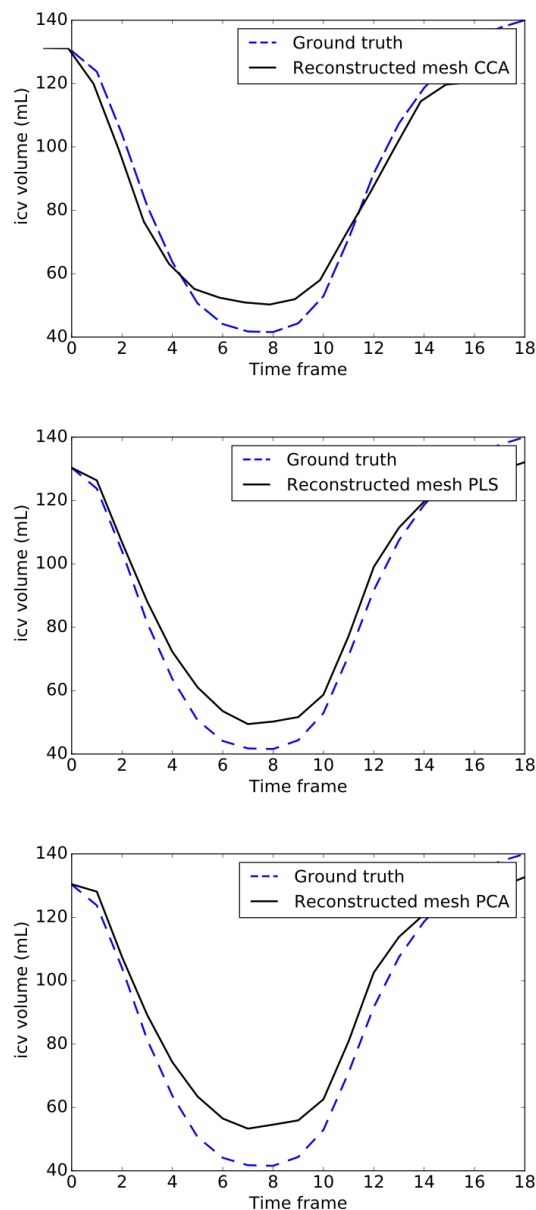


Figure 5.14: US LV volume before (blue-dashed) and after (black) applying dimensionality reduction algorithms.

Furthermore, the following clinical metrics were computed from the LV volume for each subject: LVM as the mean of the ED and ES LV volume multiplied by 1.05 g/mL (Lang et al., 2015), and the LVEF, which measures the fraction of outbound blood pumped from the heart with each heartbeat.

Table 5.1 summarises the LVESV, LVM and LVEF errors with respect to the ground truth over all multimodal data set subjects for the reconstructed MR and US, and the predicted MR from US using the different dimensionality reduction algorithms investigated. A Student's t-test (99% confidence) between the ground truth values and those reconstructed using each method was used to test the accuracy of the different methods. A significant difference in mean is shown with an asterisk in the table.

	LVESV (mL)	LVEF %	LVM (g)
<i>MR only</i>			
GT	72.54 (14.10)	56.98 (7.22)	101.68 (14.71)
PCA	6.13 (14.7) [*]	-3.48 (5.22) [*]	-6.77 (17.85) [*]
CCA	7.32 (16.21) [*]	-3.18 (6.40) [*]	-5.09 (14.73) [*]
PLS	7.11 (16.79) [*]	-3.15 (6.10) [*]	-2.78 (14.38)
<i>US only</i>			
GT	61.09 (16.81)	52.07 (8.94)	92.96 (19.17)
PCA	7.44 (18.04) [*]	-8.56 (7.67) [*]	-7.83 (15.95) [*]
CCA	2.57 (15.57) [*]	-3.52 (5.97) [*]	-2.41 (13.87) [*]
PLS	0.45 (14.08)	-1.36 (4.88)	-2.51 (14.16) [*]
<i>US-MR predicted</i>			
GT	72.54 (14.10)	56.98 (7.22)	101.68 (14.71)
PCA	-18.02 (18.22) [*]	-13.52 (8.22) [*]	-26.94 (22.56) [*]
CCA	-3.18 (6.68)	-5.23 (4.86) [*]	-28.01 (20.65) [*]
PLS	-4.50 (2.19)	-3.12 (3.71)	-20.77 (19.95) [*]

Table 5.1: Mean and standard deviation of the errors with respect to the ground truth (GT) for LVESV, LVM and LVEF for the different dimensionality reduction algorithms. The first row corresponds to the MR reconstructed data, the second row to the US reconstructed data, and the last one corresponds to the predicted MR from US data. An asterisk indicates a significant difference in mean between the data and the GT, which is shown as the first entry in blue in each row for reference. In brown the row with the lowest error.

From Figure 5.14 and Table 5.1 it can be observed that PLS generally reconstructs the clinical parameters more accurately compared to CCA and PCA. More specifically, in the US-MR predicted row one can notice that there was no significant difference in mean between the PLS reconstructed LVESV and LVEF and the ground truth. However, from Table 5.1 it seems that all algorithms underestimated the contraction of the LV, leading to a lower volume at ES. There are several possible reasons for this underestimation. First, the proposed framework only uses linear dimensionality reduction techniques, and it is possible that the underlying manifold that represents the variation of cardiac cycle motions is nonlinear, and therefore it is not captured using only linear methods. Second, the choice of the number of retained dimensions affects the accuracy of the algorithms, and could lead to a slight underestimation of the displacement magnitude and hence LVEF. Finally, the use of a medial mesh rather than the epicardial boundary to compute volumetric measures may also cause a slight underestimation.

From a clinical point of view, healthy individuals typically have LVEF between 50% and 65% (Kumar et al., 2014) depending on the modality, and values outside of this range are considered abnormal. Results show that for MR data all the algorithms reconstructed a mean LVEF inside the normal range. However, for US, the difference between the ground truth and the reconstructed LVEF for PCA is high enough to consider a subject pathological, which may have an impact on diagnosis and treatment.

Overall, based on the UK Biobank data set and the multimodal data set results it can be noticed that PLS and CCA have similar errors and both have lower errors than PCA. However, PLS seems to have the most faithful reconstructed LV volume, when compared to CCA. Additionally, experiments showed that sometimes CCA was unstable when the number of features was higher than the number of subjects. A similar problem has also been reported in the literature where X and Z are nearly collinear (Wegelin et al., 2000, Wold, 1985).

Temporal normalisation

This section aims to evaluate the temporal normalisation method proposed in Section 5.2.4 against only using a global rescaling with respect to the length of the cardiac cycle. To this end, the volume of the LV cavity for each time point was computed. In theory, the volume of the cavity is greater in the ED frame, and is lower in the ES frame, where the heart is more contracted. In Figures 5.15a, 5.15b and 5.15c the original and temporally normalised volume curves of the LV medial mesh for each subject at the different time points are presented. To enable easier visualisation of the alignment of the cardiac timings all volumes were rescaled to between 0 and 1. Results show that after the temporal normalisation the volume changes looked physiologically plausible. Furthermore, it can be noticed that the three considered cardiac timings - beginning of isovolumetric contraction phase, beginning of isovolumetric relaxation phase and beginning of atrial systole phase - are correctly aligned for the two modalities MR and US after the proposed normalisation technique but not after the global rescaling approach.

Figure 5.16 compares the results of the different dimensionality reduction algorithms using the proposed temporal normalisation and only rescaling by cardiac cycle length. It can be observed that the proposed temporal normalisation reduces the errors for all three algorithms. It is likely that the higher errors for the global rescaling are because frames may not correspond to the same position in the cardiac cycle and therefore displacements from different cardiac timings will be compared.

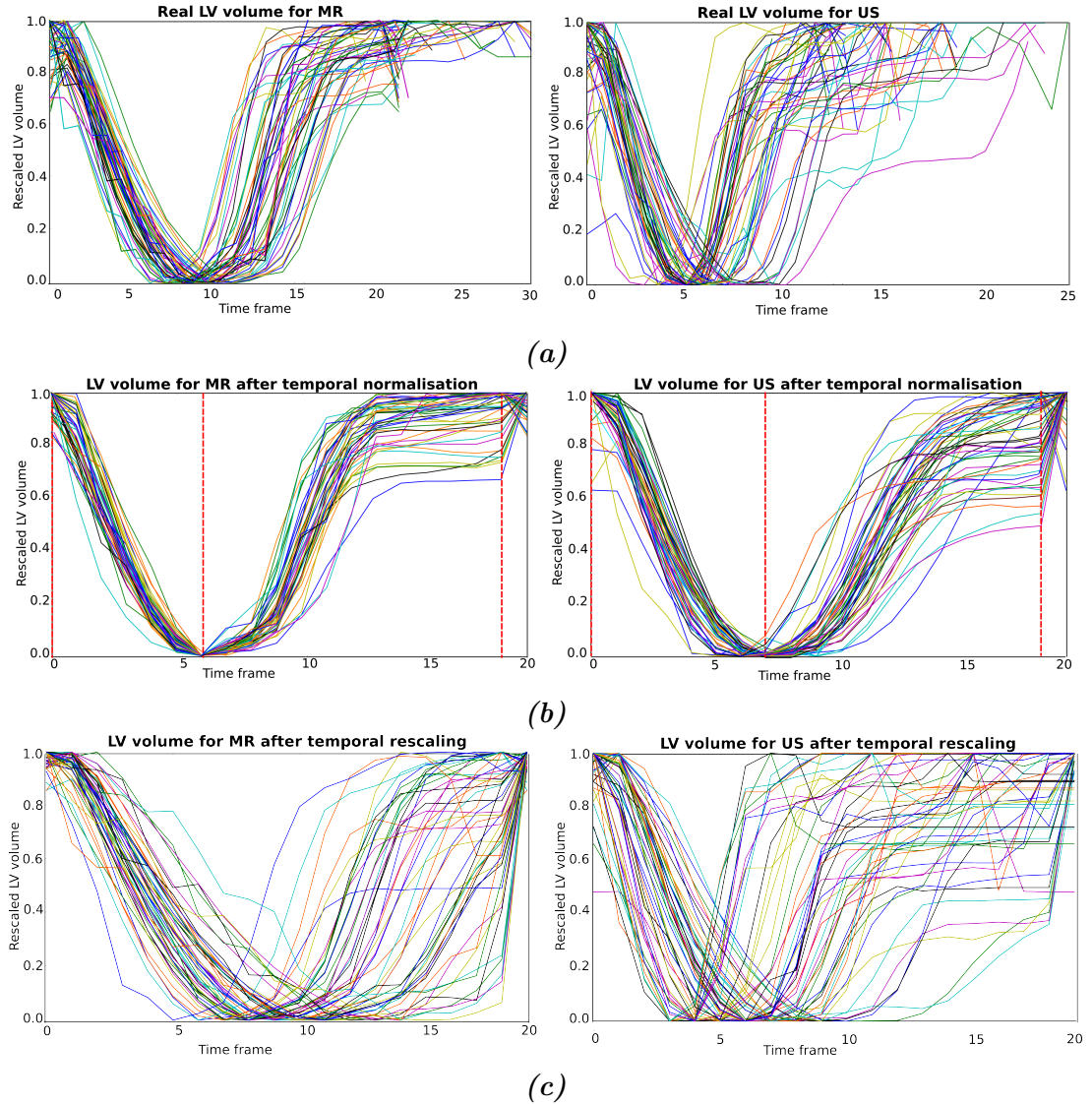


Figure 5.15: Rescaled LV volume for each subject over the cardiac cycle (a) before applying the proposed temporal normalisation, (b) after applying temporal normalisation, (c) after rescaling with respect to the length of the cardiac cycle. The red dotted lines correspond to the three cardiac timings defined in Section 5.2.4.

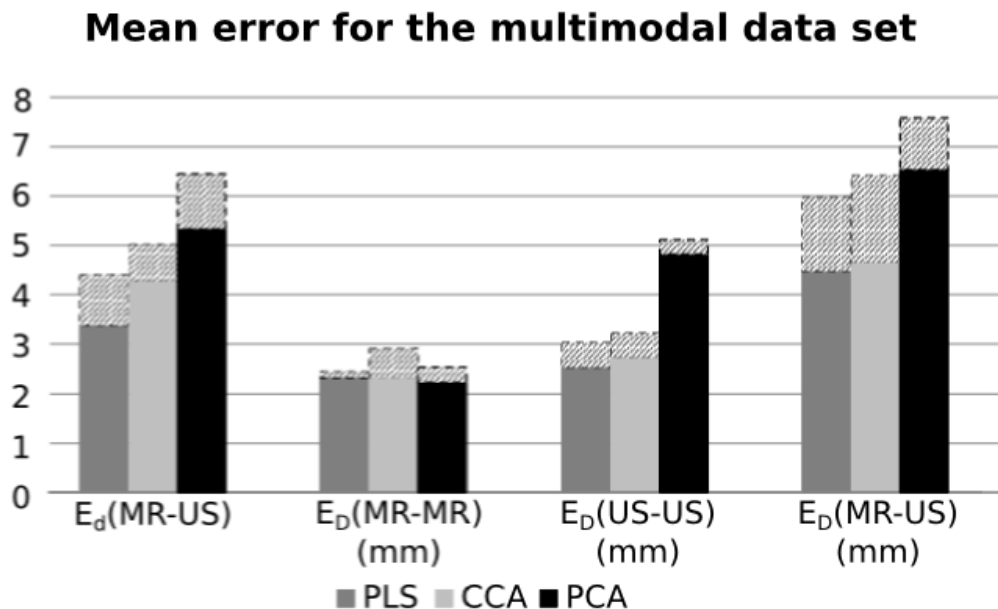


Figure 5.16: Mean errors for the multimodal data set using the proposed temporal normalisation, and (stacked) using global rescaling by cardiac cycle length.

Similarity between MR and US data

Based on the results presented so far, the PLS algorithm seems to have the better performance in terms of errors and stability. Therefore, the remaining experiments only use PLS. The next experiment aims to find the areas where MR and US derived motion are more similar. To this end, the mean point in the low dimensional space (i.e. the average motion) was computed and then back projected to the high-dimensional atlas space using the transposed MR and US projection matrices. The Euclidean distances between the MR and US displacements on a vertex-by-vertex basis were computed. To help us to visualise the areas where PLS finds greater similarities between MR and US derived motions, the average such distance for each AHA segment was then computed.

Figure 5.17 shows the Euclidean distances between the mean MR and US motions in each AHA segment for each time point of the cardiac cycle. Results show that the AHA regions with higher distances are segments 1,2,7,8, which correspond to the base and mid anterior and anteroseptal wall. In diagnostic US, it is common that the anterior wall of the myocardium is masked by noise and by limited acoustic windows through the subject's rib cage and lungs ([Armstrong and Ryan, 2012](#)). Figure 5.18 shows an example where the anterior wall is missing. This area corresponds to segments 1,2,7,8.

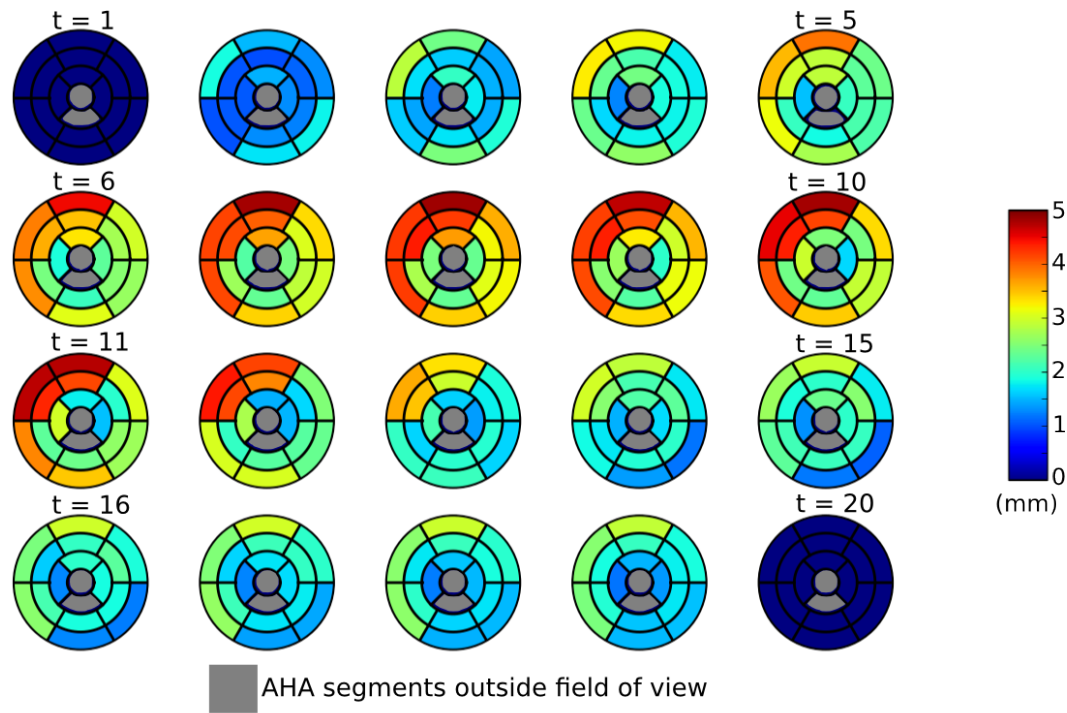


Figure 5.17: Euclidean distance in mm between mean MR and US motion for PLS.

In addition, Figure 5.17 shows that the higher distances occur in frames 6-11, which correspond to the ejection phases (see Figure 2.2), where the myocardium has higher contractility.

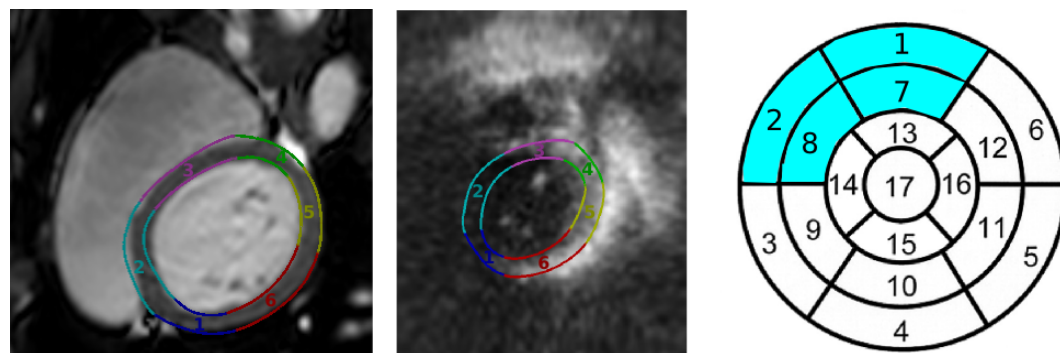


Figure 5.18: AHA segments on the base for the ED frame on MR and US, and the 17 standardised AHA segments.

Next, a comparison of the mean MR and US reconstructed medial meshes with each subject's medial mesh (in atlas space) was carried out to identify regions with higher inter-subject variability and to assess whether MR or US-derived motion has more variability in the database. Figures 5.19 and 5.20 show the mean Euclidean distances between the mean MR and US reconstructed medial meshes and the medial mesh for each subject. Results show that MR-derived motion has slightly higher inter-subject variability than US-derived motion. For both MR and US motion this variability is focused on AHA segments 1,4-6 which corresponds to the free wall of the base of the LV. From a clinical point of view it is known that the basal septum has less myocardial muscle, and therefore exhibits less wall motion than the free wall (Kaul et al., 1983).

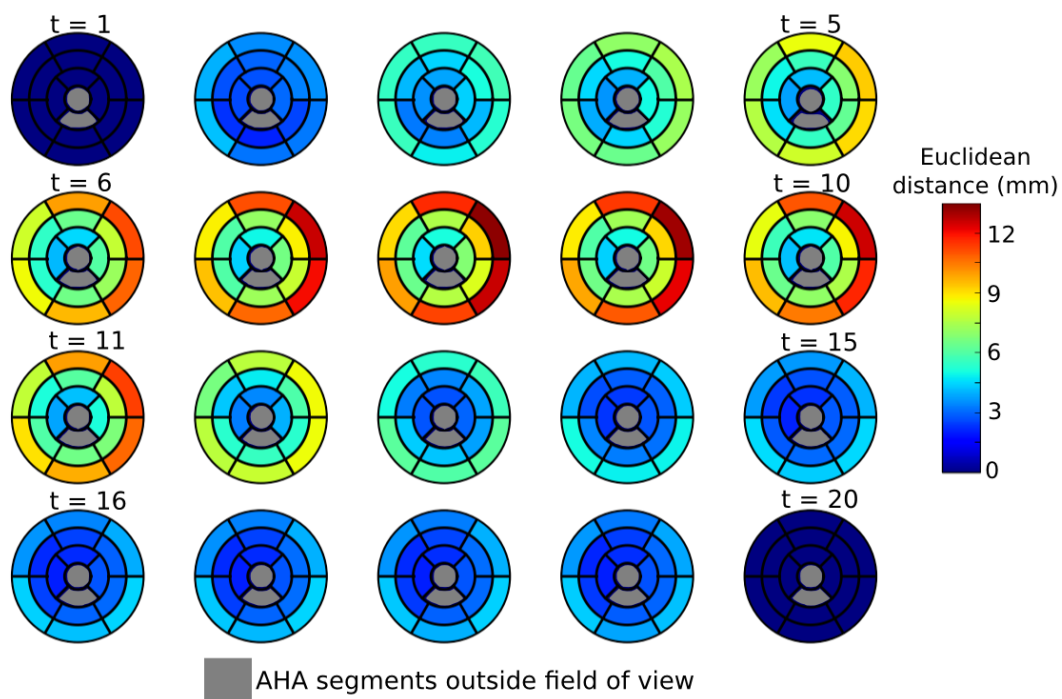


Figure 5.19: Mean Euclidean distance in mm between mean MR motion and the motion of each subject in the multimodal data set.

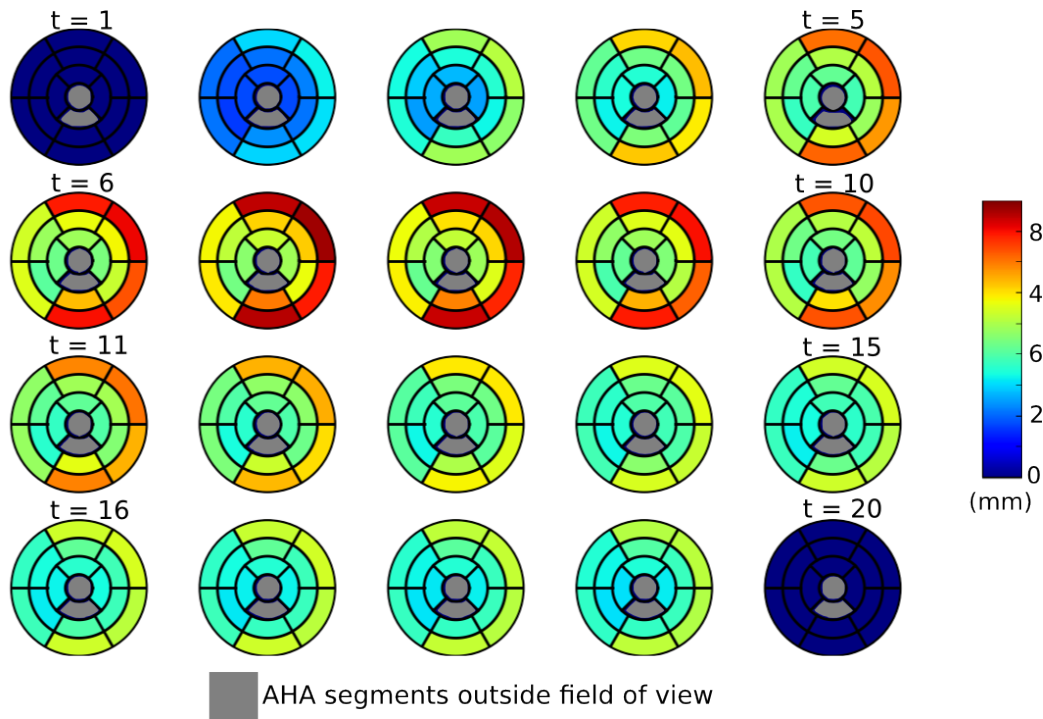


Figure 5.20: Mean Euclidean distance in mm between mean US motion and the motion of each subject in the multimodal data set.

Statistical model of the motion variability across subjects.

The last experiment focuses on analysing the main modes of variation of the displacement vectors found using the PLS algorithm. Figure 5.21 shows the first two modes of variation at ES. The view shows mainly the free wall of the LV, which corresponds to the region with higher variation identified in the previous experiment (see Section 5.3.3). The colour bars represent the Euclidean distance between the mean reconstructed medial mesh and the medial meshes reconstructed at low dimensional coordinates of $\pm \sigma$ along the appropriate axis (σ corresponds to the standard deviation of the embedding space along each axis). The colour bar for the mean motion mesh represents the 17 AHA segments.

In addition, Table 5.2 shows the mean Euclidean distances for the longitudinal, radial and circumferential axes. One can see that there are some differences in the motion captured by the two modalities. However, in both cases, the first mode captures mostly the torsion of the LV, and the second mode captures the longitudinal shortening of the LV. More specifically, it is possible to notice that in the first mode the higher variability is at the base which agrees with the results found in the previous section.

Figure 5.21: First 2 modes of variation for PLS with colour bars representing the Euclidean distance between the mean MR reconstructed medial mesh and the σ reconstructed medial mesh. The colour bar of the mean motion mesh represents the 17 AHA segments.

		MR	US
Mode 1	Radial	2.01	0.18
	Longitudinal	1.98	0.21
	Circumferential	2.26	2.39
Mode 2	Radial	1.19	0.27
	Longitudinal	1.21	2.49
	Circumferential	1.09	0.29

Table 5.2: Mean Euclidean distance in mm for the longitudinal, radial and circumferential axes for the first 2 modes of variation for PLS. Bold numbers highlight the results with the highest mean Euclidean distance for each mode/modality.

5.4 Discussion and conclusion

In this Chapter, a new framework for the formation of a multimodal statistical atlas of cardiac motion was presented, from its construction steps to the impact of different dimensionality reduction algorithms. The three algorithms proposed to build the multimodal cardiac motion atlas were: (1) PCA; (2) CCA; and (3) PLS. This is the first time that such a framework has been described, and the validation and analysis presented offer valuable insights into the nature and utility of multimodal MR and US data for analysing cardiac function. Each modality offers the possibility to observe the heart’s motion from a distinct perspective, and sometimes they offer complementary information. In clinical practice, MR is increasingly accepted as the gold standard for characterising cardiac function and anatomy, as it enables the acquisition of high contrast and high resolution sequences. However, MR is contraindicated for patients with cardiac pacemakers or metallic cardiovascular electronic devices, and furthermore it is a high cost technology. In contrast, US is commonly used in the clinic for assessing cardiac function due to its low cost, portability and good spatial resolution. However, it suffers from image artefacts and limited field of view. A multimodal atlas will benefit from the synergies between the motion features derived from the two modalities, and furthermore it could be used in clinics to detect cardiovascular disease using only US data.

Results show that a multimodal atlas based on PLS and using US-derived motion alone can be used to analyse a new subject’s motion whilst exploiting the multimodal (MR+US) data of a population sample. Figure 5.13 shows that the accuracy of this process (i.e. $E_D(MR - US)$) is approximately 2.5 mm, which is similar to the magnitude of motion tracking errors (Tobon-Gomez et al., 2013). Note that $E_D(MR - US)$ effectively quantifies how accurate the US processing pipeline is for analysing motion compared to the “gold standard” of MR.

A possible limitation of the proposed framework to build the multimodal atlas is the temporal normalisation step, which relies on the correct identification of cardiac timings. For instance, the beginning of the atrial systole phase may vary between healthy and diseased subjects, and might be more difficult to identify in patient data. Ideally, instead of using the proposed cardiac timing, it would be possible to use cardiac timings derived from valve events as they would be more accurate. However, the spatiotemporal quality of both TAG and cine MR data (as obtained in the clinical setting) is currently not sufficient to allow for accurate detection of cardiac valve timings. Furthermore, 3D US imaging suffers from the same problem.

Another limitation of the current approach is that all of the dimensionality reduction algorithms are linear, and therefore they cannot capture the nonlinear structure of high-dimensional data. However, the advantages of linear models are that they are simpler, and the results are more easily interpreted. In addition, CCA suffers from numerical problems in its eigen-decompositions, as the CCA optimisation procedure involves computation of two inverses. Thus, it is only stable in problems in which the number of features does not exceed the number of observations. The next Chapter will focus on applying the multimodal atlas to clinical problems to learn the representation of pathological motion patterns from certain cardiac diseases for the task of classification. To this end, the next Chapter will extend the proposed algorithms to nonlinear versions to take into account the non-linearities of the motion of the heart.

The UK Biobank data set was used to compare the performances of the different algorithms in a controlled manner, i.e. varying number of samples/features and similarity between modalities. The results provided an approximate lower bound of the errors of the algorithms as well as how many subjects would be necessary to achieve a good level of accuracy. However, a limitation of the proposed method to construct the synthetic US displacements is the use of a global Gaussian noise model to model the variability between modalities. Greater realism could be achieved by using a locally varying model, but at the expense of the clarity and conciseness of the experimental results.

The current clinical data set is composed of data from two different centres, which might introduce some bias into the model. In order to minimise this bias data could have been acquired using identical machines (both MR and US). More specifically, in the multimodal data set used in this thesis there is some variation in spatial and temporal resolution, which presumably is due to the lack of standardisation in clinical imaging protocols. This variation was noticeable both between images acquired at the same centre as well between images acquired at different centres. No systematic differences between centres in terms of spatial and temporal resolution were found.

In the current framework (see Figure 5.1) the MR and US geometry/motion estimation pipelines are performed independently, and the results are combined using a multi-view subspace learning algorithm. This strategy was used to preserve the potentially complementary motion information provided by the two modalities. However, alternative pipelines in which the processing of the two modalities is more closely coupled are possible, e.g. joint segmentation and/or joint motion tracking approaches (Liu et al., 2017).

In conclusion, this Chapter has presented a new framework to build a multimodal statistical cardiac motion atlas from MR and US, simulating a scenario in which a high quality atlas was formed using MR and US data, and a new subject is related to this atlas using only low cost US data, which is widely available in clinics and can be acquired for almost every subject. Such a pipeline potentially widens the applicability of statistical cardiac motion atlases in clinics. The next Chapter builds upon this work by proposing a diagnostic pipeline based on US data but at the same time taking advantage of the multimodal cardiac motion atlas.

6 | Multi-view classification

6.1 Introduction

Better understanding the motion of the heart through the cardiac cycle can give useful insight for a range of different pathologies. In particular, quantifying regional cardiac motion can help clinicians to better determine cardiac function by identifying regions of thickened, ischemic or infarcted tissue.

Chapter 5 described a complete framework for the formation of a multimodal atlas of cardiac motion, from its construction steps to the impact of different dimensionality reduction algorithms. This opened up the possibility of exploiting the learnt inter-modality relationship to construct a diagnostic pipeline based on US data that is at the same time informed by a training database of multimodal (MR and US) data. The aim of this Chapter is to first propose such a pipeline in a global based approach and then extend it to a regional level using the AHA regions. As an exemplar application this Chapter illustrates the use of the framework for classifying subjects as DCM/normal.

The novelties presented in this Chapter are: (1) use of multi-view dimensionality reduction and classification in a single step, enabling the embedding to be optimised for the classification task; (2) a novel regional approach for multi-view classification, which enables the regional dependence of the multi-view relationship to be exploited in the classification task. Preliminary work (using only a linear global multi-view classifier) was presented in Puyol-Antón et al. (2017a). To the authors' knowledge, this is the first time that MvML has been used for disease diagnosis using multimodal data.

The remainder of this Chapter is organised as follows. Section 6.2 describes details of the different multi-view learning algorithms used to identify patients suffering from DCM. Results are presented in section 6.3, while section 6.4 discusses the findings of this paper in the context of the literature.

6.2 Methods

Figure 6.1 summarises the proposed pipeline for detecting patients with DCM using only US data. The top box of the figure corresponds to the atlas formation pipeline described in Chapter 5, the middle box corresponds to the proposed global and regional multi-view classification approaches, and the bottom box corresponds to the application of the multimodal atlas for multi-view classification using US and/or MR data. Section numbers in the figure indicate which of the following sections provides further detail on the methods.

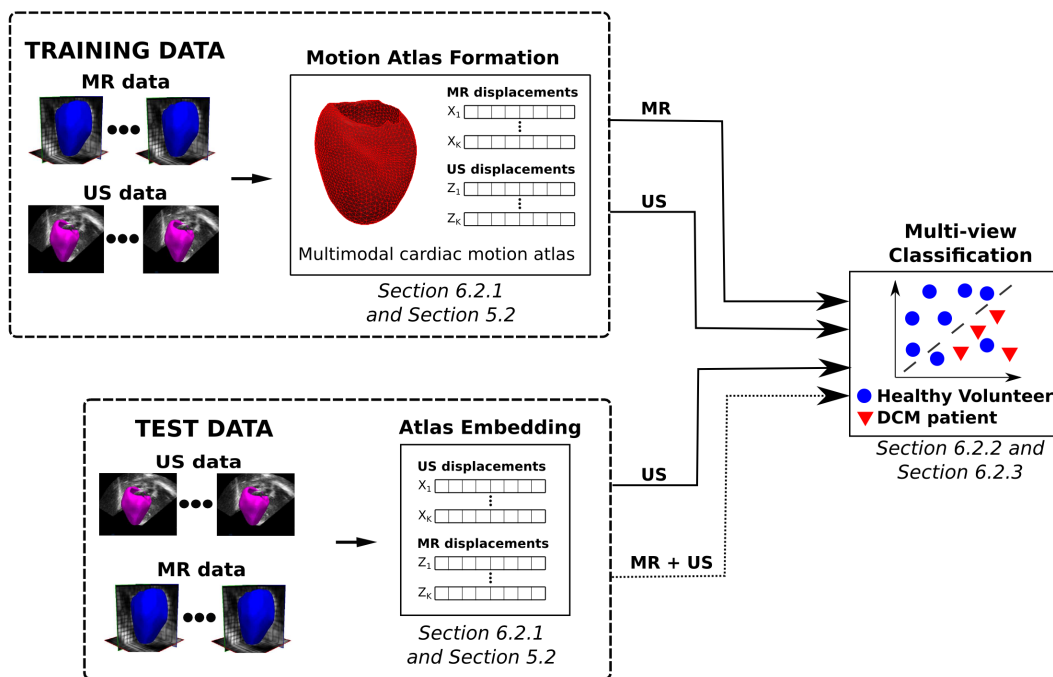


Figure 6.1: Overview of the proposed framework for forming and applying a motion atlas-based multi-view learning approach.

6.2.1 Motion atlas formation

As described in the previous chapters, cardiac motion atlases provide a space of reference in which population comparisons of motion (i.e. displacements and velocities) and deformation (i.e. strains and strain rates) can be carried out. The main steps involved in the formation of a cardiac motion atlas are: definition of the geometry, spatial and temporal normalisation, and reorientation of subjects' cardiac geometry and motion both spatially and over time. These steps transform the subject-specific motion/deformation data so that they can be directly compared, removing biases due to heart orientation, size, shape and cardiac phase. A complete description of the different steps used to build the multimodal cardiac motion atlas can be found in Chapter 5.

6.2.2 Multi-view classification: A global approach

This section describes the novel methodological contributions of this chapter, specifically the use of MvML techniques to exploit the information in the multimodal atlas for a supervised classification task.

As described in section 5.2.10 the MR and US displacements in the atlas were concatenated to form the matrices X and Z . This Chapter uses the same matrices as input for the multi-view classification algorithms.

The proposed application of the multimodal atlas is to classify subjects as DCM/normal using only US data, but taking advantage of the multimodal cardiac motion atlas. To this end, linear and non-linear multi-view classifiers are proposed:

Linear method: For the linear case, the multi-view linear discriminant analysis (MLDA) (Sun et al., 2016) algorithm was used. MLDA seeks to find a common space while simultaneously preserving the correlation between modalities and the discriminating information in each modality. The optimisation problem of MLDA is given by:

$$\begin{aligned} \max_{\mathbf{w}_x, \mathbf{w}_z} \quad & \mathbf{w}_x^T S_{bx} \mathbf{w}_x + \mathbf{w}_z^T S_{bz} \mathbf{w}_z + 2\gamma \mathbf{w}_x^T C_{xz} \mathbf{w}_z \\ \text{subject to} \quad & \mathbf{w}_x^T C_{xx} \mathbf{w}_x + \sigma \mathbf{w}_z^T C_{zz} \mathbf{w}_z = 1 \end{aligned} \quad (6.1)$$

where \mathbf{w}_x is the projection matrix for the first view (i.e. MR) and \mathbf{w}_z is the projection matrix for the second view (i.e. US); C_{xx} and C_{zz} are respectively the covariance matrices of the first view X (i.e. MR) and the second view Z (i.e. US); C_{xz} is the cross-covariance matrix of the two views (i.e. MR/US); and $\sigma = \text{tr}(C_{xx})/\text{tr}(C_{zz})$. S_{bx} and S_{bz} denote the between-class matrices for each view (Sun et al., 2016) that can be formulated as $S_{bx} = \frac{1}{LL} \sum_{i=1}^{LL} (\mu_i - \mu)(\mu_i - \mu)^T$, μ is the mean of X and μ_i is the mean of X in the class i among LL classes. The left-most two terms of Eq. 6.1 attempt to minimise the within-class distance, while the rightmost term attempts to find a common space between the two views. γ is a regularisation parameter that balances the relative significance between these two objectives. Note that Eq. 6.1 has a closed form solution.

In Eq. 6.1, the correlation between the different views and the discrimination of each view can be maximised simultaneously. Therefore, using the Lagrangian multiplier technique, the equation can be solved by a generalised multivariate eigenvalue problem as follows (Sun et al., 2016):

$$\begin{bmatrix} S_{bx} & \gamma C_{xz} \\ \gamma C_{xz}^T & S_{bz} \end{bmatrix} \begin{bmatrix} \mathbf{w}_x \\ \mathbf{w}_z \end{bmatrix} = \lambda \begin{bmatrix} C_{xx} & 0 \\ 0 & \sigma C_{zz} \end{bmatrix} \begin{bmatrix} \lambda_x \mathbf{w}_x \\ \lambda_z \mathbf{w}_z \end{bmatrix} \quad (6.2)$$

After solving the generalised eigenvalue problem of Eq. 6.2 and retaining only the first d components, a subject k can be embedded into the low dimensional space according to the following strategies (Sun et al., 2016):

- Using only MR data: $\boldsymbol{\tau}_k = \mathbf{w}_x^T \hat{\mathbf{x}}_k$
- Using only US data: $\boldsymbol{\tau}_k = \mathbf{w}_z^T \hat{\mathbf{z}}_k$
- Using both MR and US data: $\boldsymbol{\tau}_k = \mathbf{w}_x^T \hat{\mathbf{x}}_k + \mathbf{w}_z^T \hat{\mathbf{z}}_k$

In the low dimensional space, a n-nearest neighbours algorithm is used to classify between healthy and DCM patients, and produce the predicted label, \hat{y}_k .

Non-linear method: For the non-linear case, the semi-supervised multi-view Laplacian support vector machines (MvLapSVM) algorithm introduced in Sun (2011) was modified to only use labelled data. MvLapSVM integrates manifold regularisation, which imposes local constraints on samples, and multi-view learning. MvLapSVM is an extension of the Laplacian SVM algorithm for multi-view data. The MvLapSVM primal problem can be formulated as:

$$\begin{aligned}
 & \min_{\alpha_x, \alpha_z, \xi_x, \xi_z} \quad \frac{1}{2K} \sum_{i=1}^K (\xi_x^i + \xi_z^i) + \gamma_1 (\alpha_x^T G_x \alpha_x + \alpha_z^T G_z \alpha_z) + \\
 & \quad \gamma_2 (\alpha_x^T G_x L_x G_x \alpha_x + \alpha_z^T G_z L_z G_z \alpha_z) + \\
 & \quad \gamma_3 (K_x \alpha_x - K_z \alpha_z)^T (K_x \alpha_x - K_z \alpha_z) \\
 & \text{subject to} \quad y_i \left(\sum_{j=1}^K \alpha_x^j k_x(x_j; x_i) \right) \geq 1 - \xi_x \\
 & \quad y_i \left(\sum_{j=1}^K \alpha_z^j k_z(z_j; z_i) \right) \geq 1 - \xi_z \\
 & \quad \xi_x^i, \xi_z^i \geq 0, \quad i = 1, \dots, K
 \end{aligned} \tag{6.3}$$

where α_x, α_z are respectively the weight vectors for the first view X (i.e. MR) and the second view Z (i.e. US); ξ_x and ξ_z are the slack variables for the first view and the second view, used to make the objective function differentiable; G_x and G_z are the Gram matrices for the first and second views; L_x and L_z are the graph Laplacian matrices for the first and the second views; K_x and K_z are the kernel matrices for the first and second views; $\gamma_1, \gamma_2, \gamma_3 > 0$ are the norm regularisation terms; $y_i \in \{-1, 1\}^K$ are the classification labels and $k(\cdot, \cdot)$ is the kernel function.

The leftmost three terms of Eq. 6.3 can be rewritten as the sum of two Laplacian SVM optimisers (Melacci and Belkin, 2011), which assumes that the marginal probability distribution underlying the data is supported on a low-dimensional manifold, and the Laplacian matrix learning exploits the connections among features, which is able to generalise over intra-class variations and provide inter-class discrimination. The rightmost term corresponding to γ_3 models the multi-view learning, using the assumption that a good learner can learn from each view, and consequently, these good learners in different views should be consistent to a large extent with respect to their predictions on the same examples.

After optimisation of Equation 6.3, a subject k can classified according to the following strategies (Sun, 2011):

- Using only MR data: $\hat{y}_k = \boldsymbol{\alpha}_x^T \mathbf{g}_{x,k}$
- Using only US data: $\hat{y}_k = \boldsymbol{\alpha}_z^T \mathbf{g}_{z,k}$
- Using both MR and US data: $\hat{y}_k = \frac{1}{2} (\boldsymbol{\alpha}_x^T \mathbf{g}_{x,k} + \boldsymbol{\alpha}_z^T \mathbf{g}_{z,k})$

where \hat{y}_k is the predicted label, and $\mathbf{g}_{x,k}$ and $\mathbf{g}_{z,k}$ are respectively the Gram matrices from views X and Z for subject k

6.2.3 Multi-view classification: A regional approach

As described in the previous section, global and regional LV functions are well-known indicators of cardiac disease. However, regional function can capture changes in function due to diseases specific to each region. Therefore, this section aims to extend the global multi-view approach to learn region-specific patterns to characterise disease and use them for the classification task. Figure 6.2 summarises this approach. As shown, the AHA segmentations generated by the fitted mesh (see Section 5.2.1 for more details) are used to divide the displacements by AHA region. Then, for each AHA segment s the two multi-view classifiers (MLDA and MvLapSVM) are applied. Finally, a weighted majority voting is used to combine the regional results of each classifier. To compute the optimal weights for each AHA segment, a randomised search on hyper parameters algorithm (Bergstra and Bengio, 2012) is used. Details of the calculation of the weights are provided in Section 6.3.3.

Formally, the MR displacements in atlas space $\mathbf{x}_{m,n,k}$ were concatenated by AHA segment into row vectors such that for subject k , $\dot{\mathbf{x}}_k^{\text{AHA}_s} \in \mathbb{R}^{1 \times D_s}$, where $D_s = (3 \times N \times M_s)$ with N the number of cardiac phases and M_s the number of points in the atlas medial surface mesh in AHA segment s . The row vectors $\dot{\mathbf{x}}_k^{\text{AHA}_s}$ for each subject were stacked to produce matrices $X_{\text{AHA}_s} = [(\dot{\mathbf{x}}_1^{\text{AHA}_s})^T, \dots, (\dot{\mathbf{x}}_K^{\text{AHA}_s})^T] \in \mathbb{R}^{K \times D_s}$, where K is the number of subjects. Likewise, the US displacements $\mathbf{z}_{m,n,k}$ were concatenated to form matrices $Z_{\text{AHA}_s} = [(\dot{\mathbf{z}}_1^{\text{AHA}_s})^T, \dots, (\dot{\mathbf{z}}_K^{\text{AHA}_s})^T] \in \mathbb{R}^{K \times D_s}$.

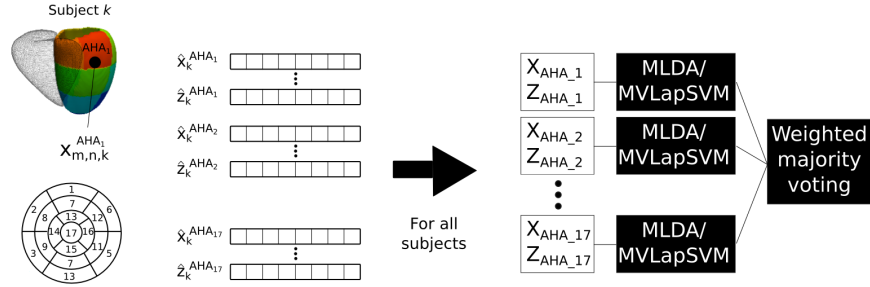


Figure 6.2: Overview of the proposed framework for the regional approach for multi-view classification.

Next, for each AHA segment s we applied the two multi-view classifiers independently: MLDA and MvLapSVM. As a result, for each AHA region the multi-view classifiers predict a label \hat{y}_k^s . A weighted majority voting strategy was used to combine the regional results of each classifier. Details of the calculation of the weights are provided in Section 6.3.3.

6.3 Experiments and results

Two sets of experiments were performed. The first set of experiments aimed to validate the global multi-view learning approach proposed in Section 6.2.2 for identifying patients with DCM, while the second set of experiments aimed at validating the proposed regional approach detailed in Section 6.2.3 on the same task.

Identification of DCM patients was selected as the application as DCM is the third most common cause of HF (of America et al., 2010), and a better understanding of the disease and the mechanisms underlying its development and progression would be beneficial for early identification. Furthermore, DCM patients normally have an impaired systolic function, and regional wall motion abnormality features can be beneficial to improve disease classification and treatment stratification. However, the same pipeline could be applied to other groups of patients. This is an exemplar application to demonstrate the proposed novel techniques.

For all experiments in this Chapter the full cohort of the multimodal data set (see Chapter 4.1 for more details) was used. All experiments were carried out using the Python programming language, using standard Python libraries (Numpy, SciPy, etc.), VTK libraries, and the scikit-learn Python toolkit (Pedregosa et al., 2011). Section 6.3.1 details the error measures used for the validation of the proposed algorithms, Section 6.3.2 describes the first set of experiments and presents the results, and Section 6.3.3 presents the validation of the regional approach.

6.3.1 Cross validation and evaluation metrics

An 8-fold repeated stratified cross-validation (RSCV) with 100 repetitions was used to compare the performances of the proposed multi-view approaches. In each fold, 44 healthy volunteers and 17 patients were used as training and 2 patients and 6 healthy volunteers as test. As a pre-processing step, the intrinsic dimensionality of both matrices X and Z was estimated using PCA. The number of PCA modes, L , that capture 95% of the data variance was computed. Then, the first L modes were used when evaluating the PLS and PCA algorithms (see Sections 6.3.2 and 6.3.3). In each fold, to evaluate the performance of the algorithms the confusion matrix was computed, which contains the true positives (TP), true negatives (TN), false positives (FP) and false negatives (FN) ratio. As the classes are unbalanced, the balanced accuracy (i.e. the average accuracy obtained on each class individually – $BACC = \frac{1}{2} (\frac{TP}{P} + \frac{TN}{N})$), as well as the sensitivity (the proportion of patients with DCM correctly classified – $SEN = \frac{TP}{TP+FN}$) and the specificity (the proportion of healthy subjects correctly classified – $SPE = \frac{TN}{TN+FP}$) were computed. Finally, the average accuracies, sensitivities and specificities as well as their standard deviations over all folds were computed.

6.3.2 Evaluation of global multi-view learning methods

The proposed MLDA and MvLSVM algorithms simultaneously reduce the dimensionality and perform the classification. Therefore, we refer to these two algorithms as ‘one-step methods’. The results in the previous Chapter showed that PLS ([Wold et al., 1984](#)) was the optimal multi-view dimensionality reduction algorithm to form a common space between MR and US. Therefore, an obvious extension would be to apply PLS to reduce the dimensionality of the multimodal data, and then use a classifier: LDA for the linear case and SVM with radial basis function (RBF) kernel for the non-linear case. Therefore, these two comparative approaches will be classed as ‘two-step methods’, as the dimensionality reduction and the classification are done independently.

This first experiment aims to validate the proposed one-step global multi-view approach for classification. A summary of the proposed approach and the comparative methods is illustrated in Figure [6.3](#). As can be seen, the proposed approach is compared with two-step method but also with single modality methods.

The aim of comparing with single modality methods is to evaluate the impact of the multimodal atlas in the classification. To this end, the proposed methods are compared to the use of PCA followed by either LDA or SVM with a RBF kernel classifier (see Figure [6.3](#)). The PCA technique trained using US motion data only was considered as a baseline, as it represents the current state-of-the-art in the use of US data alone for statistical analysis of motion. Since MR is considered to be the gold standard for analysis of cardiac function, we consider the PCA technique trained using only MR data as a reference techniques, regardless of cost or other considerations.

The aim of comparing with the multiple modality two-step approaches is to evaluate the impact of our proposed one-step multi-view learning approach over the obvious two-step approach of embedding followed by classification.

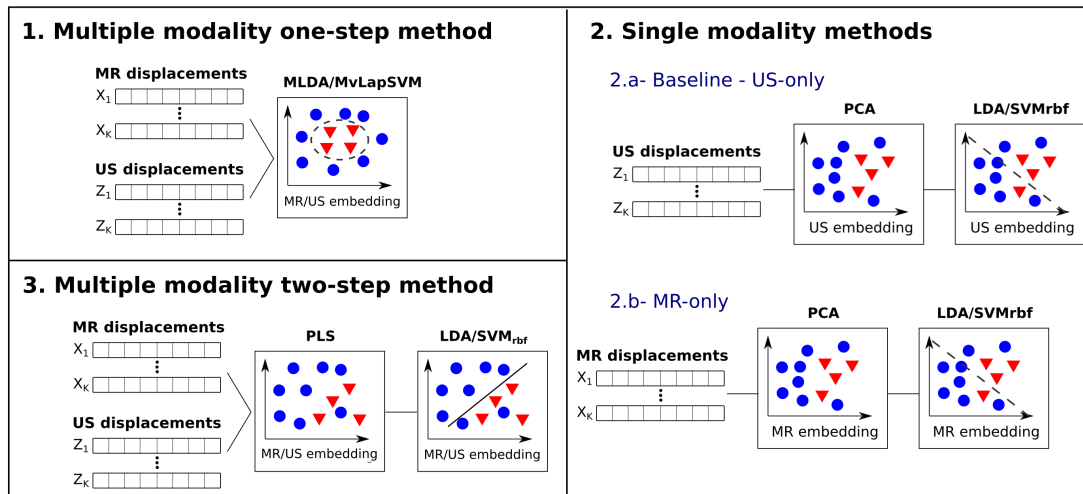


Figure 6.3: Different approaches for classification: 1. Proposed method (multiple modality one-step method). Comparative approaches: 2. Single modality methods (2.a- US-only pipeline, 2.b- MR-only pipeline); 3. Multiple modality two-step method.

Table 6.1 shows the results of this experiment. For the MLDA classifier the regularisation parameter γ was optimised across values [1, 5, 10, 15, 20] (Sun et al., 2016). The RSCV was performed for each of these values of γ , and based on the results, the optimal value of γ was chosen. Similarly, for the MvLapSVM algorithm an RBF kernel was used, and the σ_{RBF} parameter was optimised across values [1E-4, 1E-3, 1E-2, 1E-1, 1, 1E2] and $\gamma_1, \gamma_2, \gamma_3$ were optimised across values [1E-10, 1E-6, 1E-4, 1E-2, 1, 1E2, 1E3]. The RSCV was performed for each of these values of $\gamma_1, \gamma_2, \gamma_3$ and σ , and based on the results, the optimal values were chosen. Note that the test database was used for optimising the parameters and also for the evaluation of the different algorithms due to the limited size of the database. Furthermore, we assess the statistical significance of the accuracy using the proposed method compared to the performance of PCA trained on US data (i.e. the baseline technique) using a Student's t-test (99% confidence).

Table 6.1: US-based classification balanced accuracy (BACC), sensitivity (SEN) and specificity (SPE) of the proposed and comparative methods and Student's t-test (99% confidence) results. For each group, the first row corresponds to the linear method and the second row to the non-linear method. An asterisk indicates a statistically significant improvement in accuracy over the baseline comparative approach (i.e. 2.a: Single modality US method - PCA + LDA for the linear case and PCA + SVM for the non-linear case). Bold text indicates the method with the highest classification accuracy for the linear and non-linear cases.

Proposed method	BACC (%)	SEN (%)	SPE (%)
1. Multiple modality one-step method			
MLDA	82.18 (15.0)*	80.50 (26.5)	83.86 (9.9)
MvLapSVM	92.71 (10.4)*	89.00 (20.8)	95.14 (6.8)
Comparative approaches	BACC (%)	SEN (%)	SPE (%)
2.a. Single modality US method			
PCA _{US} + LDA	74.79 (15.8)	71.05 (28.6)	78.57 (10.1)
PCA _{US} + SVM _{rbf}	87.32 (12.9)	84.50 (23.2)	90.14 (6.6)
2.b. Single modality MR method:			
PCA _{MR} + LDA	84.21 (15.4)*	74.00 (28.8)	90.43 (6.8)
PCA _{MR} + SVM _{rbf}	90.89 (11.7)*	86.50 (22.3)	95.29 (6.7)
3. Multiple modality two-step method			
PLS + LDA	80.07 (16.8)*	75.51 (27.1)	81.86 (9.5)
PLS + SVM _{rbf}	90.39 (12.1)*	87.50 (21.8)	90.57 (10.9)

The results in Table 6.1 show that in both the linear and non-linear cases, the use of multi-view algorithms (row 1 - Multiple modality one-step method) results in a statistically significant increase in the accuracy. Both multi-view one-step classifiers have the highest accuracy compared to the two-step approach (row 3 - Multiple modality two-step methods). The highest accuracy is achieved using MvLapSVM, the non-linear multiple modality one-step approach. The MvLapSVM algorithm achieved similar accuracy, sensitivity and specificity to the use of only MR data.

Furthermore, note that the proposed multi-view algorithms (i.e. one-step and two-step, linear and non-linear) are capable of performing classification using data from either view, or both views. Table 6.1 focuses on only using US as the input data, while Table 6.2 shows the results for the combination of both MR and US data.

Table 6.2: *MR and US classification BACC, SEN and SPE of the proposed and comparative methods. For each group, the first row corresponds to the linear method and the second row to the non-linear method. Bold text indicates the method with the highest classification accuracy for the linear and non-linear cases.*

Proposed method	BACC (%)	SEN (%)	SPE (%)
<i>1. Multiple modality one-step method</i>			
MLDA	88.93 (11.4)	88.00 (21.5)	89.22 (8.1)
MvLapSVM	94.86 (9.5)	91.00 (19.3)	96.57 (6.1)
<i>Comparative approaches</i>			
<i>3. Multiple modality two-step method</i>			
PLS + LDA	77.25 (16.9)	72.50 (29.6)	82.00 (10.1)
PLS + SVM _{rbf}	93.79 (9.7)	94.00 (16.3)	95.71 (6.6)

A comparison between Tables 6.1 and 6.2 shows that the multi-view classifier algorithms have a higher accuracy when using both views as input data. Furthermore, for the comparative multiple modality two-step method, accuracy in the linear case is significantly lower, while in the non-linear case the accuracy is slightly lower. This can be explained by the observation that non-linear classifiers can learn the non-linear structure of the data which is likely to result in improved classification performance.

It is likely that MvML algorithms provided the optimal performance when using the two views as they were better able to exploit the inter-modality relationship when performing classification. This section showed that the use of only one view (i.e. US) only slightly reduced the accuracy of the proposed algorithms when compared to the use of both views (i.e. MR and US). In both cases, MLDA and MvLSVM, the prediction function (Eqs. 6.1 and 6.3) is the average of the prediction functions from the two views. In the ideal case, the embedding space for MR and US should be the same, but as the data might have some noise and the number of training subjects is limited, this embedding might vary as reported in the previous Chapter (see Figure 5.13). For this reason, it is probable that the use of the two views provided a more robust embedding space.

Based on the presented results, it is possible to conclude that the highest accuracy is achieved using the proposed multiple modality one-step multi-view classifiers, whether using only US data or both MR and US data as input.

6.3.3 Evaluation of regional multi-view learning methods

This section reports classification results for the regional approach described in Section 6.2.3. Table 6.3 shows the results of the proposed regional approach compared to the global approach. A Student's t-test (99% confidence) was used to evaluate the statistical significance of the accuracy results between global and regional methods.

Similar to the global approach, but now for each AHA region, the regularisation parameter γ for MLDA was optimised across values [1, 5, 10, 15, 20], and for the MvLapSVM algorithm the σ parameter was optimised across values [1E-4, 1E-3, 1E-2, 1E-1, 1, 1E2] and $\gamma_1, \gamma_2, \gamma_3$ were optimised across values [1E-10, 1E-6, 1E-4, 1E-2, 1, 1E2, 1E3]. Once the parameters for the linear and non-linear method were optimised per AHA region, the predicted labels were stored. These regional predicted labels were combined using a weighted majority voting strategy. The optimal weights for each AHA segment were optimised using a randomised search on hyper parameters algorithm (Bergstra and Bengio, 2012). More specifically, the weights for each AHA segment were sampled from a uniform distribution in the interval [0,1], then the sampled weights were used to combine the predicted labels and the accuracy, sensitivity and specificity were computed. This process was iteratively repeated 500 times and the optimal weights were selected according to the highest accuracy.

Table 6.3: US-based classification BACC, SEN and SPE of global and regional approaches and Student's t-test (99% confidence) results. An asterisk indicates a statistically significant improvement in accuracy over the global approach.

Global Methods	BACC (%)	SEN (%)	SPE (%)
MLDA	82.18 (15.0)	80.50 (26.5)	83.86 (9.9)
MvLapSVM	92.71 (10.4)	89.00 (20.8)	95.14 (6.8)
Regional Methods	BACC (%)	SEN (%)	SPE (%)
MLDA	87.71 (12.6)*	85.00 (23.1)	90.43 (6.7)
MvLapSVM	94.32 (11.1)*	93.00 (17.5)	96.57 (6.2)

The results in Table 6.3 show that the regional method outperforms the global method in both linear and non-linear cases, with both differences being statistically significant.

Figure 6.4 shows the estimated weights for the linear and non-linear cases. These show that the basal and mid segments of the anterior wall are the areas with the highest impact for classification. This is consistent with the findings of previous work that reported large motion in the basal and mid free wall segments ([Kleijn et al., 2014](#)) and the importance of these areas for cardiac function ([Carlssoon et al., 2007](#)). US based assessment of the motion of the basal anterior wall of the myocardium is known to be subject to uncertainty ([Armstrong and Ryan, 2012](#)), due to limited acoustic windows and significant noise in the far field of the US beam. This could explain the improvement seen in our method, as inclusion of MR-derived information in the multimodal motion atlas adds complementary information.

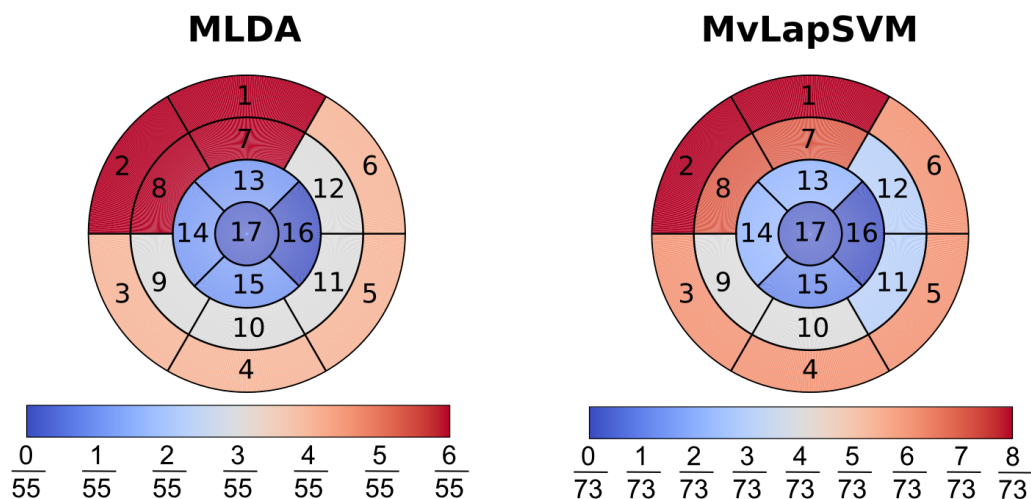


Figure 6.4: Weights for the majority voting scheme in the regional approach for classification. On the left estimated weights for MLDA, and on the right estimated weights for MvLapSVM using the randomised search on hyper parameters algorithm. The colour bar shows the ranges of values for the estimated weights.

Similar to the previous section, the accuracy of the different classifiers using both MR and US data was also computed. Table 6.4 shows the results of the proposed regional algorithms using both modalities. A similar pattern to that in the previous section can be observed. The use of both modalities provides a richer motion description and therefore the classifiers achieve a higher accuracy. However, in this case there is only a statistically significant increase in accuracy for the linear method compared to the global method.

Table 6.4: MR and US classification BACC, SEN and SPE of global and regional approaches and Student's t-test (99% confidence) results. An asterisk indicates a statistically significant improvement in accuracy over the global approach.

Global Methods	BACC (%)	SEN (%)	SPE (%)
MLDA	88.93 (11.4)	88.00 (21.5)	89.22 (8.1)
MvLapSVM	94.86 (9.5)	91.00 (19.3)	96.57 (6.1)
Regional Methods	BACC (%)	SEN (%)	SPE (%)
MLDA	91.25 (10.5)*	91.50 (18.9)	91.00 (6.9)
MvLapSVM	94.96 (10.2)	90.50 (19.7)	97.43 (5.5)

6.3.4 Clinical validation

As described at the beginning of this section, to validate the proposed algorithms an 8-fold RSCV with 100 repetitions was used. In addition to computing the accuracy, sensitivity and specificity for each fold, the amount of times that each subject was misclassified was also recorded. This section aims to investigate whether a relationship exists between the subjects who were frequently misclassified and clinical parameters normally used to detect patients suffering from DCM. As described in Section 2.4.1, DCM diagnosis criteria include reduced global LVEF, ventricular dilatation, as well as impaired systolic function.

Figure 6.5 reports the relationship between LVEF and the misclassification rate, which is defined as the number of times a subject was misclassified over the 100 repetitions divided by the total number of classifications for that subject. For both global and regional methods, results show that the misclassification rate for DCM patients increases with higher LVEF, which is consistent with the clinical perspective that LVEF decreases with the progression of DCM, as the LV dilates and the cardiac function decreases. The EFs for the most misclassified DCM patients are typically over 50%, which is in the same range as the volunteer EFs reported in Table 4.1. Similarly, the EFs for the most misclassified healthy subjects are closer to the EFs for DCM patients.

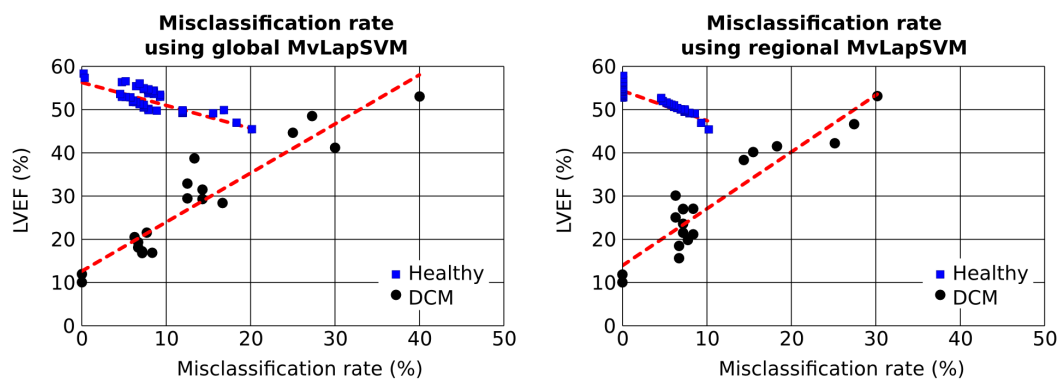


Figure 6.5: Relationship between LVEF (%) and misclassification rate for the preferred method (MvLapSVM) for the global approach (left figure) and the regional approach (right figure).

As a final experiment the accuracy of detecting DCM patients using only LVEF values was computed, which is considered the primary diagnosis criterion to identify patients suffering from DCM. In this case, the values reported in Table 4.1 of LVEF for each subject were used to train a LDA classifier. Similar to the previous experiments, the balanced accuracy, sensitivity and specificity were computed.

Table 6.5: Comparison between LVEF classifier and regional non-linear multi-view classifier: BACC, SEN and SPE and Student's t-test (99% confidence) results. An asterisk indicates a statistically significant improvement in accuracy over the global approach.

Method	BACC (%)	SEN (%)	SPE (%)
LDA for LVEF	82.5 (17.1)	100 (0)	65.0 (34.2)
MvLapSVM	94.32 (11.1)*	93.00 (17.5)	96.57 (6.2)

The results in Table 6.5 show that the proposed method achieves higher accuracy than only using LVEF values. Furthermore, the LVEF based classifier always correctly classifies healthy patients (the sensitivity), but is less successful in classify DCM patients (specificity). Therefore, it would appear that the use of the atlas and more localised motion descriptors helps in the identification of DCM patients.

6.4 Discussion and conclusion

The previous Chapter described a framework to construct and evaluate a multi-modal cardiac motion atlas that related MWMA parameters derived from MR and US data. This Chapter proposed a novel extension to this atlas and demonstrated its application to the task of identifying DCM patients using only US data but at the same time taking advantage of the implicit relationship between MR and US learned from the atlas. This was made possible by the inclusion of multi-view learning algorithms in which MR and US were considered as different views of the same underlying phenomenon (i.e. cardiac mechanics). More specifically, two multi-view classifiers were evaluated (MLDA and MvLapSVM), and both were implemented using global and regional approaches. To the best of the author's knowledge this is the first time that multi-view learning has been applied to cardiac motion data. The application in this paper was the identification of DCM, but the same pipeline could be used to identify other cardiovascular diseases.

The results showed that the use of MvML algorithms resulted in a statistically significant increase in classification accuracy compared to the use of only US data without the multimodal atlas. Furthermore, the comparison of the global and regional approaches showed that the regional approach resulted in a statistically significant improvement in terms of accuracy. The highest accuracy was 95.78% and it was achieved using regional MvLapSVM.

The better performance of the regional approach compared to the global approach can be explained by the high dimensionality of the input data and the limited size of the training database. The regional approach was able to find more meaningful descriptors from the lower dimensional regional data to detect patients suffering from DCM. Furthermore, it was better able to capture the regional dependencies of cardiac mechanics and its variation between MR and US based estimates.

All the proposed MvML algorithms concatenated the spatial and temporal information of the data, thereby losing the spatio-temporal relationships of the motion data, which could be important to localise regional abnormal cardiac motion patterns. A possible extension of this work would be to extend the multi-view algorithms to take as input a 3-way tensor (i.e. stack of all the spatial parameters along time and for all subjects) and exploit the different information contained in the temporal and spatial dimensions.

A clear indicator for detecting DCM is the size of the LV. However, this pipeline aimed to use only motion-based information to detect this group of patients without including shape information. For this application, DCM subjects were used as an exemplar application to demonstrate the power of the proposed methods, but another group of patients could also be employed. In reality, it is likely that the inclusion of morphological information would be beneficial to the identification of DCM or other patient groups, and this could be another extension of the project.

In conclusion, I believe that the work presented in this Chapter represents an important contribution to the understanding of cardiac motion using cardiac motion atlases. The intended workflow of the developed pipeline is to make use of the prior knowledge from the multimodal atlas to enable robust extraction of indicators from US images for detecting DCM patients. In a clinical setting, we can envisage a scenario in which the pipeline would be embedded into the US scanner to provide real-time information to the sonographer during acquisition.

This Chapter and the previous one have focused on characterising cardiac motion based on displacements. The next Chapter aims to integrate automatically estimated strain values into the pipeline.

7 | Strain analysis

MWMA allows for precise and comprehensive assessment of LV and RV contractile function. Myocardial strain and strain rate provide a relatively load-independent quantitative evaluation of myocardial wall motion, and have been shown to enable earlier and more sensitive detection of myocardial diseases compared to global measures of cardiac function, such as ventricular volumes and ejection fraction (Claus et al., 2015). Compared to displacements, strain values are more widely understood clinically. In US, strain can be measured by tracking naturally occurring acoustic markers ('speckles') in the myocardium throughout the cardiac cycle. However, the limited acquisition windows severely restrict the ability to interrogate total myocardial wall motion. MR is the current gold standard for assessment of global and regional myocardial function, and does not suffer from limited acquisition windows. Several MR imaging techniques have been proposed for strain analysis, such as myocardial tagging (Axel and Dougherty, 1989, Zhou et al., 2015), phase contrast velocity imaging (van Dijk, 1984, Bryant et al., 1984), displacement encoding (Aletras et al., 1999, Kim et al., 2004), and strain encoding (Osman et al., 2001). Although all of these MR techniques provide useful information on myocardial function, they are not typically used in routine clinical MR as they require additional imaging and complex, time-consuming post-processing. Instead, MR feature tracking (MR-FT) (Wu et al., 2014, Hor et al., 2011) has been proposed as a more accessible MWMA technique. By tracking features between consecutive frames from SSFP cine acquisitions, in a way analogous to speckle tracking US, MR-FT is able to derive strain and strain rate values from routinely acquired MR images. However, current MR-FT techniques typically require manual delineation of cardiac volumes and frequent reassessment of annotations based on tracking results, which is skill and experience dependent. This results in increased processing times and a significant degree of inter and intra-observer variability (Schuster et al., 2015).

The two most common commercially available software packages offering MR-FT are TomTec (TomTec Imaging Systems, Unterschleissheim, Germany) and CVI₄₂ (Circle Cardiovascular Imaging, Calgary, Canada). Both require manual segmentation of the ED frame and identification of RV-LV and mitral valve insertion points. Furthermore, manual readjustment of the automatically propagated ED segmentations is frequently needed, resulting in significant processing time and interobserver variability, limiting its current use for clinical assessment in large groups of patients. Some semi-automatic methods have been proposed, for example Mansi et al. (2009) presented an improvement of the diffeomorphic Demons algorithm for cine MR sequences. They compared the estimated strain using the proposed motion tracking algorithm to tagged-MR estimated strains for a healthy volunteer, and with ultrasound 2-D strain for a patient with congenital pulmonary valve regurgitations. However, their method required manual input for segmentation and motion correction. Few automatic pipelines have been proposed before and most either focus on one type of strain, or on a single slice. For example, Jolly et al. (2017) proposed an automatic pipeline to measure LV mean mid-wall Eulerian circumferential strain from cine SSFP. More recently, Vigneault et al. (2017) proposed an automatic pipeline for estimation of circumferential cardiac strain using deep learning, although they did not make a direct comparison to any clinical software.

The remainder of this Chapter is organised as follows. Section 7.1.1 presents a fully automatic pipeline to quantify myocardial longitudinal, radial and circumferential strain from 2D cine MR sequences. The pipeline enables fast and accurate assessment of LV strains and completely eliminates manual intervention and thus inter and intra-observer variation. Section 7.1.2 introduces an extension of this pipeline to compute strain from 3D US and TAG imaging data. This extension includes some manual interaction for the segmentation of 3D US data compared to the fully automated proposed for the 2D case. Section 7.1.3 integrates the 3D strain calculation method with the multi-view pipeline from Chapters 5 and 6. Validation and results for the automatic 2D strain pipeline are presented in Section 7.2.1, similarly Section 7.2.2 presents the validation of the 3D estimated strain approach, and Section 7.2.4 presents the results of the integration of strain within the multi-modal cardiac atlas. Finally, Section 7.3 discusses the results obtained in relation with previous Chapters.

7.1 Methods

This section is divided into three parts: subsection 7.1.1 presents the automatic framework for quantifying myocardial strain from 2D cine MR sequences, which is based on the work published in [Puyol-Antón et al. \(2018a\)](#). Subsection 7.1.2 presents the 3D extension for computing strain values from 3D US and TAG data. Finally subsection 7.1.3 integrates the the 3D strain calculation method with the multi-view pipeline from Chapters 5 and 6.

7.1.1 Automatic 2D strain computation from cine MR data

The proposed pipeline to compute strain from cine MR data is summarised in Figure 7.1, and each step is described below.

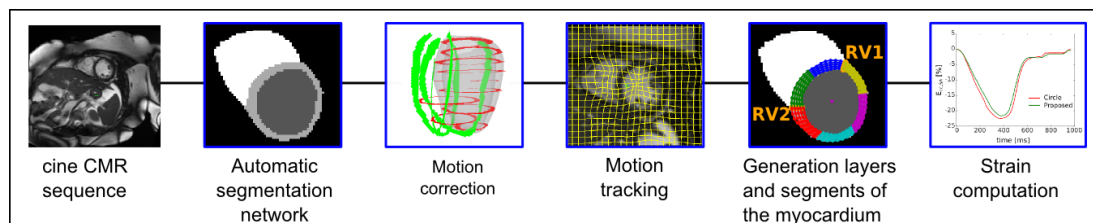


Figure 7.1: Overview of the proposed framework for automatic quantification of myocardial strain from cine MR sequence.

Automatic segmentation network: A fully-convolutional network (FCN) with a 17 convolutional layer VGG-like architecture was used for the automatic segmentation of the LV myocardium and blood-pool at ED ([Sinclair et al., 2017](#), [Bai et al., 2017](#)), as shown in Figure 7.2. Batch-normalisation (BN) is used after each convolutional layer, and before a rectified linear unit (ReLU) activation. The BN operation removes internal covariate shift, improving training speed. After every two convolutional layers, a stride of 2 is used in the convolution to downsample the feature map and learn features at a more global scale. The last layer is followed by a softmax function with a cross-entropy loss, which can be interpreted as the normalised probability that each pixel is assigned to the correct label class (i.e. LV myocardium and blood-pool).

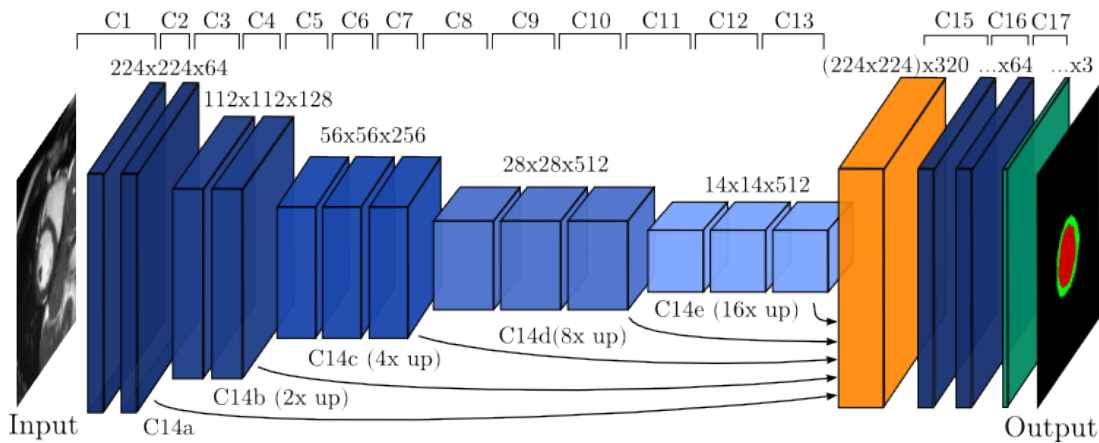


Figure 7.2: The VGG-like FCN architecture with 17 convolutional layers used for segmentation. Feature map volumes are colour-coded by size, reported above the volumes. Figure adapted from [Sinclair et al. \(2017\)](#)

In the case of the SA stack, each slice is segmented independently, i.e. in 2D. In the case of LA slices, independent networks are trained for 2Ch and 4Ch LA sequences. SA and LA networks were trained using an independent cohort of the UK Biobank. More specifically, the SA segmentation network was trained with 1000 ED and ES images, and the 2Ch and 4Ch LA networks with 140 ED images each. All images were manually segmented by experts, and reshaped to 224×224 pixels by zero-padding. Finally, from the segmentations, a bounding box was generated and used to crop the image to only include the desired FoV, improving pipeline speed and reducing errors in motion tracking.

Motion correction: Automatic SA and LA segmentations were used to correct breath-hold induced motion artefacts using the iterative registration algorithm proposed in [Sinclair et al. \(2017\)](#). The motion correction algorithm iteratively registers each image plane from the SA sequence to the intersection with the 2Ch and 4Ch LA image planes, which are kept fixed in space. The alignment is performed only on the ED frame and then propagated to the other frames. Only in-plane translations were considered as minimal in-plane rotation was assumed, and gradient descent was used to minimise the sum of squared differences between the SA segmented image for each slice and the segmented image computed from the 2Ch and 4CH LA plane intersections. Nearest-neighbour interpolation of the intersecting planes was used in order to preserve the segmentation labels of the myocardium and blood-pool. The final translation for each slice of the SA sequence from its original position was computed as the summation over all iterations.

Figure 7.3 shows an example of a case with severe motion artefacts before and after motion correction.

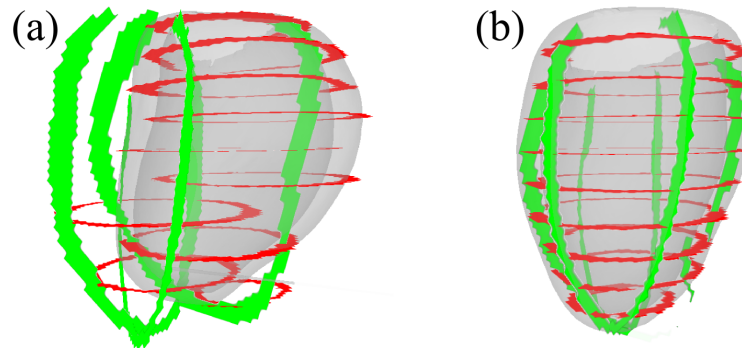


Figure 7.3: Example of motion correction algorithm, myocardial label in the SA (red) and LA (green) views is shown before (a) and after (b) alignment. Figure adapted from [Sinclair et al. \(2017\)](#)

Motion tracking: Motion tracking was performed on each 2D plane in both SA and LA views using MIRTK. More specifically, a 2D B-spline multi-level FFD registration with normalised mutual information as similarity metric was used ([Rueckert et al., 1999](#)) to estimate LV motion between consecutive frames of the cine MR sequences. Subsequently, the estimated FFD deformation fields were composed to obtain the FFD transformation from each cardiac phase to the reference ED phase. Figure 7.4 shows an example of the resulting 2D B-spline multi-level FFD registration between the ED and ES frame.

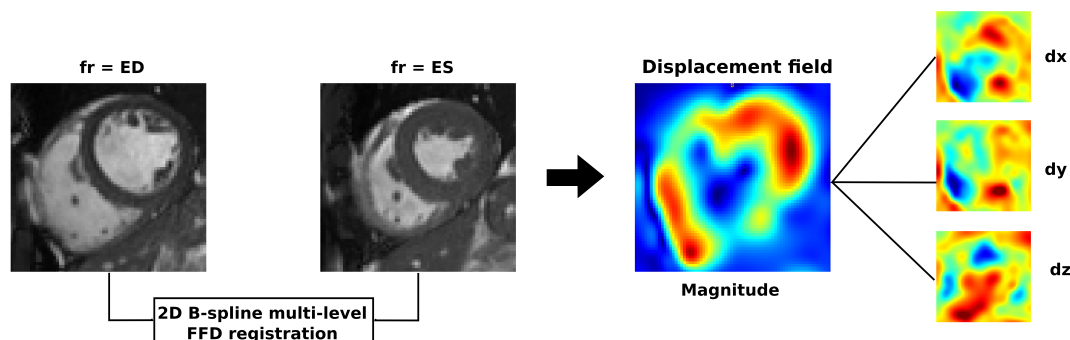


Figure 7.4: Example of motion tracking between ED and ES frame, showing the magnitude of the displacement field, and displacement field for components x, y and z .

Generation of layers and segments of the myocardium. In the ED frame, the LV myocardium was automatically divided into 3 layers and 6 segments as illustrated in Fig. 7.5 and these layers and segments were propagated through the cardiac cycle. More details of the steps involved to generate the layers are described below and illustrated in Figure 7.6.

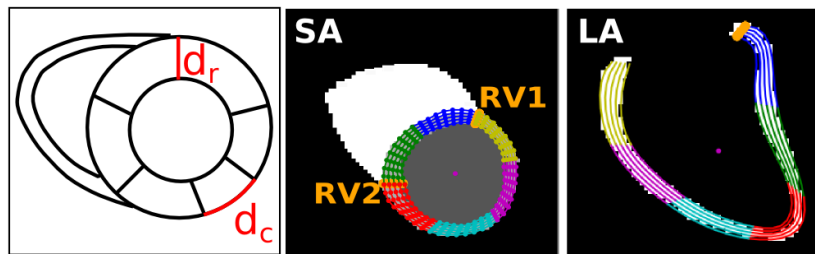


Figure 7.5: *Left:* Schema of the SA segments with radial distance d_r and circumferential distance d_c . *Middle:* SA segmentation with 5 concentric contours within the LV wall and six sectors. *Right:* LA segmentation split into 5 layers and 6 segments. Colours represent segments.

1. *Detection of RV-LV intersections.* In the SA view, RV-LV intersections were automatically detected (RV1 and RV2 in Fig. 7.5) by first extracting the edges using the Canny edge detector algorithm (Canny, 1987), and then a hit-or-miss transformation (Zhao and Daut, 1991) was used to locate the points with three junctions.
2. *Contours extraction.* From the SA and LA segmentations, the contours defining the boundaries of the LV endocardium and epicardium were extracted using standard morphological operations. First the points in the image with the myocardium segmentation labels were extracted, and the Convex Hull algorithm (Barber et al., 1996) was used to find the minimal convex shape. These vertices were used to find the outer and inner points of the segmentation.
3. *Interpolation of contours.* The extracted point contours were smoothed by fitting B-splines, to represent them as N-dimensional curves. Then, the B-spline curves were used to identify for both contours the same number of equally-spaced points. Furthermore, on the SA images the points were re-interpolated circularly using the RV-LV intersection points and the centroid as references. In the LA view, the starting point was selected using the RV-LV intersection.

4. *Generation of layers.* From the myocardial segmentations in both the SA and LA views a centre line was generated using a skeletonisation algorithm (Lee et al., 1994), which reduces foreground regions in a binary image to a skeletal remnant that largely preserves the extent and connectivity of the original region while eliminating most of the original foreground pixels. Similar to the previous step, the points belonging to the skeleton image were extracted and smoothed by fitting a further spline. Two additional contours were generated at the midlines of the centreline-epicardium and centreline-endocardium, resulting in a total of 5 concentric trans-mural contours.
5. *Generation of segments.* Six myocardial sectors were identified in each slice. In the LA views, the myocardium was divided into 6 equally sized sectors. In the SA view, RV-LV intersections were used to divide the septum and LV free-wall into respectively 2 and 4 equally sized sectors along the arc-length of the myocardial centreline.
6. *Propagation of contours over time.* All spline points for LA 2Ch and LA 4Ch and SA were transformed with the motion tracking displacement fields to produce transformed contours at each cardiac phase.
7. *Detection of mid-slices.* The intersections between the propagated 2Ch and 4Ch spline points and the ED frames of the SA sequence were used to detect the mid-slices. Only the SA slices that enclose the LA propagated points were retained, then the 3 most central slices were selected.

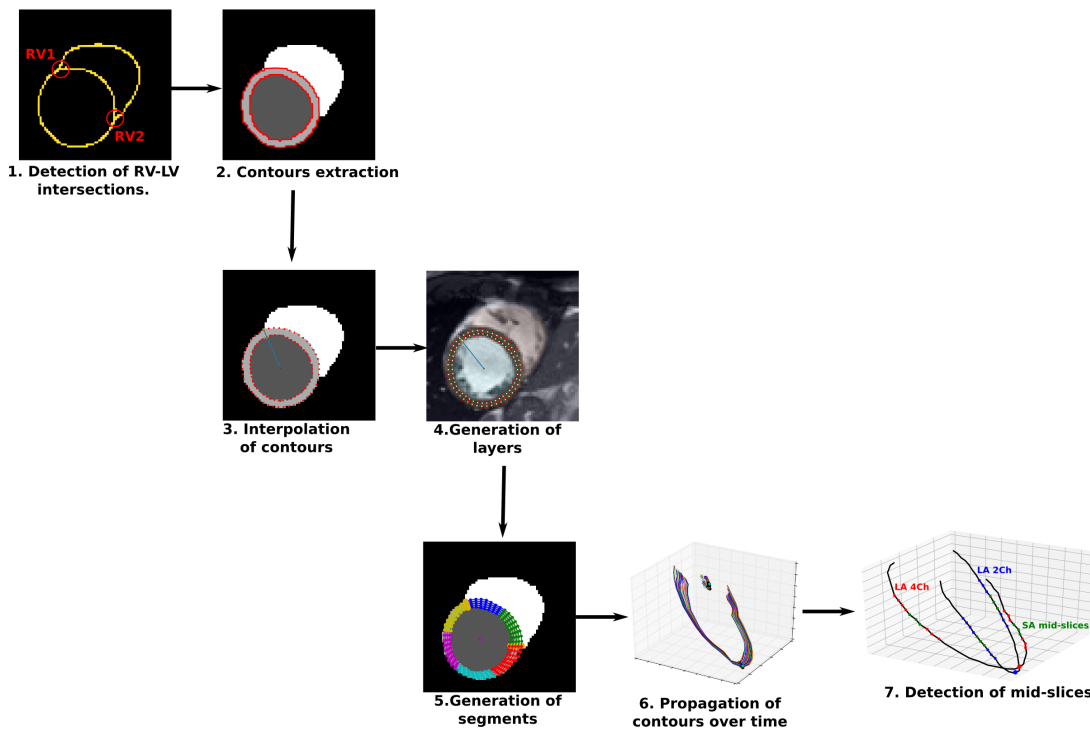


Figure 7.6: Framework to generate the layers and segments of the myocardium.

Strain computation: Myocardial strain defines the total deformation of a region of tissue during the cardiac cycle relative to its initial configuration at the onset of the cardiac cycle, and it is normally expressed in percentages. Three components of myocardial strain (radial, rr , circumferential, cc , and longitudinal, ll) are typically measured, and each component used to quantify different aspects of cardiac function. More specifically, the mean Lagrangian strain over the whole myocardium for each strain component j (i.e. rr , cc or ll) at each time point n was computed as follows:

$$E_{j,v}^n = \sum_{s=1}^S \sum_{q=1}^Q \frac{1}{SK} \frac{d_{j,v,q,s}^n - d_{j,v,k,s}^{ED}}{d_{j,v,k,s}^{ED}} \quad (7.1)$$

where $d_{j,v,k,s}^{ED}$ is the length at ED of the segment s , layer q and view v (i.e. SA or LA) for strain component j .

Radial strain was computed using the transmural distance (d_r in Fig. 7.5) from SA/LA slices; circumferential strain using the circumferential segment arclength (d_c in Fig. 7.5) from SA slices; and longitudinal strain using the longitudinal segment arclength from LA slices. Because there are five layers (endocardial, epicardial, midwall, endo-midwall and epi-midwall) strain values for each layer were computed separately. Global strain was computed as the average of the estimated strains from each segment and layer to reduce noise.

7.1.2 3D strain for TAG and US data

The previous section described a robust pipeline for automatic strain estimation from 2D cine MR images. A limitation of this pipeline is that it uses only the middle SA slices. Cine SA images are not fully 3D images as the voxel sizes are not isotropic and for this reason it is complicated to correctly compute 3D strain values from SA sequences. Furthermore, normally the most basal and apical slices are not used to estimate strain due to the in-plane motion. Instead LA sequences are used to estimate longitudinal strain, however, they are not 3D. This section aims to extend the pipeline to compute strain from 3D TAG and 3D US images, which both have isotropic voxel size. Figure 7.7 summarises the steps involved in estimating the 3D strain values.

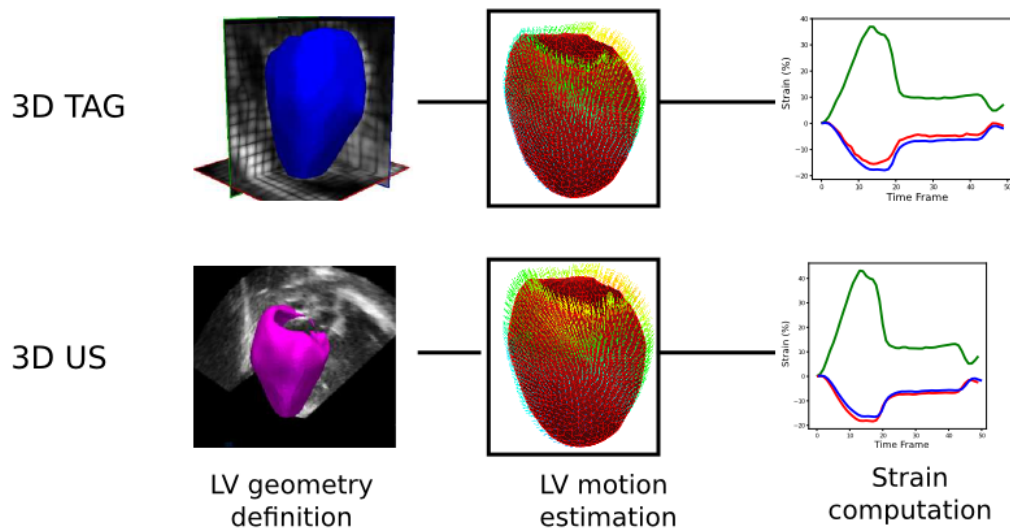


Figure 7.7: Overview of the proposed framework for computing strains from 3D MR and 3D US images.

LV geometry definition: For each subject, the LV myocardium was automatically segmented in the ED phase of the cine SA and LA MR images using the FCN network described in Section 7.1.1. The MR SA and LA segmentations were used to correct for breath-hold induced motion artefacts using the motion correction algorithm described in Section 7.1.1. The motion-corrected LA/SA segmentations were fused to form a 3D smooth myocardial mask. The 3D US images were manually segmented as described in Section 5.2.1. Finally, as described in Section 5.2.2 the cine SA and TAG sequence were rigidly aligned with the aim of applying the mesh generated from cine SA to the TAG sequence.

In contrast to Section 5.2.1, a template mesh obtained using 3D Harp (Zhou et al., 2015) was optimised to fit to the LV binary mask. Compared to the proposed pipeline in Section 5.2, the 3D Harp mesh is volumetric and contains an inner layer between the endocardium and epicardium. Also, this mesh is sampled regularly in radial, longitudinal and circumferential directions. Six landmarks were manually localised in the TAG and 3D US images (1 landmark was placed in the apex, 4 in the basal planes and 1 at mid- level in the septum), then the template mesh was rotated and scaled to match the set of landmarks. Next, the surface mesh was converted to a volumetric dense mesh that also contains an inner layer between endocardium and epicardium, and in which, the LV domain is sampled regularly in radial, longitudinal and circumferential directions. The resampling was performed by casting rays from the long axis to the endocardial and epicardial surfaces (see Figure 7.8 for more details). The mid part of the LV was discretised using a cylindrical sampling, while apical and basal parts were sampled in a spherical manner (for more details the interested reader is referred to (Zhou et al., 2015)).

For the 2D strain estimation, from each segmentation slice, the contours were extracted and regularly spaced points were identified from the contours. However, this strategy could not be applied to the 3D volumes, as the longitudinal component would not be accurate. Instead, in this section it is proposed to use the volumetric hexahedral dense mesh regularly sampled in radial, longitudinal and circumferential directions to facilitate strain computation.

LV motion estimation: Similar to Section 5.2.3 a 3D GPU-based B-spline FFD registration was used to estimate LV motion between consecutive frames of the TAG and 3D US sequences. Furthermore, a $3D+n$ cyclic B-spline was fitted to the composed 3D transformations in order to estimate a full cycle $3D+n$

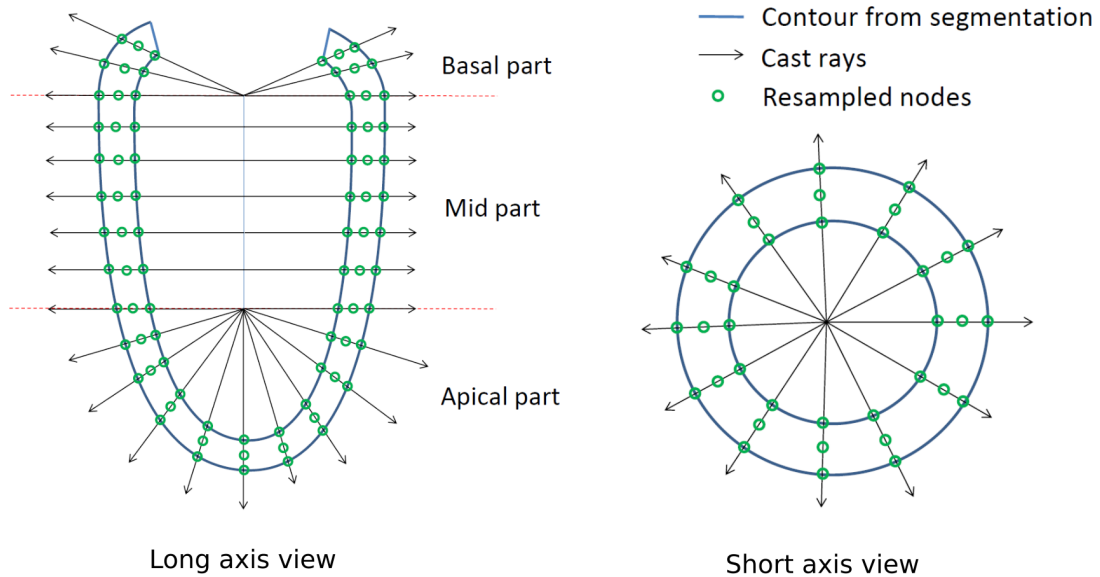


Figure 7.8: LV geometry definition and fitting volumetric dense mesh (image adapted from Zhou et al. (2015))

transformation.

Strain computation: Similar to the 2D case, myocardial strain is computed in three components, radial, rr , circumferential, cc , and longitudinal, ll , using a 3D extension of the Lagrangian strain. The main steps to estimate the 3D strain are described below:

- *Compute distances in each cell.* To compute strain values, similar to the 2D strain estimation, first the distances for each cell of the mesh are computed. Figure 7.9 shows an example of how the distances are computed for each cell of the mesh.

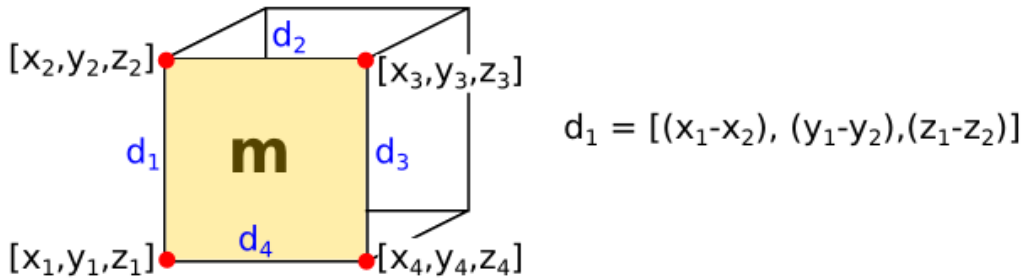


Figure 7.9: Strain computation from the hexahedral dense mesh. This image shows a hexahedron cell of the mesh, m , and how the distances d_1-d_4 computed.

- *Compute strain in each cell.* From the hexahedral mesh, strain was computed at each time point n as follows:

$$\varepsilon_{m,n} = \frac{1}{4} \sum_{z=1}^4 \frac{d_z^t}{d_z^{ED}} - 1 \quad (7.2)$$

where d_z^n is the length of edge z at cardiac phase n . As shown in Figure 7.9 the length of the edge z can be computed as the distance between two nodes of the cell m , i.e. d_1 , d_2 , d_3 and d_4 in Figure 7.9.

- *Transform strains into local coordinate system.* Strains for each node were reoriented into the local coordinate system (i.e. rr , cc , ll) as follows:

$$\mathbf{E}_{m,n} = \varepsilon_{m,n} \cdot [\hat{e}_{rr}, \hat{e}_{cc}, \hat{e}_{ll}] \quad (7.3)$$

where \hat{e}_{rr} , \hat{e}_{cc} and \hat{e}_{ll} are the unit column vectors in the radial, circumferential and longitudinal directions.

Finally, strain values were averaged between endocardial and epicardial surfaces, to generate the mean strain values per cell.

7.1.3 Integration of 3D strain with atlas

The previous Section presented a new pipeline to compute strain values from 3D MR and 3D US images. This section integrates the estimated 3D strains into the multimodal cardiac atlas described in Chapter 5. Only the steps which are different from the pipeline described in Chapter 5 are listed below.

Motion reorientation: The estimated strains from different subjects were re-oriented into the atlas coordinate system as follows. First, for each node of the hexahedral mesh of subject k , the strain tensor was generated as follows:

$$F_{m,n,k} = \begin{pmatrix} \varepsilon_{m,n,k}^x & 0 & 0 \\ 0 & \varepsilon_{m,n,k}^y & 0 \\ 0 & 0 & \varepsilon_{m,n,k}^z \end{pmatrix} \quad (7.4)$$

where $\varepsilon_{m,n,k}^x$, $\varepsilon_{m,n,k}^y$ and $\varepsilon_{m,n,k}^z$ are the estimated strains for each cell in the Euclidean space using Equation 7.2.

These strain tensors were reoriented into the atlas coordinate system under a small deformation assumption (Ashburner, 2007) using a push-forward action (Rao et al., 2004, Perperidis et al., 2005a, Peressutti et al., 2017)

$$F_{m,n,k}^{atlas} = \mathbf{J}_{\phi^k(\mathbf{v}_{m,ED,k})} F_{m,n,k} \mathbf{J}_{\phi^k(\mathbf{v}_{m,ED,k})}^{-1} \quad (7.5)$$

where $\mathbf{J}_{\phi^k(\mathbf{v}_{m,ED,k})}$ is the Jacobian of the anatomical transformation ϕ^k mapping each subject's reference ED volumetric mesh to the atlas ED volumetric mesh, computed at location $\mathbf{v}_{m,ED,k}$ (Peressutti et al., 2017).

Finally, the reoriented strain $F_{m,n,k}^{atlas}$ was projected into a local atlas coordinate system in radial, rr , longitudinal, ll , and circumferential, cc , directions by the transformation

$$\mathbf{E}_{m,n,k}^{atlas} = [\hat{e}_{rr}, \hat{e}_{cc}, \hat{e}_{ll}]^T \cdot F_{m,n,k}^{atlas} \cdot [\hat{e}_{rr}, \hat{e}_{cc}, \hat{e}_{ll}] \quad (7.6)$$

The estimated strains are now represented in a common coordinate system, and as described in Section 5.2.10 the MR and US strains in the atlas were concatenated to form the matrices X and Z . Note that the strain in the local coordinate system for each subject $\mathbf{E}_{m,n}$ cannot be directly reoriented into the atlas space because the Jacobian of the anatomical transformation $\mathbf{J}_{\phi^k(\mathbf{v}_{m,ED,k})}$ that maps each volumetric mesh to the atlas space is computed in the Cartesian space and it is a global transformation that affects all the cells of the mesh, while the mapping to the local transformation varies in each cell, making it only locally Cartesian.

7.2 Experiments and results

For the 2D strain method, Section 7.2.1 presents a comparison between the obtained strain values and those computed using CVI₄₂, a widely used clinical tissue-tracking MR software package. For the 3D strain method, Section 7.2.2 repeats the experiments from Chapters 5 and 6 using the estimated strain values and compares the results to those obtained using displacements. All experiments were carried out using the Python programming language, using standard Python libraries (Numpy, SciPy, etc.), VTK libraries, and the scikit-learn Python toolkit (Pedregosa et al., 2011).

7.2.1 2D strain

Materials

This part of the Chapter uses 40 healthy volunteers and 40 ischemic patients from the UK Biobank data set, with demographics displayed in Table 7.1. Details of this cohort of the UK Biobank can be found in Section 4.2.

Table 7.1: Study demographics: end-diastolic volume (LVEDV); end-systolic volume (LVESV); ejection fraction (LVEF), all expressed as mean (standard deviation); and age expressed as mean (min-max).

	Healthy volunteers	Ischemic patients
Number of participants, <i>n</i>	40	40
Age (years)	60.20 (43-73)	66.75 (51-73)
LVEDV (mL)	141.43 (33.74)	175.47 (48.82)
LVESV (mL)	55.61 (15.67)	84.28 (35.72)
LVEF (%)	60.85 (4.78)	55.08 (7.93)

Experiment: Comparison of estimated 2D strain with CVI₄₂ strain values

The strain values obtained using the proposed automatic method were compared with strain analysis obtained by an expert MR trained cardiologist using CVI₄₂. Importantly, the manual segmentations created in CVI₄₂ were made independently of the proposed automated framework and strain results were computed as the mean of three analysis repetitions, according to clinical consensus ([Schuster et al., 2015](#)).

The 2Ch and 4Ch LA slices were used to determine LV longitudinal strain and LV radial strain ($E_{ll,LA}^n$ and $E_{rr,LA}^n$) alongside the time to peak (TPK) strain duration. LV SA circumferential ($E_{cc,SA}^n$) and radial ($E_{rr,SA}^n$) strains and the corresponding TPK strain durations were calculated from three mid-ventricular SA slices determined automatically in the proposed approach (see Section 7.1.1 for more details). The same slices were also used in CVI₄₂.

Figure 7.10 shows an example of the three strains estimated for a healthy volunteer and an ischemic patient using both the automated technique and CVI₄₂.

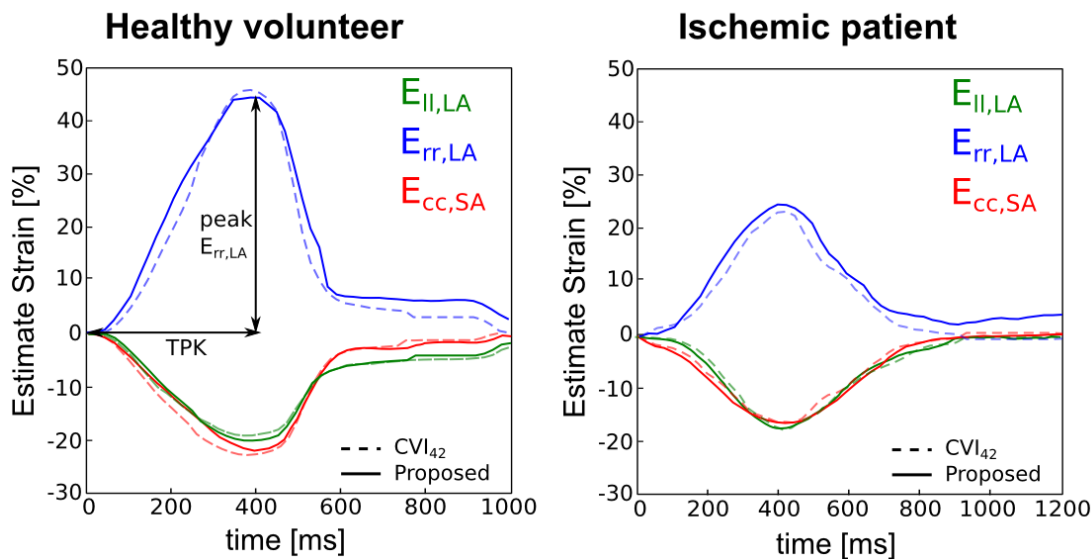


Figure 7.10: Examples of estimated strains for a healthy volunteer and an ischemic patient. Figure shows global strain curves, peak strain and TPK.

Results: Quantification of LV strain

Peak LV strain values obtained using the proposed method and CVI_{42} were compared using a paired sample t -test (significant differences reported for p -value < 0.01 with Bonferroni's correction). Moreover, peak LV strain values between healthy volunteers and ischemic patients were compared using an unpaired t -test (significant differences reported for p -value < 0.01 with Bonferroni's correction) for the proposed method and CVI_{42} . Tables 7.2 and 7.3 show the average peak strain values of the 40 healthy volunteers and 40 ischemic patients using both methods. Results show that there is no statistically significant difference between the two methods for peak $E_{rr,LA}$ and $E_{rr,SA}$ in both patients and volunteers, but there is a slight underestimation in $E_{ll,LA}$ and $E_{cc,SA}$ in healthy volunteers with the proposed method compared to CVI_{42} . Furthermore, the proposed method was successful in detecting a statistically significant decreased peak strain in ischemic patients compared to healthy volunteers, similarly to CVI_{42} .

Table 7.2: Comparison of strain results derived from CVI₄₂ and the proposed pipeline for the healthy cohort, reported as mean (standard deviation). Asterisks indicate significant differences between proposed method and CVI₄₂.

Healthy volunteers		
	CVI ₄₂	Proposed
Peak $E_{ll,LA}$ (%)	-20.26 (2.44)	-18.17 (2.49)*
TPK $E_{ll,LA}$ (ms)	343.75 (44.41)	383.68 (53.83)
Peak $E_{rr,LA}$ (%)	37.11 (7.52)	36.70 (7.97)
TPK $E_{rr,LA}$ (ms)	343.75 (44.41)	387.33 (52.24)
Peak $E_{rr,SA}$ (%)	43.07 (7.10)	42.31 (8.48)
TPK $E_{rr,SA}$ (ms)	336.25 (36.04)	337.93 (33.97)
Peak $E_{cc,SA}$ (%)	-22.02 (2.11)	-19.94 (2.56)*
TPK $E_{cc,SA}$ (ms)	330.60 (40.63)	331.58 (46.92)

Table 7.3: Comparison of strain results derived from CVI₄₂ and the proposed pipeline for the ischemic patients, reported as mean (standard deviation). Daggers indicate statistically significant differences between healthy volunteers and ischemic patients.

Ischemic patients		
	CVI ₄₂	Proposed
Peak $E_{ll,LA}$ (%)	-17.19 (4.26)†	-16.09 (4.29)†
TPK $E_{ll,LA}$ (ms)	367.50 (66.02)	366.90 (62.53)
Peak $E_{rr,LA}$ (%)	29.67 (10.36)†	31.54 (10.33)†
TPK $E_{rr,LA}$ (ms)	339.00 (58.74)	369.64 (64.72)
Peak $E_{rr,SA}$ (%)	32.32 (8.99)†	31.70 (9.81)†
TPK $E_{rr,SA}$ (ms)	355.27 (34.28)	349.73 (35.26)
Peak $E_{cc,SA}$ (%)	-18.22 (3.40)†	-18.02 (3.78)†
TPK $E_{cc,SA}$ (ms)	362.03 (45.56)	362.03 (61.84)

Results: Variability between CVI_{42} and proposed method.

The variation in peak strain estimation between the two methods was assessed using Bland-Altman analysis and Intraclass correlation coefficients (ICC) (see Fig. 7.11 and 7.12). The level of agreement was defined as in Schuster et al. (2015): excellent for $\text{ICC} > 0.74$, good for $\text{ICC} = 0.6-0.74$, fair for $\text{ICC} = 0.40-0.59$, and poor for $\text{ICC} < 0.4$. Results show excellent agreement between our method and CVI_{42} , with the lowest variation in peak $E_{ll,LA}$ and $E_{cc,SA}$, whereas a larger spread was observed for peak radial strain. The latter is in line with the larger intra and inter observer variability seen in radial strain assessment in previously published MR-FT literature (Claus et al., 2015).

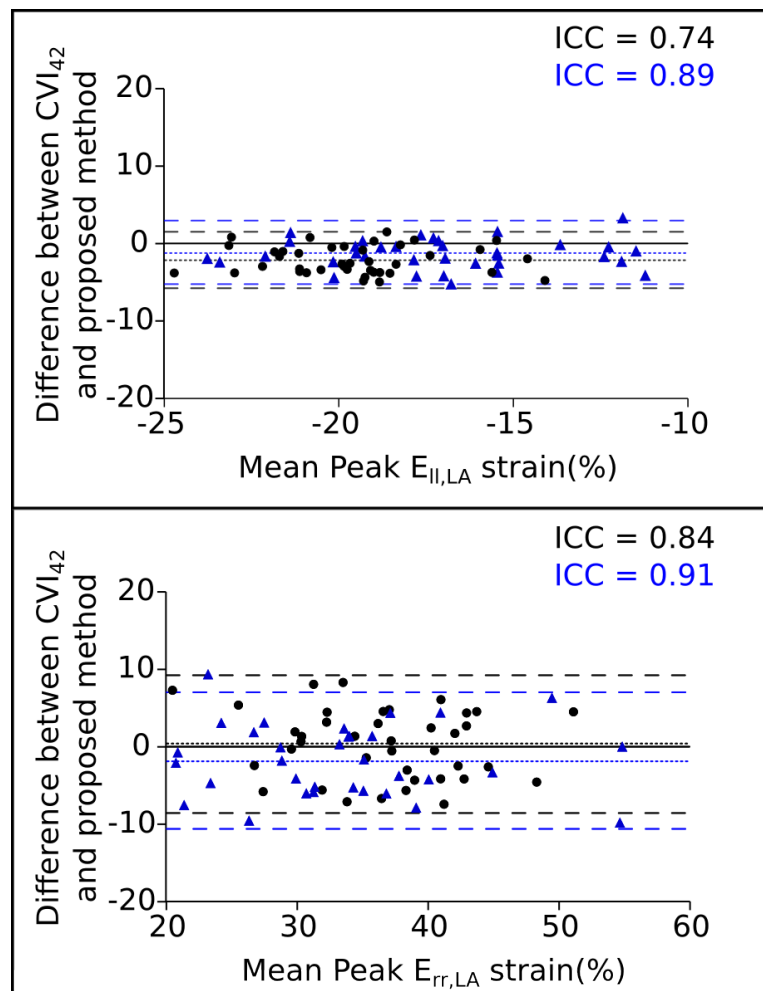


Figure 7.11: Bland Altman plots between CVI_{42} and the proposed pipeline for peak longitudinal and radial LA global strain (%). Healthy volunteers are shown as black circles and ischemic patients as blue triangles. Dotted lines correspond to the mean difference between methods, and dashed lines correspond to the limits of agreement (99% confidence).

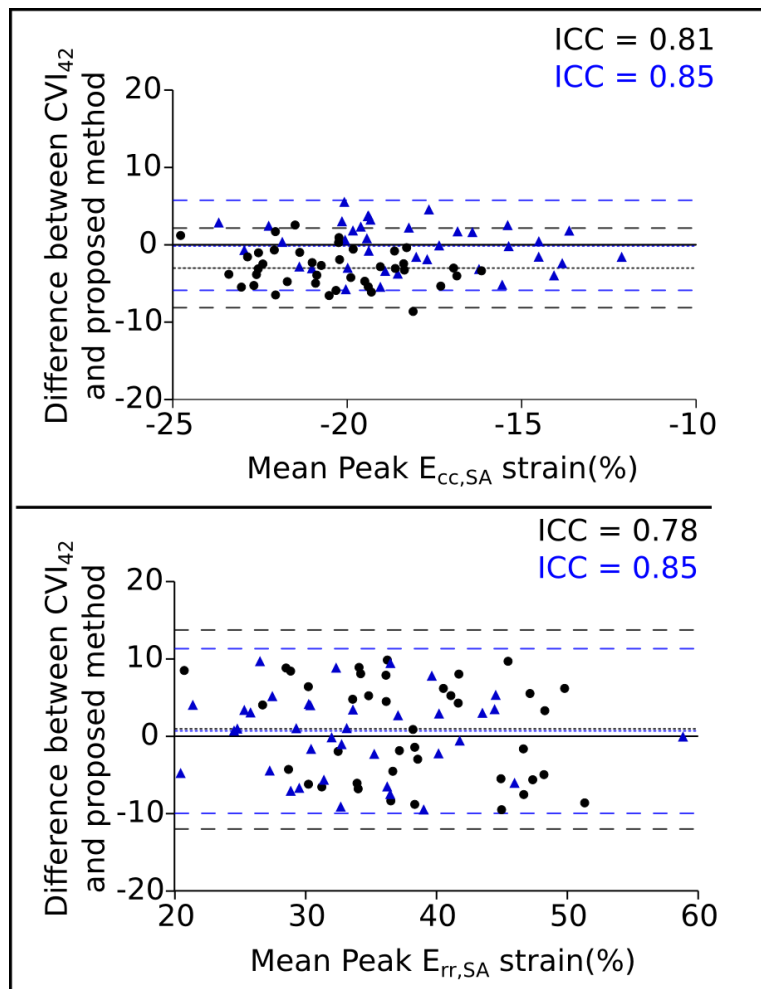


Figure 7.12: Bland Altman plots between CVI₄₂ and the proposed pipeline for peak radial and circumferential SA global strain (%). Healthy volunteers are shown as black circles and ischemic patients as blue triangles. Dotted lines correspond to the mean difference between methods, and dashed lines correspond to the limits of agreement (99% confidence).

Results show that the proposed method slightly underestimated peak longitudinal and circumferential strain compared to CVI₄₂, most likely reflecting minor differences in motion tracking algorithms. However, this underestimation was consistent throughout the range of strains observed in the study. In addition, although tools such as CVI₄₂ are widely used clinically, they cannot be considered as gold standards for strain quantification due to their intra and inter observer variability.

7.2.2 3D strain values

The previous sections aimed to validate the automatic pipeline proposed for 2D strain estimation from cine MR acquisitions. This section aims to validate the proposed pipeline to compute 3D strain values in 3D TAG and 3D US imaging data.

Materials

This part of the Chapter uses the multimodal database described in Section 4.1, which contains 19 patients with DCM and 50 healthy volunteers.

7.2.3 Experiments

The proposed 3D method computes strain for each node of the mesh. In this section we aim to validate the proposed method by computing peak global strain values and peak strain values by AHA region from both modalities (i.e. MR and US). To date, no commercially available software package is capable of computing 3D strain, therefore it is not possible to perform a comparative validation as in the 2D case.

Figure 7.13 shows an example of the three strains estimated using TAG data for a healthy volunteer and a DCM patient.

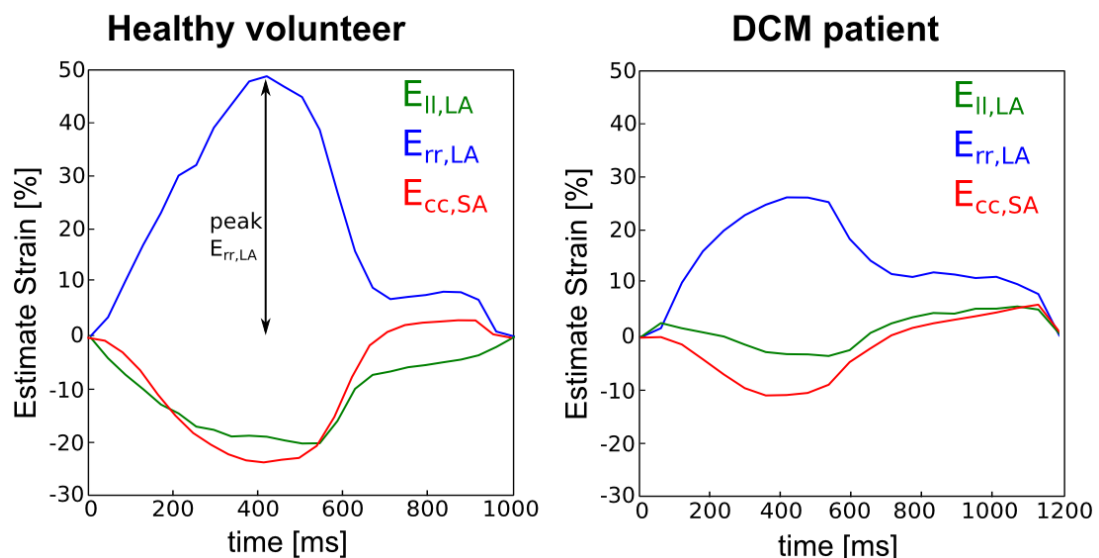


Figure 7.13: Examples of estimated strains for a healthy volunteer and a DCM patient. Figure shows global strain curves, and peak strain.

Figure 7.14 shows an example of the three strains estimated using 3D US data for a healthy volunteer and a DCM patient from TAG MR data.

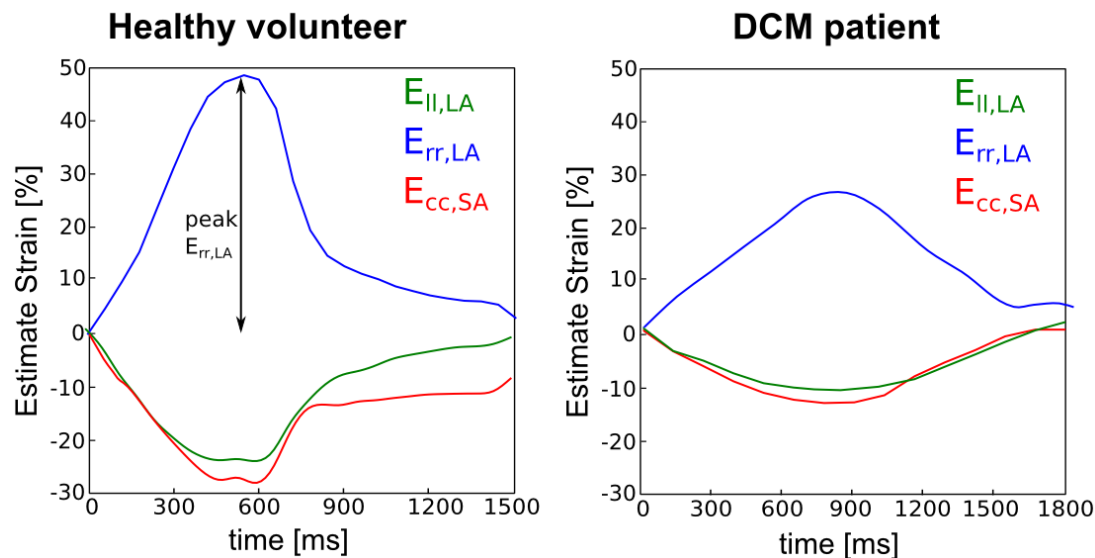


Figure 7.14: Examples of estimated strains for a healthy volunteer and a DCM patient from 3D US data. Figure shows global strain curves and peak strain.

Peak LV strain values for TAG and 3D US sequences were obtained using the proposed 3D strain estimation method. The peak strain values per AHA region were computed using the AHA regions derived from the mesh. Table 7.4 shows the average peak strain values of healthy volunteers and DCM patients using TAG and US data. Peak LV strain values between healthy volunteers and DCM patients were compared using an unpaired t -test (significant differences reported for p -value < 0.01 with Bonferroni's correction).

Table 7.4: Estimated strain values from TAG and 3D US data on the multimodal database. Daggers indicate statistically significant differences between healthy volunteers and DCM patients.

TAG strains		
	Healthy volunteers	DCM patients
Peak E_{ll} (%)	-18.85 (5.05)	-8.21 4.14) [†]
Peak E_{rr} (%)	33.79 (9.25)	10.40 (4.39) [†]
Peak E_{cc} (%)	-26.77 (7.69)	-10.85 (4.53) [†]

3DUS strains		
	Healthy volunteers	DCM patients
Peak E_{ll} (%)	-16.55 (5.19)	-7.44 (4.49) [†]
Peak E_{rr} (%)	34.69 (9.40)	10.56 (4.59) [†]
Peak E_{cc} (%)	-26.65 (7.83)	-9.97 (4.73) [†]

Furthermore, Tables 7.5, 7.6, 7.7 summarise longitudinal, radial and circumferential peak strain per AHA region, averaged over the volunteers and DCM patients for TAG and 3D US data.

The results in Table 7.4 show a statistically significant decrease in radial, longitudinal and circumferential strain between healthy volunteers and DCM patients, which is consistent with previous findings in the literature (Duan et al., 2012, Chuang et al., 2010). Furthermore, the results in Tables 7.5, 7.6, 7.7 show that the largest variations in strain values between groups are in radial strain for both modalities. A number of studies have reported reduced radial strain in DCM patients, and this could be explained by the reduced wall thickening due to the deteriorated contractile function (Duan et al., 2012, Chuang et al., 2010). Even though global strain measures provide a clear distinction between normals and patients for radial and circumferential strain, characterisation of regional strain distributions was more challenging, as there was no clear variation for specific regions, hindering the classification process. Overall the global and regional values show realistic values based on those reported in the clinical literature.

Table 7.5: Estimated longitudinal regional strain values from TAG and 3D US data on the multimodal database.

TAG strains			
		Healthy volunteers	DCM patients
Basal	Anterior	-13.68 (4.48)	-9.82 (4.83)
	Anteroseptal	-17.86 (4.23)	-6.78 (3.81)
	Inferoseptal	-14.22 (3.56)	-6.24 (3.02)
	Inferior	-17.41 (4.40)	-8.32 (3.87)
	Inferolateral	-15.67 (4.70)	-11.00 (4.35)
	Anterolateral	-15.72 (6.50)	-10.63 (4.44)
Mid	Anterior	-15.91 (5.76)	-7.36 (4.44)
	Anteroseptal	-18.03 (4.52)	-7.24 (3.72)
	Inferoseptal	-18.23 (3.71)	-7.81 (4.28)
	Inferior	-18.45 (4.44)	-7.28 (6.147)
	Inferolateral	-20.56 (6.37)	-6.77 (3.28)
	Anterolateral	-18.79 (4.71)	-6.67 (2.71)
Apical	Anterior	-24.84 (5.29)	-8.00 (3.71)
	Septal	-20.44 (6.44)	-10.70 (3.62)
	Inferior	-29.89 (6.132)	-9.03 (6.79)
	Lateral	-21.92 (5.48)	-7.69 (3.22)

3DUS strains			
		Healthy volunteers	DCM patients
Basal	Anterior	-13.80 (4.69)	-8.72 (5.23)
	Anteroseptal	-11.85 (4.68)	-6.66 (4.52)
	Inferoseptal	-16.14 (3.92)	-5.19 (3.96)
	Inferior	-14.53 (4.27)	-8.17 (3.90))
	Inferolateral	-12.52 (5.10)	-9.65 (5.45)
	Anterolateral	-13.44 (6.52)	-9.95 (4.51)
Mid	Anterior	-14.86 (5.67)	-6.77 (5.18)
	Anteroseptal	-15.68 (4.71)	-6.76 (4.00)
	Inferoseptal	-16.22 (3.71)	-6.73 (3.56)
	Inferior	-17.46 (4.89)	-6.50 (2.24)
	Inferolateral	-15.95 (6.55)	-6.40 (4.41)
	Anterolateral	-21.61 (4.87)	-5.37 (4.65)
Apical	Anterior	-17.06 (5.21)	-6.84 (5.53)
	Septal	-26.69 (6.83)	-10.27 (4.94)
	Inferior	-18.35 (6.27)	-8.23 (6.75)
	Lateral	-18.61 (5.51)	-6.79 (3.26)

Table 7.6: Estimated radial regional strain values from TAG and 3D US data on the multimodal database.

TAG strains			
		Healthy volunteers	DCM patients
Basal	Anterior	36.13 (7.05)	14.00 (5.33)
	Anteroseptal	36.02 (9.24)	9.63 (3.74)
	Inferoseptal	30.90 (6.76)	10.95 (4.87)
	Inferior	27.57 (8.44)	10.67 (4.73)
	Inferolateral	33.36 (9.68)	11.95 (4.96)
	Anterolateral	35.51 (8.11)	14.21 (5.25)
Mid	Anterior	44.58 (12.37)	9.59 (4.36)
	Anteroseptal	36.92 (10.33)	10.91 (3.75)
	Inferoseptal	34.81 (8.96)	10.28 (4.84)
	Inferior	30.38 (8.95)	9.92 (4.19)
	Inferolateral	38.03 (9.69)	9.92 (4.19)
	Anterolateral	44.57 (13.39)	8.53 (3.93)
Apical	Anterior	30.17 (9.86)	9.64 (4.32)
	Septal	28.31 (8.00)	8.94 (4.34)
	Inferior	25.61 (8.01)	10.08 (3.72)
	Lateral	27.80 (9.20)	7.15 (3.52)

3DUS strains			
		Healthy volunteers	DCM patients
Basal	Anterior	38.44 (6.88)	13.51 (5.46)
	Anteroseptal	31.28 (9.52)	9.77 (4.20)
	Inferoseptal	29.12 (7.53)	10.86 (5.22)
	Inferior	34.54 (8.73)	10.46 (4.65)
	Inferolateral	37.53 (9.77)	12.11 (5.12)
	Anterolateral	46.95 (7.97)	14.28 (5.57)
Mid	Anterior	40.40 (11.92)	9.47 (4.42)
	Anteroseptal	34.83 (10.31)	11.92 (4.07)
	Inferoseptal	30.51 (9.06)	10.23 (5.20)
	Inferior	36.87 (9.17)	10.68 (4.39)
	Inferolateral	47.02 (10.46)	9.85 (4.69)
	Anterolateral	30.11 (14.01)	8.47 (4.11)
Apical	Anterior	29.92 (9.54)	9.57 (4.31)
	Septal	27.94 (8.24)	9.82 (4.34)
	Inferior	28.61 (7.77)	10.50 (4.04)
	Lateral	31.15 (9.56)	7.35 (3.68)

Table 7.7: Estimated circumferential regional strain values from TAG and 3D US data on the multimodal database.

TAG strains			
		Healthy volunteers	DCM patients
Basal	Anterior	-20.87 (5.85)	-10.85 (3.31)
	Anteroseptal	-20.59 (6.75)	-8.91 (3.57)
	Inferoseptal	-26.14 (6.75)	-10.22 (4.53)
	Inferior	-25.24 (5.59)	-10.77 (3.54)
	Inferolateral	-26.60 (6.88)	-12.70 (5.66)
	Anterolateral	-21.23 (9.97)	-12.70 (5.66)
Mid	Anterior	-22.46 (8.74)	-9.95 (3.67)
	Anteroseptal	-22.79 (7.18)	-11.86 (5.05)
	Inferoseptal	-31.57 (7.84)	-11.96 (4.56)
	Inferior	-32.57 (4.96)	-10.96 (4.34)
	Inferolateral	-30.48 (5.59)	-11.17 (4.37)
	Anterolateral	-25.23 (7.85)	-10.04 (4.43)
Apical	Anterior	-27.53 (9.64)	-9.50 (4.95)
	Septal	-35.723 (12.29)	-10.57 (5.46)
	Inferior	-31.04 (10.49)	-10.96 (5.62)
	Lateral	-28.29 (8.47)	-10.44 (4.32)

3DUS strains			
		Healthy volunteers	DCM patients
Basal	Anterior	-18.12 (5.57)	-10.56 (3.72)
	Anteroseptal	-26.98 (4.80)	-7.14 (3.86)
	Inferoseptal	-24.63 (6.73)	-8.87 (4.77)
	Inferior	-25.15 (5.87)	-9.73 (3.50)
	Inferolateral	-21.24 (6.77)	-11.53 (5.73)
	Anterolateral	-22.74 (9.86)	-12.93 (5.58)
Mid	Anterior	-24.69 (8.60)	-9.13 (4.11)
	Anteroseptal	-31.07 (7.75)	-10.44 (5.17)
	Inferoseptal	-29.24 (8.86)	-11.34 (4.51)
	Inferior	-28.07 (5.06)	-9.66 (4.56)
	Inferolateral	-24.49 (5.52)	-10.80 (4.24)
	Anterolateral	-27.74 (7.65)	-9.33 (4.42)
Apical	Anterior	-36.01 (9.29)	-8.45 (5.17)
	Septal	-34.47 (12.88)	-9.59 (5.91)
	Inferior	-27.07 (11.23)	-10.88 (5.95)
	Lateral	-27.66 (9.08)	-9.42 (4.47)

7.2.4 Integration of 3D strain values with motion atlas

The previous section aimed to validate the 3D strains computed from TAG and US data. This section shows the results of integrating these strain values into the pipeline for forming the multimodal atlas. The first experiment aims to validate the atlas formation pipeline described in Section 5.2 by recomputing the embedding, reconstructed and reconstruction errors for the three dimensionality reduction algorithms proposed in Section 5.2.10. The second experiment aims to validate the use of strain values within the global and regional one-step multi-view classifiers proposed in Sections 6.2.2 and 6.2.3.

Multimodal atlas formation using strain values

This section evaluates the performances of the three proposed dimensionality reduction algorithms (PCA, CCA and PLS) for the purpose of atlas formation using 3D strain values.

Similar to Section 5.3.3, the mean embedding distances $E_d(MR - US)$, the mean reconstruction errors $E_D(MR - MR)$ and $E_D(US - US)$, and the mean prediction errors $E_D(MR - US)$ were computed using a leave-one-out cross validation (see Figure 7.15).

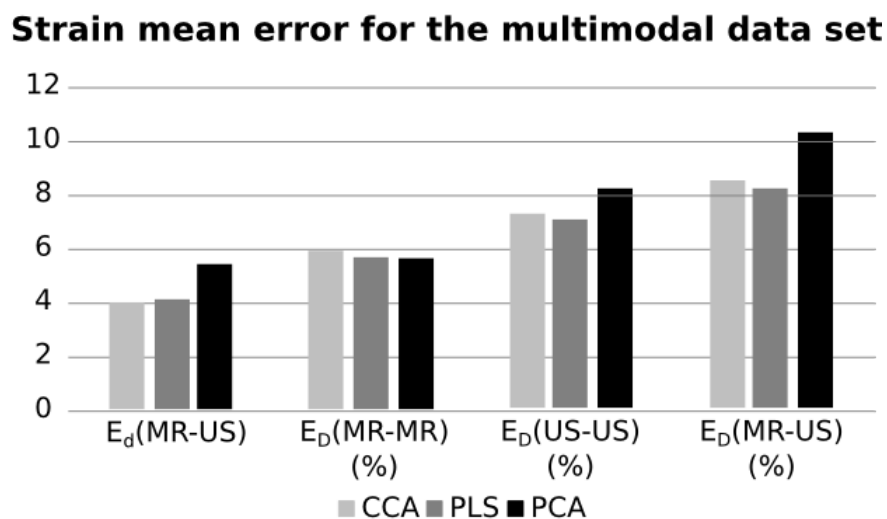


Figure 7.15: Mean errors for embedding distance ($E_d(MR - US)$), reconstruction error ($E_D(MR - MR)$ and $E_D(US - US)$) and prediction error ($E_D(MR - US)$) for the multimodal data set using estimated strain values.

The results follow the same trend as for displacements, showing that CCA and PLS have much lower errors than PCA for all measures apart from $E_D(MR - MR)$. Recall that in Section 5.3.3 for the MR data the three algorithms had similar errors, while for the US data PLS had the best results. Furthermore, $E_d(MR - US)$ has similar errors for the atlas formed using displacement and strain values. The reconstructed and prediction errors cannot be directly compared between strains and displacements as they have different units, but it is possible to observe similar patterns in both cases. In the strain case, the $E_D(US - US)$ is around 6% and the $E_D(MR - US)$ around 8%. Previously, it has been shown that the variability of strain values in a population can be about 10% (Yingchoncharoen et al., 2013), which is in the same range as these reconstructed and predicted errors.

Multi-view classification for strain values

This section compares the performances of the global and regional multi-view learning approaches proposed in Sections 6.2.2 and 6.2.3 to identify patients with DCM using strain values.

Similar to Sections 6.3.2 and 6.3.3 an 8-fold RSCV with 100 repetitions was used to compare the performances of the proposed multi-view approaches. In each fold to evaluate the performance of the classification algorithms the balanced accuracy as well as the sensitivity and the specificity were computed. Finally, the average accuracies, sensitivities and specificities as well as their standard deviations over all folds were computed.

Table 7.8 shows the results of the proposed regional approach compared to the global approach using the estimated US strain. A t -test was used to evaluate the statistical significance of the accuracy results between global and regional methods with a significance level of 0.01.

Table 7.8: US derived strain classification accuracy, sensitivity and specificity of global and regional approaches using the estimated strain values and *t*-test results. An asterisk indicates a statistically significant improvement in accuracy over the global approach.

Global Methods	BACC (%)	SEN (%)	SPE (%)
MLDA	80.33 (9.41)	80.25 (20.38)	81.60 (5.35)
MvLapSVM	88.90 (6.31)	88.26 (15.89)	85.17 (6.55)
Regional Methods	BACC (%)	SEN (%)	SPE (%)
MLDA	82.55 (7.24)*	81.13 (19.85)	83.50 (6.04)
MvLapSVM	91.02 (5.51)*	90.40 (16.51)	88.90 (5.61)

The results in Table 7.8 show that the use that the regional method outperforms the global method in both linear and non-linear cases, with both differences being statistically significant. Similar results were found using displacements in Table 6.3 where regional methods also had statistically significant improvement over global methods. In this case, results from Tables 6.3 and 7.8 can be directly compared as both measure classification performances. In general, the use of strain values slightly decreases the performances of both global and regional multi-view classifiers. More specifically, in the case of displacements the highest accuracy was 94.32% using MvLapSVM, while using strain values the accuracy was 91.02%. Furthermore, there is a significant decrease in specificity using strain values compared to displacements in the non-linear methods. Possible reasons for the lower performance using strain are discussed in Section 7.3.

Figure 7.16 shows the estimated weights for the weighted majority voting classifier for the linear and non-linear cases. These show that the basal segments and mid segments of the anterior wall are the areas with the highest impact for classification, which were also observed to be the more discriminative regions in DCM diseases in Chuang et al. (2010) and Duan et al. (2012). This pattern is similar to the one observed with displacements. However, for the strain values more basal segments contribute to the classification. In the literature it has been reported that for longitudinal strain the basal-septal region has a higher importance, for circumferential strain the basal-lateral region, and for radial strain the anterior lateral region (Duan et al., 2012).

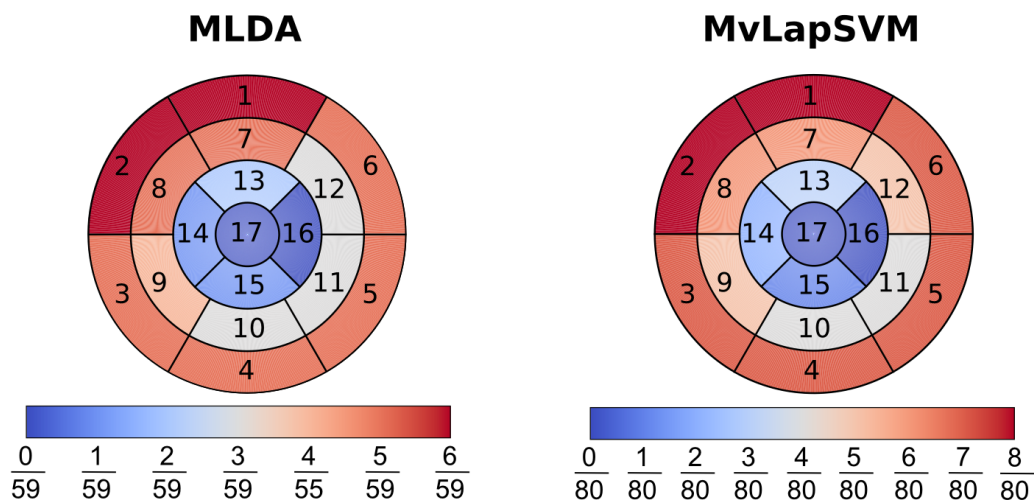


Figure 7.16: Weights for the majority voting scheme in the strain regional approach for classification. On the left estimated weights for MLDA, and on the right estimated weights for MvLapSVM using the randomised search on hyper parameters algorithm. The colour bar shows the ranges of values for the estimated weights.

The accuracy of the different classifiers using both MR and US data was also computed. Table 7.9 shows the results of the proposed regional algorithms using both modalities. The results show that only the linear method had a statistically significant increase using the regional method compared to the global method, which is consistent with the finding for displacements.

Table 7.9: MR and US derived strain classification accuracy, sensitivity and specificity of global and regional approaches and *t*-test results. An asterisk indicates a statistically significant improvement in accuracy over the global approach.

Global Methods	BACC (%)	SEN (%)	SPE (%)
MLDA	83.93 (7.15)	83.88 (20.18)	84.10 (5.48)
MvLapSVM	90.16 (5.64)	89.46 (18.53)	89.13 (5.39)
Regional Methods	BACC (%)	SEN (%)	SPE (%)
MLDA	86.19 (6.66)*	87.88 (16.50)	88.80 (4.22)
MvLapSVM	91.55 (4.70)*	90.67 (14.27)	89.63 (4.44)

The results in Table 7.9 when compared to Table 6.3 for displacements are slightly lower using only US or both modalities (i.e. MR and US), but in general they follow the same pattern. As for the displacement-based approach, the strain-based regional approach shows better accuracy with a statistically significant increase. The maximum accuracy is achieved using MvLSVM and it is around 91% using only US data and around 92% using MR and US data. These results suggest that the benefit of using both modalities using strain is lower compared to the displacement case.

7.3 Discussion and Conclusion

Automatic quantification of cardiac function has the potential to increase the accessibility of MWMA for assessment of cardiac diseases by eliminating time consuming manual post-processing steps and reducing inter- and intra-observer variation. This Chapter aimed to first present a fully automated pipeline for LV longitudinal, radial and circumferential strain estimation from routinely acquired 2D MR imaging. To the best of the author’s knowledge this is the first time that such a pipeline has been described. For validation, strain estimated using the automatic pipeline was compared with strain estimated using CVI₄₂, one of the two commercially available software packages for MR-FT, showing excellent agreement between them.

The last part of this Chapter aimed to extend the pipeline to estimation of strain values using 3D TAG and 3D US sequences. Furthermore, 3D TAG and US strain values were used to validate the proposed pipeline from Chapters 5 and 6 for atlas formation and identification of DCM patients. Results showed similar patterns using displacement and strain values. In general, there is a slight decrease in performance using strain values for the atlas formation and multi-view classification techniques. It is possible that this is caused by using the volumetric mesh instead of the medial surface mesh, or the generic motion tracking algorithm used to compute the deformations. As discussed in Section 5.2.6 the use of a medial surface reduces the noise and the errors in the segmentation and motion tracking steps. However, strain values are more widely understood clinically. In future work, strain can be computed more robustly using specific motion tracking algorithms for 3D US and TAG sequences, such as speckle tracking and HARP methods which might be less sensitive to noise.

To reduce the errors of the motion tracking algorithms another option for future work would be to develop a deep learning network to automatically segment US images and enforce the segmentation during the motion tracking.

In conclusion, this Chapter has presented a complete pipeline to compute strain from cine MR, TAG and US images, which are known to have additional beneficial value for improved disease classification and treatment stratification. In addition, the estimated TAG and US strain values were integrated into the previously developed pipeline to form and apply the multimodal cardiac motion atlas to identify DCM patients. This is potentially an important step for furthering the clinical acceptance of multimodal atlas based techniques into a clinical setting.

The next Chapter aims to apply the proposed automatic pipeline for 2D strain to a cohort of normal healthy Caucasian participants in the UK Biobank project, establishing reference values for LV function (i.e. volume and strain).

8 | MR reference ranges for cardiac function from a large population

Quantification of cardiac chamber sizes and function is the cornerstone of cardiac imaging, as it provides important prognostic information in patients with heart disease. Cardiac MR is nowadays considered the gold standard for the assessment of cardiac structure and function. Establishment of the range of reference values and associated variations of MR-derived size and function parameters is a prerequisite for its routine clinical use. Accurate automatic quantification of volumes and EFs is of critical importance since several therapeutic decisions are made on the basis of volumetric and EF measurements in different clinical scenarios. Similarly the definition of normal values of left ventricular global longitudinal strain (E_{ll}), global circumferential strain (E_{cc}), and global radial strain (E_{rr}) is of critical importance to the clinical application of this modality. This Chapter aims to establish normal reference range values for cardiac function on a large population using the automatic pipeline described in Chapter 7. Previously, some studies have reported normal reference volume ranges from US (Levy et al., 2017, Greupner et al., 2012), cine MR (Maceira et al., 2006, Alfakih et al., 2003), and strain reference values from 3D US (Yingchoncharoen et al., 2013, Kleijn et al., 2014) and MR (Taylor et al., 2015, Kawel-Boehm et al., 2015). However, all of these studies established the normal ranges on small databases of less than 300 subjects. The only study that used a large population for determining normal ventricular reference ranges was published recently by Petersen et al. (2017), but they only include volumetric parameters. Therefore, to the author's knowledge the values reported in this Chapter represent the first time that reference volumetric and strain values were computed for the same large-scale database, and this can provide a valuable reference standard in clinical practice for interpretation of disease states.

8.1 Methods

This section outlines the procedure used to compute the MR reference ranges for cardiac function, and can be divided into three parts: (1) Estimation of the volumetric parameters, which describes the pipeline used to compute the reference ranges for the volumetric parameters; (2) Estimation of strain parameter, which presents the automatic framework for qualifying myocardial strain from cine 2D MR sequences; (3) Quality control, which describes the proposed methods to ensure that the reference ranges are based only on subjects with high quality medical images.

Estimation of the volumetric parameters. The automatic segmentation network described in Section 7.1.1 was used to segment the LV blood pool, LV myocardium and RV over time. Based on these segmentations, the LV and RV volumes were computed using the modified Simpson’s rule (see Section 2.3.1 for more details) and used to generate the LV and RV curves.

Estimation of strain parameters. The automatic pipeline described in Chapter 7 was used to estimate the radial, longitudinal and circumferential strain from cine SA and LA images.

Quality control. To ensure that the reference ranges are based only on subjects with high quality medical images and correct volumetric and strain values, three quality control (QC) methods were implemented to automatically reject subjects with insufficient quality or incorrect segmentations, and these are described below:

- *QC1.* SA images with insufficient image quality were excluded using the pipeline described in Oksuz et al. (in press 2018). This approach used a 3D CNN network to automatically identify images with motion-related artefacts such as mistriggering, arrhythmia and breathing artefacts. Another problem that images might suffer from is wrong cardiac MR planning, which might lead to inaccurate quantification of cardiac function. Therefore, in addition, subjects with incorrectly planned 4Ch LA images were automatically excluded using the network described in Oksuz et al. (2018). This pipeline used a CNN to identify images containing the left ventricular outflow tract, which is a common feature of poorly planned 4Ch images.

Figure 8.1 shows examples of MR images that have been excluded from the analysis.

Incorrect SA: breathing artefacts

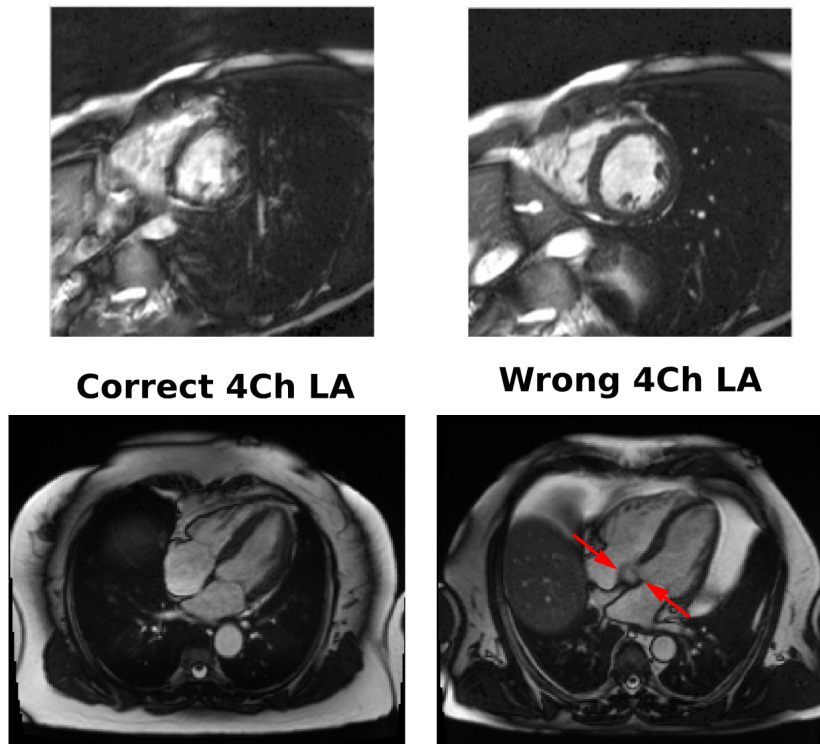


Figure 8.1: Example of images with insufficient quality (top: SA sequences with breathing artefacts, bottom: 4Ch LA with left ventricular outflow tract (red arrow)).

- *QC2.* Automatic identification of incorrect segmentation is essential to accurately compute volumetric metrics. Based on the LV and RV volumes curves, an automatic pipeline is used to identify curves with unrealistic properties, which is likely due to inaccurate segmentation. The LV and RV curves are divided into diastole and systole and treated independently to identify unrealistic LV and RV curves. On the systole part of the curve (see Figure 2.7 for an example of a LV volume curve), the downslope should be smooth and continuous and therefore the first derivative should only contain one peak. Cases with more than one peak are therefore excluded.

On the diastole part the curves are divided into the rapid inflow, diastasis, and atrial systole. On the rapid inflow the upslope should be smooth and continuous and therefore the first derivative should only contain one peak. Cases with more than one peak are therefore excluded. On the diastasis phase the curve should be flat and with no variation, the first and second derivative were used to exclude any cases with changes of volume higher than 10%. Finally, in the atrial systole phase the upslope should be smooth and continuous and therefore the first derivative should only contain one peak. Cases with more than one peak are therefore excluded. However, there are a few subjects where the diastasis phase is not visible due to the rapid filling of the LV and in these cases the PFR, AC and PAFR should be excluded as they could not be placed correctly on the LV volume curve. This step excluded all the LV and RV curves where the volumetric parameters cannot be computed with enough confidence which is likely to be caused by inaccurate segmentation. Figure 8.2 shows a few examples unrealistic LV curves, and 8.3 shows a few examples of correct and incorrect automatic segmentations.

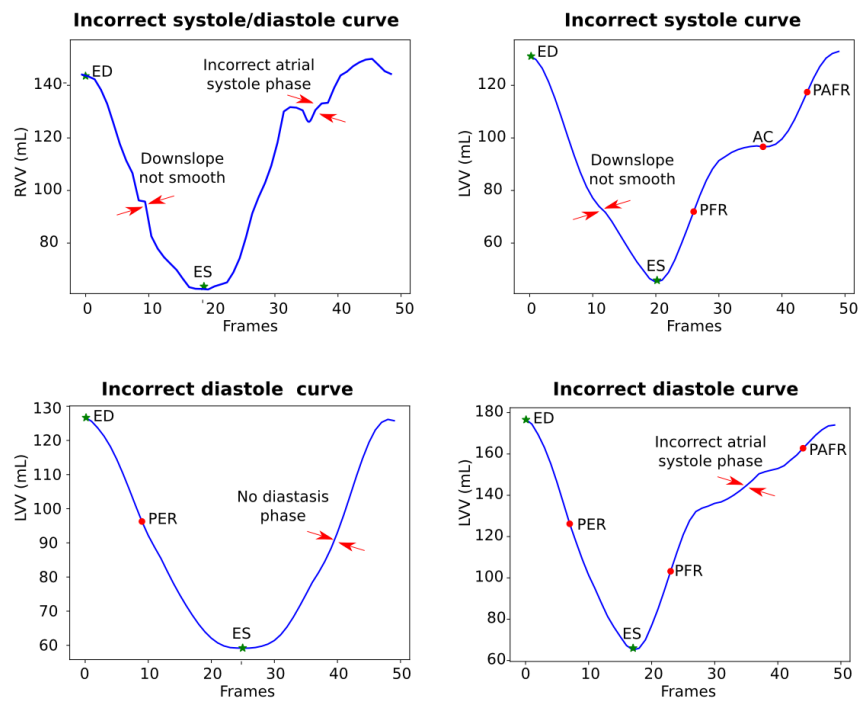


Figure 8.2: Examples of LV unrealistic curves excluded for the analysis. Top left: incorrect systolic and diastolic phase curve; top right: incorrect systolic phase curve; bottom left: LV curve with no diastasis phase; bottom right: LV curve with incorrect atrial systole phase.

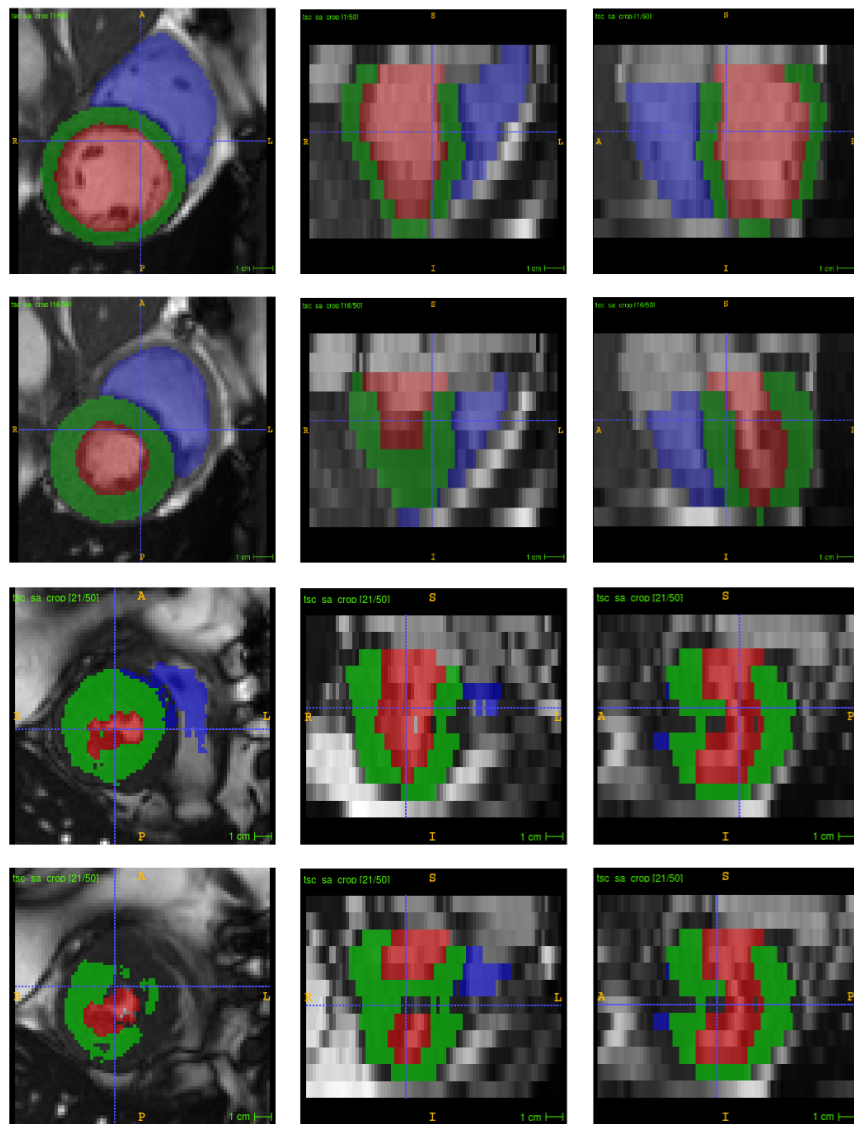


Figure 8.3: Examples of automatic segmentation. **Top two rows:** Correct segmentations at ED and ES. **Bottom two rows:** Incorrect segmentations over the cardiac cycle.

- *QC3.* The last quality control step aims to reject unrealistic strain curves. To this end a subset of 600 subjects was manually selected and classified as having either correct or incorrect strain curves for each of the strain components. A SVM classifier was then trained to perform the classification automatically based only on the strain curves. The total accuracy on the training set to detect incorrect strain curves is this way was around 80%, with a specificity and sensitivity of 80% and 80%. Figure 8.4 shows a few examples of unrealistic strain curves that are rejected by the classifier.

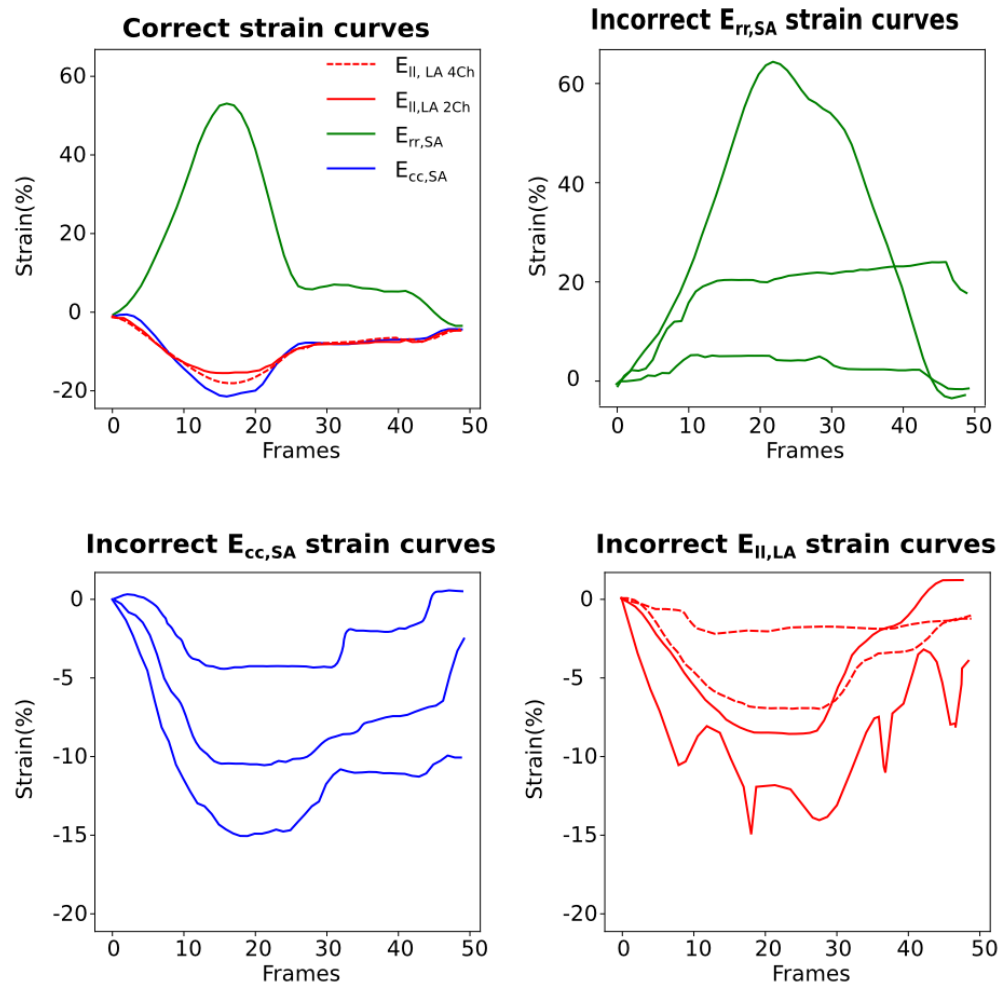


Figure 8.4: Example of realistic strain curves (top left). Examples of unrealistic strain curves excluded by the classifier. Top right: incorrect radial strain; bottom left: incorrect circumferential strain; bottom right: incorrect longitudinal strain.

8.2 Materials

Similar to Petersen et al. (2017) a healthy cohort of the UK Biobank was used to compute the reference ranges. From a total of 9619 MR examinations from the UK Biobank database, 24 subjects were excluded as the MR identifier did not match the participant ID. Of the remaining participants, those with non-Caucasian ethnicity, known cardiovascular disease, hypertension, respiratory disease, diabetes mellitus, hyperlipidaemia, haematological disease, renal disease, rheumatological disease, malignancy, symptoms of chest pain or dyspnoea, current- or ex-tobacco smokers, those taking medication for diabetes, hyperlipidaemia or hypertension and those with body mass index (BMI) $\geq 30 \text{ kg/m}^2$ were excluded from the analysis. Using these exclusion criteria 6982 patients were excluded (see Appendix A for a breakdown of the number of participants meeting individual exclusion criteria). Of the remaining 2613, 806 subjects were excluded due to insufficient image quality using the QC1 step. For the ventricular volume analysis 7 subjects were excluded due to incorrect automatic segmentations using the QC2 step. For the strain analysis, 64 subjects were rejected due to inaccurate motion tracking using the QC3 step. After QC2 and QC3 steps, 1800 subjects were included in the ventricular analysis and 1743 subjects in the strain analysis (see Figure 8.5 for more details.)

Demographics of the used cohort are displayed in Table 8.1, and details of this cohort of the UK Biobank can be found in Section 4.2.

Table 8.1: Baseline characteristics for the healthy cohort from the UK Biobank data set. All continuous values are reported in mean (SD), while categorical values are reported as number (percentage).

	Age groups (years)		
	45-54	55-64	65-74
Number of participants	617	720	470
Age (years)	50 (2)	59 (2)	67 (2)
Male gender (n(%))	313 (49.7%)	423 (43.3%)	353 (44.9%)
Systolic blood pressure (mmHg)	125 (11)	130 (14)	137 (15)
Diastolic blood pressure (mmHg)	76 (7)	77 (8)	79 (8)
HR (bpm)	66 (8)	67 (9)	70 (8)
Weight (kg)	72 (11)	70 (11)	69 (10)
Height (cm)	170 (9)	169 (12)	168 (9)
Body surface area (m^2)	1.84 (0.19)	1.81 (0.20)	1.80 (0.18)
Body mass area (kg/m^2)	24.7 (2.7)	24.59 (2.72)	24.73 (2.66)

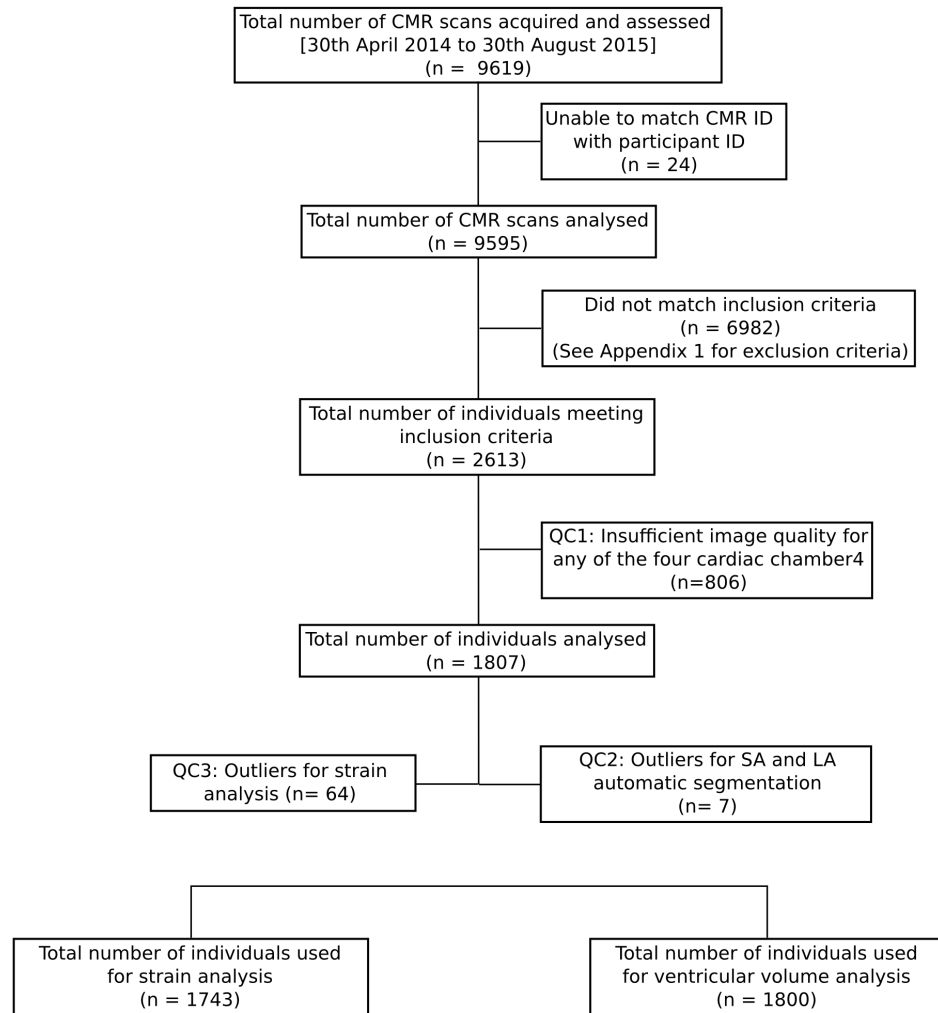


Figure 8.5: Case selection flowchart for ventricular and strain analysis.

8.3 Experiments

Two experiments were performed. The first experiment aimed to compute the normal ranges of ventricular global function. To this end, the automatic segmentations from the FCN network (see Section 7.1.1) were used to compute metrics of global ventricular function. In addition to the classical metrics such as volume and ejection fraction, this section also computed the LV filling and ejection rate (Bacharach et al., 1979), which are sensitive markers of myocardial function, especially in early disease (see Section 2.3.1 for more details of these parameters). The second experiment aimed to compute the normal ranges of strain values. In this case, the pipeline described in Section 7.1.1 was used to automatically estimate strain values from the healthy cohort of the UK Biobank.

For a better understanding of cardiac function over time, mean values for all cardiac parameters are presented by gender and decade (45–54, 55–64, 65–74). For both experiments results are presented in three tables:

1. *Mean and standard deviation table.* This table shows the mean and SD for the full healthy cohort, and also by gender.
2. *Traffic light table.* This table shows values in a traffic light format for the whole cohort regardless of their age group. In this case the normal ranges (highlighted in green) for the whole cohort (aged 45–74) were defined as the range where the measured value fell within the 99% confidence interval for the whole cohort regardless of age decade. The borderline zone (highlighted in yellow) was defined as the upper and lower ranges where the measured value lay outside the 99% confidence interval for at least one age group. The abnormal zone (highlighted in red) was defined as the upper and lower ranges where the measured values were outside the 99% prediction interval for all age groups.
3. *Age-specific table.* This table shows age-specific reference ranges for those measured values in the borderline (yellow) zone.

8.3.1 Results: Reference ranges for ventricular global function

The reference ranges for LV global function were computed for the following indicators: LVEDV, LVESV, LVSV, LVM, LVEF, LV mass to volume ratio, indexed LVEDV, indexed LVESV, indexed LVSV and indexed LVM, where indexed values are computed as volume values divided by body surface area (BSA), which is provided in the UK Biobank database. Furthermore, PER, PFR, AC and PFR were also computed (see Section 2.3.1 for more details of the used metrics). The reference ranges for RV global function were computed for the following indicators: RV end diastolic volume (RVEDV), RV end systolic volume (RVESV), RV stroke volume (RVSV), RV ejection fraction (RVEF), indexed RVEDV, indexed RVESV and indexed RVSV. For all of these metrics the automatic segmentation pipeline described in Section 7.1.1 was used, and the resulting segmentations were automatically processed to exclude failure cases (QC2).

Table 8.2 shows LV reference global function ranges as mean and SD for the full population and then by age for both absolute and indexed values in a numerical format. Tables 8.3 and 8.4 show LV global reference ranges in a traffic light format for the whole cohort regardless of their age group for men and women respectively. Tables 8.5 and 8.6 show age-specific reference ranges for those measured MR values in the borderline (yellow) zone. A Student's t-test (99% confidence) was used to compare the mean values of volumetric parameters between men and women.

Left Ventricle:

LVEDV and LVESV were significantly larger in males (LVEDV: absolute = 172 ± 28 ml, indexed = 88 ± 12 ml; LVESV: absolute = 65 ± 28 ml, indexed = 37 ± 7 ml) compared to females (LVEDV: absolute = 135 ± 18 ml, indexed = 78 ± 9 ml; LVESV: absolute = 47 ± 20 ml, indexed = 31 ± 5 ml) for both absolute and indexed values (see Table 8.2). In men, LVEDV, LVESV and LSVS were lower with older age for both absolute and indexed values (see Table 8.5). In women LVEDV, LVESV and LSVS volume were smaller with advancing age for absolute and indexed values (see Table 8.6). LVEF was significantly greater in females ($61 \pm 5\%$) compared to males ($58 \pm 5\%$). LVEF demonstrated no correlation with age in either males or females. LVM was significantly higher in males (104 ± 16 g) compared to females (73 ± 10 g). LVM to LVEDV ratio, a measure of distinct patterns of anatomical adaptations, increased significantly with age. PER, PFR, PARF and AC were all significantly higher in males (PER: 477 ± 77 (ml/s); PFR: 369 ± 94 (ml/s); PAFR: 261 ± 85 (ml/s); AC: 33 ± 10 (ml/s)) compared to females (PER: 375 ± 57 (ml/s); PFR: 337 ± 71 (ml/s); PAFR: 213 ± 75 (ml/s); AC: 26 ± 8 (ml/s)) (see Table 8.2). Furthermore, all decrease with age in both genders, but PER is less affected by ageing (see Tables 8.5 and 8.6). Finally, the computed LV volumes were in concordance with the volume values presented in Petersen et al. (2017).

Right Ventricle:

RVEDV and RVESV were significantly larger in males (RVEDV: absolute = 189 ± 32 ml, indexed = 96 ± 14 ml; RVESV: absolute = 84 ± 18 ml, indexed = 42 ± 8 ml) compared to females (RVEDV: absolute = 140 ± 20 ml, indexed = 83 ± 13 ml; RVESV: absolute = 57 ± 11 ml, indexed = 33 ± 6 ml) for both absolute and indexed values. Both RVEDV and RVESV were lower in older age groups in males and females for absolute and indexed values. RVEF was significantly higher in females (59 ± 5%) compared to males (56 ± 5%). Similar to the LV, the computed RV volumes were broadly in concordance with the volume values presented in [Petersen et al. \(2017\)](#) but in this case the difference is slightly bigger.

Ventricular parameters stratified by gender			
	All	Males	Females
Left Ventricle			
LVEDV (ml)	157 (30)	172 (28)	135 (18)
LVESV (ml)	58 (26)	65 (28)	47 (20)
LVSV (ml)	93 (18)	100 (18)	82 (13)
LVM (g)	93 (21)	104 (16)	73 (10)
indexed LVEDV (ml/m ²)	84 (12)	88 (13)	78 (9)
indexed LVESV (ml/m ²)	34 (7)	37 (7)	31 (5)
indexed LVSV (ml/m ²)	50 (8)	51 (9)	48 (7)
indexed LVM (g/m ²)	49 (8)	53 (7)	43 (5)
LVEF (%)	59 (5)	58 (5)	61 (5)
LVM to volume ratio (g/ml)	0.52 (0.20)	0.55 (0.20)	0.48 (0.18)
PER (ml/s)	437 (86)	477 (77)	375 (57)
PFR (ml/s)	355 (87)	369 (94)	337 (71)
PAFR (ml/s)	242 (84)	261 (85)	214 (75)
AC (ml)	31 (10)	33 (10)	26 (8)
Right Ventricle			
RVEDV (ml)	169 (36)	189 (32)	140 (20)
RVESV (ml)	73 (20)	84 (18)	57 (11)
RVSV (ml)	96 (19)	105 (18)	83 (13)
indexed RVEDV (ml/m ²)	90 (15)	96 (14)	81 (11)
indexed RVESV (ml/m ²)	39 (9)	42 (8)	33 (6)
indexed RVSV (ml/m ²)	51 (8)	54 (9)	48 (7)
RVEF (%)	57 (5)	56 (5)	59 (5)

Table 8.2: LV global function reference ranges and LV filling and ejection rate for the healthy population regardless of their age groups, and then by gender. SV stroke volume; indexed volume values where computed as volumes values divided by BSA; PER: peak ejection rate, PFR: peak filling rate, PAFC: peak atrial filling rate, AC: atrial contribution.

Ventricular reference range for Caucasian man			
	Abnormal low	Normal zone	Abnormal high
Left Ventricle			
LVEDV (ml)	<90	101 to 219	>229
LVESV (ml)	<36	38 to 99	>106
LVSV (ml)	<57	69 to 138	>147
LVM (g)	<49	49 to 94	>99
indexed LVEDV (ml/m ²)	<54	57 to 110	>113
indexed LVESV (ml/m ²)	<18	19 to 50	>53
indexed LVSV (ml/m ²)	<33	33 to 65	>67
indexed LVM (g/m ²)	<31	33 to 68	>69
LVEF (%)	<48	49 to 69	>71
LVM to volume ratio (g/ml)	<0.43	0.44 to 0.79	>0.82
PFR (ml/s)	<231	240 to 585	>607
PFR (ml/s)	<150	158 to 523	>537
PAFR (ml/s)	<61	67 to 378	>401
AC (ml)	<10	13 to 50	>51
Right Ventricle			
RVEDV (ml)	<95	120 to 242	>259
RVESV (ml)	<30	41 to 123	>133
RVSV (ml)	<55	59 to 130	>139
indexed RVEDV (ml/m ²)	<55	66 to 121	>125
indexed RVESV (ml/m ²)	<20	22 to 63	>69
indexed RVSV (ml/m ²)	<33	35 to 67	>69
RVEF (%)	<42	47 to 66	>68

Table 8.3: LV global function reference ranges in a traffic light format for Caucasian man. Abnormal low and high refer to the lower and upper reference limits, respectively. They are defined as measurements which lie outside the 99% prediction interval at all age groups. The borderline zone was defined as the upper and lower ranges where the measured value lay outside the 99% prediction interval for at least one age group.

Ventricular reference range for Caucasian woman			
	Abnormal low	Normal zone	Abnormal high
Left Ventricle			
LVEDV (ml)	<80	88 to 162	>185
LVESV (ml)	<30	30 to 71	>75
LVSV (ml)	<50	50 to 104	>117
LVM (g)	<49	49 to 94	>99
indexed LVEDV (ml/m ²)	<56	56 to 98	>110
indexed LVESV (ml/m ²)	<19	19 to 45	>53
indexed LVSV (ml/m ²)	<31	31 to 60	>65
indexed LVM (g/m ²)	<30	30 to 54	>57
LVEF (%)	<49	49 to 70	>71
LVM to volume ratio (g/ml)	<0.40	0.40 to 0.72	>0.78
PFR (ml/s)	<256	256 to 588	>601
PFR (ml/s)	<117	177 to 511	>529
PAFR (ml/s)	<72	72 to 407	>421
AC (ml)	<9	9 to 51	>51
Right Ventricle			
RVEDV (ml)	<86	86 to 169	>201
RVESV (ml)	<28	28 to 75	>99
RVSV (ml)	<50	50 to 107	>109
indexed RVEDV (ml/m ²)	<56	56 to 99	>113
indexed RVESV (ml/m ²)	<18	18 to 47	>57
indexed RVSV (ml/m ²)	<33	33 to 56	>63
RVEF (%)	<47	47 to 68	>69

Table 8.4: LV global function reference ranges in a traffic light format for Caucasian woman. Abnormal low and high refer to the lower and upper reference limits, respectively. They are defined as measurements which lie outside the 99% prediction interval at all age groups. The borderline zone was defined as the upper and lower ranges where the measured value lay outside the 99% prediction interval for at least one age group.

Age-specific ventricular ranges for Caucasian man									
	45-54			55-64			65-74		
	lower	mean	upper	lower	mean	upper	lower	mean	upper
Left Ventricle									
LVEDV (ml)	101	168	229	100	167	223	90	157	219
LVESV (ml)	38	73	106	38	75	101	36	66	99
LVSV (ml)	57	97	136	58	96	139	52	91	127
LVM (g)	69	107	147	67	103	139	57	96	140
indexed LVEDV (ml/m ²)	57	84	110	56	83	112	54	82	113
indexed LVESV (ml/m ²)	19	35	50	18	35	51	18	35	53
indexed LVSV (ml/m ²)	33	50	65	33	50	66	33	49	67
indexed LVM (g/m ²)	33	53	68	31	52	69	31	50	69
LVEF (%)	48	59	71	49	59	69	48	59	69
LVM to volume ratio (g/ml)	0.44	0.62	0.79	0.43	0.61	0.82	0.44	0.60	0.81
PER (ml/s)	240	424	607	236	413	599	231	403	585
PFR (ml/s)	150	343	537	157	338	528	158	331	523
PAFR (ml/s)	64	233	401	61	232	398	67	230	378
AC (ml)	13	31	51	12	30	50	10	29	51
Right Ventricle									
RVEDV (ml)	120	197	259	106	188	253	95	179	242
RVESV (ml)	41	88	133	40	83	123	30	83	127
RVSV (ml)	59	99	139	58	95	135	55	91	130
indexed RVEDV (ml/m ²)	66	96	125	56	91	122	55	90	121
indexed RVESV (ml/m ²)	22	44	69	20	41	66	20	40	63
indexed RVSV (ml/m ²)	35	51	67	34	50	69	33	49	68
RVEF (%)	42	54	66	47	57	68	46	56	68

Table 8.5: LV global reference function ranges for Caucasian man detailing mean, lower reference limit and upper reference limit by age group. Reference limits are derived by the upper and lower bounds of the 99% prediction interval for each parameter at each age group.

Age-specific ventricular ranges for Caucasian woman						
	45-54		55-64		65-74	
	lower	mean	upper	lower	mean	upper
Left Ventricle						
LVEDV (ml)	88	129	185	84	125	162
LVESV (ml)	30	53	75	27	46	73
LVSV (ml)	50	78	117	50	73	105
LVM (g)	47	75	99	49	71	94
indexed LVEDV (ml/m ²)	56	77	104	55	74	98
indexed LVESV (ml/m ²)	17	33	53	18	29	45
indexed LVSV (ml/m ²)	31	49	65	31	46	60
indexed LVM (g/m ²)	30	44	57	30	42	54
LVEF (%)	47	59	70	49	60	70
LVM to volume ratio (g/ml)	0.40	0.56	0.72	0.38	0.59	0.75
PER (ml/s)	247	424	601	256	422	588
PFR (ml/s)	177	344	511	177	345	513
PAFR (ml/s)	63	238	413	72	239	407
AC (ml)	9	30	51	9	30	51
Right Ventricle						
RVEDV (ml)	86	140	201	83	126	169
RVESV (ml)	28	64	99	27	54	75
RVSV (ml)	45	79	108	49	76	109
indexed RVEDV (ml/m ²)	56	81	113	53	76	106
indexed RVESV (ml/m ²)	18	38	57	18	34	51
indexed RVSV (ml/m ²)	33	48	63	33	46	56
RVEF (%)	46	57	68	47	58	68

Table 8.6: LV global reference function ranges for Caucasian woman detailing mean, lower reference limit and upper reference limit by age group. Reference limits are derived by the upper and lower bounds of the 99% prediction interval for each parameter at each age group.

8.3.2 Results: Reference ranges for strain values

Similar to the previous section, Table 8.7 shows LV longitudinal, radial and circumferential strain reference ranges as mean and SD for the full population, by gender and then by age in a numerical format. Tables 8.8 and 8.9 show LV strain ranges in a traffic light format for the whole cohort regardless of their age groups for men and women respectively. Finally, Tables 8.10 and 8.11 show age-specific reference ranges for men and women respectively for those measured values in the borderline (yellow) zone. A Student's t-test (99% confidence) was used to compare the mean values of volumetric parameters between men and women.

The reference ranges for LV local function were computed for the following indicators: Peak and TPK longitudinal, radial and circumferential strain. For all of these metrics the automatic strain pipeline in Section 7.1.1 was used, and the outputs were automatically processed to exclude failure cases using the QC3 step.

Peak $E_{rr,SA}$ was significantly higher in females ($46.25 \pm 9.7\%$) compared to males ($43.10 \pm 8.8\%$), while peak $E_{ll,LA\ 2CH}$ and $E_{cc,SA}$ were significantly higher in males ($E_{ll,LA\ 2CH}: -15.54 \pm 5.1$; $E_{cc,SA}: -14.9 \pm 5.2\%$) compared to females ($E_{ll,LA\ 2CH}: -17.27 \pm 5.7$; $E_{cc,SA}: -17.81 \pm 5.8\%$). Finally, Peak $E_{cc,SA}$ did not show any correlation with gender (see Table 8.7).

Peak $E_{rr,SA}$ and $E_{cc,SA}$ demonstrates a slight positive correlation with age for both males and females. Peak $E_{ll,LA\ 2CH}$ and $E_{ll,LA\ 4CH}$ demonstrate no correlation with age in either males or females. Peak $E_{rr,SA}$ shows a slight decrease in abnormal high values in females compared to males, while abnormal low values are similar for both groups. Finally, the computed LV strain values were in concordance with strain values presented in Schuster et al. (2015), which were captured using CVI₄₂ from cine MR.

	Strain parameters stratified by gender		
	All	Males	Females
Left Ventricle			
Peak $E_{ll,LA\,2CH}$ (%)	-16.22 (5.4)	-15.54 (5.1)	-17.27 (5.7)
TPK $E_{ll,LA\,2CH}$ (ms)	366.89 (41.0)	358.55 (41.2)	379.64 (35.5)
Peak $E_{ll,LA\,4CH}$ (%)	-16.37 (5.5)	-14.93 (5.2)	-17.81 (5.8)
TPK $E_{ll,LA\,4CH}$ (ms)	361.62 (42.0)	351.87 (40.4)	378.62 (37.4)
Peak $E_{rr,SA}$ (%)	44.24 (9.3)	43.10 (8.8)	46.25 (9.7)
TPK $E_{rr,SA}$ (ms)	341.17 (32.2)	332.94 (30.1)	354.72 (29.6)
Peak $E_{cc,SA}$ (%)	-20.13 (2.8)	-19.80 (2.6)	-20.61 (2.8)
TPK $E_{cc,SA}$ (ms)	347.08 (33.9)	341.13 (34.3)	356.11 (31.8)

Table 8.7: LV strain reference ranges for the healthy population regardless of their age groups, and then by gender.

Strain reference range for Caucasian man		
	Abnormal low	Normal zone
Left Ventricle		Abnormal high
Peak $E_{l,LA\ 2CH}$ (%)	< -5.30	> -26.94
TPK $E_{l,LA\ 2CH}$ (ms)	< 282.56	> 452.72
Peak $E_{l,LA\ 4CH}$ (%)	< -4.19	> -26.36
TPK $E_{l,LA\ 4CH}$ (ms)	< 279.41	> 449.20
Peak $E_{rr,SA}$ (%)	< 24.57	> 76.80
TPK $E_{rr,SA}$ (ms)	< 275.84	> 401.92
Peak $E_{cc,SA}$ (%)	< -14.67	> -25.78
TPK $E_{cc,SA}$ (ms)	< 281.61	> 412.86

Table 8.8: LV strain reference ranges for Caucasian man in a traffic light format. Abnormal low and high refer to the lower and upper reference limits, respectively. They are defined as measurements which lie outside the 99% prediction interval at all age groups. The borderline zone was defined as the upper and lower ranges where the measured value lay outside the 99% prediction interval for at least one age group.

Strain reference range for Caucasian woman		
	Abnormal low	
Left Ventricle	Abnormal high	
Peak $E_{ll,LA\;2CH}(\%)$	< -5.55 < 283.41 < -4.23 < 281.46 < 22.21 < 275.81 < -13.98 < 278.51	-6.34 to -26.93 299.89 to 446.16 -5.23 to -25.77 287.53 to 444.7 25.34 to 65.78 286.05 to 402.98 -14.73 to -25.47 290.58 to 408.48
TPK $E_{ll,LA\;2CH}(\text{ms})$		
Peak $E_{ll,LA\;4CH}(\%)$		
TPK $E_{ll,LA\;4CH}(\text{ms})$		
Peak $E_{rr,SA}(\%)$		
TPK $E_{rr,SA}(\text{ms})$		
Peak $E_{cc,SA}(\%)$		
TPK $E_{cc,SA}(\text{ms})$		

Table 8.9: LV strain reference ranges for Caucasian woman in a traffic light format. Abnormal low and high refer to the lower and upper reference limits, respectively. They are defined as measurements which lie outside the 99% prediction interval at all age groups. The borderline zone was defined as the upper and lower ranges where the measured value lay outside the 99% prediction interval for at least one age group.

Age-specific strain ranges for Caucasian man						
Left Ventricle	45-54			55-64		
	lower	mean	upper	lower	mean	upper
Peak $E_{l,LA\ 2CH}$ (%)	-5.65	-16.21	-26.77	-5.30	-16.12	-26.94
TPK $E_{l,LA\ 2CH}$ (ms)	283.17	364.72	446.28	283.95	366.22	448.50
Peak $E_{l,LA\ 4CH}$ (%)	-4.19	-15.27	-26.35	-4.75	-15.56	-26.36
TPK $E_{l,LA\ 4CH}$ (ms)	279.41	361.26	443.11	282.83	365.11	447.38
Peak $E_{rr,SA}$ (%)	27.05	46.27	75.49	25.90	46.37	76.80
TPK $E_{rr,SA}$ (ms)	277.79	338.16	398.54	278.94	340.20	401.47
Peak $E_{cc,SA}$ (%)	-14.88	-20.17	-25.49	-14.67	-20.19	-25.70
TPK $E_{cc,SA}$ (ms)	283.00	345.14	407.28	282.15	347.33	412.52

Table 8.10: LV strain reference ranges for Caucasian man detailing mean, lower reference limit and upper reference limit by age group. Reference limits are derived by the upper and lower bounds of the 99% prediction interval for each parameter at each age group.

Age-specific strain ranges for Caucasian woman						
Left Ventricle	45-54			55-64		
	lower	mean	upper	lower	mean	upper
Peak $E_{l,LA\ 2CH}$ (%)	-6.02	-16.53	-27.04	-6.34	-16.63	-26.93
TPK $E_{l,LA\ 2CH}$ (ms)	288.32	369.76	451.20	283.41	367.89	452.38
Peak $E_{l,LA\ 4CH}$ (%)	-4.91	-15.44	-25.97	-4.23	-15.00	-25.77
TPK $E_{l,LA\ 4CH}$ (ms)	287.53	371.42	455.31	281.46	365.97	450.48
Peak $E_{rr,SA}$ (%)	22.21	45.23	68.25	25.34	45.56	65.78
TPK $E_{rr,SA}$ (ms)	275.81	344.23	412.65	275.88	339.55	403.22
Peak $E_{cc,SA}$ (%)	-13.98	-20.08	-26.18	-14.33	-20.14	-25.94
TPK $E_{cc,SA}$ (ms)	280.43	351.49	422.56	278.51	349.22	419.94

Table 8.11: LV strain reference ranges for Caucasian woman detailing mean, lower reference limit and upper reference limit by age group. Reference limits are derived by the upper and lower bounds of the 99% prediction interval for each parameter at each age group.

8.4 Discussion and Conclusion

Cardiac MR enables quantification of various functional and morphological parameters of the cardiovascular system. This Chapter has established age- and gender-specific MR reference ranges for ventricular volumes and strain values derived from a cohort of 1807 Caucasian healthy adults aged 45–74. More specifically, any subject with pathophysiological or environmental risk factors affecting cardiac structure or function have been rejected. Whilst determination of reference ranges for MR has been performed by several previous studies, this work is novel for a number of reasons. First, both ventricular volumes and strain values were computed automatically, which allows them to be used in the clinic routinely. Second, this is the first time that such a large cohort has been used to determine at the same time volume and strain values. To date, all studies have focused on one type of clinical parameter. Third, reference ranges for MR functional parameters are detailed by gender and age decade, providing increased granularity and clinical utility. Fourth, compared to previous studies, other volumetric parameters such as PER, PFR, PAFR and AC were reported, which can help to interpret disease states. For example, in patients with heart failure with preserved ejection fraction (HFpEF), classic measures such as LVEDV, LVESV and LVEF are often normal, and therefore can not be used as indicators for diagnosis. For this group of patients, PFR, PAFR and AC are important biomarkers as they can detect diastolic dysfunction (incomplete myocardial relaxation, impaired rate of ventricular filling, increased left atrial pressure in filling, increased passive stiffness and decreased distensibility of the ventricle) (Su et al., 2014). Lastly, an automatic quality control pipeline is proposed to ensure that the computed volume and strain values were correct.

For the ventricular volume analysis, results show that men have greater volume and mass compared to females in both left and right ventricles, which is consistent with previous findings (Kawel-Boehm et al., 2015, Petersen et al., 2017). Furthermore, results show that there is a correlation between decreased LVEDV /LVESV and ageing. For strain values, results show that there is a significant difference in radial and circumferential strain between men and women. However, the results do not show any correlation between strains and ageing. Different studies have showed that peak strain is preserved with age, but that the TPK strain was significantly decreased with ageing (Oxenham et al., 2003, Kaku et al., 2014).

Limitations of this study include the fact that all of the acquisitions were performed using the same MR protocol with a 1.5 Tesla scanner (MAGNETOM Aera, Syngo Platform VD13A, Siemens Healthcare, Erlangen, Germany), and that the reference intervals described were derived from a population of 45–74 year olds of Caucasian ethnicity. Comparing the reference range values to another modality, protocol or cohort might lead to slightly different results and therefore may not be generalisable.

The normal reference ranges reported in this Chapter represent an invaluable resource in the analysis of MR examinations in both clinical and research settings for interpretation of disease states. To the author's knowledge this is the first time that reference values for global and strain values have been reported from the same large population.

In the next Chapter, a summary of the methods and the findings presented in this thesis is provided, along with a discussion of clinical applications of the proposed techniques and future directions. Finally, some conclusions are drawn about contributions brought by this thesis and its possible clinical impact.

9 | Conclusion

This chapter contains the final discussion and conclusions. A summary of the novel contributions introduced in this thesis is presented in Section 9.1. Section 9.2 discusses the potential clinical impact of this work, and Section 9.3 analyses the current limitations of the proposed methods, and presents possible future directions to address these limitations. Finally, some overall conclusions are drawn in Section 9.4.

9.1 Summary

In clinical practice, several non-invasive imaging techniques are available to visualise cardiac function, and to identify patterns related to healthy motion or particular pathologies. Each modality offers the possibility to observe the heart's motion from a distinct perspective, sometimes unique, sometimes complementary to other related imaging techniques. For this reason, multi-modality data fusion has become an active research topic over recent years for detecting cardiovascular diseases.

The primary aim of the work presented in this thesis was the development of a multimodal cardiac motion atlas from MR and US data, and its application to detecting patients suffering from DCM. The proposed pipeline takes measurements from US data, estimates MWMA parameters and relates them to a pre-trained statistical atlas, which has learnt the most relevant motion patterns for pathology prediction. The multimodal atlas has also encoded the relationship between MR and US data, treating the MR exam as a hidden variable in the prediction process. Therefore, a new subject can be mapped into the atlas using only US, and as output the pipeline identifies the subject as healthy or DCM.

The first contribution of this thesis was the development of the multimodal cardiac motion atlas from MR and US data. This was built using multi-view dimensionality reduction algorithms, and represents the first attempt to build such a multimodal cardiac atlas.

The second major contribution of this thesis was the application of the multimodal cardiac motion atlas to the task of identifying DCM patients. This required the development of novel global and regional approaches using multi-view classification techniques.

Finally, the third major contribution is the automatic pipeline for estimation of strain values and the extension of the multimodal atlas to include strain values for the identification of DCM patients. This represented the first fully automatic pipeline for myocardial strain estimation, and also enabled the reporting, for the first time, of reference values for strain-based indicators from a large scale database.

9.2 Clinical impact

The potential impact of the proposed methods in terms of clinical applications can be summarised as follows:

- The proposed multimodal cardiac motion atlas allows clinicians to correctly align MR and US data from the same subject, perform motion tracking independently for each modality and extract displacements or strains from the data. Furthermore, it allows more robust estimation of global indicators of cardiac function using only US data.

- Chapter 6 proposed a novel extension to the multimodal atlas to enable the identification of DCM patients using only US data but at the same time taking advantage of the implicit relationship between MR and US learned from the atlas. This application could be particularly interesting in clinics where MR is not available, and the learned relationships between modalities can be used to enhance automated decision support systems in cardiology. In principle, this pipeline could be embedded into the US scanner to provide real-time information to the sonographer during acquisition.
- Myocardial strain provides an independent quantitative evaluation of myocardial wall motion, and has been shown to enable earlier and more sensitive detection of myocardial diseases compared to global measures of cardiac function. Chapter 7 proposed an extension of the atlas pipeline to integrate the estimated strain values into the identification of DCM patients. This enables the use of atlas based techniques on widely understood clinical parameters such as strain.
- Chapter 8 provided normal reference ranges for ventricular volumes and strains from a large healthy cohort of Caucasian adults, which is an invaluable resource in the analysis of MR examinations in both clinical and research settings. MR measurements can provide useful information for assessment of cardiac structure and function. The provided reference ranges permit differentiation between normal and pathological states. However, to be meaningful these reference ranges need to be correctly stratified by age and gender. It is known that CVD predominantly affects individuals in middle- and old-age, and it is this group of subject that most of the UK Biobank MR examinations were acquired from. As shown in this thesis, ventricular structure and function do not remain static over time and undergo changes with age, even in those without evidence of cardiovascular disease. It is in this context, that it is our belief that the volumetric and strain reference values for men and women at three different age groups: 45–54, 55–64 and 65–74 may prove invaluable in the determination of pathological states in CVD.

9.3 Current Limitations and Future Directions

This section analyses the main limitations and assumptions that affect the proposed methods. For each limitation, possible solutions that could represent future investigations are discussed and presented.

Motion descriptors. This thesis used displacements and strains as motion descriptors. However, these features can be sensitive to noise and motion tracking errors. A possible alternative to such ‘hand-crafted’ features would be to extract the features automatically using ML techniques, specifically deep learning.

Shape analysis. This thesis focused on the use of spatiotemporal atlases for the statistical analysis of normal and pathological cardiac motion. However, cardiac morphology also plays an important role in the stratification and detection of CVD. One area for future work would be to integrate shape information into the pipeline to have a more robust assessment of cardiac health.

Non-imaging data. In clinical records there are a wide range of data that are likely to be useful in forming biomarkers for different clinical problems. Therefore, the combination of motion and non-motion data could be used to assist clinicians in making decisions and planning treatments. In the future, the current pipeline could be extended to also include non-imaging data, treating it as a third view of the problem.

Feature fusion. All of the proposed algorithms first extract independently features from MR and US (i.e. displacements and strain) and combine them as a last step. This approach has the advantage of extracting modality independent features that might be useful for detecting abnormal motion patterns. However, during the feature extraction process there might be some inaccuracies such as in segmentation and motion tracking that might affect this fusion of the features. A possible solution to overcome this limitation would be an earlier integration within the pipeline such as joint segmentation and motion tracking approaches (Liu et al., 2017).

Multi-view machine learning. All of the proposed multi-view ML techniques concatenated the spatial and temporal information of the data and they are not designed specifically for imaging data. A possible extension of the proposed pipeline would be to extend or find new multi-view algorithms that take as input for each subject a matrix where one direction would correspond to the spatial information and the other one the temporal information. This scheme would be able to exploit the inherent spatiotemporal relationships of the data (Akhter et al., 2012).

MR synthesis. The work in this thesis could be extended to generate a synthetic MR image from the US images. To this end, multi-view machine learning algorithms could be used to estimate the synthetic MR image from the 3D US sequence. This extension would have the advantage of reducing some of the limitations of 3D US such as limited FoV, low SNR, but it would benefit from the portability and real time features that 3D US has compared to MR. Furthermore, as shown during this thesis and in previous publications, MR and US have significant differences in shape and function, and this proposed future work could help in reducing these limitations as their differences would be learned and then compensated for.

Deep learning. The full pipeline for multimodal dynamic image analysis could be improved by using the latest deep learning techniques. The current pipeline is based on the use of motion parameters such as displacements and strains extracted using motion tracking algorithms, which can be viewed as ‘hand-crafted’ features extracted from the imaging data, and the estimation of these features has associated errors. Therefore, one possibility would be to replace this part of the pipeline by deep learning based registration techniques, such as ConvNet with multi-resolution input (Jain et al., 2014). However, it would also be possible to replace the hand-crafted motion-based descriptors by descriptors learned directly from the images using deep learning architectures. Also, the proposed multi-view machine learning algorithms could be replaced with multi-view deep learning algorithms that have been recently proposed such as deep CCA (Andrew et al., 2013), or multi-channel CNN detection networks for the classification of healthy volunteers and DCM patients (Wang et al., 2015). This possibility is intriguing because deep learning networks can offer the possibility of combining the atlas formation and classification steps into a single model.

9.4 Conclusions

This thesis has explored the potential of MvML and motion atlases for overcoming the problem of accurate assessment of cardiac function using MR and US data. A number of related works have used statistical atlases to analyse cardiac motion, allowing for more spatially and temporally localised cardiac deformation features. However, to date all of these atlases have been built using only one modality. In this thesis, a number of MvML algorithms have been proposed to combine the motion information of both modalities to enable robust and accurate assessment of cardiac function using only US data. The promising results reported in this work might stimulate the interest of clinicians, researchers and companies to further validate the use of multi-modality data for more accurate diagnosis and follow-up of cardiac disease.

A | Exclusion criteria for UK Biobank

Table A.1: Exclusion criteria

	Number (%)
Age	
> 74	150 (1.6%)
Medical conditions	
Hypertension	2705 (28.2%)
High cholesterol	1740 (18.1%)
Asthma	1287 (13.4%)
Hypothyroidism / myxoedema	587 (6.1%)
Essential hypertension	431 (4.5%)
Diabetes	406 (4.2%)
Angina	251 (2.6%)
Heart attack/myocardial infarction	203 (2.1%)
Type 2 diabetes	186 (1.9%)
Atrial fibrillation	151 (1.6%)
Miscarriage	151 (1.6%)
Iron deficiency anaemia	148 (1.5%)
Stroke	130 (1.4%)
Emphysema/chronic bronchitis	126 (1.3%)
Hyperthyroidism/thyrotoxicosis	92 (1.0%)
Heart valve problem/heart murmur	91 (0.9%)
Transient ischaemic attack (TIA)	91 (0.9%)
Irregular heart beat	84 (0.9%)
Chronic obstructive airways disease/COPD	80 (0.8%)
Pulmonary embolism +/- DVT	70 (0.7%)
Ulcerative colitis	68 (0.7%)
Gestational hypertension/pre-eclampsia	65 (0.7%)
Heart arrhythmia	63 (0.7%)
Sleep apnoea	54 (0.6%)
Polymyalgia rheumatica	53 (0.6%)
Diabetic eye disease	44 (0.5%)
Doctor diagnosed bronchiectasis	43 (0.4%)
Heart/cardiac problem	39 (0.4%)

Table A.1: *Exclusion criteria (Continued)*

Anaemia	38 (0.4%)
Bronchiectasis	36 (0.4%)
Pernicious anaemia	34 (0.4%)
Rheumatic fever	33 (0.3%)
Ankylosing spondylitis	29 (0.3%)
Sarcoidosis	27 (0.3%)
Crohns disease	24 (0.3%)
Peripheral vascular disease	23 (0.2%)
SVT / supraventricular tachycardia	23 (0.2%)
Gestational diabetes only Yes	22 (0.2%)
Sjogren's syndrome/sicca syndrome	20 (0.2%)
Type 1 diabetes	18 (0.2%)
Low platelets/platelet disorder	17 (0.2%)
Clotting disorder/excessive bleeding	15 (0.2%)
Other respiratory problems	15 (0.2%)
Retinal artery/vein occlusion	15 (0.2%)
Systemic lupus erythematosis/SLE	13 (0.1%)
Haemochromatosis	12 (0.1%)
Renal failure not requiring dialysis	12 (0.1%)
Gestational diabetes	11 (0.1%)
Pericarditis	11 (0.1%)
Atrial flutter	11 (0.1%)
Glomerulonephritis	11 (0.1%)
Renal/kidney failure	10 (0.1%)
Grave's disease	10 (0.1%)
Nephritis	9 (0.1%)
Mitral regurgitation/incompetence	9 (0.1%)
Anorexia/bulimia/other eating disorder	9 (0.1%)
Heart failure/pulmonary edema	8 (0.1%)
Connective tissue disorder	8 (0.1%)
Hereditary/genetic haematological disorder	7 (0.1%)
Adrenocortical insufficiency/Addison's disease	7 (0.1%)
Lymphoedema	7 (0.1%)
Kidney nephropathy	7 (0.1%)
Leg claudication/intermittent claudication	7 (0.1%)
Myocarditis	6 (0.1%)
Cardiomyopathy	6 (0.1%)
Aortic stenosis	6 (0.1%)
Inflammatory bowel disease	6 (0.1%)
Surgery/amputation of toe	6 (0.1%)

Table A.1: Exclusion criteria (Continued)

Hypertrophic cardiomyopathy (HCM / HOCM)	6 (0.1%)
Hypopituitarism	6 (0.1%)
Polycythaemia vera	5 (0.1%)
Aortic regurgitation/incompetence	5 (0.1%)
Neutropenia/lymphopenia	5 (0.1%)
Monoclonal gammopathy/not myeloma	5 (0.1%)
Mitral valve disease	5 (0.1%)
Vasculitis	5 (0.1%)
Mitral valve prolapse	4 (0.04%)
Aortic aneurysm	4 (0.04%)
Interstitial lung disease	4 (0.04%)
Hyperprolactinaemia	4 (0.04%)
Surgery/amputation of leg below the knee	4 (0.04%)
Emphysema	4 (0.04%)
Liver failure/cirrhosis	3 (0.03%)
Aplastic anaemia	3 (0.03%)
Antiphospholipid syndrome	3 (0.03%)
Diabetic neuropathy/ulcers	3 (0.03%)
Pleural plaques (not known asbestosis)	3 (0.03%)
Haemophilia	3 (0.03%)
Wegners granulomatosis	3 (0.03%)
Wolff parkinson white/WPW syndrome	3 (0.03%)
Giant cell/temporal arteritis	3 (0.03%)
Myositis/myopathy	2 (0.02%)
Fibrosing alveolitis/unspecified alveolitis	2 (0.02%)
Iga nephropathy	2 (0.02%)
Pleural effusion	2 (0.05%)
Sickle cell disease	1 (0.01%)
Microscopic polyarteritis	1 (0.01%)
Hyperaldosteronism/Conn's syndrome	1 (0.01%)
Polymyositis	1 (0.01%)
Alcoholic liver disease/alcoholic cirrhosis	1 (0.01%)
Diabetes insipidus	1 (0.01%)
Respiratory failure	1 (0.01%)
Sick sinus syndrome	1 (0.01%)
Myeloproliferative disorder	1 (0.01%)
Surgery/amputation of leg above the knee	1 (0.01%)
Pericardial problem	0 (0.00%)
Pericardial effusion	0 (0.00%)

Table A.1: Exclusion criteria (Continued)

Medications	
Cholesterol lowering medication	2208 (23.0%)
Blood pressure medication	2266 (23.6%)
Hormone replacement therapy	594 (6.2%)
Insulin	81 (0.8%)
Symptoms	
Shortness of breath walking on level ground	977 (10.2%)
Chest pain due to walking ceases when standing still	529 (5.5%)
Chest pain when walking uphill or hurrying	464 (4.8%)
Unable to walk up hills or to hurry	254 (2.6%)
Smoking history	
Ex-smoker	3118 (32.5%)
Current smoker	823 (8.6%)
High body mass index	
BMI ≥ 30	1820 (19.0%)
Ethnicity	
Indian	69 (0.7%)
Other ethnic group	39 (0.4%)
Pakistani	24 (0.3%)
Caribbean	32 (0.3%)
Chinese	27 (0.3%)
African	22 (0.2%)
Any other mixed background	19 (0.2%)
Prefer not to answer	16 (0.2%)
Any other Asian background	14 (0.1%)
White and Black Caribbean	8 (0.1%)
White and Black African	8 (0.1%)
White and Asian	7 (0.1%)
Bangladeshi	3 (0.03%)
Do not know	2 (0.02%)
Asian or Asian British	1 (0.01%)
Any other Black background	0 (0.00%)
Black or Black British	0 (0.00%)

Bibliography

- I. Akhter, T. Simon, S. Khan, I. Matthews, and Y. Sheikh. Bilinear spatiotemporal basis models. *ACM Transactions on Graphics (TOG)*, 31(2):17, 2012.
- A.H. Aletras, S. Ding, R.S. Balaban, and H. Wen. DENSE: displacement encoding with stimulated echoes in cardiac functional MRI. *Journal of magnetic resonance*, 137(1):247, 1999.
- K. Alfakih, S. Plein, H. Thiele, T. Jones, J.P. Ridgway, and M.U. Sivananthan. Normal human left and right ventricular dimensions for MRI as assessed by turbo gradient echo and steady-state free precession imaging sequences. *Journal of Magnetic Resonance Imaging*, 17(3):323–329, 2003.
- E. Alpaydin. *Introduction to machine learning*. MIT press, 2014.
- G. Andrew, R. Arora, J. Bilmes, and K. Livescu. Deep canonical correlation analysis. In *International Conference on Machine Learning*, pages 1247–1255, 2013.
- S. Ardekani, R.G. Weiss, A.C. Lardo, R.T. George, J.A.C. Lima, K.C. Wu, M.I. Miller, R.L. Winslow, and L. Younes. Cardiac motion analysis in ischemic and non-ischemic cardiomyopathy using parallel transport. In *2009 IEEE International Symposium on Biomedical Imaging: From Nano to Macro*, pages 899–902. IEEE, 2009.
- W.F. Armstrong and T. Ryan. *Feigenbaum's echocardiography*. Lippincott Williams & Wilkins, 2012.
- V.I. Arnol'd. *Mathematical methods of classical mechanics*, volume 60. Springer Science & Business Media, 2013.

- V. Arsigny, O. Commowick, X. Pennec, and N. Ayache. A log-euclidean framework for statistics on diffeomorphisms. In *International Conference on Medical Image Computing and Computer-Assisted Intervention*, pages 924–931. Springer, 2006.
- T. Arts, F.W. Prinzen, T. Delhaas, J.R. Milles, A.C. Rossi, and P. Clarysse. Mapping displacement and deformation of the heart with local sine-wave modeling. *Medical Imaging, IEEE Transactions on*, 29(5):1114–1123, 2010.
- J. Ashburner. A fast diffeomorphic image registration algorithm. *Neuroimage*, 38(1):95–113, 2007.
- L. Axel and L. Dougherty. MR imaging of motion with spatial modulation of magnetization. *Radiology*, 171(3):841–845, 1989.
- F.R. Bach and M.I. Jordan. Kernel independent component analysis. *Journal of machine learning research*, 3(Jul):1–48, 2002.
- F.R. Bach, G.R.G. Lanckriet, and M.I. Jordan. Multiple kernel learning, conic duality, and the SMO algorithm. In *Proceedings of the twenty-first international conference on Machine learning*, page 6. ACM, 2004.
- S.L. Bacharach, M.V. Green, J.S. Borer, J.E. Hyde, S.P. Farkas, and G.S. Johnston. Left-ventricular peak ejection rate, filling rate, and ejection fraction–frame rate requirements at rest and exercise: concise communication. *Journal of nuclear medicine: official publication, Society of Nuclear Medicine*, 20(3):189–193, 1979.
- W. Bai, D. Peressutti, S. Parisot, O. Oktay, M. Rajchl, D. O'Regan, Stuart Cook, A. King, and D. Rueckert. Beyond the AHA 17-segment model: Motion-driven parcellation of the left ventricle. In *International Workshop on Statistical Atlases and Computational Models of the Heart*, pages 13–20. Springer, 2015a.
- W. Bai, W. Shi, A. de Marvao, T.J.W. Dawes, D.P. O'Regan, S.A. Cook, and D. Rueckert. A bi-ventricular cardiac atlas built from 1000+ high resolution MR images of healthy subjects and an analysis of shape and motion. *Medical image analysis*, 26(1):133–145, 2015b.
- W. Bai et al. Semi-supervised learning for network-based cardiac MR image segmentation. In *Med. Image Comput. Comput. Assist. Interv. (MICCAI)*, pages 253–260, 2017.

- C.B. Barber, D.P. Dobkin, and H. Huhdanpaa. The quickhull algorithm for convex hulls. *ACM Transactions on Mathematical Software (TOMS)*, 22(4):469–483, 1996.
- M.F. Beg and A. Khan. Computing an average anatomical atlas using LDDMM and geodesic shooting. In *Biomedical Imaging: Nano to Macro, 2006. 3rd IEEE International Symposium on*, pages 1116–1119. IEEE, 2006.
- J. Bergstra and Y. Bengio. Random search for hyper-parameter optimization. *Journal of Machine Learning Research*, 13(Feb):281–305, 2012.
- J.A. Bianco, A.W. Filiberti, S.P. Baker, M.A. King, L.A. Nalivaika, D. Leahey, P.W. Doherty, and J.S. Alpert. Ejection fraction and heart rate correlate with diastolic peak filling rate at rest and during exercise. *Chest*, 88(1):107–113, 1985.
- A. Blum and T. Mitchell. Combining labeled and unlabeled data with co-training. In *Proceedings of the eleventh annual conference on Computational learning theory*, pages 92–100. ACM, 1998.
- M. Borga, T. Landelius, and H. Knutsson. A unified approach to PCA, PLS, MLR and CCA. 1997.
- B. Bozkurt and D.L. Mann. Dilated cardiomyopathy. In *Cardiovascular Medicine*, pages 1233–1259. Springer, 2007.
- U. Brefeld and T. Scheffer. Co-EM support vector learning. In *Proceedings of the twenty-first international conference on Machine learning*, page 16. ACM, 2004.
- D.J. Bryant, J.A. Payne, D.N. Firmin, and D.B. Longmore. Measurement of flow with NMR imaging using a gradient pulse and phase difference technique. *J Comput Assist Tomogr*, 8(4):588–593, 1984.
- T.S. Caetano, J.J. McAuley, L. Cheng, Q.V. Le, and A.J. Smola. Learning graph matching. *IEEE transactions on pattern analysis and machine intelligence*, 31(6):1048–1058, 2009.
- J. Canny. A computational approach to edge detection. In *Readings in Computer Vision*, pages 184–203. Elsevier, 1987.

- M. Carlsson, M. Ugander, H. Mosén, T. Buhre, and H. Arheden. Atrioventricular plane displacement is the major contributor to left ventricular pumping in healthy adults, athletes, and patients with dilated cardiomyopathy. *American Journal of Physiology-Heart and Circulatory Physiology*, 292(3):H1452–H1459, 2007.
- L. Cayton. Algorithms for manifold learning. *Univ. of California at San Diego Tech. Rep.*, 12(1-17):1, 2005.
- M.D. Cerqueira, N.J. Weissman, V. Dilsizian, A.K. Jacobs, S. Kaul, W.K. Laskey, D.J. Pennell, J.A. Rumberger, T. Ryan, and M.S. Verani. Standardized myocardial segmentation and nomenclature for tomographic imaging of the heart: a statement for healthcare professionals from the cardiac imaging committee of the council on clinical cardiology of the american heart association. *Journal of the American Society of Echocardiography*, 15(5):463–467, 2002.
- R. Chandrashekara, A. Rao, G.I. Sanchez-Ortiz, R.H. Mohiaddin, and D. Rueckert. Construction of a statistical model for cardiac motion analysis using non-rigid image registration. In *Biennial International Conference on Information Processing in Medical Imaging*, pages 599–610. Springer, 2003.
- G. Chao. Multi-view sparse vector decomposition to deal with missing values in alcohol dependence study. *Neural Processing Letters*, pages 1–22, 2017.
- G. Chao and S. Sun. Consensus and complementarity based maximum entropy discrimination for multi-view classification. *Information Sciences*, 367:296–310, 2016.
- O. Chapelle, B. Scholkopf, and A. Zien, editors. *Semi-Supervised Learning*. MIT Press, Cambridge, MA, 2006. URL <http://www.kyb.tuebingen.mpg.de/ssl-book>.
- J.S. Chuang, A Zemljic-Harpf, R.S. Ross, L.R. Frank, A.D. McCulloch, and J.H. Omens. Determination of three-dimensional ventricular strain distributions in gene-targeted mice using tagged MRI. *Magnetic resonance in medicine*, 64(5):1281–1288, 2010.
- P. Claus et al. Tissue tracking technology for assessing cardiac mechanics: principles, normal values, and clinical applications. *JACC: Cardiovascular Imaging*, 8(12):1444–1460, 2015.

- C. Cortes and V. Vapnik. Support-vector networks. *Machine learning*, 20(3):273–297, 1995.
- J. Crosby, B. .H Amundsen, T. Hergum, E. W. Remme, S. Langeland, and H. Torp. 3-D speckle tracking for assessment of regional left ventricular function. *Ultrasound in medicine & biology*, 35(3):458–471, 2009.
- M. De Craene, N. Duchateau, C. Tobon-Gomez, B. Ghafaryasl, G. Piella, K.S. Rhode, and A.F. Frangi. SPM to the heart: Mapping of 4D continuous velocities for motion abnormality quantification. In *Biomedical Imaging (ISBI), 2012 9th IEEE International Symposium on*, pages 454–457. IEEE, 2012a.
- M. De Craene, G. Piella, O. Camara, N. Duchateau, E. Silva, A. Doltra, J. D’hooge, J. Brugada, M. Sitges, and A.F. Frangi. Temporal diffeomorphic free-form deformation: Application to motion and strain estimation from 3D echocardiography. *Medical Image Analysis*, 16(2):427–450, 2012b.
- T.G. Dietterich. Ensemble learning. *The handbook of brain theory and neural networks*, 2:110–125, 2002.
- A. Doltra, B. Bijnens, J.M. Tolosana, R. Borràs, M. Khatib, D. Penela, T.M. De Caralt, M.A. Castel, A. Beruezo, J. Brugada, et al. Mechanical abnormalities detected with conventional echocardiography are associated with response and midterm survival in CRT. *JACC: Cardiovascular Imaging*, 7(10):969–979, 2014.
- F. Duan, M. Xie, X. Wang, Y. Li, L. He, L. Jiang, and Q. Fu. Preliminary clinical study of left ventricular myocardial strain in patients with non-ischemic dilated cardiomyopathy by three-dimensional speckle tracking imaging. *Cardiovascular Ultrasound*, 10(1):8, 2012.
- N. Duchateau, M. De Craene, E. Silva, M. Sitges, B.H. Bijnens, and A.F. Frangi. Septal flash assessment on CRT candidates based on statistical atlases of motion. In *Medical Image Computing and Computer-Assisted Intervention–MICCAI 2009*, pages 759–766. Springer, 2009.
- N. Duchateau, M. De Craene, G. Piella, C. Hoogendoorn, E. Silva, A. Doltra, L. Mont, M.A. Castel, J. Brugada, M. Sitges, et al. Atlas-based quantification of myocardial motion abnormalities: added-value for the understanding of CRT outcome? In *Statistical Atlases and Computational Models of the Heart*, pages 65–74. Springer, 2010.

- N. Duchateau, M. De Craene, G. Piella, E. Silva, A. Doltra, M. Sitges, B.H. Bijnens, and A.F. Frangi. A spatiotemporal statistical atlas of motion for the quantification of abnormal myocardial tissue velocities. *Medical image analysis*, 15(3):316–328, 2011.
- N. Duchateau, M. De Craene, G. Piella, and A.F. Frangi. Constrained manifold learning for the characterization of pathological deviations from normality. *Medical image analysis*, 16(8):1532–1549, 2012.
- S. Durrleman, X. Pennec, A. Trouvé, J. Braga, G. Gerig, and N. Ayache. Toward a comprehensive framework for the spatiotemporal statistical analysis of longitudinal shape data. *International journal of computer vision*, 103(1):22–59, 2013.
- E.J. Eichhorn, C.M. Heesch, J.H. Barnett, L.G. Alvarez, S.M. Fass, P.A. Grayburn, B.A. Hatfield, L.G. Marcoux, and C.R. Malloy. Effect of metoprolol on myocardial function and energetics in patients with nonischemic dilated cardiomyopathy: a randomized, double-blind, placebo-controlled study. *Journal of the American College of Cardiology*, 24(5):1310–1320, 1994.
- J. Farquhar, D. Hardoon, H. Meng, J.S. Shawe-taylor, and S Szemzak. Two view learning: SVM-2K, theory and practice. In *Advances in neural information processing systems*, pages 355–362, 2006.
- S.D. Fihn, J.M. Gardin, J. Abrams, K. Berra, J.C. Blankenship, P.S. Douglas, J.M. Foody, T.C. Gerber, A.L. Hinderliter, S.B. King, et al. 2012 ACCF/AHA/ACP/AATS/PCNA/SCAI/STS guideline for the diagnosis and management of patients with stable ischemic heart disease. *Journal of the American College of Cardiology*, 60(24):e44–e164, 2012.
- R.A. Fisher. The use of multiple measurements in taxonomic problems. *Annals of human genetics*, 7(2):179–188, 1936.
- C.G. Fonseca, M. Backhaus, D.A. Bluemke, R.D. Britten, J. Do Chung, B.R. Cowan, I.D. Dinov, J.P. Finn, P.J. Hunter, A.H. Kadish, et al. The cardiac atlas project—an imaging database for computational modeling and statistical atlases of the heart. *Bioinformatics*, 27(16):2288–2295, 2011.
- A.F. Frangi, D. Rueckert, J.A. Schnabel, and ".J. Niessen. Automatic construction of multiple-object three-dimensional statistical shape models: Application

- to cardiac modeling. *IEEE transactions on medical imaging*, 21(9):1151–1166, 2002.
- Y. Freund and R.E. Schapire. A decision-theoretic generalization of on-line learning and an application to boosting. *Journal of computer and system sciences*, 55(1):119–139, 1997.
- Jerome Friedman, Trevor Hastie, and Robert Tibshirani. *The elements of statistical learning*, volume 1. Springer series in statistics New York, 2001.
- J. Garcia-Barnes, D. Gil, L. Badiella, F. Carreras, S. Pujades, E. Martí, et al. A normalized framework for the design of feature spaces assessing the left ventricular function. *Medical Imaging, IEEE Transactions on*, 29(3):733–745, 2010.
- A.S. Go, D. Mozaffarian, V.L. Roger, E.J. Benjamin, J.D. Berry, M.J. Blaha, S. Dai, E.S. Ford, C.S. Fox, et al. Heart disease and stroke statistics—2014 update: a report from the American Heart Association. *circulation*, 129(3):e28, 2014.
- M. Gönen and E. Alpaydın. Multiple kernel learning algorithms. *Journal of machine learning research*, 12(Jul):2211–2268, 2011.
- M. Gori, M. Maggini, and L. Sarti. Exact and approximate graph matching using random walks. *IEEE transactions on pattern analysis and machine intelligence*, 27(7):1100–1111, 2005.
- M.J.W. Götte, A.C. van Rossum, J.T. Marcus, J.P.A. Kuijer, L. Axel, and C.A. Visser. Recognition of infarct localization by specific changes in intramural myocardial mechanics. *American heart journal*, 138(6):1038–1045, 1999.
- M.J.W. Götte, A.C. van Rossum, J.W.R. Twisk, J.P.A. Kuijer, J.T. Marcus, and C.A. Visser. Quantification of regional contractile function after infarction: strain analysis superior to wall thickening analysis in discriminating infarct from remote myocardium. *Journal of the American College of Cardiology*, 37(3):808–817, 2001.
- J.C. Gower and G.B. Dijksterhuis. *Procrustes problems*, volume 3. Oxford University Press Oxford, 2004.

- J. Greupner, E. Zimmermann, A. Grohmann, H-P Dübel, T. Althoff, A.C. Borges, W. Rutsch, P. Schlattmann, B. Hamm, and M. Dewey. Head-to-head comparison of left ventricular function assessment with 64-row computed tomography, biplane left cineventriculography, and both 2-and 3-dimensional transthoracic echocardiography: comparison with magnetic resonance imaging as the reference standard. *Journal of the American College of Cardiology*, 59(21):1897–1907, 2012.
- R. Guerrero, C. Ledig, and D. Rueckert. Manifold alignment and transfer learning for classification of Alzheimer’s disease. In *International Workshop on Machine Learning in Medical Imaging*, pages 77–84. Springer, 2014.
- T. Guha and R.K. Ward. Learning sparse representations for human action recognition. *IEEE Transactions on Pattern Analysis and Machine Intelligence*, 34(8):1576–1588, 2012.
- J. Ham, D.D. Lee, and L.K. Saul. Semisupervised alignment of manifolds. *AISTATS 2005*, page 120, 2005.
- C. Hoogendoorn, F.M. Sukno, S. Ordás, and A.F. Frangi. Bilinear models for spatio-temporal point distribution analysis. *International Journal of Computer Vision*, 85(3):237–252, 2009.
- C. Hoogendoorn, N. Duchateau, D. Sanchez-Quintana, T. Whitmarsh, F.M. Sukno, M. De Craene, K. Lekadir, and A.F. Frangi. A high-resolution atlas and statistical model of the human heart from multislice CT. *Medical Imaging, IEEE Transactions on*, 32(1):28–44, 2013.
- K.N. Hor, R. Baumann, G. Pedrizzetti, G. Tonti, W.M. Gottliebson, M. Taylor, D.W. Benson, and W. Mazur. Magnetic resonance derived myocardial strain assessment using feature tracking. *Journal of visualized experiments: JoVE*, (48), 2011.
- H. Hotelling. Analysis of a complex of statistical variables into principal components. *Journal of educational psychology*, 24(6):417, 1933.
- H. Hotelling. Relations between two sets of variates. *Biometrika*, 28(3/4):321–377, 1936.
- Aapo Hyvärinen and Erkki Oja. Independent component analysis: algorithms and applications. *Neural networks*, 13(4-5):411–430, 2000.

- A. Jain, J. Tompson, Y. LeCun, and C. Bregler. Modeep: A deep learning framework using motion features for human pose estimation. In *Asian conference on computer vision*, pages 302–315. Springer, 2014.
- R. Jasaityte, B. Heyde, and J. D’hooge. Current state of three-dimensional myocardial strain estimation using echocardiography. *Journal of the American Society of Echocardiography*, 26(1):15–28, 2013.
- M-P Jolly et al. Automated assessments of circumferential strain from cine CMR correlate with LVEF declines in cancer patients early after receipt of cardio-toxic chemotherapy. *Journal of Cardiovascular Magnetic Resonance*, 19(1):59, 2017.
- L.P. Kaelbling, M.L. Littman, and A.W. Moore. Reinforcement learning: A survey. *Journal of artificial intelligence research*, 4:237–285, 1996.
- K. Kaku, M. Takeuchi, W. Tsang, K. Takigiku, S. Yasukochi, A.R. Patel, V. Mor-Avi, R.M. Lang, and Y. Otsuji. Age-related normal range of left ventricular strain and torsion using three-dimensional speckle-tracking echocardiography. *Journal of the American Society of Echocardiography*, 27(1):55–64, 2014.
- K. Kaluzynski, X. Chen, S.Y. Emelianov, A.R. Skovoroda, and M. O’Donnell. Strain rate imaging using two-dimensional speckle tracking. *Ultrasonics, Ferroelectrics, and Frequency Control, IEEE Transactions on*, 48(4):1111–1123, 2001.
- M. Kan, S. Shan, H. Zhang, S. Lao, and X. Chen. Multi-view discriminant analysis. *Computer Vision–ECCV 2012*, pages 808–821, 2012.
- S. Kaul, C. Tei, and P.M. Shah. Interventricular septal and free wall dynamics in hypertrophic cardiomyopathy. *Journal of the American College of Cardiology*, 1(4):1024–1030, 1983.
- N. Kawel-Boehm, A. Maceira, E.R. Valsangiacomo-Buechel, J. Vogel-Claussen, E.B. Turkbey, R. Williams, S. Plein, M. Tee, J. Eng, and D.A. Bluemke. Normal values for cardiovascular magnetic resonance in adults and children. *Journal of Cardiovascular Magnetic Resonance*, 17(1):29, 2015.
- E. Kerfoot, L. Fovargue, S. Rivolo, W. Shi, D. Rueckert, D. Nordsletten, J. Lee, R. Chabiniok, and R. Razavi. Eidolon: Visualization and computational framework for multi-modal biomedical data analysis. In *International Conference on Medical Imaging and Virtual Reality*, pages 425–437. Springer, 2016.

- D. Kim, W.D. Gilson, C.M. Kramer, and F.H. Epstein. Myocardial tissue tracking with two-dimensional cine displacement-encoded MR imaging: development and initial evaluation. *Radiology*, 230(3):862–871, 2004.
- S.A. Kleijn, N.G. Pandian, J.D. Thomas, L. Perez de Isla, O. Kamp, et al. Normal reference values of left ventricular strain using three-dimensional speckle tracking echocardiography: results from a multicentre study. *European Heart Journal-Cardiovascular Imaging*, 16(4):410–416, 2014.
- S.B. Kotsiantis, I. Zaharakis, and P. Pintelas. Supervised machine learning: A review of classification techniques. *Emerging artificial intelligence applications in computer engineering*, 160:3–24, 2007.
- V. Kumar, A.K. Abbas, N. Fausto, and J.C. Aster. *Robbins and Cotran pathologic basis of disease*. Elsevier Health Sciences, 2014.
- R.M. Lang, M. Bierig, R.B. Devereux, F.A. Flachskampf, E. Foster, P.A. Pelikka, M.H. Picard, M.J. Roman, J. Seward, J.S. Shanewise, et al. Recommendations for chamber quantification: a report from the american society of echocardiography's guidelines and standards committee and the chamber quantification writing group, developed in conjunction with the european association of echocardiography, a branch of the european society of cardiology. *Journal of the American Society of Echocardiography*, 18(12):1440–1463, 2005.
- R.M. Lang, L.P. Badano, V. Mor-Avi, J. Afilalo, A. Armstrong, L. Ernande, F.A. Flachskampf, E. Foster, S.A. Goldstein, T. Kuznetsova, et al. Recommendations for cardiac chamber quantification by echocardiography in adults: an update from the american society of echocardiography and the european association of cardiovascular imaging. *Journal of the American Society of Echocardiography*, 28(1):1–39, 2015.
- W.K. Laskey, M.S.J Sutton, G. Zeevi, J.W. Hirshfeld, and N Reichek. Left ventricular mechanics in dilated cardiomyopathy. *The American journal of cardiology*, 54(6):620–625, 1984.
- T-C Lee, R.L. Kashyap, and C-N Chu. Building skeleton models via 3-D medial surface axis thinning algorithms. *CVGIP: Graphical Models and Image Processing*, 56(6):462–478, 1994.
- F. Levy, E.D. Schouver, L. Iacuzio, F. Civaia, S. Rusek, C. Dommerc, S. Marechaux, V. Dor, C. Tribouilloy, and G. Dreyfus. Performance of new

- automated transthoracic three-dimensional echocardiographic software for left ventricular volumes and function assessment in routine clinical practice: comparison with 3 Tesla cardiac magnetic resonance. *Archives of cardiovascular diseases*, 110(11):580–589, 2017.
- H. Liu, T. Wang, X. Lei, et al. Spatiotemporal strategies for joint segmentation and motion tracking from cardiac image sequences. *IEEE Journal of Translational Engineering in Health and Medicine*, 2017.
- M. Lorenzi, B. Gutman, D.P. Hibar, A. Altmann, N. Jahanshad, P.M. Thompson, and S. Ourselin. Partial least squares modelling for imaging-genetics in Alzheimer’s disease: Plausibility and generalization. In *Biomedical Imaging (ISBI), 2016 IEEE 13th International Symposium on*, pages 838–841. IEEE, 2016.
- Y. Lu, P. Radau, K. Connelly, A. Dick, and G. Wright. Pattern recognition of abnormal left ventricle wall motion in cardiac MR. In *International Conference on Medical Image Computing and Computer-Assisted Intervention*, pages 750–758. Springer, 2009.
- A.M. Maceira, S.K. Prasad, M. Khan, and D.J. Pennell. Normalized left ventricular systolic and diastolic function by steady state free precession cardiovascular magnetic resonance. *Journal of Cardiovascular Magnetic Resonance*, 8(3):417–426, 2006.
- T. Mansi, X. Pennec, M. Sermesant, H. Delingette, and N. Ayache. iLogDemons: A demons-based registration algorithm for tracking incompressible elastic biological tissues. *International journal of computer vision*, 92(1):92–111, 2011.
- T. Mansi et al. Physically-constrained diffeomorphic demons for the estimation of 3d myocardium strain from cine-MRI. *Functional Imag. Modeling Heart.*, pages 201–210, 2009.
- M. Marciak, H. Arevalo, J. Tfelt-Hansen, K.A. Ahtarovski, T. Jespersen, R. Jabbari, C. Glinge, N. Vejlstrup, T. Engstrom, M.M. Maleckar, et al. A multiple kernel learning framework to investigate the relationship between ventricular fibrillation and first myocardial infarction. In *International Conference on Functional Imaging and Modeling of the Heart*, pages 161–171. Springer, 2017.

- K. McLeod, A. Prakosa, T. Mansi, M. Sermesant, and X. Pennec. An incompressible log-domain demons algorithm for tracking heart tissue. In *International Workshop on Statistical Atlases and Computational Models of the Heart*, pages 55–67. Springer, 2011.
- K. McLeod, C. Seiler, M. Sermesant, and X. Pennec. A near-incompressible poly-affine motion model for cardiac function analysis. In *International Workshop on Statistical Atlases and Computational Models of the Heart*, pages 288–297. Springer, 2012.
- K. McLeod, C. Seiler, M. Sermesant, and X. Pennec. Spatio-temporal dimension reduction of cardiac motion for group-wise analysis and statistical testing. In *Medical Image Computing and Computer-Assisted Intervention–MICCAI 2013*, pages 501–508. Springer, 2013.
- K. McLeod, M. Sermesant, P. Beerbaum, and X. Pennec. Descriptive and intuitive population-based cardiac motion analysis via sparsity constrained tensor decomposition. In *International Conference on Medical Image Computing and Computer-Assisted Intervention*, pages 419–426. Springer, 2015.
- P. Medrano-Gracia, B. R Cowan, J.P. Finn, C.G. Fonseca, A.H. Kadish, D.C. Lee, W. Tao, and A.A. Young. The cardiac atlas project: Preliminary description of heart shape in patients with myocardial infarction. In *STACOM/CESC*, pages 46–53. Springer, 2010.
- P. Medrano-Gracia, B.R. Cowan, D. A Bluemke, J.P. Finn, A.H. Kadish, D.C. Lee, J.A.C. Lima, A. Suinesiaputra, and A.A. Young. Atlas-based analysis of cardiac shape and function: correction of regional shape bias due to imaging protocol for population studies. *Journal of Cardiovascular Magnetic Resonance*, 15(1):80, 2013a.
- P. Medrano-Gracia, A. Suinesiaputra, B. Cowan, D. Bluemke, A. Frangi, D. Lee, J. Lima, and A. Young. An atlas for cardiac MRI regional wall motion and infarct scoring. In *Statistical atlases and computational models of the heart. Imaging and modelling challenges*, pages 188–197. Springer, 2013b.
- P. Medrano-Gracia, B.R. Cowan, B. Ambale-Venkatesh, D.A. Bluemke, J. Eng, J.P. Finn, C.G. Fonseca, J.A.C. Lima, A. Suinesiaputra, and A.A. Young. Left ventricular shape variation in asymptomatic populations: the multi-ethnic study of atherosclerosis. *Journal of Cardiovascular Magnetic Resonance*, 16(1):56, 2014a.

- P. Medrano-Gracia, B.R. Cowan, D.A. Bluemke, J.P. Finn, A.H. Kadish, D.C. Lee, J.A.C. Lima, A. Suinesiaputra, and A.A. Young. Continuous spatio-temporal atlases of the asymptomatic and infarcted hearts. In *Statistical Atlases and Computational Models of the Heart. Imaging and Modelling Challenges*, pages 143–151. Springer, 2014b.
- P. Medrano-Gracia, B.R. Cowan, A. Suinesiaputra, and A.A. Young. Atlas-based anatomical modeling and analysis of heart disease. *Drug Discovery Today: Disease Models*, 2014c.
- S. Melacci and M. Belkin. Laplacian support vector machines trained in the primal. *Journal of Machine Learning Research*, 12(Mar):1149–1184, 2011.
- S. Mendis, P. Puska, B. Norrving, et al. *Global atlas on cardiovascular disease prevention and control*. Geneva: World Health Organization, 2011.
- M. Merlo, F. Negri, D. Stolfo, A. Iorio, B. Pinamonti, M. Zecchin, L.V. Serdzo, and A. Di Lenarda. Dilated cardiomyopathy: Usefulness of imaging in prognostic stratification and choice of treatment. In *Clinical Echocardiography and Other Imaging Techniques in Cardiomyopathies*, pages 75–81. Springer, 2014.
- T.R. Miller, S.J. Grossman, K.B. Schectman, D.R. Biello, P.A. Ludbrook, and A.A. Ehsani. Left ventricular diastolic filling and its association with age. *The American journal of cardiology*, 58(6):531–535, 1986.
- Y. Mishiro, T. Oki, A. Iuchi, T. Tabata, H. Yamada, et al. Regional left ventricular myocardial contraction abnormalities and asynchrony in patients with hypertrophic cardiomyopathy evaluated by magnetic resonance spatial modulation of magnetization myocardial tagging. *Japanese circulation journal*, 63(6):442–446, 1999.
- T.M. Mitchell et al. Machine learning. 1997. *Burr Ridge, IL: McGraw Hill*, 45(37):870–877, 1997.
- Y. Mu, L. Chen, Q. Tang, and G. Ayoubi. Real time three-dimensional echocardiographic assessment of left ventricular regional systolic function and dyssynchrony in patients with dilated cardiomyopathy. *Echocardiography*, 27(4):415–420, 2010.
- I. Muslea, S. Minton, and C.A. Knoblock. Selective sampling with redundant views. In *AAAI/IAAI*, pages 621–626, 2000.

- N.M. Nasrabadi. Pattern recognition and machine learning. *Journal of electronic imaging*, 16(4):049901, 2007.
- G.S. Nelson, C.W. Curry, B.T. Wyman, A. Kramer, J. Declerck, M. Talbot, M.R. Douglas, R.D. Berger, E.R. McVeigh, and D.A. Kass. Predictors of systolic augmentation from left ventricular preexcitation in patients with dilated cardiomyopathy and intraventricular conduction delay. *Circulation*, 101(23):2703–2709, 2000.
- J. Ngiam, A. Khosla, M. Kim, J. Nam, H. Lee, and A.Y. Ng. Multimodal deep learning. In *Proceedings of the 28th international conference on machine learning (ICML-11)*, pages 689–696, 2011.
- M. Nickel, K. Murphy, V. Tresp, and E. Gabrilovich. A review of relational machine learning for knowledge graphs. *Proceedings of the IEEE*, 104(1):11–33, 2016.
- Heart Failure Society of America et al. Executive summary: HFSA 2010 comprehensive heart failure practice guideline. *Journal of cardiac failure*, 16(6):475–539, 2010.
- I. Oksuz, B. Ruijsink, E. Puyol-Antón, M. Sinclair, D. Rueckert, J.A. Schnabel, and A.P. King. Automatic left ventricular outflow tract classification for accurate cardiac MR planning. In *Biomedical Imaging (ISBI), 2012 9th IEEE International Symposium on*, pages 462–465. IEEE, 2012.
- I. Oksuz, B. Ruijsink, E. Puyol-Antón, B. Aurelien, G. Cruz, C. Prieto, D. Rueckert, J.A. Schnabel, and A.P. King. Motion artefact detection for automatic quality assessment of large imbalanced cardiac MRI datasets. In *Medical Image Computing and Computer-Assisted Intervention—MICCAI 2018*. Springer, in press 2018.
- World Health Organization. *Prevention of cardiovascular disease*. World Health Organization, 2007.
- N.F. Osman, S. Sampath, E. Atalar, and J.L. Prince. Imaging longitudinal cardiac strain on short-axis images using strain-encoded MRI. *Magnetic Resonance in Medicine*, 46(2):324–334, 2001.
- H.C. Oxenham, A.A. Young, B.R. Cowan, T.L. Gentles, C.J. Occleshaw, C.G. Fonseca, R.N. Doughty, and N. Sharpe. Age-related changes in myocardial

- relaxation using three-dimensional tagged magnetic resonance imaging: structure and function. *Journal of Cardiovascular Magnetic Resonance*, 5(3):421–430, 2003.
- F. Pedregosa, G. Varoquaux, A. Gramfort, V. Michel, B. Thirion, O. Grisel, M. Blondel, P. Prettenhofer, R. Weiss, V. Dubourg, et al. Scikit-learn: Machine learning in python. *Journal of machine learning research*, 12(Oct):2825–2830, 2011.
- G. Pedrizzetti, P. Claus, P.J. Kilner, and E. Nagel. Principles of cardiovascular magnetic resonance feature tracking and echocardiographic speckle tracking for informed clinical use. *Journal of Cardiovascular Magnetic Resonance*, 18(1):51, 2016.
- D. Peressutti, W. Bai, T. Jackson, M. Sohal, A. Rinaldi, D. Rueckert, and A. King. Prospective identification of CRT super responders using a motion atlas and random projection ensemble learning. In *International Conference on Medical Image Computing and Computer-Assisted Intervention*, pages 493–500. Springer, 2015.
- D. Peressutti, M. Sinclair, W. Bai, T. Jackson, J. Ruijsink, D. Nordsletten, L. Asner, M. Hadjicharalambous, C.A. Rinaldi, D. Rueckert, et al. A framework for combining a motion atlas with non-motion information to learn clinically useful biomarkers: Application to cardiac resynchronisation therapy response prediction. *Medical image analysis*, 35:669–684, 2017.
- D. Perperidis, R. Mohiaddin, and D. Rueckert. Construction of a 4D statistical atlas of the cardiac anatomy and its use in classification. In *International Conference on Medical Image Computing and Computer-Assisted Intervention*, pages 402–410. Springer, 2005a.
- D. Perperidis, R.H. Mohiaddin, and D. Rueckert. Spatio-temporal free-form registration of cardiac MR image sequences. *Medical image analysis*, 9(5):441–456, 2005b.
- S.E. Petersen, P.M. Matthews, J.M. Francis, M.D. Robson, F. Zemrak, R. Bouberakh, A.A. Young, S. Hudson, P. Weale, S. Garratt, et al. UK biobank’s cardiovascular magnetic resonance protocol. *Journal of cardiovascular magnetic resonance*, 18(1):8, 2016.

- S.E. Petersen, N. Aung, M.M. Sanghvi, F. Zemrak, K. Fung, J.M. Paiva, J.M. Francis, M.Y. Khanji, E. Lukaschuk, A.M. Lee, et al. Reference ranges for cardiac structure and function using cardiovascular magnetic resonance (CMR) in caucasians from the UK biobank population cohort. *Journal of Cardiovascular Magnetic Resonance*, 19(1):18, 2017.
- V. Pinto, M. Wankelmuth, and V. D'Addario. Donald school textbook of ultrasound in obstetrics and gynecology. *Asim Kurjak, Frank A Chervenak, First Ed, Jaypee Brothers, New Delhi, India*, 365, 2004.
- M. Prasad, A. Sowmya, and P. Wilson. Automatic detection of bronchial dilatation in HRCT lung images. *Journal of digital imaging*, 21(1):148–163, 2008.
- K. Punithakumar, I.B. Ayed, A. Islam, A. Goela, I.G. Ross, J. Chong, and S. Li. Regional heart motion abnormality detection: An information theoretic approach. *Medical image analysis*, 17(3):311–324, 2013.
- E. Puyol-Antón, D. Peressutti, P. Aljabar, M. De Craene, P. Piro, and A.P. King. Towards a multimodal cardiac motion atlas. In *Biomedical Imaging (ISBI), 2016 IEEE 13th International Symposium on*, pages 32–35. IEEE, 2016.
- E. Puyol-Antón, M. Sinclair, B. Gerber, M.S. Amzulescu, H. Langet, M. De Craene, P. Aljabar, J. Schnabel, P. Piro, and A.P. King. Multiview machine learning using an atlas of cardiac cycle motion. In *International Workshop on Statistical Atlases and Computational Models of the Heart*, pages 3–11. Springer, 2017a.
- E. Puyol-Antón, M. Sinclair, B. Gerber, M.S. Amzulescu, H. Langet, M. De Craene, P. Aljabar, P. Piro, and A.P. King. A multimodal spatiotemporal cardiac motion atlas from MR and ultrasound data. *Medical image analysis*, 40:96–110, 2017b.
- E. Puyol-Antón, B. Ruijsink, W. Bai, H. Langet, M. De Craene, J.A. Schnabel, P. Piro, A.P. King, and M. Sinclair. Fully automated myocardial strain estimation from cine MRI using convolutional neural networks. In *Biomedical Imaging (ISBI 2018), 2018 IEEE 15th International Symposium on*, pages 1139–1143. IEEE, 2018a.
- E. Puyol-Antón, B. Ruijsink, B. Gerber, M.S. Amzulescu, H. Langet, M. De Craene, J. Schnabel, P. Piro, and A.P. King. Regional multi-view learning for cardiac motion analysis: Application to identification of dilated cardiomyopathy patient. *IEEE Transactions on Biomedical Engineering*, 2018b.

- E. Puyol-Antón, B. Ruijsink, H. Langet, M. De Craene, J.A. Schnabel, P. Piro, and A.P. King. Learning associations between clinical information and motion-based descriptors using a large scale MR-derived cardiac motion atlas. In *International Workshop on Statistical Atlases and Computational Models of the Heart*. Springer, 2018c.
- L.R. Rabiner and B-H Juang. *Fundamentals of speech recognition*, volume 14. PTR Prentice Hall Englewood Cliffs, 1993.
- A. Rao, R. Chandrashekara, G.I. Sanchez-Ortiz, R. Mohiaddin, P. Aljabar, J.V. Hajnal, B. K Puri, and D. Rueckert. Spatial transformation of motion and deformation fields using nonrigid registration. *Medical Imaging, IEEE Transactions on*, 23(9):1065–1076, 2004.
- J.P. Ridgway. Cardiovascular magnetic resonance physics for clinicians: part I. *Journal of cardiovascular magnetic resonance*, 12(1):71, 2010.
- C.S. Rihal, R.A Nishimura, L.K. Hatle, K.R. Bailey, and A.J. Tajik. Systolic and diastolic dysfunction in patients with clinical diagnosis of dilated cardiomyopathy. relation to symptoms and prognosis. *Circulation*, 90(6):2772–2779, 1994.
- M-M. Rohé, M. Sermesant, and X. Pennec. Low-dimensional representation of cardiac motion using barycentric subspaces: a new group-wise paradigm for estimation, analysis, and reconstruction. *Medical image analysis*, 45:1–12, 2018.
- L. Rokach and O.Z. Maimon. *Data mining with decision trees: theory and applications*, volume 81. World scientific, 2014.
- N.F. Rougon, C. Petitjean, and F.J. Preteux. Building and using a statistical 3D motion atlas for analyzing myocardial contraction in MRI. In *Medical Imaging 2004*, pages 253–264. International Society for Optics and Photonics, 2004.
- S.T. Roweis and L.K. Saul. Nonlinear dimensionality reduction by locally linear embedding. *science*, 290(5500):2323–2326, 2000.
- D. Rueckert, L.I. Sonoda, C. Hayes, D.L.G. Hill, M.O. Leach, and D.J. Hawkes. Nonrigid registration using free-form deformations: application to breast MR images. *Medical Imaging, IEEE Transactions on*, 18(8):712–721, 1999.
- B. Ruijsink, E. Puyol-Antón, M. Usman, J. van Amerom, P. Duong, M.N. Velasco Forte, K. Pushparajah, A. Frigiola, D.A. Nordsletten, A.P. King, et al.

- Semi-automatic cardiac and respiratory gated MRI for cardiac assessment during exercise. In *Molecular Imaging, Reconstruction and Analysis of Moving Body Organs, and Stroke Imaging and Treatment*, pages 86–95. Springer, 2017.
- S. Sanchez-Martinez, N. Duchateau, T. Erdei, A.G. Fraser, B.H. Bijnens, and G. Piella. Characterization of myocardial motion patterns by unsupervised multiple kernel learning. *Medical image analysis*, 35:70–82, 2017.
- W.J. Schroeder, J.A. Zarge, and W.E. Lorensen. Decimation of triangle meshes. In *ACM Siggraph Computer Graphics*, volume 26, pages 65–70. ACM, 1992.
- A. Schuster et al. Cardiovascular magnetic resonance feature-tracking assessment of myocardial mechanics: Intervendor agreement and considerations regarding reproducibility. *Clinical radiology*, 70(9):989–998, 2015.
- W. Shi, X. Zhuang, H. Wang, S. Duckett, D.V. Luong, C. Tobon-Gomez, K. Tung, Edwards, et al. A comprehensive cardiac motion estimation framework using both untagged and 3-D tagged MR images based on nonrigid registration. *Medical Imaging, IEEE Transactions on*, 31(6):1263–1275, 2012.
- M. Sinclair, D. Peressutti, E. Puyol-Antón, W. Bai, M. Nordsletten, D. Hadjicharalambous, E. Kerfoot, T. Jackson, S. Claridge, C.A. Rinaldi, D. Rueckert, and A.P. King. Learning optimal spatial scales for cardiac strain analysis using a motion atlas. In *International Workshop on Statistical Atlases and Computational Models of the Heart*, pages 57–65. Springer, 2016.
- M. Sinclair, W. Bai, E. Puyol-Antón, O. Oktay, D. Rueckert, and A.P. King. Fully automated segmentation-based respiratory motion correction of multiplanar cardiac magnetic resonance images for large-scale datasets. In *International Conference on Medical Image Computing and Computer-Assisted Intervention*, pages 332–340. Springer, 2017.
- M. Sinclair, D. Peressutti, E. Puyol-Antón, W. Bai, S. Rivolo, J. Webb, S. Claridge, T. Jackson, D. Nordsletten, M. Hadjicharalambous, et al. Myocardial strain computed at multiple spatial scales from tagged magnetic resonance imaging: Estimating cardiac biomarkers for CRT patients. *Medical image analysis*, 43:169–185, 2018.
- C. Studholme, D.L.G. Hill, and D.J. Hawkes. An overlap invariant entropy measure of 3D medical image alignment. *Pattern recognition*, 32(1):71–86, 1999.

- M.Y.M. Su, L.Y. Lin, Y.H.E. Tseng, C.C. Chang, C.K. Wu, J.L Lin, and W.Y.I. Tseng. CMR-verified diffuse myocardial fibrosis is associated with diastolic dysfunction in HFrEF. *JACC: Cardiovascular Imaging*, 7(10):991–997, 2014.
- A. Suinesiaputra, A. F. Frangi, T.A.M. Kaandorp, H.J. Lamb, J.J Bax, J.H.C. Reiber, and B.P.F. Lelieveldt. Automated detection of regional wall motion abnormalities based on a statistical model applied to multislice short-axis cardiac MR images. *Medical Imaging, IEEE Transactions on*, 28(4):595–607, 2009.
- S. Sun. Multi-view laplacian support vector machines. In *International Conference on Advanced Data Mining and Applications*, pages 209–222. Springer, 2011.
- S. Sun. A survey of multi-view machine learning. *Neural Computing and Applications*, 23(7-8):2031–2038, 2013.
- S. Sun and G. Chao. Multi-view maximum entropy discrimination. In *IJCAI*, pages 1706–1712, 2013.
- S. Sun, X. Xie, and M. Yang. Multiview uncorrelated discriminant analysis. *IEEE transactions on cybernetics*, 46(12):3272–3284, 2016.
- R.J. Taylor, W.E. Moody, F. Umar, N.C. Edwards, T.J. Taylor, B. Stegemann, J.N. Townend, K.N. Hor, R.P. Steeds, W. Mazur, et al. Myocardial strain measurement with feature-tracking cardiovascular magnetic resonance: normal values. *European Heart Journal–Cardiovascular Imaging*, 16(8):871–881, 2015.
- J.B. Tenenbaum, V. De Silva, and J.C. Langford. A global geometric framework for nonlinear dimensionality reduction. *science*, 290(5500):2319–2323, 2000.
- K. Thangavel and A. Pethalakshmi. Dimensionality reduction based on rough set theory: A review. *Applied Soft Computing*, 9(1):1–12, 2009.
- C. Tobon-Gomez, M. De Craene, K. Mcleod, L. Tautz, W. Shi, A. Hennemuth, A. Prakosa, H. Wang, G. Carr-White, S. Kapetanakis, et al. Benchmarking framework for myocardial tracking and deformation algorithms: An open access database. *Medical Image Analysis*, 17(6):632–648, 2013.
- M. Unser. Splines: A perfect fit for signal and image processing. *IEEE Signal processing magazine*, 16(6):22–38, 1999.
- P van Dijk. Direct cardiac NMR imaging of heart wall and blood flow velocity. *Journal of computer assisted tomography*, 8(3):429–436, 1984.

- T. Vercauteren, X. Pennec, A. Perchant, and N. Ayache. Diffeomorphic demons: Efficient non-parametric image registration. *NeuroImage*, 45(1):S61–S72, 2009.
- D.M. Vigneault et al. Feature tracking cardiac magnetic resonance via deep learning and spline optimization. *Functional Imag. Modeling Heart.*, page 183, 2017.
- J-U Voigt, G. Pedrizzetti, P. Lysyansky, T.H. Marwick, H. Houle, et al. Definitions for a common standard for 2D speckle tracking echocardiography: consensus document of the EACVI/ASE/Industry task force to standardize deformation imaging. *European Heart Journal-Cardiovascular Imaging*, 16(1):1–11, 2014.
- A. Wang, J. Lu, J. Cai, T-J Cham, and G. Wang. Large-margin multi-modal deep learning for rgb-d object recognition. *IEEE Transactions on Multimedia*, 17(11):1887–1898, 2015.
- J. A Wegelin et al. A survey of partial least squares (PLS) methods, with emphasis on the two-block case. *University of Washington, Department of Statistics, Tech. Rep*, 2000.
- J.H. Wilkinson. *The algebraic eigenvalue problem*, volume 87. Clarendon Press Oxford, 1965.
- H. Wold. Partial least squares. *Encyclopedia of statistical sciences*, 1985.
- S. Wold, C.W.J.D. Albano, W.J. Dunn III, U. Edlund, K. Esbensen, P. Geladi, S. Hellberg, E. Johansson, W. Lindberg, and M. Sjöström. Multivariate data analysis in chemistry. In *Chemometrics*, pages 17–95. Springer, 1984.
- L. Wu, T. Germans, A. Güçlü, M.W. Heymans, C.P. Allaart, and A.C. van Rossum. Feature tracking compared with tissue tagging measurements of segmental strain by cardiovascular magnetic resonance. *Journal of Cardiovascular Magnetic Resonance*, 16(1):10, 2014.
- C. Xu, D. Tao, and C. Xu. A survey on multi-view learning. *CoRR*, abs/1304.5634, 2013. URL <http://arxiv.org/abs/1304.5634>.
- C.W. Yancy, M. Jessup, B. Bozkurt, J. Butler, D.E. Casey, M.H. Drazner, G.C. Fonarow, S.A. Geraci, T. Horwich, J.L. Januzzi, et al. 2013 ACCF/AHA guideline for the management of heart failure. *Circulation*, pages CIR–0b013e31829e8776, 2013.

- P. Yang, W. Gao, Q. Tan, and K-F Wong. Information-theoretic multi-view domain adaptation. In *Proceedings of the 50th Annual Meeting of the Association for Computational Linguistics: Short Papers- Volume 2*, pages 270–274. Association for Computational Linguistics, 2012.
- T. Yingchoncharoen, S. Agarwal, Z.B. Popović, and T.H. Marwick. Normal ranges of left ventricular strain: A meta-analysis. *Journal of the American Society of Echocardiography*, 26(2):185–191, 2013.
- A.A. Young, L. Axel, L.K.B.D. Dougherty, D.K. Bogen, and C.S. Parenteau. Validation of tagging with MR imaging to estimate material deformation. *Radiology*, 188(1):101–108, 1993.
- A.A. Young, C.M. Kramer, V.A. Ferrari, L. Axel, and N. Reichek. Three-dimensional left ventricular deformation in hypertrophic cardiomyopathy. *Circulation*, 90(2):854–867, 1994.
- A.A. Young, S. Dokos, K.A. Powell, B. Sturm, A.D. McCulloch, R.C. Starling, P.M. McCarthy, and R.D. White. Regional heterogeneity of function in nonischemic dilated cardiomyopathy. *Cardiovascular research*, 49(2):308–318, 2001.
- S. Yu, B. Krishnapuram, R. Rosales, and R.B. Rao. Bayesian co-training. *Journal of Machine Learning Research*, 12(Sep):2649–2680, 2011.
- P.A. Yushkevich, J. Piven, H.C. Hazlett, R.G. Smith, S. Ho, J.C. Gee, and G. Gerig. User-guided 3D active contour segmentation of anatomical structures. *NeuroImage*, 31(3):1116–1128, 2006.
- X. Zhang, B.R. Cowan, D.A. Bluemke, J.P. Finn, C.G. Fonseca, A.H. Kadish, D.C. Lee, J.A.C. Lima, A. Suinesiaputra, A.A. Young, et al. Atlas-based quantification of cardiac remodeling due to myocardial infarction. *PLoS One*, 9(10):e110243, 2014.
- D. Zhao and D.G. Daut. Morphological hit-or-miss transformation for shape recognition. *Journal of Visual Communication and Image Representation*, 2 (3):230–243, 1991.
- J. Zhao, X. Xie, X. Xu, and S. Sun. Multi-view learning overview: Recent progress and new challenges. *Information Fusion*, 38:43–54, 2017.
- Y. Zhou, O. Bernard, E. Saloux, A. Manrique, P. Allain, S. Makram-Ebeid, and M. De Craene. 3D harmonic phase tracking with anatomical regularization. *Medical image analysis*, 26(1):70–81, 2015.

